



Aleksei A. Nikitin

**MICROWAVE PROCESSES IN THIN-FILM
MULTIFERROIC HETEROSTRUCTURES AND
MAGNONIC CRYSTALS**



Aleksei A. Nikitin

MICROWAVE PROCESSES IN THIN-FILM MULTIFERROIC HETEROSTRUCTURES AND MAGNONIC CRYSTALS

Dissertation for the degree of Doctor of Science (Technology) to be presented with due permission for public examination and criticism in the Lecture Hall 7443 at Lappeenranta-Lahti University of Technology LUT, Lappeenranta, Finland on the 26th of November, 2021, at noon.

Acta Universitatis
Lappeenrantaensis 998

Supervisors Professor Erkki Lähderanta
LUT School of Engineering Science
Lappeenranta-Lahti University of Technology LUT
Finland

Dr. Alexey B. Ustinov
Department of Physical Electronics and Technology
St. Petersburg Electrotechnical University
Russia

Reviewers Distinguished Professor Gopalan Srinivasan
Department of Physics
Oakland University
USA

Distinguished Professor Zbigniew Celinski
Department of Physics and Energy Science
University of Colorado Colorado Springs
USA

Opponent Professor Alexander Granovskii
Faculty of Physics
Moscow State University
Russia

ISBN 978-952-335-750-1
ISBN 978-952-335-751-8 (PDF)
ISSN-L 1456-4491
ISSN 1456-4491

Lappeenranta-Lahti University of Technology LUT
LUT University Press 2021

Abstract

Aleksei A. Nikitin

Microwave processes in thin-film multiferroic heterostructures and magnonic crystals

Lappeenranta 2021

102 pages

Acta Universitatis Lappeenrantaensis 998

Diss. Lappeenranta-Lahti University of Technology LUT

ISBN 978-952-335-750-1, ISBN 978-952-335-751-8 (PDF), ISSN-L 1456-4491,

ISSN 1456-4491

Artificial spatially periodic magnetic media, known as magnonic crystals (MC), are one of the key building blocks for magnonics widely used for microwave signal processing and data transfer. The general idea of this work was to focus on the perspective multifunction approaches in the field of magnonics in order to overcome the constraints inherent to conventional MC. Artificial ferrite-ferroelectric (multiferroic) structures, exhibiting a strong coupling of magnons and microwave photons, paves a way to this aim. This coupling constitutes new quasiparticles called electromagnons and, therefore, periodic multiferroic structures are known as the electromagnonic crystals. The novelty of this work is based on solutions to the key problems of voltage-controlled microwave devices that have limited their potential for applications. Namely, known MC composed of ferrite-ferroelectric structures show limited potential for a reduction in energy consumption and miniaturisation of magnonic circuits. An understanding of the full wave spectrum of multiferroic multilayers, as well as electromagnonic crystals based on them, is the key to solving the above-mentioned problems. Accordingly, a general electrodynamic theory for dispersion characteristics of waves propagating in ferrite-ferroelectric multilayers was developed. The derivation was based on the full set of Maxwell's equations taking into account retardation effects. Applying the developed theory, an enhancement of the microwave electrodynamic coupling of waves in ferrite-ferroelectric structures was achieved. This peculiarity was used to reduce the control voltage and to increase the tuning efficiency of microwave devices, which promises to be fast and low energy consuming. Theoretical simulations are also supported by experimental results that confirmed the conclusions drawn. For these investigations, conventional microwave measurements were performed. In addition, the experiments using space- and time-resolved Brillouin Light Scattering spectroscopy were carried out to identify peculiarities of spin-wave dynamics in MC that may enrich the properties of artificial spatially periodic structures for modern magnonics.

Keywords: microwaves, magnonics, ferrites, ferroelectric materials, magnonic crystal, spin-wave dynamics, electromagnons

Acknowledgements

I would like to thank my supervisor, Professor Erkki Lähderanta, for his support and his assistance throughout the course of my graduate studies at Lappeenranta-Lahti University of Technology. My sincere appreciation is also due to Professor Alexey B. Ustinov of St. Petersburg Electrotechnical University, Russia. Both Professor Lähderanta and Professor Ustinov spent countless hours working with me on scientific activities, archival publications, and my thesis. In addition, they spent many hours answering questions related to my graduate studies. Their support and encouragement have been invaluable.

My sincere thanks also go to colleagues in University of Kaiserslautern, Germany – Professor Burkard Hillebrands's group – for introducing me to the powerful microwave spectroscopy technique. Here, I would like to acknowledge Pascal Frey, who worked with me on the Brillouin Light Scattering measurements. The samples used in these experiments were graciously provided by Professor Alexey B. Ustinov and Professor Andrii V. Chumak of University of Vienna, Austria. In addition, I wish to express my gratitude to Professor Alexander A. Serga for his participation in many insightful discussions related to these experiments. Additionally, his hospitality during my visits to the University of Kaiserslautern was greatly appreciated.

As well as this, I wish to express my deepest gratitude to late Professor Boris A. Kalinikos[†]. His personal charisma inspired my interest in a research career during my former student days. I was always in awe of his ability to provide clear explanations of non-trivial physical phenomena. Under the supervision of Professor Kalinikos, I recognised many fields of scientific practice and formulated my knowledge into a systematised education. Apart from the abovementioned, I feel inexpressibly thankful to Professor Kalinikos for directing me to attend my first international conferences in physics and for supporting my first internships. Participation in such events allowed me to learn more about advanced research in the field of my scientific interests and gave me the opportunity to discuss my scientific results with a wide range of professionals. Professor Kalinikos has been a skilful supervisor, an outstanding scientist and, above all, a man of wide sympathies.

Last, but certainly not least, I would like to thank my immediate family. Their constant support throughout the course of my graduate studies and my life has been invaluable and is gratefully acknowledged.

Aleksei A. Nikitin
April 2021
Lappeenranta, Finland

Contents

Abstract

Acknowledgements

Contents

List of publications	9
Abbreviations, terms and symbols	11
1 Introduction	13
1.1 Subject and Motivation	13
1.2 Investigation Overview	14
2 Basic concept	17
2.1 Spin waves in ferromagnetic films	17
2.2 Physical properties of ferroelectric films	23
2.3 Artificial multiferroic materials.....	25
2.4 Magnonic and electromagnonic crystals	28
3 All-thin-film multiferroics with coupled ferrite films	33
3.1 Theory for wave spectra of multilayer structures	33
3.1.1 The analytical theory.....	33
3.1.2 Validity of the obtained dispersion relation.....	37
3.2 Wave spectra of all-thin-film multiferroic structures.....	39
3.2.1 Dipole-dipole interaction of spin waves in coupled ferrite films separated by a free space.....	40
3.2.2 Dipole-dipole interaction of spin waves in coupled ferrite films separated by a thin ferroelectric layer	43
3.3 Enhancement of the electric field tuning of the wave spectra.....	48
3.3.1 General features of the doubly hybridised spin-electromagnetic waves.....	49
3.3.2 The effective electric field tuning for voltage-controlled spin-wave logic gates	53
4 All-thin-film multiferroics with coplanar waveguides	57
4.1 Theory for wave spectra of multiferroic structures with coplanar waveguides	57
4.2 General features of wave spectra.....	65
5 Microwave structures with a spatial periodic modulation based on ferrite and ferroelectric films	69
5.1 Electromagnonic crystals based on ferrite-ferroelectric thin-film multilayers.....	69

5.1.1	Theoretical model of an electromagnonic crystal	69
5.1.2	Experimental and theoretical results	71
5.2	Electromagnonic crystals based on a coplanar waveguide with periodic variation of the slot width.....	76
5.3	Reflection-less width-modulated magnonic crystal	80
6	Conclusions	89
6.1	Summary of results.....	89
6.2	Future work	90
	References	93
	Appendix: Transfer matrix	101
	Publications	

List of publications

The present thesis is based on the following papers I – VI, where Aleksei A. Nikitin was the principal author and investigator. The rights have been granted by publishers to include the papers in present dissertation.

- I. **Nikitin, A. A.**, Vitko, V. V., Nikitin, A. A., Kondrashov, A. V., Ustinov, A. B., Semenov, A. A., and Lähderanta, E. (2017) Dual tuning of doubly hybridized spin-electromagnetic waves in all-thin-film multiferroic multilayers, *IEEE Transactions on Magnetics*, 53(11), pp. 1-5.
- II. Nikitin, A. A., Ustinov, A. B., Vitko, V. V., **Nikitin, A. A.**, Kondrahov, A. V., Pirro, P., Lähderanta, E., Kalinikos, B. A., and Hillebrands, B. (2017) Spin-electromagnetic waves in planar multiferroic multilayers, *Journal of Applied Physics*, 122(1), p. 014102.
- III. **Nikitin, A. A.**, Nikitin, A. A., Ustinov, A. B., Lähderanta, E., and Kalinikos, B. A. (2018) Theory of spin-electromagnetic waves in planar thin-film multiferroic heterostructures based on a coplanar transmission line and its application for electromagnonic crystals, *IEEE Transactions on Magnetics*, 54(11), pp. 1-5.
- IV. **Nikitin, A. A.**, Vitko, V. V., Nikitin, A. A., Ustinov, A. B., and Kalinikos, B. A. (2019). Miniature multiferroic interferometer for voltage-controlled spin-wave logic gates. Conference article. In: IEEE Photonics & Electromagnetics Research Symposium - Spring (PIERS-Spring). *PIERS Proceedings*, pp. 1547-1551. City: Rome, Italy.
- V. Frey, P., **Nikitin, A. A.**, Bozhko, D. A., Bunyaev, S. A., Kakazei, G. N., Ustinov, A. B., Kalinikos, B. A., Ciubotaru, F., Chumak, A. V., Wang, Q., Tiberkevich, V. S., Hillebrands, B., and Serga, A.A. (2020) Reflection-less width-modulated magnonic crystal, *Communications Physics*, 3(1), pp. 1-7.
- VI. **Nikitin, A. A.**, Nikitin, A. A., Mylnikov, I. L., Ustinov, A. B., and Kalinikos, B. A. (2020) Electromagnonic crystals based on ferrite-ferroelectric-ferrite multilayers, *IET Microwaves, Antennas & Propagation*. 14(12), pp. 1304-1309.

Author's contribution

- I. Performing the numerical modelling with a computer script; creating the interpretation of the results; and writing the manuscript with co-authors. Corresponding author.
- II. Participation in the development of the theory; performing the numerical modelling with a computer program for the calculation of wave spectra in multiferroic multilayers; and writing the manuscript with co-authors.

- III. Development of the theory; numerical modelling; analysing the theoretical data and preparation of the paper text. Corresponding author.
- IV. Designing the multiferroic interferometer; creating the interpretation of the obtained results; and writing the manuscript with co-authors. Corresponding author.
- V. Designing the width-modulated magnonic crystal, conducting the experiments; analysing the experimental data; and writing the manuscript with co-authors.
- VI. Planning and conducting the experiments, post processed the experimental data, and theoretical analysis, writing of the manuscript with co-authors. Corresponding author.

In paper II, Andrey A. Nikitin was the corresponding author; he developed the theory; performed the literature survey; analysed the theoretical results; and prepared the paper text. In paper V, Pascal Fray was the corresponding author; he performed the experiments on the width-modulated sample; analysed the experimental data; and wrote the manuscript with co-authors.

Abbreviations, terms and symbols

ABC	approximate boundary condition	
BLS	Brillouin Light Scattering	
BST	barium-strontium titanate	
CW	coplanar waveguide	
EMC	electromagnonic crystal	
EMW	electromagnetic wave	
MC	magnonic crystal	
SEW	spin-electromagnetic wave	
SW	spin wave	
TPS	tunable phase shifter	
VNA	vector network analyser	
YIG	yttrium iron garnet	
c	speed of light	$299\,792\,458 \text{ m}\cdot\text{s}^{-1}$
\mathbf{E}	electric field vector	V/m
E_n, ϵ_{00}	phenomenological parameters of ferroelectrics	–
f	frequency	Hz
\mathbf{H}	magnetic field vector	Oe
H_e	uniform external magnetic field	Oe
i	imaginary unit	–
j	number of a layer	–
\mathbf{k}	wave vector	rad/m
M_0	saturation magnetisation	G
\hat{N}	demagnetising tensor	–
S_{eff}	effective length of the electric field strength line	m
U	control voltage	V
Γ	rejection coefficient	–
γ	gyromagnetic ratio of an electron	$1.76 \times 10^{11} \text{ C}\cdot\text{kg}^{-1}$
ΔH	half width of a ferromagnetic resonance curve	Oe
δ	thickness of a ferrite film	m
ϵ	permittivity	–
ϵ_0	vacuum permittivity	$8.85 \times 10^{-12} \text{ F}\cdot\text{m}^{-1}$
κ	transverse wavenumber	rad/m
Λ	length of a period in a magnonic crystal	m
$\hat{\mu}$	vacuum tensor	–
μ_0	vacuum permeability	$4\pi \times 10^{-7} \text{ H}\cdot\text{m}^{-1}$
π, \exp	$\pi = 3.14159 \dots$ and exponent= $2.7183\dots$ (mathematical constants)	

σ	conductivity	S/m
φ	phase shift of a microwave signal	rad
ω	angular frequency	rad/s

1 Introduction

1.1 Subject and Motivation

The dynamics of waves in frequency-agile materials are rich in possibilities but still unknown. The recent increase in the amount of scientific literature related to microwave applications of such materials is an indication of the urgency of the research in this field. Among different physical phenomena that shape the main-stream research directions of wave dynamics, propagation of spin waves (SW) in ferromagnetic film structures attracts considerable attention in connection with their applications in novel data transfer and processing technologies (Kruglyak, 2010; Chumak, 2015). This strong research interest is determined by efficient mechanisms of signal transmission based on the idea that characteristics of spin-wave quanta, such as their phase and occupation numbers, can be regarded as state variables. This is different from a charge in conventional electronics. Therefore, this approach, known as magnonics, is considered novel beyond the complementary metal-oxide-semiconductor platform.

One of the key issues inherent to magnonics is associated with exploiting spin-wave phenomena for efficient data transfer and enhanced logic functionality. An investigation of novel multifunctional approaches paves the way to this aim. An artificial multiferroic structure, which simultaneously exhibits ferroelectricity and ferromagnetism, is a strong candidate for the extension of the functionality of microwave devices (Lu, 2015; Vopson, 2015). This is caused by the possibility to combine the advantages of miniature spin-wave elements with the tunability of their physical properties by both electric and magnetic fields, i.e., dual tunability.

Artificial multiferroics are usually fabricated by combining ferrite and ferroelectric (or piezoelectric) materials to obtain composite or layered micro- and nanostructures in the form of multilayers, pillars, spheres, wires, amongst others (Sun, 2012). The tunability of these structures is provided basically by two effects: the first is the magnetoelectric effect based on the mechanical interaction between ferrite and piezoelectric crystal lattices (Shastry, 2004); and the second effect is the electrodynamic coupling of SW and electromagnetic waves (EMW) in the ferrite-ferroelectric layered structures (Demidov, 2002a). The coupled excitations are known as hybrid spin-electromagnetic waves (SEW).

From the point of view of theoretical and experimental science, SEW excitations in ferrite-ferroelectric bilayers are very suitable for dually controllable devices. However, an effective hybridisation of SW and EMW at microwave frequencies was achieved in multiferroic structures fabricated with relatively thick ferroelectric layers (in the order of hundreds of micrometres). Such thicknesses of a ferroelectric layer led to a relatively high control voltage (up to 1000 V) requirement for an effective electric tuning of the SEW dispersion characteristics. Besides this, a new class of the voltage-controlled microwave devices, which combines multiferroic features and frequency selective

properties inherent in periodic spatial structures, is attractive for the applications at microwave frequencies. In order to distinguish the periodic multiferroic structure from known magnonic (Kruglyak, 2010) and photonic (Erokhin, 2010) crystals, this structure is called the artificial electromagnonic crystal (EMC). Such a name justifies itself because quanta of SEW can be considered electro-active magnons or electromagnons. In contrast to the conventional magnonic crystals, periodic multiferroic structures are characterised by electrically and magnetically tunable band-gaps in the wave spectrum, where propagation of the electromagnons is forbidden.

Aside from the advancement in this field, there are two main motivations for the investigations presented in this thesis. The first is related to the possibility of reducing the control voltage and increasing the tuning efficiency in layered ferrite-ferroelectric structures. This could be achieved for all-thin-film ferrite-ferroelectric-ferrite multilayers and planar structures, such as a coplanar waveguide composed of ferrite and ferroelectric thin films. These features make SEW excitations in layered multiferroic structures promising as a possible replacement for some spin-wave devices presently used in microwave systems.

The second motivation for this investigation is that utilising the all-thin-film multiferroic structures in electromagnonic crystals allows the exploitation for further improvement of the logic gates as well as for tunable microwave devices. These electromagnonic crystals offer promising technological features, such as their small size and low energy consumption. In addition, electromagnonic crystals are compatible with conventional magnonic devices, enabling efficient data transfer and enhanced logic functionality. As a result, the considered structures look favourable not only for investigations of the new physical phenomena but also for applications as a complimentary part to the traditional approach for general computing and microwave signal processing.

1.2 Investigation Overview

A significant amount of work in the area of artificial multiferroics and the voltage-controlled microwave devices have already been published. In their work, Lu and Vopson (Lu, 2015; Vopson, 2015) provided a general theoretical and experimental review, as well as possible applications, of thin-film multiferroics. Demidov, Kalinikos, and Edenhofer dealt with the general dipole-exchange theory for the spectrum of SEW propagating in multiferroic layered structures composed of a ferrite-ferroelectric bilayer (Demidov, 2002a). In contrast, Semenov et al. (Semenov, 2008) performed the first experimental realisation of the planar multiferroic structure combined with a narrow slot transmission line. These structures facilitate voltage tuning in comparison with ferrite-ferroelectric bilayers. Nikitov and Chumak (Nikitov, 2015; Chumak, 2017) gave general reviews of artificial ferromagnetic media, magnonic crystals, as well as their prospects for voltage-controlled microwave devices. Ustinov and Kalinikos dealt with the first prototype of the dual-tunable electromagnonic crystal consisting of a thin-film

magnonic crystal and a ferroelectric slab (Ustinov, 2014). The above research provides an overview of the background work which pertains to this thesis. From these references it can be determined that ferrite-ferroelectric structures provide many unique possibilities for the investigation of various physical phenomena that constitute a basis for novel microwave devices.

One part of this thesis is related to an improvement of an electric field tunability of wave spectra in multiferroics. This improvement is shown for two configurations: (i) coplanar waveguides composed of ferrite and ferroelectric thin films; and (ii) all-thin-film layered structures with coupled ferrites. The latter utilises dipole-dipole interactions of spin-wave modes. It should be noted that, through the application of this phenomenon, the miniature multiferroic interferometer for voltage-controlled spin-wave logic gates was realised for the first time in the present work.

The second part of this work is related to the theoretical and experimental investigations of novel electromagnonic crystals composed of ferroelectric and ferrite films. By analogy with conventional magnonic crystals, periodic multiferroic structures demonstrate the formation of spectral regions, band-gaps, with prohibited wave propagation caused by Bragg scattering. However, the electromagnonic crystals are a marked improvement over spatially periodic ferromagnetic films due to their tunability by an electric field. Moreover, proposed electromagnonic crystals enrich the properties of known multiferroic periodic structures because of a low control voltage required for an effective tuning of band-gaps. Aside from the structures to undergo Bragg scattering, a novel periodic structure with negligible Bragg reflections and a pronounced band-gap in its transmission characteristic will be also discussed. Up till now, a detailed investigation of these structures had not been performed.

Chapter 2 will present a brief literature review which pertains to the results presented in this thesis, while Chapter 3 will focus on the theory for wave spectra of ferrite-ferroelectric multilayers as well as on practical applications of these structures. In Chapter 4 an emphasis will be given to a derivation of a dispersion relation for planar all-thin-film multiferroic structures containing a coplanar waveguide. At the end of Chapter 4, general features of wave spectra of these structures will be discussed. These chapters will provide the basis for the results presented in Chapter 5 which presents experimental and theoretical investigations of the voltage-controlled electromagnonic crystals. Where relevant, an analysis clarifying a mechanism responsible for the band-gap formation in spatial periodic waveguides will be carried out. Finally, Chapter 6 will give a summary of, and a conclusion to this thesis, and present ideas on possible future work.

2 Basic concept

The goal of this chapter is to clarify the origin of wave excitations in various functional media and to present current trends in physics of microwave phenomena. Specifically, the unique properties of ferromagnetic and ferroelectric materials, as well as those of coupled structures based on these media, will be considered.

Ferromagnetics and ferroelectrics will be considered in Sections 2.1 and 2.2, respectively; these materials are widely used for the fabrication of various microwave devices due to their certain advantages. Section 2.3 will describe multiferroic media, where the unique properties of ferromagnetics are combined with functional entities, such as ferroelectrics. In addition, a review of the current status of scientific research as well as a description of fundamental problems, in this hybrid-topic will be given. Finally, Section 2.4 will discuss artificial media created by a spatial periodic modulation of magnetic and multiferroic structures.

2.1 Spin waves in ferromagnetic films

The scientific interest in high-frequency propagating magnetisation waves, known as spin waves (SW), as the elementary excitations in ordered magnetic materials results from not only a possible practical yield, but also from fundamental scientific problems devoted to the physics of microwave phenomena which appeared in ferro-, antiferro- and ferrimagnets. According to the theoretical investigations of dispersion properties in magnetic films, the mechanisms of SW dynamic are determined by two types of interactions between magnetic moments (Gurevich, 1996). The first one is a dipole-exchange interaction, which operates with short waves, as well as thin films with a thickness smaller than the length of the dipole-exchange spin wave. The second interaction considers a SW spectrum in a non-exchange limit when only the dipole-dipole interactions are taken into account. In some literature, this is also called magnetic dipole-dipole interaction. The dispersion characteristics of purely dipole (non-exchange) waves that are known as magnetostatic waves are critical to the analyses presented in this thesis. One should note that hereinafter the terms “spin wave” and “magnetostatic wave” will be used with the same meaning.

The spin wave belongs to the class of slow electromagnetic waves, since its phase velocity is much lower than the speed of light. Therefore, the effects of an electromagnetic retardation can be neglected and the displacement current is not taken into account in the full system of Maxwell equations. In the literature, this approach is known as magnetostatics. Here, the variable components of the magnetic field vector \mathbf{H} and the magnetic flux density vector \mathbf{B} satisfy the magnetostatic equations:

$$\begin{aligned} \operatorname{rot} \mathbf{H} &= 0 \\ \operatorname{div} \mathbf{B} &= 0 \end{aligned} \tag{2.1}$$

where $\mathbf{B} = \mu_0(\mathbf{H} + \mathbf{M})$, and μ_0 is the magnetic permeability of a vacuum. The magnetic field and magnetisation are the sum of the constant and variable components: $\mathbf{H} = \mathbf{H}_0 + \mathbf{h}$, $\mathbf{M} = \mathbf{M}_0 + \mathbf{m}$.

In 1961, for the first time, Damon and Eshbach developed the theory of the spectrum of magnetostatic waves for a magnetised ferrite layer in the non-exchange limit, which is valid only for sufficiently thick films (Damon, 1961). This theory was then modified by Damon and Van de Vaart for the case of a normally magnetised layer (Damon, 1965).

In this research, a relation between the variable component of magnetisation \mathbf{M} and the magnetic field \mathbf{H} , i.e., the magnetic permeability tensor, was found according to the linearised Landau-Lifshitz equation of motion for the magnetisation:

$$\frac{\partial \mathbf{M}}{\partial t} = -|\gamma|[\mathbf{M}, \mathbf{H}]. \quad (2.2)$$

In the general case, the magnetic permeability tensor can be written in the following form:

$$\hat{\mu} = \begin{vmatrix} \mu & i\mu_a & 0 \\ -i\mu_a & \mu & 0 \\ 0 & 0 & 1 \end{vmatrix} \quad (2.3)$$

where $\mu = \frac{\omega_H(\omega_H + \omega_M) - \omega^2}{\omega_H^2 - \omega^2}$; $\mu_a = \frac{\omega\omega_M}{\omega_H^2 - \omega^2}$; $\omega_H = \gamma H_i$; $\omega_M = 4\pi\gamma M_0$;

$H_i = H_e - \hat{N} M_0$; γ is the gyromagnetic ratio of an electron; H_e is the uniform external magnetic field; \hat{N} is the demagnetising tensor; and M_0 is the saturation magnetisation.

Then, the magnetostatic equations were solved. These equations were reduced to differential ones by introducing a scalar magnetostatic potential. In this case, the dispersion relations obtained described the dependence of the frequency on the wave vector $\omega(k)$ in an implicit form. The disadvantage of this algorithm is associated with a possibility to analyse an influence of a material's magnetic parameters on SW dynamics only by numerical simulations, which hinders the physical interpretation of the wave spectra.

In 1967, the method of introducing a scalar magnetostatic potential was used for the first time to find the dispersion characteristics of dipole-exchange SW propagating in ferromagnetic films (Gann, 1967). After that, a large number of scientific work was carried out in this topic; in particular, the theory of dipole-exchange spin-wave spectra was derived by also using the method of Green's tensor functions. A review of studies on dipole-exchange SW was reported by Kalinikos (Kalinikos, 1994), and the obtained

results will not be duplicated here. One should note that both exact and approximate dispersion relations $\omega(k)$ could be explicitly found using the method of Green's tensor functions. However, an application of this method for multilayered structures consisting of two or more magnetic layers is associated with a quite complex formalism, which leads to computational difficulties in the solving of dispersion relations as well as Green's functions.

Regardless of the selected method for the derivation of SW dispersion relations in a ferromagnetic film, a solution of these relations gives three types of spin waves, the properties of which depend critically on the direction of a bias magnetic field \mathbf{H}_0 relative to a film surface. The condition for the propagation of forward volume SW is the perpendicularity of the vector \mathbf{H}_0 and the wave vector ($\mathbf{H}_0 \perp \mathbf{k}$). Such a direction of the field corresponds to a perpendicularly magnetised ferromagnetic film (see Figure 2.1a). In the general case, the spectrum of these waves is multimode. However, higher-order modes are out of consideration for applications in spin-wave devices due to weakly excitations and relatively low group velocities.

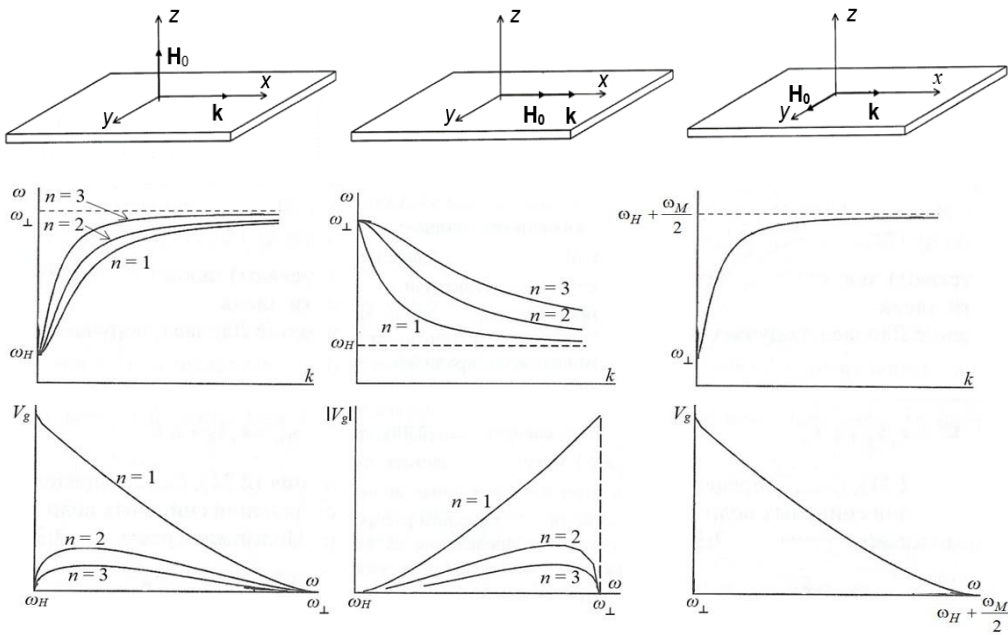


Figure 2.1: Wave spectra and group velocities of SW in a ferromagnetic film for three types of magnetostatic waves: (a) a forward volume SW; (b) a backward volume SW; (c) a surface SW.

Other types of SW existence in the ferromagnetic film magnetised to saturation tangentially to its surface. This configuration corresponds to the parallel magnetisation

case. In contrast to the previous configuration, the properties of such waves depend significantly on the angle between the vectors \mathbf{H}_0 , and \mathbf{k} . In practice, the most commonly used cases are the longitudinal and transverse propagations of SW shown in Figures 2.1b and 2.1c, respectively. The longitudinal wave propagation leads to the formation of backward volume SW having reciprocal behaviour. The term “volume” is derived from the fact that the magnitude of the dynamic magnetic field is distributed harmonically across the film thickness. The transverse wave propagation provides the condition for propagations of surface SW. The term “surface” refers to the nonsymmetric distribution of the dynamic magnetic field having a maximum at one surface of the ferromagnetic film. The dispersion equation of such waves is given by:

$$\omega^2 = \omega_{\perp}^2 + \frac{\omega_M^2}{4}(1 - e^{-2kL}) \quad (2.4)$$

where $\omega_{\perp}^2 = \omega_H(\omega_H + \omega_M)$ and L is the film thickness. A feature of this type of waves is a nonreciprocal behaviour. Physically, this means that waves travelling in opposite directions are pressed against different lateral surfaces of a ferromagnetic film.

In 1980, Grünberg extended the theory of Damon and Eshbach to ferromagnetic double layer systems (Grünberg, 1980, 1981), and since then, many theoretical and experimental work investigating magnetic multilayers has been carried out (Hillebrands, 1990; Kalinikos, 1992; Camley, 1993). It is worth mentioning that theories for spin-wave spectra were developed mostly with a magnetostatic approximation neglecting an electromagnetic retardation. Exceptions are found in the work of Barnas (Barnas, 1988, 1991) and others (Liu, 2008; Ziolkowski, 2001). In these projects, ferrite-dielectric superlattices were investigated for identical parameters of magnetic layers. Dielectric layers between these layers were assumed to be air or dielectric films with a relatively small dielectric permittivity of about 10.

From a historical point of view, the first and widely used tuning mechanism in ferrite media is based on the interaction between the magnetisation of the ferrite and the RF magnetic field. Another tunability mechanism utilises the influence of a conductive plane on the propagation of surface SW which originates from the work of Seshadri (Seshadri, 1970). Here, wave spectra propagating in a metallised ferromagnetic plate was experimentally investigated for the first time. The dispersion relation for this configuration was obtained in the following form:

$$\left(1 + 2 \frac{\omega_H}{\omega_M} + 2s \frac{\omega_H}{\omega_M}\right) \frac{\omega_H + \omega_M - s\omega}{\omega_H + \omega_M + s\omega} = e^{-2kL} \quad (2.5)$$

where s is a parameter taking into account the nonreciprocal behaviour of surface SW. If s is equal to -1, the waves propagate along the ferromagnetic-dielectric interface, and therefore limits for spin-wave excitations correspond to the frequency range

$\omega_{\perp} \leq \omega \leq \omega_H + \frac{\omega_M}{2}$. This range is similar to a case of a free-standing ferromagnetic film (see Figure 2.2a). However, the propagation of surface SW along the ferromagnetic-metal interface leads to the expansion of this frequency region (i.e. $\omega_{\perp} \leq \omega \leq \omega_H + \omega_M$). This behaviour is shown in Figure 2.2b and is described by Equation (2.5) at $s = 1$.

Two years later after Seshadri's work, a ferrite-dielectric-metal structure was experimentally investigated by Bongianni (Bongianni, 1972). In this case, the surface spin-wave dispersion relation is given by:

$$\left(1 + 2 \frac{\omega_H}{\omega_M} + 2s \frac{\omega_H}{\omega_M}\right) \frac{\omega_M + (\omega_H - s\omega)(1 + \tanh(kt))}{\omega_M + (\omega_H + s\omega)(1 + \tanh(kt))} = e^{-2kL} \tag{2.6}$$

where t is the distance between a ferromagnetic film and a perfectly conducting metal plane. The dispersion characteristic for surface SW in these layered structures is shown in Figure 2.2c. It is clear in the figure that the dispersion characteristic demonstrates a nonmonotonic behaviour and has an inflection point at a certain frequency.

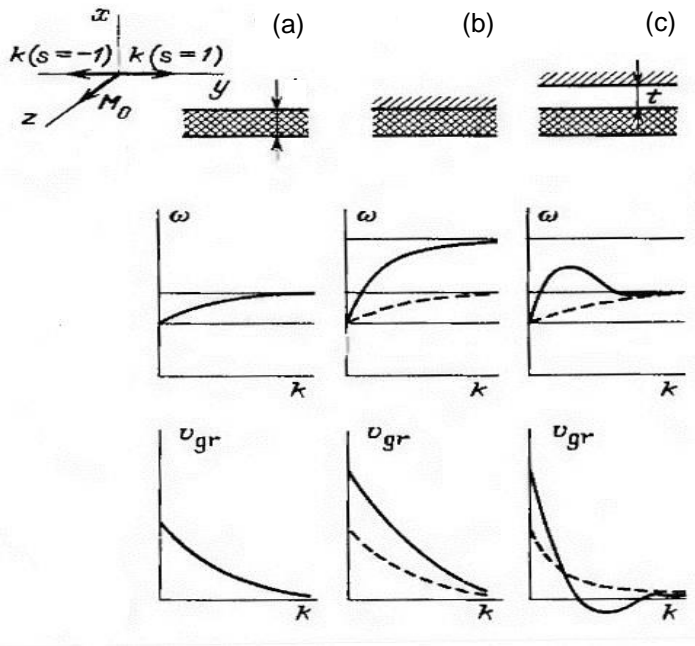


Figure 2.2: Influence of a metal screen on the spectra of surface SW and their group velocities in a ferrite film: (a) Damon-Eshbach configuration; (b) Seshadri configuration; (c) Bongianni configuration.

Microwave devices are produced using different types of magnetic materials: metals such as Ni and Co; alloys such as Permalloy ($\text{Ni}_{80}\text{Fe}_{20}$) and CoFeB; Heusler compounds such as $\text{Co}_2(\text{Fe}_{0.4}\text{Mn}_{0.6})\text{Si}$; and dielectrics like yttrium iron garnets (YIG, $\text{Y}_3\text{Fe}_5\text{O}_{12}$). The main practical advantages of μm -thick single-crystal YIG films over nm-thick metallic materials such as Permalloy or CoFeB are the small magnetic damping, higher group velocity of SW, and wide tunability of their properties at microwave frequencies (Adam, 2002; Özgür, 2009; Serga, 2010). Usually a YIG sample is fabricated in the form of strip cut out from low-damping (less than 5×10^{-4} at 15 GHz) single-crystal films, epitaxially grown on a gadolinium gallium garnet (GGG) substrate.

A strong interest in investigations of spin-wave dynamics in ferromagnetic media and the development of thin-film deposition techniques emerged in the 1970s, leading to the appearance the fundamental research area in this field, known as magnetostatic wave technology (Ishak, 1988). The operation principle of spin-wave devices is based on the phenomena of excitation, propagation and the reception of coherent spin waves. To excite these waves in a wide frequency range (from hundreds of megahertz to hundreds of gigahertz), the microstrip antennas are commonly fed by the microstrip transmission lines of 50- Ω characteristic impedance located on the surface of a YIG film. Figure 2.3 shows an example of the experimental layout and its transmission characteristic.

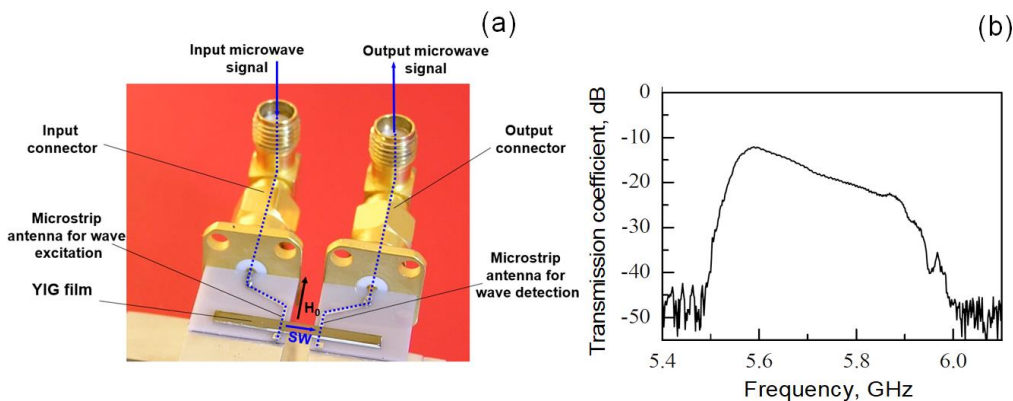


Figure 2.3: (a) Experimental layout; (b) Transmission characteristic of surface SW in a 9.8- μm -thick YIG film with saturation magnetisation 1750 G placed in external magnetic field $H_0 = 1249$ Oe. The distance between the microstrip antennas is 4.5 mm.

One should note that the main advantages of SW in μm -thick YIG films are low propagation losses, a diversity of dispersion characteristics, a nonreciprocal behaviour, and also low phase velocities. As a result, microwave ferrites found a wide variety of applications in spin-wave devices. Among such devices are the filters (Song, 2009), delay lines (Beginin, 2009), phase shifters (Ustinov, 2008), directional couplers (Wang 2018), and multiband filters (Zhang, 2011).

Additionally, increased research interest in the development of the reconfigurable elements for logic circuit construction is apparent. Various platforms exist, including complementary metal-oxide-semiconductor (CMOS), optical, molecular, and magnonic logic circuits. The latter have recently received a great deal of attention beyond the CMOS platform that promises a more efficient mechanism for information processing (Csaba, 2007). A general idea of this mechanism is that a spin-wave quantum can be regarded as a state variable instead of a charge in conventional electronics. This approach allows one to transmit and process a bit of information by exploiting spin-wave phenomena.

From a historical point of view, the first spin-wave logic gate was a Mach-Zender type current-controlled interferometer based on a ferromagnetic film (Kostylev, 2005). Following this, a number of theoretical and experimental research projects have been carried out. For example, a Mach-Zehnder-type spin-wave interferometer for universal logic functions (Lee, 2008); an all-spin logic device with built-in memory (Srinivasan, 2011); a micrometre-scale spin-wave interferometer (Fischer, 2017); and a spin-wave majority gate (Behin-Aein, 2010) were developed. In addition, microwave nonlinear spin waves in ferromagnetic films pave the way to implementation of novel logic elements, especially due to the possible miniaturization of real nonlinear phase shifters [Hansen, 2009] and their compatibility with existing semiconductor technology [Kuanr, 2015].

The performance characteristics of YIG-film devices are controlled by the variation of an externally applied magnetic field; this tuning mechanism was previously mentioned. However, the disadvantage of such devices is connected to the magnetic subsystem, which has large dimensions, a slow operation speed (units of microseconds), and significant power consumption. From a practical point of view, it is beneficial to use a combination of spin-wave waveguides with ferroelectrics or piezoelectrics in order to increase the tunability efficiency of microwave magnetic devices. Electric field tunability will be explained in more detail in the next Section.

2.2 Physical properties of ferroelectric films

Ferroelectrics belong to the group of dielectrics that have a nonlinear dependence of physical properties under an applied external electric field. By analogy with ferromagnetism, the microwave applications are based on a dependence of dielectric permittivity of a ferroelectric material on a control voltage. Its controllability is maintained in a wide range between low and extremely high frequencies. For a microwave engineering of various tunable elements, the ratio of the dielectric permittivity of ferroelectrics at zero electric field $\varepsilon(0)$ to the permittivity at some non-zero electric field $\varepsilon(U_0)$ is important. This ratio is known as tunability and is obtained in the following form (Tagantsev, 2003):

$$n = \frac{\varepsilon(0) - \varepsilon(U_0)}{\varepsilon(0)} = \frac{\varepsilon_{\max} - \varepsilon_{\min}}{\varepsilon_{\max}} (\%). \quad (2.7)$$

Among various ferroelectrics, polycrystalline barium-strontium titanate (BST) is currently considered one of the most suitable dielectric materials for voltage-controlled microwave devices, receiving significant fundamental research interest over the past number of decades. Typical representatives of such materials are a solid solution of BaTiO_3 and SrTiO_3 denoting as $\text{Ba}_x\text{Sr}_{1-x}\text{TiO}_3$, where x is a stoichiometric ratio of Ba and Sr varied from 0 to 0.7. The BST ferroelectrics are widely used in microwave applications due to certain advantages: (i) a high dielectric permittivity in a wide temperature and frequency range; (ii) the absence of frequency dispersion of ε up to 100 GHz; and (iii) a low dielectric loss tangent equal to $(3..5) \cdot 10^{-2}$ at microwaves (Setter, 2006). The BST unit cell exhibits the perovskite structure shown in Figure 2.4.

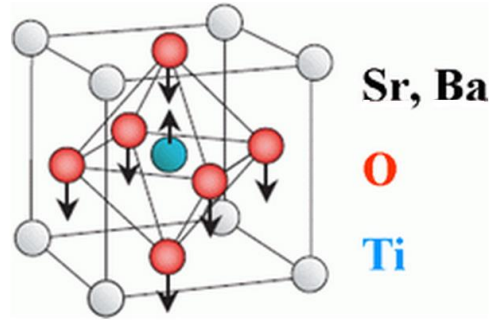


Figure 2.4: Unit cell of a barium-strontium titanate $(\text{Ba,Sr})\text{TiO}_3$.

The perovskite structure is characterised by the general chemical formula ABO_3 , where A and B are cations, while O is an anion. As seen in the cubical lattice, the Ba^{2+} ion is located at its apex. The Ti^{4+} ion occupying the geometrical centre of the cell is surrounded by O^{2-} ions which are located at the centres of the faces of the cube and form the oxygen octahedron. The application of an external electric field causes a deformation of the unit cell and leads to the appearance of spontaneous polarisation.

It should be emphasised that dielectric loss in ferroelectrics is relatively low at temperatures above the phase transition temperature T_c , where a maximum dielectric permittivity is observed. At temperatures below T_c , the material is in a ferroelectric phase spontaneous polarisation. However, ferroelectrics are in the paraelectric phase at $T > T_c$ and do not exhibit the spontaneous polarisation. Utilization of ferroelectrics in the microwave applications is mainly possible in the temperature range of the paraelectric phase. This is caused not only by a low dielectric loss in ferroelectrics, but also by a stronger dependence of the dielectric permittivity on the magnitude of the external electric field.

From a technological point of view, one of the simplest ways to change the polarisation of ferroelectrics is to apply a voltage to thin metal electrodes deposited on its surface. The expression approximating the dependence of the ferroelectric permittivity versus the control voltage U is given by:

$$\varepsilon(U) = \frac{\varepsilon(0) - \varepsilon(\infty)}{1 + (U / U_{00})^2} + \varepsilon(\infty) \quad (2.8)$$

where $\varepsilon(0)$ and $\varepsilon(\infty)$ are ferroelectric permittivities at zero bias voltage and at dielectric breakdown voltage, respectively; $U_{00} = \frac{3}{2} S_{eff} E_n \left(\frac{\varepsilon_{00}}{\varepsilon(0)} \right)^{3/2}$. Here E_n and ε_{00} are phenomenological parameters dependent on the Curie temperature, and S_{eff} is an effective length of the electric field strength line.

The features of BST ferroelectrics mentioned above enable them to be implemented in a set of microwave applications including tunable filters (Nath, 2005), switches (Karmanenko, 2004), parametric generators (Vendik, 1999), and other voltage-controlled devices. In comparison with magnetic tuning, the advantages of the electric tuning of microwave devices based on ferroelectrics are operation speed, power consumption, and the size of the control system, but such devices lose on a range of this tuning.

2.3 Artificial multiferroic materials

Increased demands in frequency-agile materials used for microwave applications have led to the appearance of composite materials known as multiferroic structures. Endowed with both ferromagnetic and ferroelectric features they are potentially capable of enhancing the functionality of microwave devices by adding the advantages of electric tuning to spin-wave elements. However, the key issue inherent to applications of multiferroics is associated with the strength of the magneto-electric coupling.

In general, multiferroics may be divided into two major categories, the first of which is single-phase homogeneous media ordered in a certain range of temperatures, both ferroelectrically and ferromagnetically (e.g., BiFeO_3). However, such natural multiferroics show a limited potential for real microwave devices due to extremely low values of magneto-electric coefficients. In order to overcome this limitation, a second category of multiferroics has been proposed. Usually, these multiferroics are fabricated by a thin-film deposition in the form of layered (composite or monolithic) materials, where the coupling interactions between different phases are realised [Sun, 2012]. Such composite structures are widely known as artificial or extrinsic multiferroics.

The interaction between different layers of composite structures exhibiting ferromagnetic and ferroelectric nature may be due to two effects. The first explores the

magneto-elastic properties of most ferromagnetic materials combined with ferroelectrics that are usually excellent piezoelectrics (e.g., lead zirconate titanate). The general idea of the magnetoelectric interaction is that an external electric field is applied to a piezoelectric produces mechanical strain. This strain leads to a variation of the internal static magnetic field and consequently to a shift of a spin-wave spectrum. The theory of this effect was developed by Shastry et al. (Shastry, 2004).

A second effect utilises the electrodynamic interaction between microwave electromagnetic and spin waves in the layered ferrite-ferroelectric structures. This interaction leads to a formation of hybrid spin-electromagnetic waves (SEW) (Anfinogenov, 1989; Demidov, 2002a). Dispersion characteristics of hybrid SEW combine features of electromagnetic waves in ferroelectric-based materials and spin waves in ferrites. Therefore, the resulting wave spectrum is dually controllable by both electric and magnetic fields. The electric tuning is realised through a variation of the dielectric permittivity of a ferroelectric layer by changing an applied electric field, while the magnetic tuning is provided by a dependence of the magnetic permeability of ferrites on a bias magnetic field.

The general dipole-exchange theory of SEW spectra in layered multiferroic structures consisting of ferrite-ferroelectric bilayer structure was developed in 2002 (Demidov, 2002a). The theory predicted that only relatively thick ferroelectric layers (on the order of hundreds of micrometres) provide effective hybridisation of spin waves and electromagnetic waves at microwave frequencies and, consequently, an effective electric field tuning of the SEW dispersion (see Figure 2.5). These findings were also confirmed by experiments (Fetisov, 2005). In later research, the electrodynamic theory of SEW spectra was extended to an arbitrary number of ferrite and ferroelectric layers (Grigorieva, 2009). These theories were developed with a tensorial Green's function method taking into account electromagnetic retardation. However, an application of the extended theory for the investigation of SEW modes in complex multilayered structures consisting of two or more magnetic layers has not yet been published. This is obviously due to computational difficulties with finding the zeroes of an infinite matrix determinant, which represents the dispersion equation within the Green's function method.

One of the main trends in the development of modern physics and electronics is associated with the development of miniature microwave devices and electronically tunable devices with a high performance, small size, and low power consumption. These features may be achieved by utilising multiferroic structures containing ferroelectric and ferrite films. As seen in the literature, the multiferroic structures had a great success in the development of microwave devices. Among them are the delay lines (Fetisov, 2005), the tunable microwave resonators (Ustinov, 2006), and the ferromagnetic resonance phase shifters (Leach, 2010).

A further development of microwave multiferroic devices for general computing and microwave signal processing is connected with thin-film structures (Zhu, 2017). In

particular, thin-film ferrite-ferroelectric structures provide an opportunity to reduce the control voltage that is desirable for exploiting of the tunable devices based on them. Therefore, from a practical point of view, it would be beneficial to investigate novel thin-film heterostructures exploiting the spin-electromagnetic waves for enhanced logic control as well as for tunable microwave devices.

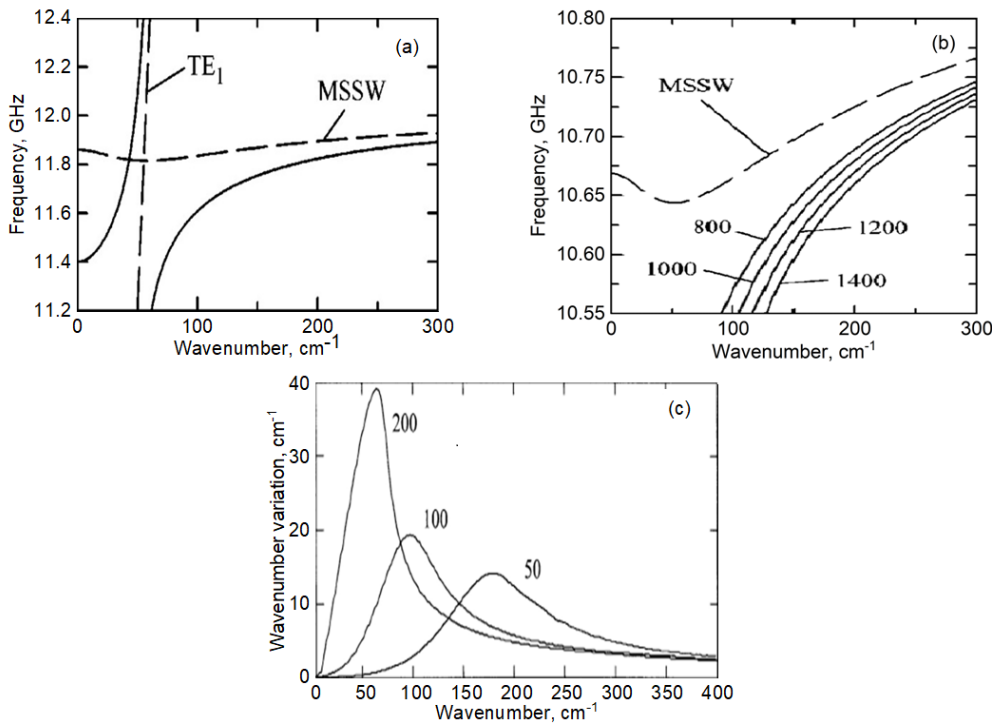


Figure 2.5: (a) Spectrum of the hybrid SEW formed due to an electrodynamic interaction between fundamental mode of a surface SW and electromagnetic mode TE₁; (b) Electric field tuning of the dispersion characteristic. Adapted from (Demidov, 2002a); (c) Wavenumber variation as a function of the absolute value of the wavenumber when dielectric permittivity varies between 1000 and 500 for different dielectric layer thicknesses: 50 μm , 100 μm , and 200 μm . Adapted from (Demidov, 1999).

Until now, high research activity has mainly given to two-layered multiferroic structures consisting of one ferrite and one ferroelectric layers. As previously mentioned, there is an essential disadvantage in this configuration. An effective coupling at microwave frequencies was achieved in multiferroic structures fabricated with a relatively thick (200–500 μm) ferroelectric layer. Such thicknesses of the ferroelectric layer lead to relatively high control voltages (up to 1000 V) required for an effective electric tuning of the SEW dispersion characteristics.

In order to increase the energy efficiency of microwave devices based on layered multiferroic structures, Semenov et al. proposed to use thin-film ferrite-ferroelectric structures combined with a slot line (Semenov, 2008). In this case, the SEW are originated from an electrodynamic coupling of the EMW propagating in a slot transmission line with the SW existing in a ferrite film. Moreover, the obtained results were validated by both experimental measurements and theoretical analysis (Nikitin, 2014; Nikitin, 2015b). However, other thin-film ferrite-ferroelectric structures exhibiting an effective hybridisation of waves in the range of microwave frequencies have not been proposed until now. Thus, theoretical and experimental investigations of wave dynamics in novel all-thin-film ferrite-ferroelectric structures will be presented in this thesis.

2.4 Magnonic and electromagnonic crystals

In the last decade, extensive investigations of peculiarities of spin-wave dynamics in diverse magnetic materials have opened up new avenues resulting in a novel scientific direction known as magnonics. An increased research activity in this field is largely due to the features of the dynamic eigen-excitations of a magnetically ordered material. Opposed to the conventional electronics, the modern magnonics operates with quanta of spin waves in magnetically ordered media (Khitun, 2008; Chumak, 2014). These wave quanta are widely known as magnons, the use of which opens up possibilities to develop novel microwave devices for data transmission free from the drawbacks inherent to modern electronics, such as dissipation of energy due to Ohmic losses.

One of the most promising building blocks for magnonic devices is constituted by artificial spatially periodic magnetic media, known as magnonic crystals (MC) (Krawczyk, 2014; Chumak, 2017). In these structures, the formation of spectral regions, band-gaps, with prohibited wave propagation is caused by Bragg scattering. Among the different types of magnetic materials, the epitaxial yttrium-iron garnet films are widely used for MC fabrication due to certain essential advantages: (i) small out-of-band insertion losses; (ii) deep rejection bands; (iii) a charge-less propagation; and (iv) well-developed techniques of MC fabrication including a metal deposition, a chemical etching, an ion implantation, or other methods to produce a periodic variation of any magnetic parameter. Therefore, magnonic crystals based on YIG films are an excellent testbed for the observation of a wide variety of fundamentally important effects that have immense practical importance for modern signal processing applications.

From the point of view of experimental science, the pioneer work devoted to the propagation of SW in a spatially periodic ferromagnetic film was carried out in the late 1970s (Sykes, 1976). Following this, MC attracted an increased research interest due to the detection of many linear and nonlinear spin-wave phenomena in spatially periodic YIG films. These include selective SW propagations (Ordóñez-Romero, 2016), chaotic behaviour (Grishin, 2011), and soliton formations (Grishin, 2014), for example.

A large number of published experimental investigations devoted to various linear and nonlinear spin-wave phenomena in the range of microwave frequencies were performed by the space- and time-resolved Brillouin Light Scattering (BLS) spectroscopy (Demokritov, 2001; Nikitov, 2015, Sorensen 2019). The application of this technique possess a strong potential for experimental physics mostly due to three factors. First, various spin-wave dynamics governed by the strength of the magnetic field and its orientation relative to the plane of the film are observed by this powerful tool method. The second factor is that both low-amplitude thermal and high-amplitude SW excited by an external microwave field could be detected. Last but not least is high spatial resolution, which is commonly equal to 30-50 microns in diameter and depends on the size of the laser beam focus. Thus, optical spectroscopy based on the BLS technique provides a unique opportunity to study the dynamics of spin-wave excitations in magnetically ordered materials.

For example, Sheshukova et al. dealt with investigations of SW dynamic in the MC based on the width-modulated YIG film by using the space- and time-resolved BLS spectroscopy (Sheshukova, 2014). The dispersion and transmission characteristics of the proposed structure are shown in Figure 2.6, which shows the periodicity of the YIG film results in the appearance of the band-gaps in the spin-wave spectrum. This modifies the dispersion of waves in the vicinity of the band-gaps. Thus, the width-modulated MC shows the formation of several pronounced band-gaps where the level of attenuation sharply increases. These regions of enhanced microwave attenuations are marked by I and III in Figure 2.6. In addition, there is a region II around the band-gaps, where SW modes are transmitted with a relatively low attenuation. The frequencies marked in Figure 2.6 by black dots were chosen for detailed analysis of the SW dynamics for the different propagation regimes by BLS measurements. Some of these results showing spatial distributions of SW intensities are shown in Figure 2.7.

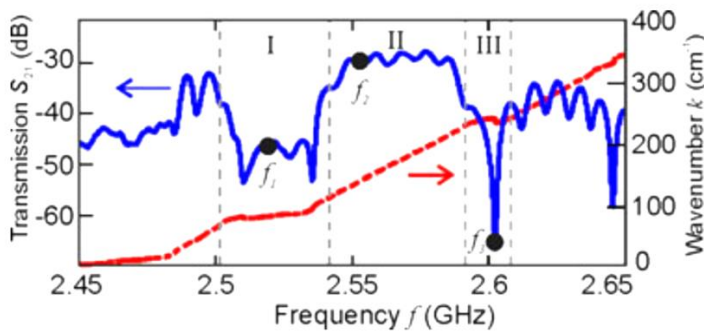


Figure 2.6: Transmission characteristic (blue solid line) and dispersion characteristic of surface spin waves (red dashed line). The black circles indicate the frequencies, where the BLS measurements were performed: $f_1 = 2.519$ GHz, $f_2 = 2.55$ GHz, $f_3 = 2.608$ GHz. Regions I, II, and III denote the areas with different spin-wave dynamics. Adapted from (Sheshukova, 2014). © [2014] IEEE

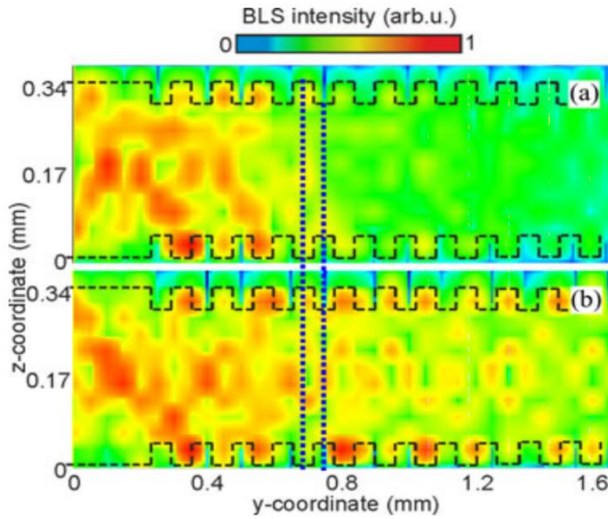


Figure 2.7: Spatial distribution of spin-wave intensity in the magnonic crystal at different frequencies of the input microwave signal: (a) $f_1 = 2.519$ GHz; (b) $f_2 = 2.55$ GHz. Adapted from (Sheshukova, 2014). © [2014] IEEE

As shown in Figure 2.7a, the spatial distribution of intensities of surface SW is characterised by an enhanced microwave attenuation at a frequency of the initial signal $f_1 = 2.519$ GHz corresponding to the first band-gap. Basically, this is caused by reflections of a microwave signal from the boundaries of the periodic waveguide. In order to take into account this effect, both wave propagations in an unstructured ferrite film and reflections from the junctions of the consecutive sections of a MC should be considered. Thus, the rejection coefficient for the waveguide junction is given by (Chumak, 2009b):

$$\Gamma_{0-1} = (k_1 - k_0) / (k_1 + k_0) \quad (2.9)$$

where k_0 and k_1 are the wavenumbers of the SW in the unstructured film corresponding to consecutive sections of a MC.

Apart from the fundamental investigations given above, the magnonic crystals are successfully utilised for the realisation of various microwave devices such as power limiters (Ustinov, 2010), magnetic field sensors (Inoue, 2011), microwave oscillators (Bankowski, 2015), spin-wave logic gates (Nikitin, 2015a), and magnon transistors (Chumak, 2014), to name but a few. In addition, another type of periodic spatial structure, known as dynamic magnonic crystals, were proposed by Chumak et al. (Chumak, 2009a). Promising functionalities of these crystals arise from the nonreciprocal behaviour and dynamic controllability that provides altering of the band-gaps from full rejection to full transmission.

Despite the functional advantages of magnonic crystals, there is a list of challenges to be solved to enhance their practical value, among which are the reduction in energy consumption and miniaturisation of magnonic circuits. Voltage (or electric field) control of magnon currents promises to be fast and low energy consuming. As previously shown, this can be achieved using ferrite-ferroelectric (multiferroic) heterostructures, where an electrodynamic interaction between high-frequency electromagnetic and spin waves leads to a formation of the hybrid SEW. By analogy with natural multiferroic solids, the quanta of these waves are considered electro-active magnons or electromagnons. Thus, the multiferroic periodic structures, known as electromagnonic crystals (EMC), demonstrate electrically and magnetically tunable band-gaps where propagation of the electromagnons is forbidden.

The EMC are usually fabricated as a combination of a spatially periodic magnetic film with a ferroelectric slab into a layered structure. Advantages of the multiferroic periodic waveguides in comparison with conventional MC are due to their tunability through an application of an electric field to a ferroelectric layer. The first prototype of the electromagnonic crystal consisting of a thin-film magnonic crystal and a ferroelectric slab was proposed by Ustinov and Kalinikos (Ustinov, 2014). Figure 2.8 shows the frequency responses of such a multiferroic periodic structure for different values of an external magnetic field where $H = 1748$ Oe (Figure 2.8a), and $H = 1853$ Oe (Figure 2.8b) at zero electric field E , as well as for $H = 1748$ Oe and $E = 15$ kV/cm (Figure 2.8c).

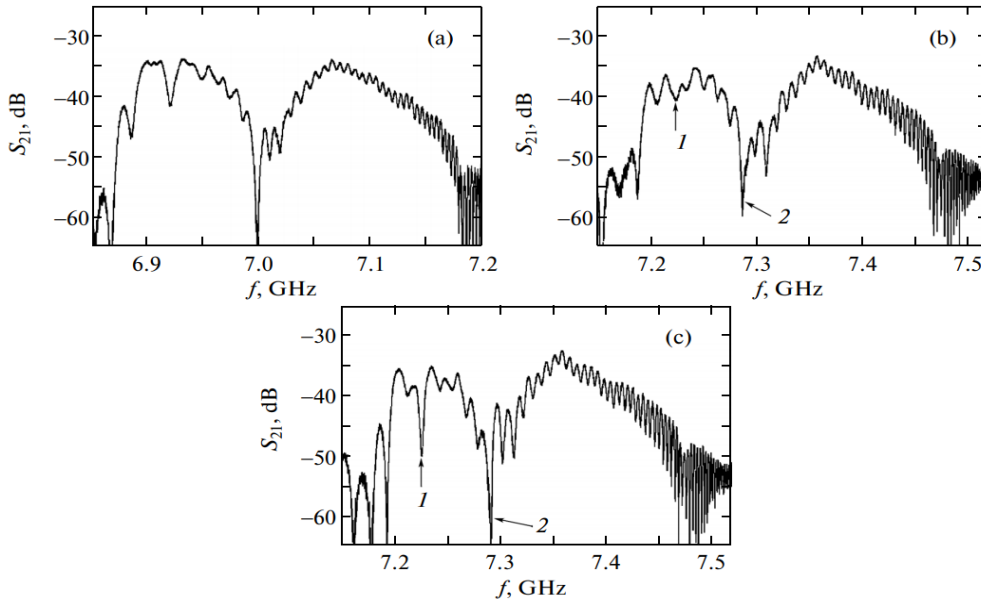


Figure 2.8: Frequency responses of the spatially periodic multiferroic structure for different external magnetic fields H and electric fields E : (a) $H = 1748$ Oe and $E = 0$ kV/cm; (b) $H = 1853$ Oe and $E = 0$ kV/cm; and (c) $H = 1853$ Oe and $E = 15$ kV/cm. The thickness of the ferroelectric slab is $200 \mu\text{m}$. Adapted from (Ustinov, 2014).

This first working prototype device was of considerable importance for the development of electromagnonic crystals. Since then, a number of theoretical and experimental projects have been carried out (Morozova, 2014, 2016; Ustinova, 2016). For example, a dynamic EMC demonstrating a voltage-controlled depth of band-gaps has been realised recently (Ustinov, 2019). Promising functionalities of these spatially periodic multiferroic structure arise from the desired band structure, which originates from a spatial variation of a dielectric permittivity of periodically poled regions of a ferroelectric slab by an application of a local electric field.

It is worth noting that the above mentioned structures were fabricated with a relatively thick (more than 100 μm) ferroelectric layer to provide an effective hybridisation of the SW and the EMW at microwave frequencies. As a result, a relatively high control voltage up to 1000 V was applied to multiferroic periodic structures to achieve an effective electric tuning of band-gap positions. Therefore, it would be of an immense practical benefit to engineer an electromagnonic crystal demonstrating an enhanced electric field control of band-gaps at a low voltage. An improvement on such a multiferroic periodic structure is one of the aims of this thesis. This modification can be realised through utilising all-thin-film multiferroics providing the opportunity to reduce a control voltage that is desirable for exploiting EMC.

3 All-thin-film multiferroics with coupled ferrite films

In this chapter, a general electrodynamic theory is developed for dispersion characteristics of spin-electromagnetic waves (SEW) propagating in multiferroic structures consisting of multiple ferrite and ferroelectric layers. In contrast to the pioneering work of Grünberg (Grünberg, 1980, 1981), this theory takes into account an electromagnetic retardation and is developed for multiferroic structures composed of an infinite number of layers. In addition, the dispersion relation is found by using the transfer matrix method, which is a marked improvement over those theories using the tensorial Green's function method (Demidov, 2002a; Grigorieva, 2009). An application of these theories for the investigation of SEW modes in complex multilayered structures consisting of two or more magnetic layers has not yet been published. This is obviously due to computational difficulties with finding the zeroes of an infinite matrix determinant, which represents the dispersion equation within the Green's tensor functions. In this context, it is appropriate to remember the work of Barnas (Barnas, 1994), which used a transfer matrix method to calculate the spectra of retarded waves. Finally, in contrast to the work of Barnas, different parameters of ferrite and ferroelectric layers are used in the developed theory. As a result, the derived dispersion relation for the multiferroic structures can be used for a wide range of various tasks that have promising applications for information processing at microwave frequencies.

3.1 Theory for wave spectra of multilayer structures

As previously shown in Chapter 2, the magnetostatic approximation to Maxwell's equations can be used for a theoretical analysis of spin waves with phase velocities much lower than the speed of light. In addition, the spin-wave spectrum in the non-exchange limit, when only the dipole-dipole interactions are taken into account, is considered. Usually, the inhomogeneous exchange interaction is excluded from a consideration for high-frequency magnetisation waves with wavenumbers less than 10^4 rad/cm. This approach is widely used in magnetostatic wave technology.

3.1.1 The analytical theory

Figure 3.1 shows schematically a magnetic multilayered structure surrounded by a free space. It consists of the $2N+1$ layers stacked along the y -axis, the wave propagates along the x -axis. The structure is magnetised to saturation by a uniform magnetic field \mathbf{H} directed along the z -axis. For the particular case of the single ferrite layer, this geometry corresponds to the Damon-Eshbach configuration providing the propagation of surface SW. A detailed discussion of these waves was given in Chapter 2.

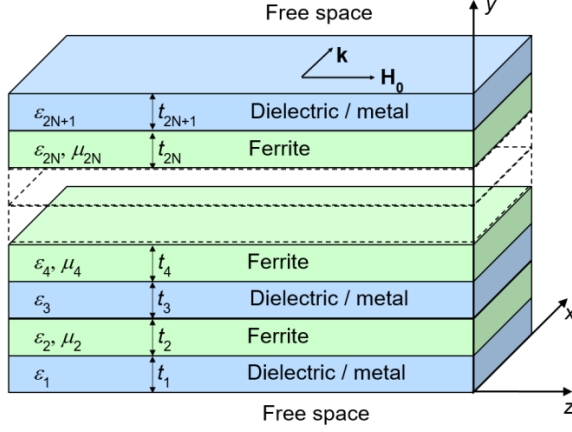


Figure 3.1: Multilayered heterostructure.

Each layer with number j in the proposed structure exhibits magnetic or dielectric properties based on its magnetic permeability and dielectric permittivity. For example, dielectric layers can be ferroelectrics in a paraelectric phase or conductive layers by means of a complex permittivity:

$$\boldsymbol{\epsilon}_{2j+1} = \boldsymbol{\epsilon}'_{2j+1} - i\boldsymbol{\epsilon}''_{2j+1} = \boldsymbol{\epsilon}_{2j+1} - i \frac{\boldsymbol{\sigma}_{2j+1}}{\epsilon_0 \omega} \quad (3.1)$$

where j is any integer from 1 to N ; ϵ_0 is the vacuum permittivity; ϵ_{2j+1} and σ_{2j+1} are the dielectric permittivity and conductivity of an odd layer, respectively.

In accordance with Figure 3.1, ferrite layers have different thickness t_{2j} , dielectric permittivity ϵ_{2j} , and saturation magnetisation M_{2j} . The magnetic properties of the ferrite layers are described by magnetic complex permeability tensors $\hat{\mu}_{2j}$ that is given by:

$$\hat{\mu}_{2j} = \begin{pmatrix} \mu_{d2j} & i\mu_{a2j} & 0 \\ -i\mu_{a2j} & \mu_{d2j} & 0 \\ 0 & 0 & 1 \end{pmatrix} \quad (3.2)$$

where $\mu_{d2j} = 1 + \frac{(\omega_h + i\alpha_{2j}\omega)\omega_{m2j}}{(\omega_h + i\alpha_{2j}\omega)^2 - \omega^2}$; $\alpha_{2j} = \gamma\mu_0\Delta H_{2j}/\omega_h$; $\mu_{a2j} = \frac{\omega\omega_{m2j}}{(\omega_h + i\alpha_{2j}\omega)^2 - \omega^2}$;

$\omega_h = \gamma\mu_0 H_0$; $\omega_{m2j} = \gamma\mu_0 M_{2j}$; $\gamma = 1.76 \times 10^{11} \text{C} \cdot \text{kg}^{-1}$ is the gyromagnetic ratio of an electron; $\mu_0 = 4\pi \times 10^{-7} \text{H} \cdot \text{m}^{-1}$ is the vacuum permeability; ΔH_{2j} is the half width of

the ferromagnetic resonance curve; and ω is an angular frequency. Each ferrite is surrounded by the dielectric or metal layers with thickness t_{2j+1} . Thereby even j corresponds to a ferrite layer and odd j corresponds to a dielectric or metal layer.

It is well known that Maxwell's equations can be divided into two systems of differential equations describing two fundamental sets of TE and TM modes (Collin, 1991). For the considered geometry shown in Figure 3.1, the TE and TM modes have the following field structures: $\mathbf{E}(E_x, 0, 0)$, $\mathbf{H}(0, H_y, H_z)$ and $\mathbf{E}(0, E_y, E_z)$, $\mathbf{H}(H_x, 0, 0)$, respectively. As shown in Demidov's work (Demidov, 2002a) for a ferrite-ferroelectric bilayer, the surface SW mode of a ferrite layer has the strongest coupling with the TE modes of a ferroelectric layer due to an effective overlapping of their dynamic components of the magnetic fields. Therefore, only the TE modes of the EMW spectrum will be considered.

The Helmholtz equations are derived from the Maxwell's equations for the electric field component E_z of the TE modes for each layer. These Helmholtz equations have the following form:

$$\frac{\partial^2 E_z}{\partial y^2} + \frac{\partial^2 E_z}{\partial x^2} + \omega^2 \mu_0 \mu_m \varepsilon_0 \varepsilon_m E_z = 0 \quad (3.3)$$

where m is an order number corresponding to ferrite ($m = 2j$) or dielectric ($m = 2j + 1$) layers; $\mu_{2j} = \mu_{\perp 2j} = (\mu_{d2j}^2 - \mu_{a2j}^2) / \mu_{d2j}$; $\mu_{2j+1} = 1$; and $\varepsilon_0 = 8.85 \times 10^{-12} \text{ F} \cdot \text{m}^{-1}$ is the vacuum permittivity.

Solutions of Equation (3.3) are

$$\begin{aligned} E_z &= A_{2N+2} e^{-\kappa_0 y} e^{-ikx} \\ E_z &= A_0 e^{\kappa_0 y} e^{-ikx} \end{aligned} \quad (3.4)$$

for the free space above and below the structure, respectively. Here, $\kappa_0 = \sqrt{k^2 - \omega^2 \mu_0 \varepsilon_0}$ is the transverse wavenumber for a free space, and k is the wavenumber of the carrier wave. Inside the ferrite and ferroelectric layers, the solutions are

$$\begin{aligned} E_z &= A_{2N+2} e^{-\kappa_{2j} y} e^{-ikx} \\ E_z &= A_0 e^{\kappa_{2j} y} e^{-ikx} \end{aligned} \quad (3.5)$$

where $\kappa_{2j} = \sqrt{\omega^2 \mu_0 \varepsilon_0 \varepsilon_{2j} \mu_{\perp 2j} - k^2}$ is the transverse wavenumber for the ferrite layers ($m = 2j$) and $\kappa_{2j+1} = \sqrt{\omega^2 \mu_0 \varepsilon_0 \varepsilon_{2j+1} - k^2}$ is the transverse wavenumber for the dielectric

layers ($m = 2j + 1$); $D_m = \sum_{s=1}^m t_s$ is the total thickness of the layers. The transverse wavenumbers κ_{2i} are imaginary in the frequency ranges corresponding to the surface SW spectra from $\omega_{\perp 2j}^2 = \omega_H(\omega_H + \omega_{M2j})$ to $\omega_H + \omega_{M2j}/2$ that embody the surface character for the SW in the Damon-Eshbach configuration (see Figure 2.2a).

The connection between the magnetic field component H_x and the electric field component E_z was found from Maxwell's equations for each layer. Finally, unknown coefficients A_m and B_m for all layers (see Equations (3.4) and (3.5)) are connected through the electrodynamic boundary conditions. Such a connection between the coefficients in adjacent layers can be expressed as follows:

$$\mathbf{P}_j \begin{bmatrix} A_j \\ B_j \end{bmatrix} = \mathbf{Q}_j \begin{bmatrix} A_{j+1} \\ B_{j+1} \end{bmatrix}, \quad (3.6)$$

where \mathbf{P}_j and \mathbf{Q}_j are matrices that connect the unknown coefficients A_j , B_j with A_{j+1} , B_{j+1} in the adjacent layers with numbers j and $j+1$.

Finally, the substitution of the field components to the electrodynamic boundary conditions for the interfaces between the layers makes it possible to express the coefficient A_0 by the coefficient A_{2N+2} . The derived system of equations has the following form:

$$\begin{cases} A_0 = (T_{11} + T_{12})A_{2N+2} \\ A_0 = (T_{21} + T_{22})A_{2N+2} \end{cases}, \quad (3.7)$$

where T_{11} , T_{12} , T_{21} , and T_{22} are the elements of the square matrix

$$\mathbf{T} = \prod_{m=0}^{2N+1} (\mathbf{P}_m)^{-1} \cdot \mathbf{Q}_m: \quad \mathbf{P}_0 = \begin{pmatrix} -1 & 0 \\ 0 & -\kappa_0 \end{pmatrix}, \quad \mathbf{P}_{2j} = \begin{pmatrix} 0 & -1 \\ \frac{\kappa_{2j}}{\mu_{\perp 2j}} & \frac{\kappa \mu_{a2j}}{\mu_{d2j} \mu_{\perp 2j}} \end{pmatrix},$$

$$\mathbf{P}_{2N+1} = \begin{pmatrix} 0 & -1 \\ \kappa_{2N+1} & 0 \end{pmatrix}, \quad \mathbf{P}_{2j+1} = \begin{pmatrix} 0 & -1 \\ \kappa_{2j+1} & 0 \end{pmatrix}, \quad \mathbf{Q}_0 = \begin{pmatrix} \tan(\kappa_1 t_1) & 1 \\ -\kappa_1 & -\kappa_1 \tan(\kappa_1 t_1) \end{pmatrix},$$

$$\mathbf{Q}_{2j} = \begin{pmatrix} \tan(\kappa_{2j+1}t_{2j+1}) & 1 \\ -\kappa_{2j+1} & -\kappa_{2j+1}\tan(\kappa_{2j+1}t_{2j+1}) \end{pmatrix},$$

$$\mathbf{Q}_{2j+1} = \begin{pmatrix} \tan(\kappa_{2j+2}t_{2j+2}) & 1 \\ \frac{\kappa\mu_{a2j+2}\tan(\kappa_{2j+2}t_{2j+2})}{\mu_{d2j+2}\mu_{\perp 2j+2}} - \frac{\kappa_{2j+2}}{\mu_{\perp 2j+2}} & \frac{-\kappa_{2j+2}\tan(\kappa_{2j+2}t_{2j+2})}{\mu_{\perp 2j+2}} \end{pmatrix}, \mathbf{Q}_{2N+1} = (-1)\mathbf{P}_0.$$

The determinant of Equation (3.7) is denoted as $f(\omega, k) = T_{11} + T_{12} - T_{21} - T_{22}$. The vanishing of the determinant results in the dispersion relation

$$f(\omega, k) = 0 \quad (3.8)$$

To summarise, the developed theory describes the spectrum of the spin-electromagnetic waves in the ferrite-dielectric-metal structures with an arbitrary sequence of layers. The obtained dispersion relation has a complex form, where $k = k' + jk''$ is the complex propagation constant and where k' and k'' are the phase and attenuation constants, respectively.

3.1.2 Validity of the obtained dispersion relation

In order to demonstrate proof-of-concept of the proposed theory, it is necessary to obtain dispersion characteristics for some configurations that can be compared with the results of earlier work.

First, the dispersion characteristics of SW propagating in different ferrite-dielectric-metal multilayered structures were calculated. Figure 3.2 shows the dispersion characteristics calculated for various layered structures, listed below, based on the ferrite film and placed in the external magnetic field of $H_0 = 1500$ Oe. Here, the solid lines show dispersion characteristics calculated according to the developed theory. The symbols correspond to the results obtained by the Damon-Eshbach, Seshadri, and Bongianni dispersion relations (see Equations (2.4) - (2.6)). The black line and open squares show the dispersion characteristics of the SW in the free ferrite layer (all layers except the ferrite with the number $j = 2$ have zero thicknesses, $t_2 = 20$ μm , $\varepsilon_2 = 14$, and $M_2 = 1750$ G). The blue line and open circles correspond to the spin-wave spectrum for the ferrite layer covered by a perfectly conducting metal plane ($t_2 = 20$ μm , $\varepsilon_2 = 14$, $\sigma_5 \rightarrow \infty$, and all the other layers have zero thicknesses). The red line and open triangles, as well as the green solid line and open rhombi correspond to the spin-wave spectrum for the ferrite-dielectric structure covered by a perfectly conducting metal plane for a distance of $t_3 = 5$ μm and $t_3 = 25$ μm , respectively. Other parameters are $t_2 = 20$ μm , $\varepsilon_2 = 14$, $\varepsilon_3 = 1$, $\sigma_5 \rightarrow \infty$, while all the other layers have zero thicknesses.

As seen in Figure 3.2, the SW spectra calculated according to the developed theory coincide with high accuracy with the expressions previously obtained (Damon, 1961; Seshadri, 1970; Bongianni, 1972). For a more detailed comparison, a difference between the dispersion characteristics corresponding to configurations of Damon-Eshbach, Seshadri, and Bongianni from one side and the developed theory from the other are shown in Table 3.1. Here, $|\Delta f| = |f_1 - f_2|$ is a module of the frequency difference, where f_1 and f_2 are frequencies obtained according to Equation (3.8) and Equations (2.4) - (2.6), respectively.

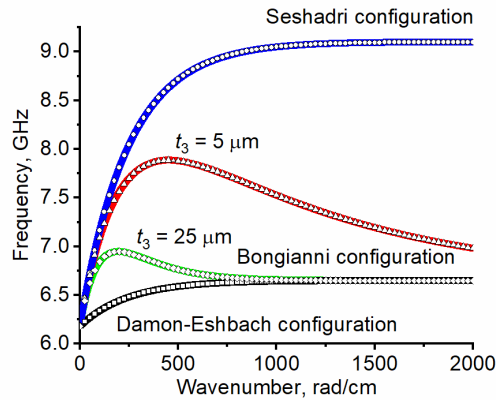


Figure 3.2: Spin-wave dispersion characteristics for the configurations of Damon-Eshbach (black line and open squares), Seshadri (blue line and circles), and Bongianni (green line and rhombs, red line and triangles).

Table 3.1: Comparison of the solutions founded according to the obtained and known dispersion relations for different ferrite-dielectric-metal structures.

Seshadri configuration						
k , rad/cm	25	125	225	325	425	825
$ \Delta f $, kHz	3041	506	205	92	51	9
Bongianni configuration ($t_3 = 5 \mu\text{m}$)						
$ \Delta f $, kHz	2914	395	124	44	26	5
Bongianni configuration ($t_3 = 25 \mu\text{m}$)						
$ \Delta f $, kHz	2443	165	47	37	23	2
Damon-Eshbach configuration						
$ \Delta f $, kHz	301	90	61	48	37	18

As seen in the table, the frequency difference $|\Delta f|$ decreases as the wavenumber k increases. This behaviour is caused by an influence of the retardation effect, which is taken into account in the developed theory. One should note that the decrease in the distance between the ferrite film and perfectly conducting metal plane shifts the spin-wave dispersion closer to the Seshadri configuration at low wavenumbers (see red line and open triangles in Figure 3.2).

In the next step, the wave spectra for the layered structure with ferroelectric slab were considered. In Demidov's work (Demidov, 2002b), the structures composed of a ferrite-ferroelectric-dielectric-metal multilayers were investigated. The obtained experimental and theoretical dispersion characteristics of the SEW for different external magnetic fields are shown in Figure 3.3a by points and solid lines, respectively. The comparison of the wave spectra with the developed theory is shown in Figure 3.3b.

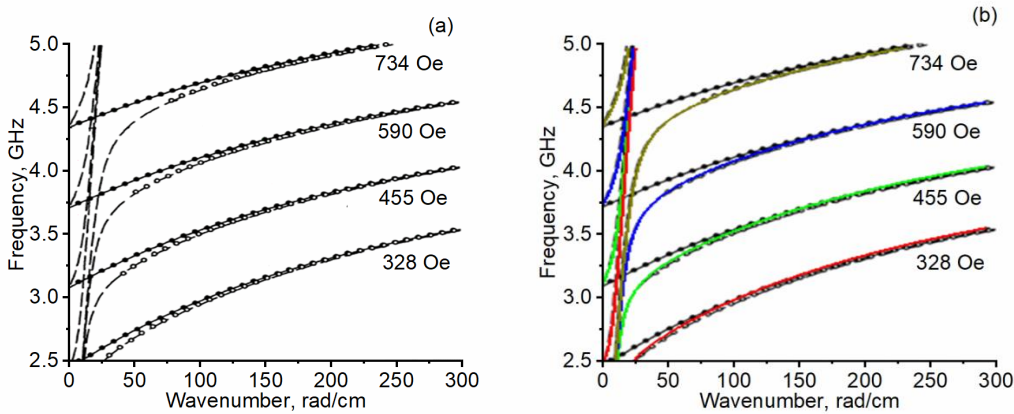


Figure 3.3: (a) Spectra of the hybrid SEW for different external magnetic fields. Adapted from (Demidov, 2002b). (b) Comparison of dispersion characteristics.

As is seen Figure 3.3b, the dispersion characteristics obtained according to the developed theory are in a good agreement with the experimental and theoretical results presented in previous research (Demidov, 2002b). A small deviation of the experimental dependences from the theoretical ones is explained by the existence of a thin air gap between ferrite and ferroelectric layers in a real-life experiment.

3.2 Wave spectra of all-thin-film multiferroic structures

The above-derived dispersion relation describes the spectra of hybrid waves in multilayers composed of an infinite number of ferrite and ferroelectric layers with arbitrary thicknesses, as well as arbitrary magnetic and electric parameters. In this Section, the formation of the dispersion characteristics of hybrid waves in two coupled ferrite films separated by free space or a ferroelectric layer is analysed. One of the main

features of these structures is the existence of a dipole-dipole interaction between the magnetic films. These investigations would be of an immense practical benefit to enhance the electric field tunability of wave spectra in layered ferrite-ferroelectric structures by the proper choice of the magnetic parameters.

3.2.1 Dipole-dipole interaction of spin waves in coupled ferrite films separated by a free space

The numerical simulations of the dispersion characteristics of spin-electromagnetic waves propagating in the structure shall now be considered, as shown in Figure 3.4. This structure consists of two ferrite layers contacted with dielectric layers and separated by a free space. The influence of a dipole-dipole interaction on the formation of the SW spectra is analysed both for identical ($t_2 = t_4 = 20 \mu\text{m}$, $M_2 = M_4 = 1750 \text{ G}$, and $\varepsilon_2 = \varepsilon_4 = 14$), and for different ($t_2 = 20 \mu\text{m}$, $M_2 = 1750 \text{ G}$, $t_4 = 6 \mu\text{m}$, $M_4 = 1790 \text{ G}$, $\varepsilon_2 = \varepsilon_4 = 14$) ferrite films. One should note that hereinafter the typical parameters of experimental structures are used in numerical simulations.

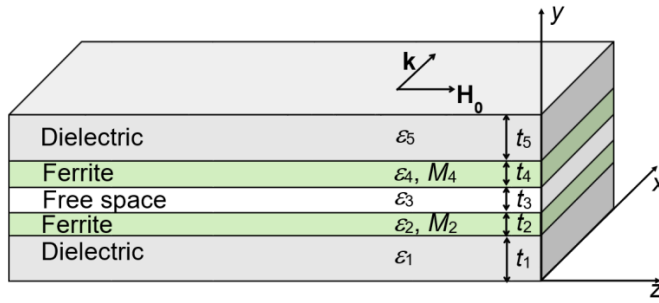


Figure 3.4: Thin-film structure composed of two coupled ferrite films.

Dispersion characteristics calculated for the identical ferrite layers are shown in Figure 3.5. The distance t_3 between the ferrites was varied from $1 \mu\text{m}$ to infinity.

As Figure 3.5 shows, spin waves propagate independently in the identical ferrite layers for $t_3 \rightarrow \infty$ and, therefore, their dispersion characteristics denoted by a black solid line coincide. For the investigated configuration, the surface SW propagates along the bottom surfaces of the ferrite layers. A decrease of the t_3 leads to reconfiguration of wave fields and splits the dispersion characteristic into two spin-wave dispersion branches (see Figure 3.5). The lower branch corresponds to a spin wave propagating along the interface between the upper ferrite layer and a free space, while the upper branch corresponds to a spin wave propagating along the interface between the lower ferrite and bottom dielectric layers. A further decrease in t_3 provides a stronger interaction between these coupled modes in a wide frequency range. The wave propagating at the interface between the upper ferrite layer and free space slows down due to this interaction. For the case of $t_3 = 1 \mu\text{m}$ (see the dashed lines in Figure 3.5a),

the upper dispersion branch almost coincides with the SW spectrum for the ferrite film of double thickness. For the intermediate values of t_3 , the interaction between the waves propagating in the different layers depends on the wavenumber. Namely, the waves demonstrate a strong coupling for relatively small wavenumbers. An increase in the wavenumbers leads to a decrease in the interaction. This is explained by the dependence of the damping decrements of the alternating fields outside the ferrite films on the wavenumber. Therefore, waves having relatively large wavenumbers propagate independently and their dispersion branches tend to follow the dispersion of the separate ferrite film.

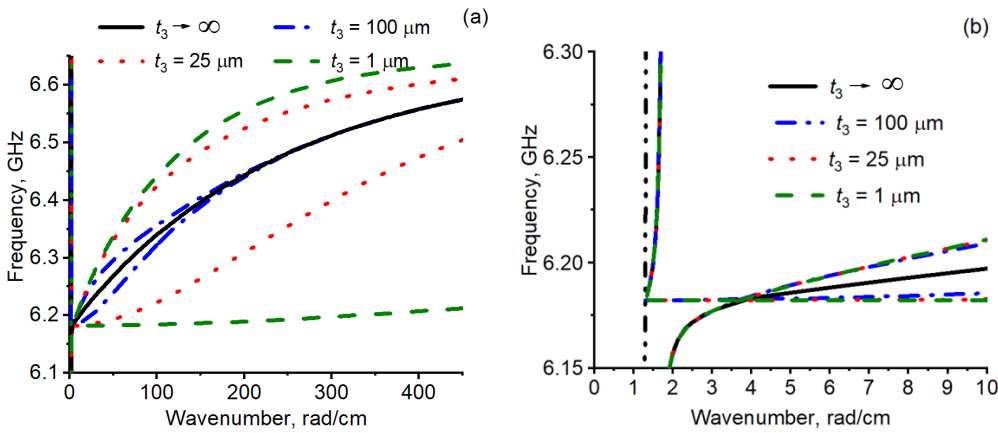


Figure 3.5: (a) Dispersion characteristics of the SEW calculated for a heterostructure consisting of two similar ferrite layers separated by free space; (b) The same characteristics in the expanded scale showing the influence of the electromagnetic retardation.

The results also show that the waves manifest a hybrid spin-electromagnetic nature for small wavenumbers up to 3 rad/cm, as shown in Figure 3.5b. This is due to the small values of the wavenumber k for the fundamental electromagnetic mode of the considered structure in the microwave range. The black dot-dashed almost vertical line in Figure 3.5 represents the dependence $\omega = c \cdot k$, where c is the speed of light in a vacuum. The electromagnetic retardation can be neglected for larger wavenumbers. Therefore, the calculated dispersion branches demonstrate the well-known behaviour for magnetostatics. Indeed, the results for $k > 3$ rad/cm are similar to those reported in previous research (Grünberg, 1981; Camley, 1993). On the one hand, this confirms the correctness of the developed theory. On the other hand, these results will be useful for the treatment of the spin-electromagnetic wave spectrum, which will be investigated for multiferroic heterostructures in the next part of this Section.

Those features of spin waves transmitted through a structure containing two ferrite films with different parameters shall now be considered. Here, the strength of SW interactions is determined by a phase velocity contrast, which is affected by a ratio of the

thicknesses t_2 , t_4 and the saturation magnetisation M_2 , M_4 of the ferrite layers. Some possible cases are summarised in Figure 3.6.

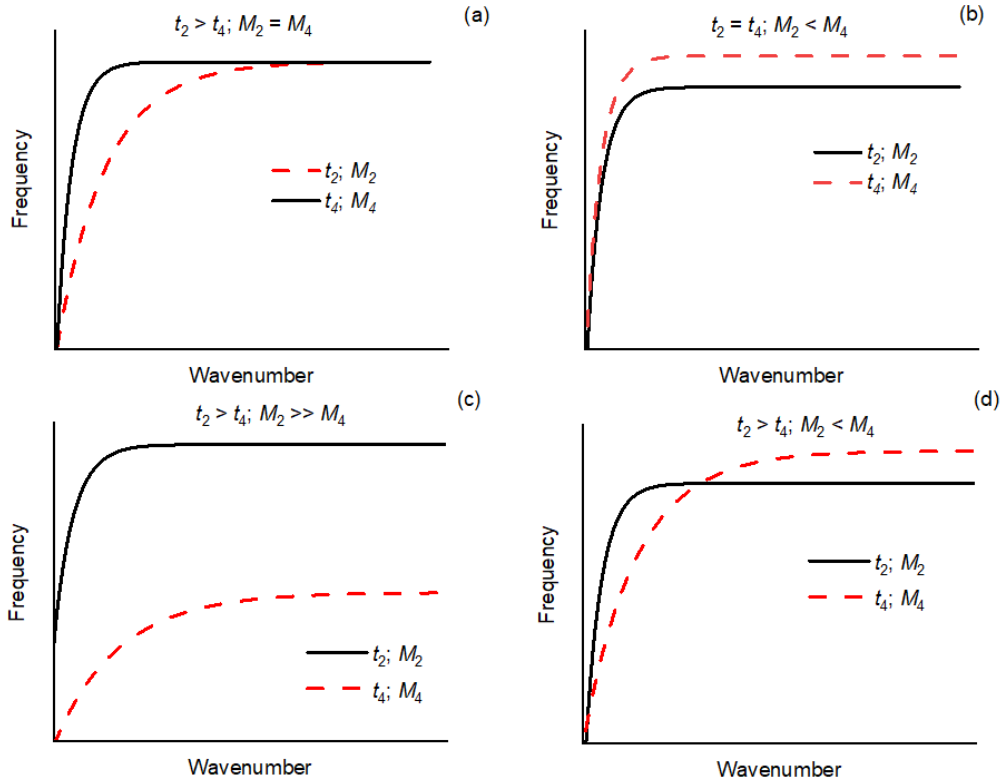


Figure 3.6: Qualitative pictures of SW dispersion characteristics of uncoupled ferrite films with various thicknesses (t_2 , t_4) and saturation magnetisations (M_2 , M_4).

From a practical point of view, further research will be conducted for the layered structures with two ferrite films fulfilling the following condition: $t_2 > t_4$ and $M_2 < M_4$ (see Figure 3.6d). Here, the main distinguishing feature is that the dispersion branches for thin and thick ferrite layers cross each other in the magnetostatic region. The intersection of the dispersion branches arises from different saturation magnetisations M_2 and M_4 and from different group velocities of the spin waves in magnetic films of different thickness. Therefore, the dipole-dipole interaction of spin waves in these structures is enhanced in comparison with other configurations (see Figures 3.6a-c).

Dispersion characteristics for the hybrid waves propagating in the multilayer structure containing two different ferrite films are shown in Figure 3.7. In the considered case, SW group velocities in the upper thin ferrite film are smaller than those in the lower thick ferrite. The region of relatively small wavenumbers of $k < 30$ rad/cm will be under examination for multiferroic heterostructures in the next Section. In this region, the

condition $M_2 < M_4$ leads to the situation that the upper dispersion branch corresponds to the spin waves in the upper thin film and the lower branch describes the spin-wave dynamics in the lower thick film. Hereinafter, these denominations will be used for the pure spin-wave dispersion branches.

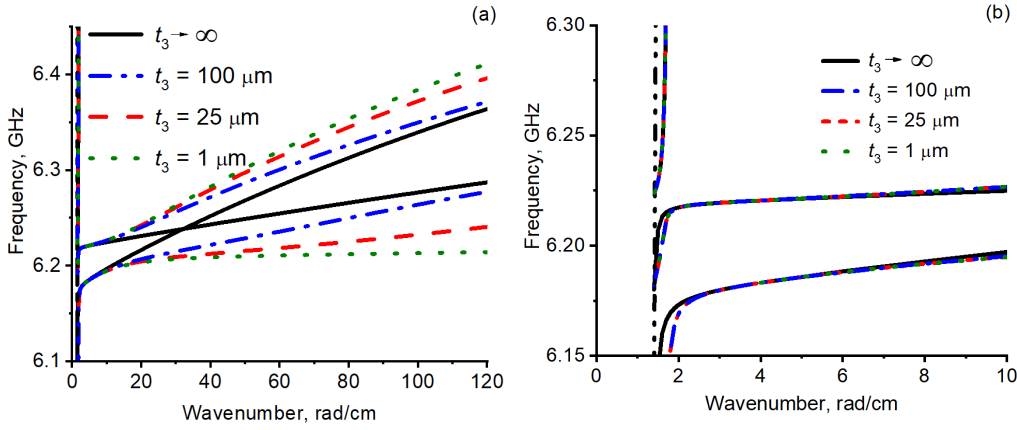


Figure 3.7: (a) Dispersion characteristics of the waves calculated for the heterostructure consisting of two different ferrite layers separated by a free space; (b) The same characteristics in the expanded scale.

As seen in Figure 3.7a, a reduction in t_3 leads to a coupling between the spin-wave modes due to the dipole-dipole interaction. This interaction manifests itself in the repulsion of the dispersion branches around the point of the intersection of the uncoupled spin-wave modes. The repulsion becomes more pronounced for smaller distances between the ferrite layers because of an increase in the spin-wave coupling. In contrast to the symmetric structure considered earlier, here the region of the strong spin-wave coupling is around $k = 30$ rad/cm. For $k < 30$ rad/cm, the upper dispersion branch describes the coupled spin waves localised mainly in the upper ferrite layer, while the lower dispersion branch corresponds to the spin waves propagating mostly in the lower ferrite layer. This behaviour is reversed for $k > 30$ rad/cm, where the upper dispersion branch describes the coupled spin waves localised mainly in the lower ferrite layer, while the lower one corresponds to the spin waves propagating mostly in the upper ferrite layer. Figure 3.7b clearly demonstrates that the coupling does not affect the spectrum for $k < 10$ rad/cm. One should note that the different saturation magnetisations define different frequencies when the wave-vector approaches zero.

3.2.2 Dipole-dipole interaction of spin waves in coupled ferrite films separated by a thin ferroelectric layer

In this Section, an all-thin-film multiferroic heterostructure consisting of two ferrites separated by a ferroelectric layer is considered (see Figure 3.8). During simulations, the following three parameters were varied, namely, the saturation magnetisation M_4 of the

top ferrite layer, the ferroelectric layer thickness t_3 , and its dielectric permittivity ε_3 . All the remaining parameters are fixed: these are $t_2 = 20 \mu\text{m}$, $M_2 = 1750 \text{ G}$, $t_4 = 6 \mu\text{m}$, $t_1 = t_5 = 500 \mu\text{m}$ and $\varepsilon_1 = \varepsilon_5 = 14$. An important feature of this structure is the controllable dipole-dipole interaction between the magnetic films achieved by a variation of the ferroelectric thickness as well as its dielectric permittivity.

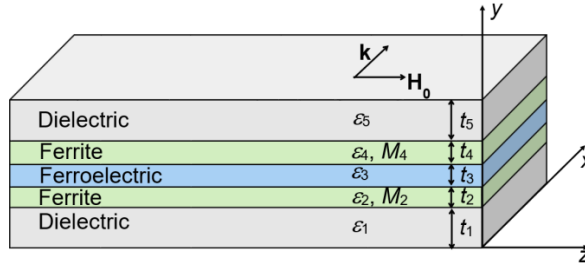


Figure 3.8: Thin-film structure consisting of two ferrites separated by a ferroelectric layer.

Consider now the formation of SEW spectra of the investigated structure. Solid red curves in Figure 3.9 show the dispersion characteristics calculated for $\varepsilon_3 = 1500$ and different values of t_3 and M_4 . The spectra were calculated for two opposite directions of the wave propagation. Positive values of the wavenumber correspond to the SEW propagation to positive the x -axis direction.

As seen in Figure 3.9, the SEW spectrum consists of three dispersion branches that will be referred to as lower, middle, and upper branches. Such a spectrum is formed as a result of the electrodynamic interaction of an electromagnetic mode TE_1 with two spin-wave modes. Due to the thin ferroelectric layer, the dipole-dipole interaction between the ferrite layers considered in the previous Section also influences the formation of SEW spectrum for the particular set of the heterostructure parameters. Possible situations shall now be considered in detail.

Figure 3.9a presents the case of a relatively large difference in the saturation magnetisations for $t_3 = 25 \mu\text{m}$ providing the situation of a negligibly small spin-wave coupling for $k < 30 \text{ rad/cm}$. It is easy to see the hybridisations between one electrodynamic mode and two spin-wave modes, which manifests themselves as repulsions between the SEW dispersion branches. The hybridisations become more pronounced in the vicinity of the points, where the dispersion branches of the electromagnetic mode TE_1 and the upper and lower spin-wave modes cross each other. Strictly speaking, the hybrid SEW that are controllable with both electric and magnetic fields exist around these points. Far from these points, the SEW dispersion branches tend to be the branches of a pure spin-wave (see blue dashed line in Figure 3.9a) or electromagnetic (see green dash-dot line in Figure 3.9a) modes. Similar to the coupled ferrite-film structure considered earlier, the upper and lower spin-wave modes describe the wave propagation in the upper and the lower ferrite layers, respectively.

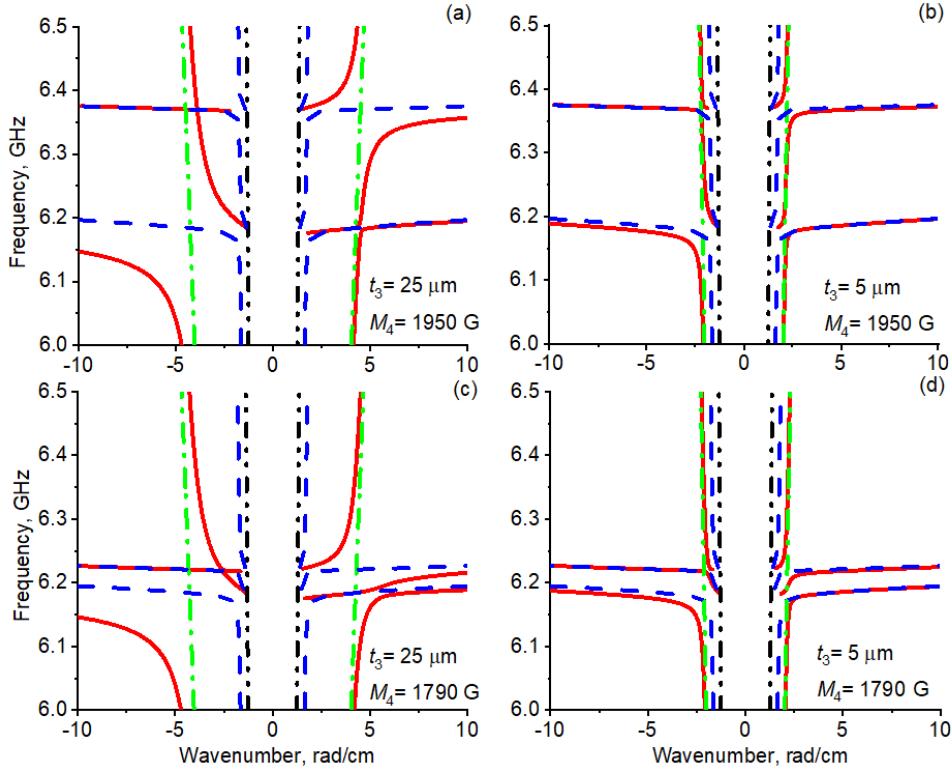


Figure 3.9: Spectra of the hybrid SEW (red solid curves) in the ferrite-ferroelectric-ferrite thin-film structures calculated for different thicknesses of the ferroelectric layer t_3 and for varying saturation magnetisation M_4 of the top ferrite layer. The green dashed-dotted lines show the electromagnetic mode TE_1 of the structure. The blue dashed curves show the hybrid SEW for coupled ferrite films (i.e., for $\epsilon_3 = 1$). The black short dashed line represents the dependence $\omega = c \cdot k$, where c is the speed of light in a vacuum.

For positive wavenumbers, a relatively weak repulsion takes place between the lower and middle SEW branches around the lower point of the intersection of the modes that are hybridised. At the same time, a relatively strong repulsion between the middle and upper SEW branches occurs around the upper point. This is explained as follows: the dynamic magnetic fields of the spin waves propagating along the x -axis in the lower and upper ferrite layers have weak exponential transverse distributions with the maxima lying at the bottom surfaces of the both layers. Simultaneously, the electromagnetic wave fields are changed strongly in the cross section of the structure. The maximum of these fields is localised close to the middle of the structure and is much smaller outside of the structure. Therefore, the interaction between the spin and electromagnetic waves is much stronger for the inner ferrite-ferroelectric interface than for the outer interface between the ferrite film and the dielectric substrate.

A completely different situation is observed for waves propagating in the opposite x -axis direction, i.e., for negative wavenumbers. The maxima of the spin-wave magnetic

fields are now located at the top surfaces of the both ferrite layers. Therefore, a strong interaction between the SW and EMW takes place only on the interface between the lower ferrite and ferroelectric layers. As a result, the strong repulsion happens between the lower and middle SEW branches.

A reduction of the ferroelectric layer thickness t_3 does not principally change the described behaviour of the SEW spectrum (see Figure 3.9b). One should note only that this leads to an increase in a group velocity of the fundamental electromagnetic mode TE_1 of the layered structure and, therefore, the regions of the hybridisation are shifted closer to the ordinate axis.

Consider now the case of a relatively small difference in the saturation magnetisations for the thick ($M_2 = 1750$ G) and thin ($M_4 = 1790$ G) ferrite layers. As shown in Figure 3.9c, the SEW middle branch is clamped between the upper and lower SW branches. Therefore, its group velocity changes significantly with a reduction in the ferroelectric thickness t_3 . This can be clearly seen by comparing the SEW dispersion characteristics shown in Figures 3.9c and 3.9d. A direct influence of the spin-wave coupling on the spin-electromagnetic hybridisation takes place only for the lower SEW branch with negative wavenumbers shown in Figure 3.9c. This effect is absent for the other hybridisations because of their relative weakness. As shown in the previous Section, the coupling affects the spectrum for $k > 10$ rad/cm.

Following this, the investigation of the electric field tuning of the dispersion characteristics of the SEW shown in Figure 3.10 will be examined. As it is well known, the application of an electric field to a ferroelectric layer decreases its relative dielectric permittivity. Therefore, the dispersion characteristics were calculated for two values of the ferroelectric layer permittivity ϵ_3 , 1500 and 700, where the result is shown by red solid and blue dashed lines in Figure 3.10, respectively.

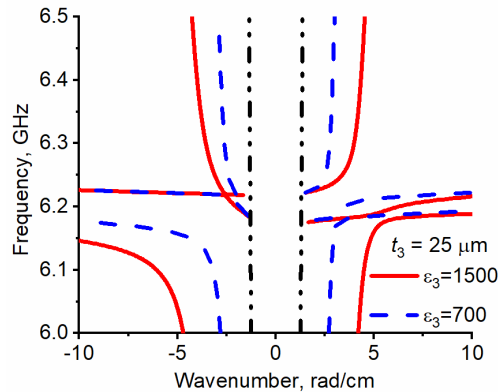


Figure 3.10: Spectra of the hybrid SEW in the ferrite-ferroelectric-ferrite thin-film structures calculated for different dielectric permittivities $\epsilon_3 = 1500$ and 700 . The ferroelectric thickness t_3 is equal to $25 \mu\text{m}$. The black short dashed lines represent the dependence $\omega = c \cdot k$.

As seen in Figure 3.10, a decrease in ϵ_3 shifts the regions of wave hybridisation towards the ordinate axis and decreases the wavenumbers of the SEW for fixed frequencies. This phenomenon is promising for applications of the all-thin-film multiferroic structure as a phase shifter. A detailed study of the influence of the ferroelectric layer permittivity on the SEW spectrum also shows changes in the spectrum far from spin- and electromagnetic wave hybridisation regions. Namely, outside these regions, a reduction in ϵ_3 leads to a shift of the dispersion branches just like a reduction in the thickness t_3 of the ferroelectric layer. Such a change increases the coupling between the spin-wave modes of the ferrite layers previously discussed.

To estimate the range of the electrical field tuning the wavenumber variations versus the frequency for SEW, both propagation directions were calculated for different ferroelectric layer thickness t_3 in case the ferroelectric layer permittivity ϵ_3 was reduced from 1500 to 700. The results are shown in Figure 3.11 by solid, dashed, and dash-dot lines for the lower, middle, and upper SEW dispersion branches, respectively. The parameters were taken to be the same as those for Figures 3.9c and 3.9d. Figures 3.11a-c and 3.11d-f correspond to SEW dispersion branches for the forward and the opposite propagation to the x -axis directions, respectively.

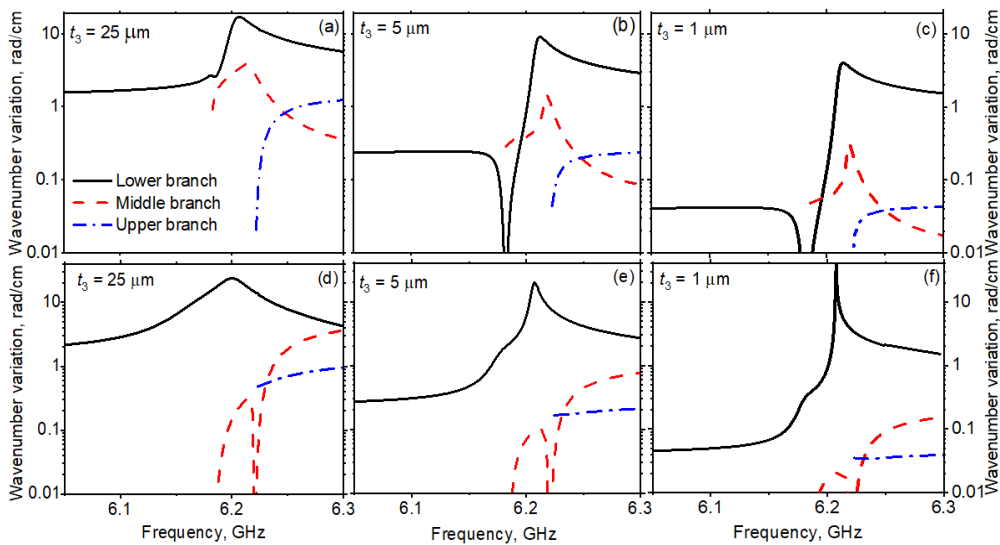


Figure 3.11: Wavenumber variation of the lower, middle, and upper SEW dispersion branches versus the frequency calculated for different ferroelectric layer thickness t_3 for the (a)-(c) forward and (d)-(f) opposite to x -axis propagation directions.

As previously mentioned, the hybridisation of SW and EMW depends on the propagation direction. Features of the wavenumber tuning in the range of 6.175 - 6.25 GHz for the forward propagation shown in Figure 3.11c are determined by the strong hybridisation of the EMW and SW in the upper ferrite layer. At the same

time, for the opposite propagation direction (see Figure 3.11f), a strong hybridisation occurs between the EMW and SW in the lower ferrite layer. This provides an increase in the tuning of the SEW mode in the range of 6.15 - 6.25 GHz in comparison with a tuning of the electromagnetic mode.

Figure 3.12 shows the SEW phase shifts calculated for a 1 cm long structure with different thicknesses of the ferroelectric film, where the phase shift for the 1 μm thick ferroelectric film at a frequency of 6.21 GHz is even larger than that for the 25 μm thick film. For the 1 μm film, a phase shift of more than 2π is achieved in a 6 MHz wide frequency range. In spite of this relatively narrow frequency range, this phenomenon can be tuned over a broad frequency range by a variation of the bias magnetic field. This feature demonstrates the yield of the all-thin-film heterostructures.

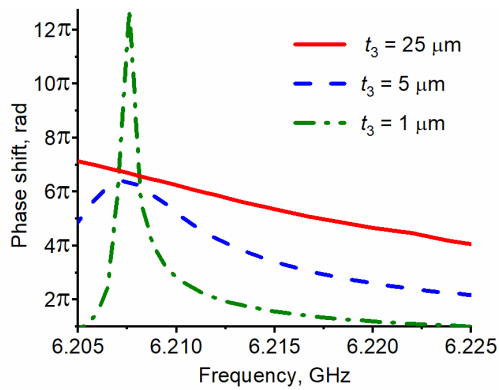


Figure 3.12: Phase shift versus frequency for the lower SEW mode propagating in the propagation direction opposite x -axis propagation directions. Characteristics were calculated for different ferroelectric thicknesses t_3 as indicated.

3.3 Enhancement of the electric field tuning of the wave spectra

As previously mentioned, the electric field tunability of dispersion characteristics of hybrid SEW propagating in thin-film ferrite-ferroelectric-ferrite structures is determined by two mechanisms of wave interactions. The first one is dictated by a hybridisation of spin-wave modes in the ferrite films with the pure electromagnetic mode TE_1 in a ferroelectric medium. Within this mechanism, a change in the ferroelectric permittivity leads to a shift of the EMW dispersion branch, which provides a displacement of cross points between the dispersion curves of the modes. The second mechanism is dictated by an increase in the dipole-dipole interaction of spin-wave modes in the coupled ferrite films due to a decrease in the ferroelectric permittivity.

In order to ensure the implementation of the above-mentioned mechanisms, an interaction between the pure electromagnetic mode TE_1 and the spin-wave modes is required. One should note that this coupling strength strongly depends on the

overlapping of the dynamics fields of the EMW and SW. Thus overlapping depends on the geometry of the layered structures and parameters of the materials. Thus, two relative positions of the modes are possible (see Figure 3.13).

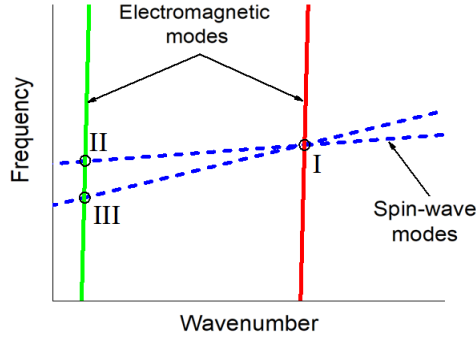


Figure 3.13: Qualitative picture showing possible relative positions of two pure spin-wave modes (blue dashed lines) and the electromagnetic mode (green or red solid line).

According to Figure 3.13, the first interaction takes place in the point I between two spin-wave modes shown by the dashed lines, while the second one appears in the other points (e.g., points II or III). This situation was previously studied in detail in previous Section. However, the interaction between the electromagnetic and spin-wave modes could take place in one point (see point I in Figure 3.13). In this case, the coupling strength between these modes is enhanced providing a significant change in the wave spectrum. In order to distinguish the difference between the interactions of EMW and SW at one and at different points, the term “double hybridisation” is introduced.

3.3.1 General features of the doubly hybridised spin-electromagnetic waves

A thin-film multilayered structure consisting of two ferrite layers separated by a ferroelectric film is shown in Figure 3.14. In order to fulfil the conditions for double hybridised waves in the proposed structure, the numerical simulations were carried out for the following parameters: $t_1 = t_5 = 500 \mu\text{m}$; $t_2 = 20 \mu\text{m}$; $t_3 = 1 \mu\text{m}$; $t_4 = 6 \mu\text{m}$; $\varepsilon_1 = \varepsilon_5 = \varepsilon_2 = \varepsilon_4 = 14$; $\varepsilon_3 = 1500$; $M_2 = 1750 \text{ G}$; $M_4 = 1713 \text{ G}$; and $H = 1500 \text{ Oe}$. This set of parameters was chosen to provide an intersection of spin-wave modes. As previously mentioned, this intersection takes place if ferrite layers have a different magnetisation and thickness. One should note that for the present set of parameters, the interaction of the spin waves occurs for $k = 1.75 \text{ rad/cm}$. To realise a double hybridisation, the magnetisation of the top ferrite layer was chosen to be $M_4 = 1713 \text{ G}$, which is less than the value of the magnetisation for the bottom ferrite film. The magnetization of the top ferrite should be increased for the case of spin-wave interaction at larger wavenumbers.

An application of a control voltage U to thin metal electrodes deposited on both surfaces of the ferroelectric film results in a decrease of its dielectric permittivity ε_3 . This dependence was calculated according to Equation (2.8). In this expression, the

following parameters of the barium-strontium titanate ferroelectric ($\text{Ba}_{0.5}\text{Sr}_{0.5}\text{TiO}_3$) were used: $\varepsilon_2(0) = 1500$, $\varepsilon(\infty) = 300$, $S_{\text{eff}} = 1 \mu\text{m}$, $E_n = 40 \text{ V}/\mu\text{m}$, and $\varepsilon_{00} = 300$ (see details Section 2.2). It is assumed that the thickness of the electrodes is much smaller than the skin depth at the operating frequencies. Therefore, these electrodes are transparent to the microwave electromagnetic fields, and can be neglected in numerical simulations.

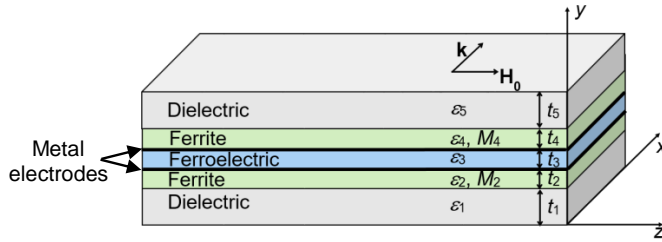


Figure 3.14: Thin-film multiferroic structure consisting of two ferrite layers and a ferroelectric film between them.

Figure 3.15 shows by solid curves the dispersion characteristics of doubly hybridised SEW propagating in the proposed structure. As shown in this figure, a relatively strong repulsion between all SEW branches takes place for waves propagating in the forward and backward directions along the x -axis (i.e., for positive and negative wavenumbers). This repulsion is produced by the dipole-dipole interaction between the ferrite films for $k = 1.7 \text{ rad}/\text{cm}$ for both propagation directions. Taking into account that a propagation of EMW is sensitive to the external electric field, it is possible to modify the doubly hybridised SEW spectrum into a spectrum of hybrid waves. As a result, the wave spectrum is significantly changed due to a variation in the dielectric permittivity ε_3 . The latter makes it possible to exploit SEW phenomena for more efficient electric field tuning.

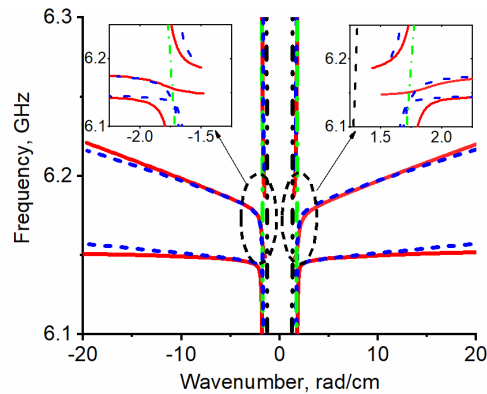


Figure 3.15: Spectra of the doubly hybridised SEW (solid red curves). The dashed-dotted green lines show electromagnetic mode TE_1 . The short dashed blue curves show the hybrid SEW for ferrite films (i.e., for $\varepsilon_3 = 1$). The black dashed line represents the dependence $\omega = c \cdot k$.

In order to analyse the range of the electric field tuning of a doubly hybridised SEW spectrum, the phase shifts accumulating in the 1 mm long structure were calculated for the case of the reduction in the ferroelectric layer permittivity ϵ_3 by two times. Such a change is achieved by a variation of a control voltage from $U = 0$ V to $U = 12.83$ V, applied to the ferroelectric film, the results of which are shown in Figure 3.16.

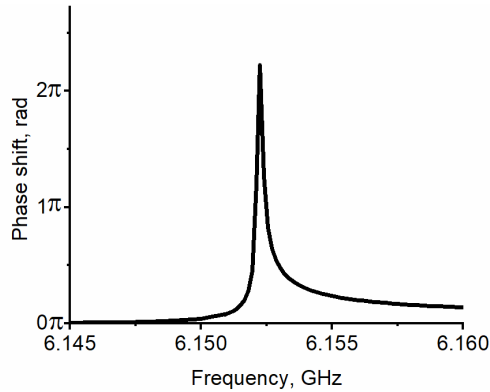


Figure 3.16: Phase shift versus frequency for the lower SEW branch propagating in the direction opposite the x -axis.

As shown in Figure 3.16, a significant phase shift of the SEW of more than 2π rad is achieved for the lower SEW branch propagating in the direction opposite the x -axis. This phenomenon can be explained as follows: as previously mentioned, transverse distributions of a magnetostatic potential for surface spin waves with positive k have maxima on the bottom surfaces of the magnetic films. These distributions have maxima on the top surfaces for reversed propagation direction. In this case, the spatial distance between the maxima is less for negative k . This leads to a stronger overlapping of alternating electric and magnetic fields of spin waves propagating in neighbouring magnetic films and consequently to a stronger coupling of the waves. As a result, the group velocity of the SEW bottom branch is reduced significantly, and this branch demonstrates huge electric field tuning of the wavenumbers in a relatively narrow frequency band.

From a physical point of view, the electric field tuning described above for the doubly hybridised waves originates from the change of the dipole-dipole interaction between the ferrite films by a variation of the dielectric permittivity ϵ_3 of a thin ferroelectric film. A decrease in ϵ_3 can be considered a reduction in an effective spatial distance between the magnetic films, leading to an increase in the coupling of spin waves in the magnetic films.

As shown previously, the largest electric field tuning, which could be of interest to practical applications, is observed for the negative wavenumbers of the lower SEW dispersion branch. Therefore, the electric field tuning of this branch for various physical parameters of the layered structure will be further considered. The influences of ferrite

and ferroelectric thicknesses on the phase shift of SEW are shown in Figure 3.17. Here, black solid lines represent the reference dependence shown in Figure 3.16.

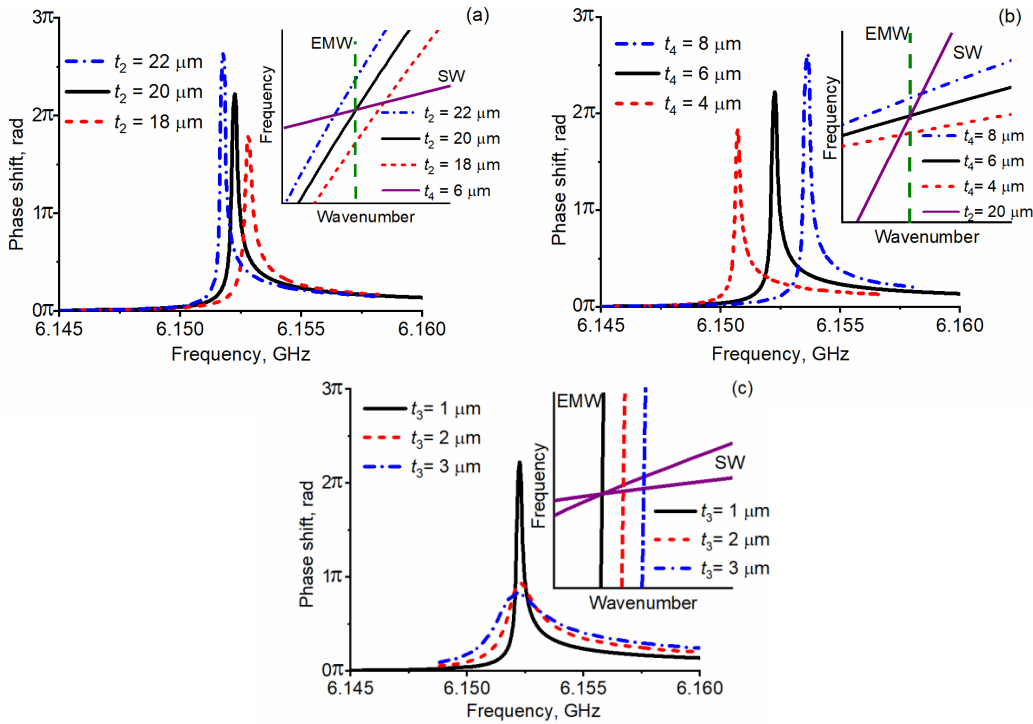


Figure 3.17: Wavenumber variation versus frequency calculated for different thicknesses of (a) bottom ferrite film, (b) top ferrite film, and (c) ferroelectric film. The insets show the qualitatively dispersion characteristics of pure spin and electromagnetic modes.

As shown in the inset of Figure 3.17a, an increase in the thicknesses of the thick ferrite layer t_2 shifts the point of the hybridisation between two spin-wave modes to the lower wavenumbers. This leads to a downshift of the frequency of the electric tuning maximum shown in Figure 3.17a. The inverse effect is observed with an increase in the thickness of the thin ferrite film (see Figure 3.17b).

Figure 3.17c demonstrates the influence of the ferroelectric film thickness t_3 on the phase shift of SEW. In contrast to multiferroic structures previously studied, the ferrite-ferroelectric-ferrite structure demonstrates the following unique feature: a reduction in the ferroelectric thickness sufficiently increases the electric field tuning. For example, a decrease in the thickness t_3 from $2 \mu\text{m}$ to $1 \mu\text{m}$ increases the phase shift by more than two times. Double hybridisation of SEW plays a crucial role in this effect. Indeed, as is clear from the inset in Figure 3.17c, a decrease in the thickness of the ferroelectric film

shifts the dispersion branch of EMW toward the point of the double hybridisation, which increases the tuning efficiency.

A weakness of the proposed thin-film multiferroics is the narrow frequency band, where effective electric field tuning is realised. For example, a phase shift larger than π rad is realised only in a bandwidth of 15 MHz. However, the band of a large wavenumber variation can be shifted by changing an external magnetic field. Therefore, the all-thin-film multiferroic multilayers are preferable to the development of tunable microwave devices.

3.3.2 The effective electric field tuning for voltage-controlled spin-wave logic gates

A schematic view of a microwave interferometer, shown in Figure 3.18a, represents a bridge circuit with two branches, which is commonly used in Mach-Zehnder interferometers. The first branch comprises a tunable phase shifter (TPS) represented in Figure 3.18b, while the second branch contains a variable attenuator. The thin-film structure based on a ferrite-ferroelectric-ferrite waveguide (see Figure 3.14) is used to implement the TPS that demonstrated a large electric tuning of the phase shift with a low control voltage.

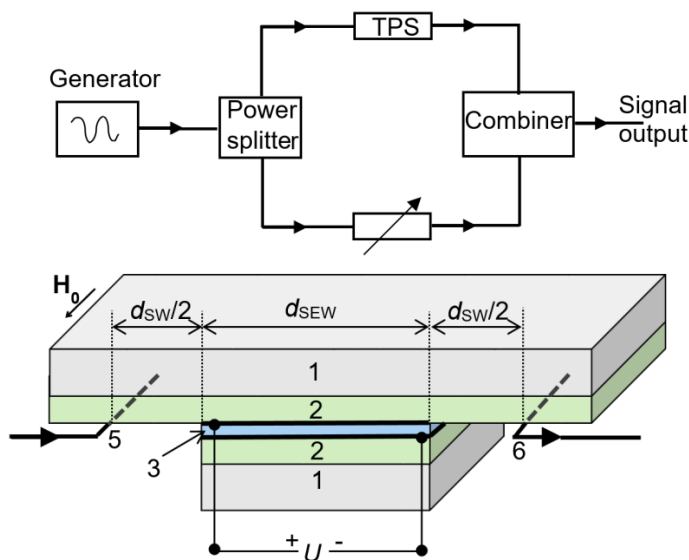


Figure 3.18: (a) Schematic diagram of the Mach-Zehnder interferometer; (b) Tunable phase shifter (TPS) based on a thin-film multiferroic structure.

The operation principle of the miniature multiferroic interferometer shall now be considered. A microwave signal is applied to the input and is split into two signals that

accumulate different phase shifts in the interferometer branches. In the first branch (see Figure 3.18b), the microstrip antenna (5) excites a SW in the YIG film (2) grown on dielectric substrates (1). After travelling a short distance $d_{SW}/2 = 1.375$ mm in this film, the waves enter the multiferroic structure. This is the region where the YIG film (2) is in contact with the BST-YIG (3)-(4) bilayer. At the border of this region, the SW transforms into the SEW. Here, the phase shift of the microwave signal is controlled due to a variation in the polarisation of the ferroelectric film. After passing the layered structure with a length of $d_{SEW} = 1$ mm, the SEW propagates through the YIG film (2), where it is transformed back to the SW and is received by the output microstrip antenna (6). After passing different branches, the signals interfere in the combiner. The power of the output signal can be calculated as follows:

$$P_{out} = P_{out1} + P_{out2} + 2\sqrt{P_{out1}P_{out2}} \cos(\varphi_2 - \varphi_1), \quad (3.9)$$

where P_{out1} , φ_1 , P_{out2} , and φ_2 are the powers and phase shifts of microwave signals in the branches, respectively. The phase shift φ_1 is determined as follows:

$$\varphi_1 = k_{SW}d_{SW} + k_{SEW}d_{SEW} + \varphi_0, \quad (3.10)$$

where k_{SW} and k_{SEW} are the wavenumbers of the SW and SEW, respectively, and φ_0 is the phase shift in rest of the microwave circuit of the first branch, which is assumed to be equal to φ_2 . The wavenumbers k_{SW} were found according to the dispersion relation for surface spin waves (2.4). The wavenumbers of the SEW in the ferrite-ferroelectric-ferrite structures were obtained according to the dispersion relation (3.8).

Previously it was shown that an effective electric field tuning of SEW spectrum for ferrite-ferroelectric-ferrite structures is carried out for the lower wave branch subject to the condition of the double hybridisation of the two spin-wave modes in ferrite films with the pure electromagnetic mode TE_1 in a ferroelectric film. This feature was used to obtain a phase shift in one of the arms of the interferometer. In particular, Figure 3.19a demonstrates the SEW bottom branch calculated for $U = 0$ V (solid line) and $U = 6.57$ V (dashed line) that correspond to the change in the dielectric permittivity of the BST film from 1500 to 1100 in accordance with Equation (2.8).

Figure 3.19b shows the dependence of the phase shift on the frequency by dashed line for $U = 6.57$ V in the 1 mm long TPS. The control voltage provides the phase shift of a microwave signal in the first branch of more than 180 degrees.

Figure 3.19c shows the transmission characteristic of the interferometer for $U = 0$ V (solid black line) and $U = 6.57$ V (dashed red line), where one of the maxima in the transmission coefficient profile is observed at the frequency $f_0 = 6.1522$ GHz for zero voltage. The application of 6.57 V leads to the phase shift of 180 degrees at the frequency f_0 , which provides the destructive interference of the microwave signals and the minimum signal transmission.

In order to clarify the influence of the control voltage on the performance characteristics of the proposed interferometer, Figure 3.20a presents the dependence of the phase shift of interfering signals on the applied voltage at the frequency f_0 . Here, it can be seen that an increase of the control voltage leads to an increasing in the phase shift. At $U = 13.6$ V the phase shift attains the value of 360 degrees that provides the constructive interference and the maximum at the transmission characteristic, which is shown in Figure 3.20b.

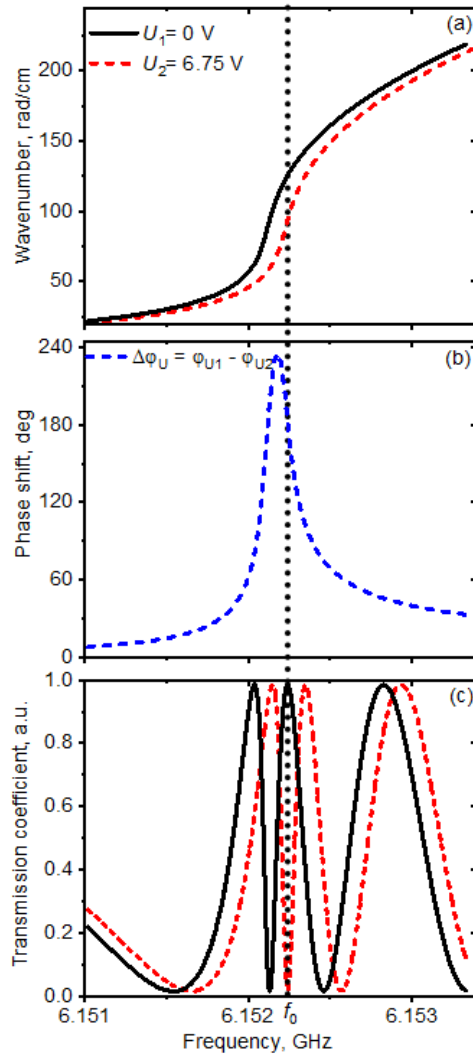


Figure 3.19: (a) Calculated spectra of the hybrid SEW in the TPS; (b) the phase shift of the interfering signals; and (c) the transmission characteristic of the interferometer for control voltage $U = 0$ V (solid black line) and $U = 6.57$ V (dashed red line).

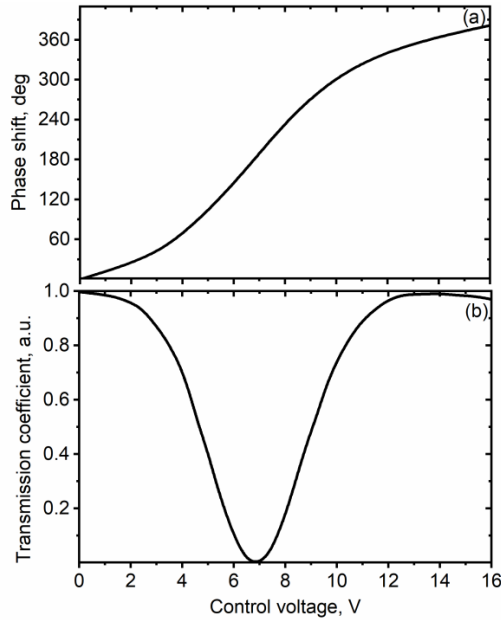


Figure 3.20: Dependences of (a) the phase difference of the interfering signals and (b) the transmission coefficient of the interferometer on the applied voltage at the fixed frequency $f_0 = 6.1522$ GHz.

A possible limitation of the proposed interferometer applications is the narrow frequency band, where effective electric-field tuning is possible. However, the frequency width of this band can be easily tuned through changing the external magnetic field. Thus, a magnetic-field tuning in a range of 500–2500 Oe offers an opportunity to realise a highly effective electric tuning for any desirable frequency in a range from 3 to 9 GHz.

Therefore, utilisation of the thin-film ferrite-ferroelectric-ferrite structures is promising for miniaturisation of the microwave Mach-Zehnder interferometers. In addition, these structures provide a significant reduction in the control voltage down to unities of volts. As a result, an interest in the proposed interferometer arises from possible practical applications in spin-wave logic circuits. One should note that the studied device represents the NO logic gate. The use of similar tunable phase shifters in the both interferometer arms allows the obtaining of XNOR or XOR gates.

4 All-thin-film multiferroics with coplanar waveguides

As shown in Chapter 3, an enhancement of an electric field tuning of the wave spectra of layered multiferroic structures is achieved due to the controllable dipole-dipole interactions between the coupled ferrite films. Another way to reduce a control voltage can be realised by utilising planar structures consisting of thin ferrite and ferroelectric films in a combination with a coplanar waveguide. The distinctive feature of coplanar waveguides composed of thin ferrite and ferroelectric films is the absence of undesirable irregularities in a dispersion for relatively low frequencies when the wavelength approaches the thickness of the ferroelectric layer. However, up until now, a detailed investigation of wave spectra of such a waveguide has not been performed due to the lack of a theory describing the dispersion characteristics of spin-electromagnetic waves.

4.1 Theory for wave spectra of multiferroic structures with coplanar waveguides

The development of an analytical theory for wave spectra of multiferroic structures in combination with a coplanar waveguide (CW) is a complex electrodynamic problem. In order to simplify a derivation of a dispersion law, an approximate relation can be obtained by an analytical solution of the full set of Maxwell's equations utilising a method of approximate boundary conditions (ABC). In this method, the dispersion characteristics of the waves propagating in layered structures consisting of thin ferrite layers can be found using the following approximations: (i) the field components inside a ferrite layer are taken equal to the average values of the fields at the interfaces between the neighbouring layers; and (ii) the derivatives of the field components are replaced by their increments between the ferrite boundaries divided by the ferrite thickness. The applicability of the ABC method is determined by a relatively weak exponential dependence of the electric and magnetic field distributions on the transverse coordinate for the long-wave dipolar surface SW in a thin ferrite film having the unpinned surface spins. A high accuracy of this method was shown for thin ferrite films and layered ferrite-dielectric structures (Nikitin, 2014).

The studied structure is shown in Figure 4.1, where a central metal strip of the width h and two metal ground electrodes are placed in the $y=0$ plane between dielectric (or ferroelectric) layers. The metal electrodes are transparent to the microwave electromagnetic field and are therefore neglected in the numerical simulations. This assumption is valid because the thickness of the electrodes is much smaller compared to the skin depth at the operating frequencies. Below and above the electrodes, there are six homogeneous dielectric layers in total with the dielectric permittivities ϵ_j and thicknesses t_j , where j is a layer number according to Figure 4.1. The thickness of the

ferrite layer is δ and its permittivity is ϵ_f . One should note that the SEW propagates along the CW along x -direction; the ferrite layer is tangentially magnetised along z -axis.

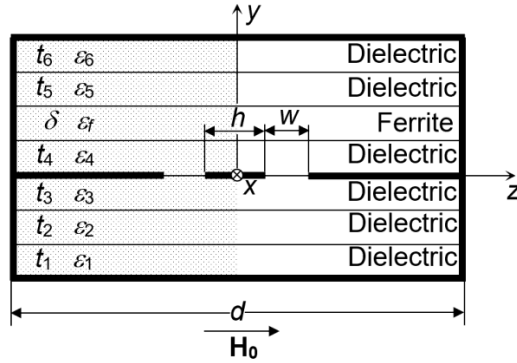


Figure 4.1: Cross section of a coplanar waveguide.

To treat the multiferroic structure with the coplanar waveguide as a boundary-value problem, some general comments regarding the electrodynamic model should be mentioned:

- The solution of the boundary-value problem will be reduced to the derivation of a dispersion equation for a symmetrical rectangular waveguide loaded with a CW surrounded by perfectly conducting metal walls (see Figure 4.1). This approach is physically applicable because the electric and magnetic fields of a CW with narrow gaps w are symmetrical and are localised in the gaps of the planar transmission line. Therefore, if the distance between the metal walls is significant, then their influence on wave processes is negligible;
- During the derivation of the dispersion equation, it is assumed that a CW is surrounded by the metal walls, where the tangential components of the magnetic field are equal to zero. This boundary condition is known as a "magnetic wall" and is given by:

$$\mathbf{\Pi}_j^e = \frac{\partial}{\partial z} \mathbf{\Pi}_j^h = 0 \quad (4.1)$$

where $\mathbf{\Pi}^e$ and $\mathbf{\Pi}^h$ are the magnetic and electric Hertzian potential functions, respectively.

An electromagnetic wave in a rectangular waveguide loaded with a transmission line is a superposition of the longitudinal-section magnetic (LSM) and the longitudinal-section electric (LSE) modes (Collin, 1990). Using this, the electric and magnetic field components in the dielectric layers of the considered structure are expressed as the sums of the LSM and

4.1 Theory for wave spectra of multiferroic structures with coplanar waveguides 59

LSE modes $\mathbf{E}_j = \mathbf{E}_j^{\text{LSM}} + \mathbf{E}_j^{\text{LSE}}$, $\mathbf{H}_j = \mathbf{H}_j^{\text{LSM}} + \mathbf{H}_j^{\text{LSE}}$. These fields are expressed using the Hertzian potentials as $\mathbf{E}_j^{\text{LSE}} = -\nabla \times \mathbf{\Pi}_j^h / \epsilon_j$; $\mathbf{H}_j^{\text{LSM}} = \nabla \times \mathbf{\Pi}_j^e$.

The electrodynamic potentials $\mathbf{\Pi}^e$ and $\mathbf{\Pi}^h$ have a single component directed normally to the interfaces between the layers of the multiferroic structure, i.e. along the y -axis. Taking into account the boundary condition “magnetic wall” on the side metal walls and in the centre of the waveguide, these components can be written in the following form:

$$\begin{aligned}\mathbf{\Pi}_j^e &= \sum_{n=0}^{\infty} (A_{jn}^e(y) \cos(a_n z) e^{i(\omega t - kx)} \mathbf{e}_y) \\ \mathbf{\Pi}_j^h &= \sum_{n=0}^{\infty} (A_{jn}^h(y) \sin(a_n z) e^{i(\omega t - kx)} \mathbf{e}_y)\end{aligned}\quad (4.2)$$

where $a_n = \pi n / d$, d is width of the CW, k is the wavenumber, A_{jn}^h and A_{jn}^e are the arbitrary coefficients for the j -layer.

For a source-free region of a homogeneous and isotropic medium, the Hertzian potentials satisfy the scalar Helmholtz equations in each layer except in the ferrite:

$$\frac{\partial^2 A_j^e(y)}{\partial y^2} + \kappa_{jn}^2 A_j^e(y) = 0, \quad \frac{\partial^2 A_j^h(y)}{\partial y^2} + \kappa_{jn}^2 A_j^h(y) = 0 \quad (4.3)$$

where $\kappa_{jn} = \sqrt{\omega^2 \mu_0 \epsilon_0 \epsilon_j - k^2 - a_n^2}$ are the transverse wavenumbers. Solutions of Equation (4.3) for the dielectric layers, except for the upper and lower layers, are given by:

$$\begin{aligned}A_{jn}^h(y) &= A_{jn} \cos(\kappa_{jn}(y - y_j)) + B_{jn} \frac{\sin(\kappa_{jn}(y - y_j))}{\kappa_{jn}} \\ A_{jn}^e(y) &= C_{jn} \frac{\sin(\kappa_{jn}(y - y_j))}{\kappa_{jn}} + D_{jn} \cos(\kappa_{jn}(y - y_j))\end{aligned}\quad (4.4)$$

where $y_j = \sum_{m=1} t_m$. Therefore, Equations (4.2)-(4.4) give the components of the fields for each dielectric layer in the following form:

$$\begin{aligned}
H_{jx} &= \sum_{n=0}^{\infty} - \left(a_n A_{jn}^e(y) + \frac{k}{\omega\mu_0} \frac{\partial A_{jn}^h(y)}{\partial y} \right) \cos(a_n z) e^{i(\omega t - kx)}, \\
H_{jy} &= \sum_{n=0}^{\infty} -i(a_n^2 + k^2) A_{jn}^h(y) \cos(a_n z) \frac{e^{i(\omega t - kx)}}{\omega\mu_0}; \\
H_{jz} &= \sum_{n=0}^{\infty} i \left(\frac{a_n}{\omega\mu_0} \frac{\partial A_{jn}^h(y)}{\partial y} - k A_{jn}^e(y) \right) \sin(a_n z) e^{i(\omega t - kx)};
\end{aligned} \tag{4.5}$$

$$\begin{aligned}
E_{jx} &= \sum_{n=0}^{\infty} - \left(a_n A_{jn}^h(y) + \frac{k}{\omega\epsilon_0\epsilon_j} \frac{\partial A_{jn}^e(y)}{\partial y} \right) \sin(a_n z) e^{i(\omega t - kx)}; \\
E_{jy} &= \sum_{n=0}^{\infty} -i(a_n^2 + k^2) A_{jn}^e(y) \sin(a_n z) \frac{e^{i(\omega t - kx)}}{\omega\epsilon_0\epsilon_j}; \\
E_{jz} &= \sum_{n=0}^{\infty} i \left(k A_{jn}^h(y) - \frac{a_n}{\omega\epsilon_0\epsilon_j} \frac{\partial A_{jn}^e(y)}{\partial y} \right) \cos(a_n z) e^{i(\omega t - kx)}.
\end{aligned} \tag{4.6}$$

These expressions contain four unknown coefficients A_{jn} , B_{jn} , C_{jn} , D_{jn} for each layer. It is possible to reduce the number of the unknowns for the top ($j = 6$) and the bottom ($j = 1$) layers because they are metallised and, therefore, the boundary conditions at the surface of a perfect electric conductor can be used. For these layers only two unknown coefficients A_{1n} , C_{1n} and A_{6n} , C_{6n} remain:

$$A_{jn}^h(y) = A_{jn} \cos(\kappa_{jn}(y - y_j)), \quad A_{jn}^e(y) = C_{jn} \frac{\sin(\kappa_{jn}(y - y_j))}{\kappa_{jn}}. \tag{4.7}$$

As the first step in solving the problem, the unknown coefficients in these two dielectric layers adjacent the metal electrodes of the CW will be related to those in the top and the bottom ones. To accomplish this, the tangential components of both fields that are continuous across the interfaces $y = -t_3$ and $y = -t_3 - t_2$ fulfil the electromagnetic boundary conditions.

This gives a system of eight homogeneous algebraic equations for the coefficients A_{3n} , B_{3n} , C_{3n} , D_{3n} , A_{2n} , B_{2n} , C_{2n} , D_{2n} , A_{1n} , C_{1n} . Since boundary conditions at a particular surface link only the unknown coefficients in two adjacent layers, the matrix corresponding to the above-mentioned system of equations has a characteristic bloc diagonal structure, which allows its factorisation. Thus, A_{3n} , B_{3n} , C_{3n} and D_{3n} are expressed using A_{1n} and C_{1n} in the following form:

4.1 Theory for wave spectra of multiferroic structures with coplanar waveguides 61

$$[A_{3n}, B_{3n}, C_{3n}, D_{3n}] = \mathbf{MB} \cdot [A_{1n}, C_{1n}]^T \quad (4.8)$$

where \mathbf{MB} is a matrix presented in Appendix.

Similar mathematical manipulations were carried out for the layers above the electrodes of the CW. The tangential components of magnetic and electric fields across the interface $y = t_4 + \delta + t_5$, i.e. between the layers with $j = 5$ and $j = 6$, are substituted into the electrodynamic boundary conditions. This leads to a system of four homogeneous algebraic expressions for $A_{5n}, B_{5n}, C_{5n}, D_{5n}$ and A_{6n}, C_{6n} . Using the ABC method, these coefficients are found at the interface between ferrite and dielectric layers, i.e. $y = t_4$ and $y = t_4 + \delta$. This gives the following derivatives from Maxwell's equations:

$$\frac{\partial H_x}{\partial y}; \frac{\partial H_z}{\partial y}; \frac{\partial E_x}{\partial y}; \frac{\partial E_z}{\partial y}.$$

In the next step, a system of homogeneous algebraic equations $A_{4n}, B_{4n}, C_{4n}, D_{4n}, A_{5n}, B_{5n}, C_{5n}, D_{5n}$ is obtained. Then unknown coefficients for the layer $j = 4$ are related to those for the top layer $j = 6$

$$[A_{4n}, B_{4n}, C_{4n}, D_{4n}] = \mathbf{MT} \cdot [A_{6n}, C_{6n}]^T \quad (4.9)$$

where \mathbf{MT} is a matrix presented in the Appendix.

The fulfilment of the conditions of the continuity for the tangential components of the vectors \mathbf{H} (4.5) and \mathbf{E} (4.6) at the boundaries of the layers makes it possible to relate the unknown coefficients:

$$\begin{aligned} \sum_{n=0}^{\infty} X_{11} \cos(a_n z) \frac{2}{d} \varphi_n \int_{-w/2}^{w/2} g(z) \cos(a_n z) dz + \sum_{n=0}^{\infty} X_{12} \cos(a_n z) \frac{2}{d} \varphi_n \int_{-w/2}^{w/2} f(z) \sin(a_n z) dz = 0 \\ \sum_{n=0}^{\infty} X_{21} \sin(a_n z) \frac{2}{d} \int_{-w/2}^{w/2} g(z) \cos(a_n z) dz + \sum_{n=0}^{\infty} X_{22} \sin(a_n z) \frac{2}{d} \varphi_n \int_{-w/2}^{w/2} f(z) \sin(a_n z) dz = 0 \end{aligned} \quad (4.10)$$

where $g(z)$ and $f(z)$ are unknown distributions of the electric field normal components; and $X_{11}, X_{12}, X_{21}, X_{22}$ are the elements of the matrix \mathbf{X} that could be written as $\mathbf{X} = \mathbf{HT} \cdot \mathbf{MT} \cdot (\mathbf{ET} \cdot \mathbf{MT})^{-1} - \mathbf{HB} \cdot \mathbf{MB} \cdot (\mathbf{EB} \cdot \mathbf{MB})^{-1}$. Here,

$$\mathbf{ET} = \begin{bmatrix} \frac{-kW_{1n}}{\omega \varepsilon_0 \varepsilon_1} & \frac{-k}{\omega \varepsilon_0 \varepsilon_1} & -a_n & a_n V_{1n} \\ \frac{a_n W_{1n}}{\omega \varepsilon_0 \varepsilon_1} & \frac{a_n}{\omega \varepsilon_0 \varepsilon_1} & -k & k V_{1n} \end{bmatrix}, \quad \mathbf{HT} = \begin{bmatrix} -a_n & a_n V_{1n} & \frac{kW_{1n}}{\omega \mu_0} & \frac{k}{\omega \mu_0} \\ k & -k V_{1n} & \frac{a_n W_{1n}}{\omega \mu_0} & \frac{a_n}{\omega \mu_0} \end{bmatrix} \quad (4.11)$$

matrices \mathbf{EB} and \mathbf{HB} are obtained from the matrix by the following replacements: ε_4 by ε_3 , V_{4n} by $-V_{3n}$, and W_{4n} by $-W_{3n}$.

Since the unknown distributions $g(z)$ and $f(z)$ enter Equation (4.10) inside integrals, their solution can be obtained using the Galerkin method. For the convenience of integration inside the gap, the unknown distributions of the electric field normal components $g(z)$ and $f(z)$ are represented as a function of the normalised coordinate ξ having zero at the centre of this gap. Therefore, the origin of the z -axis can be transformed to the centre of the gap, which corresponds to $z_0 = (h+w)/2$ (see Figure 4.1). According to the new location of the coordinate system, a new coordinate $\xi = z - (h+w)/2$ can be introduced and normalised to $w/2$. Therefore, $\xi = 2\xi^*/w$. One should note that the variable ξ varies on the width of the gap in the interval $[-1, +1]$.

An efficiency of the Galerkin method is determined by the rate of the convergence, which depends on a system of approximating functions for currents on electrodes or fields inside gaps of a CW. For the considered case, the Chebyshev polynomials of the first (T_{2m}) and second (U_{2m+1}) kinds are used as an orthogonal basis for expanding $g(z)$ and $f(z)$, respectively. This choice is conditioned by the need to take into account a finiteness of an electromagnetic energy near an infinitely thin layer of a perfectly conducting metal.

Unknown distributions of the tangential components $g(z)$ and $f(z)$ of the electric field can be written as functions of the normalised variable ξ in form:

$$f(\xi) = \sum_{m=0}^M r_m \frac{T_{2m}(\xi)}{\sqrt{1-\xi^2}}, \quad g(\xi) = \sum_{m=0}^M u_m \sqrt{1-\xi^2} U_{2m+1}(\xi) \quad (4.12)$$

where r_m and u_m are the unknown coefficients; $m = 0, 1 \dots M$; and M is the index of the Chebyshev polynomial order determined by the width of the gap w . By substituting Equation (4.12) into Equation (4.10), the following expressions are obtained:

$$\begin{aligned} & \sum_{n=0}^{\infty} X_{11} \cos(a_n z) \sum_{m=0}^M u_m \int_{-w/2}^{w/2} \sqrt{1-\xi^2} U_{2m+1}(\xi) \cos(a_n z) dz + \\ & + \sum_{n=0}^{\infty} X_{12} \cos(a_n z) \phi_n \sum_{m=0}^M r_m \int_{-w/2}^{w/2} \frac{T_{2m}(\xi)}{\sqrt{1-\xi^2}} \sin(a_n z) dz = 0; \\ & \sum_{n=0}^{\infty} X_{21} \sin(a_n z) \sum_{m=0}^M u_m \int_{-w/2}^{w/2} \sqrt{1-\xi^2} U_{2m+1}(\xi) \cos(a_n z) dz + \\ & + \sum_{n=0}^{\infty} X_{22} \sin(a_n z) \phi_n \sum_{m=0}^M r_m \int_{-w/2}^{w/2} \frac{T_{2m}(\xi)}{\sqrt{1-\xi^2}} \sin(a_n z) dz = 0 \end{aligned} \quad (4.13)$$

4.1 Theory for wave spectra of multiferroic structures with coplanar waveguides 63

$$\text{where } \phi_n = \begin{cases} 1/2 & \text{at } n = 0 \\ 1 & \text{at } n \neq 0 \end{cases}.$$

According to the fact that $z = w\xi/2 + (h+w)/2$ it is found that:

$$\begin{aligned} \cos(a_n z) &= \cos(q_n \xi) \cos(a_n (h+w)/2) - \sin(q_n \xi) \sin(a_n (h+w)/2) \\ \sin(a_n z) &= \sin(q_n \xi) \cos(a_n (h+w)/2) + \cos(q_n \xi) \sin(a_n (h+w)/2) \end{aligned} \quad (4.14)$$

$$\text{where } q_n = \frac{n\pi w}{2d}.$$

Taking into account the even character of the Chebyshev polynomials in $f(z)$ and the odd character of these polynomials in $g(z)$, the following expressions are obtained:

$$\begin{aligned} \int_{-w/2}^{w/2} \sqrt{1-\xi^2} U_{2m+1}(\xi) \cos(a_n z) dz &= -\sin(a_n (h+w)/2) \int_{-1}^1 \sqrt{1-\xi^2} U_{2m+1}(\xi) \sin(q_n \xi) d\xi; \\ \int_{-w/2}^{w/2} \frac{T_{2m}(\xi)}{\sqrt{1-\xi^2}} \sin(a_n z) dz &= \sin(a_n (h+w)/2) \int_{-1}^1 \frac{T_{2m}(\xi)}{\sqrt{1-\xi^2}} \cos(q_n \xi) d\xi. \end{aligned} \quad (4.15)$$

In accordance with (Gradshteyn, 2007), the integrals in the last relations can be calculated analytically:

$$\begin{aligned} \int_{-1}^1 T_{2m}(q_n) \cos(q_n \xi) \frac{d\xi}{\sqrt{1-\xi^2}} &= (-1)^m \pi J_{2m}(q_n) \\ \int_{-1}^1 \sqrt{1-\xi^2} U_{2m+1}(q_n) \sin(q_n \xi) d\xi &= (-1)^m \pi \frac{J_{2m+2}(q_n)}{q_n} \end{aligned} \quad (4.16)$$

where $J_{2m}(q_n)$ and $J_{2m+2}(q_n)$ are the Bessel functions of the first kind; $n = 0, 1 \dots N$; and N is the value, where the Bessel functions converge.

Taking into account Equations (4.12)-(4.16), Equation (4.10) can be written as:

$$\begin{aligned} -\sum_{n=0}^{\infty} X_{11} \cos(a_n z) \sum_{m=0}^M u_m (-1)^m \frac{J_{2m+2}(q_n)}{q_n} \sin(a_n (h+w)/2) + \\ + \sum_{n=0}^{\infty} X_{12} \cos(a_n z) \phi_n \sum_{m=0}^M r_m (-1)^m J_{2m}(q_n) \sin(a_n (h+w)/2) = 0; \end{aligned} \quad (4.17)$$

$$\begin{aligned}
& -\sum_{n=0}^{\infty} X_{21} \sin(a_n z) \sum_{m=0}^M u_m (-1)^m \frac{J_{2m+2}(q_n)}{q_n} \sin(a_n (h+w)/2) + \\
& + \sum_{n=0}^{\infty} X_{22} \sin(a_n z) \phi_n \sum_{m=0}^M r_m (-1)^m J_{2m}(q_n) \sin(a_n (h+w)/2) = 0.
\end{aligned} \tag{4.18}$$

Using the Galerkin method, Equations (4.17) and (4.18) are multiplied by $T_{2m}(q_n)/\sqrt{1-\xi^2}$ and $\sqrt{1-\xi^2}U_{2m+1}(q_n)$, respectively. After changing the order of summation and integration, the following expressions are obtained:

$$\begin{aligned}
& -\sum_{n=0}^N X_{11} \sum_{m=0}^M u_m (-1)^m \frac{J_{2m+2}(q_n)}{q_n} \sin(a_n (h+w)/2) \int_{-1}^1 \frac{T_{2s}(\xi)}{\sqrt{1-\xi^2}} \cos(a_n z) dz + \\
& + \sum_{n=0}^N X_{12} \phi_n \sum_{m=0}^M r_m (-1)^m J_{2m}(q_n) \sin(a_n (h+w)/2) \int_{-1}^1 \frac{T_{2s}(\xi)}{\sqrt{1-\xi^2}} \cos(a_n z) dz = 0;
\end{aligned} \tag{4.19}$$

$$\begin{aligned}
& -\sum_{n=0}^N X_{21} \sum_{m=0}^M u_m (-1)^m \frac{J_{2m+2}(q_n)}{q_n} \sin(a_n (h+w)/2) \int_{-1}^1 \sqrt{1-\xi^2} U_{2m+1}(q_n) \sin(a_n z) dz + \\
& + \sum_{n=0}^N X_{22} \phi_n \sum_{m=0}^M r_m (-1)^m J_{2m}(q_n) \sin(a_n (h+w)/2) \int_{-1}^1 \sqrt{1-\xi^2} U_{2m+1}(q_n) \sin(a_n z) dz = 0.
\end{aligned} \tag{4.20}$$

Similar mathematical manipulations, as for Equations (4.12) - (4.16), are performed for the integration of Equations (4.19) and (4.20):

$$\begin{aligned}
& -\sum_{n=0}^N X_{11} Y11_{n,m,s} + \sum_{n=0}^N X_{12} Y12_{n,m,s} = 0 \\
& -\sum_{n=0}^N X_{21} Y21_{n,m,s} + \sum_{n=0}^N X_{22} Y22_{n,m,s} = 0
\end{aligned} \tag{4.21}$$

$$\begin{aligned}
\text{where } Y11_{n,m,s} &= (-1)^{1+m+s} J_{2s}(q_n) \frac{(2m+2)J_{2m+2}(q_n)}{q_n} \sin^2(a_n (h+w)/2), \\
Y12_{n,m,s} &= (-1)^{m+s} \phi_n J_{2m}(q_n) J_{2s}(q_n) \sin^2(a_n (h+w)/2), \\
Y21_{n,m,s} &= (-1)^{1+m+s} \frac{(2m+2)J_{2m+2}(q_n)}{q_n} \frac{(2s+2)J_{2s+2}(q_n)}{q_n} \sin^2(a_n (h+w)/2), \\
Y22_{n,m,s} &= (-1)^{m+s} \phi_n J_{2m}(q_n) \frac{(2s+2)J_{2s+2}(q_n)}{q_n} \sin^2(a_n (h+w)/2).
\end{aligned}$$

Equation (4.21) represents a homogeneous system of linear algebraic equations. The vanishing of its determinant results in the dispersion relation:

$$\sum_{n=0}^N \det \begin{bmatrix} X_{11} \cdot Y11_{n,m,s} & X_{12} \cdot Y12_{n,m,s} \\ \phi_n \cdot X_{21} \cdot Y21_{n,m,s} & \phi_n \cdot X_{22} \cdot Y22_{n,m,s} \end{bmatrix} = 0. \tag{4.22}$$

The dispersion relation (4.22) describes the spectrum of spin-electromagnetic waves in planar all-thin-film multiferroic structures containing a coplanar waveguide. As proof-of-concept of the proposed theory, the wave spectra of CW with various ferroelectric films and dielectric substrates were calculated according to the developed theory and were compared with the results given in previous research (Iskander, 1989; Mironenko, 2001). Thus, the results of numerical modelling are in a good agreement with both theoretical and experimental data.

4.2 General features of wave spectra

Before an explanation of the main features of SEW spectra in the CW composed of ferrite and ferroelectric films, some comments about the analytical theory should be made:

- An order of Equation (4.22) depends on the number of Chebyshev polynomials approximating the field distribution inside the gaps of the CW. Therefore, it is necessary to determine the number of polynomials M providing a stable solution of the dispersion relation. According to estimations, this number depends on the width of the gap. In general, at least seven polynomials should be taken into account to achieve an error not exceeding 1%. However, a reduction of a gap width w provides a decrease of M . For example, for $w = 25 \mu\text{m}$, a stable solution of the dispersion relation with the indicated 1% error was obtained at $M = 3$;
- The elements of the matrix \mathbf{Y} in Equation (4.22) are a slowly converging series of products of Bessel functions. Therefore, it is necessary to determine the number of terms N providing enough high accuracy of a solution of the dispersion relation. The final value of N also depends on the width of the gap, because the argument of the Bessel functions is equal to $q_n = n\pi w/2d$. Thus, in accordance with the handbook of mathematical functions (Abramowitz, 1965), the following estimation was made: a sufficient number of Bessel function terms ensuring an asymptotic approximation error less than 1%, was $N = 10^4$ for a narrow gap ($w = 25 \mu\text{m}$). In the case of a wide gap ($w = 150 \mu\text{m}$) the same error is already achieved at $N = 10^5$;
- To implement the conditions of a CW placed in free space, the thicknesses t_1 and t_6 of the dielectric layers adjacent to the metal, as well as the distance d between the side walls of the waveguide, should be obtained. According to estimations, the optimal values of these parameters are $t_1 = t_6 = 0.1 \text{ m}$ and $d = 0.04 \text{ m}$. Their further increase changes the result of the numerical calculation of Equation (4.22) by less than 1%, but provides an increase in the number of terms of the Bessel functions N ;
- To reduce a control voltage in a CW with narrow gaps, less than $100 \mu\text{m}$, will be considered hereinafter.

Following this, investigations of wave spectra of the CW shown in Figure 4.2 will be examined. This consists of two dielectric layers ($j = 1$ and $j = 4$), a ferroelectric film

($j = 2$), metal electrodes and a ferrite film ($j = 3$). During simulations, the parameters were as follows: $\epsilon_2 = 10$, $t_2 = 500 \text{ } \mu\text{m}$; $\epsilon_3 = 1500$, $t_3 = 2 \text{ } \mu\text{m}$; $\epsilon_f = 14$, $\delta = 10 \text{ } \mu\text{m}$, $M_0 = 1750 \text{ G}$, $\epsilon_5 = 14$, $t_5 = 500 \text{ } \mu\text{m}$; $H = 1350 \text{ Oe}$; $w = 50 \text{ } \mu\text{m}$, $h = 50 \text{ } \mu\text{m}$. One should note that the thickness of the electrodes is assumed to be much smaller compared to the skin depth at the operating frequencies.

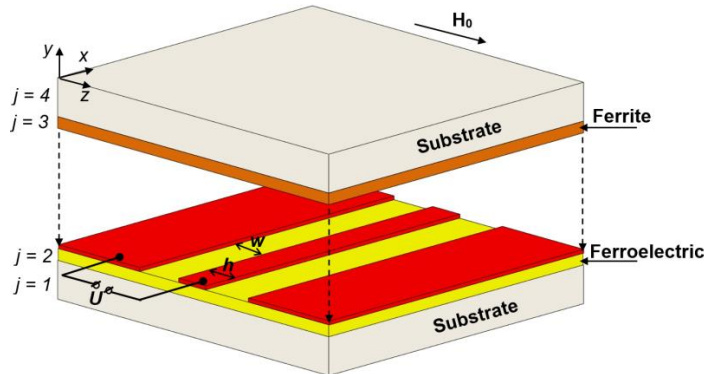


Figure 4.2: Coplanar waveguide composed of ferrite and ferroelectric films.

Figure 4.3 illustrates the effect of the hybridisation of two principal electromagnetic modes, which play a fundamental role in this investigation. The solid curves represent typical dispersion characteristics actually featured by the waveguide, while the dash lines show, for the sake of comparison, the dispersion law of the eigen-modes that are hybridised, namely, the branch for the fundamental electromagnetic mode (see blue line) of the individual CW on a ferroelectric film and the branch of the surface spin-wave mode (see red line) in the uncovered ferrite film. One can clearly see that the hybridisation becomes more pronounced in the vicinity of the point, where the two dispersion branches cross each other.

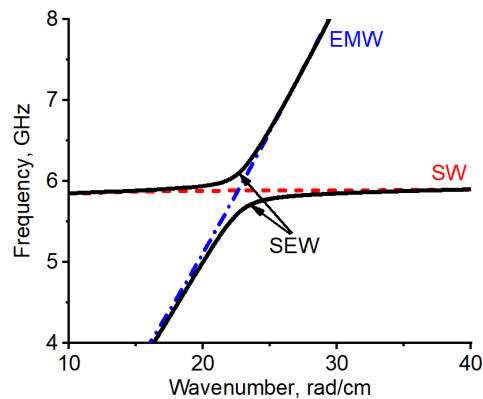


Figure 4.3: Spectrum of the hybrid SEW in the all-thin-film multiferroic structure with the coplanar waveguide.

As Figure 4.3 shows, the dispersion characteristics of the EMW and SEW coincide far from the ferromagnetic resonance frequency. Near this resonance frequency, the SEW phase velocity decreases due to the hybridisation of the SW and the EMW. A distinctive feature of the all-thin-film multiferroic structure with a CW is an absence of undesirable irregularities in dispersion for relatively low frequencies when the wavelength approaches the thickness of ferroelectric layer. This is in contrast to the open ferrite-ferroelectric waveguiding structure without metallisation.

With regard to investigations of an influence of structure parameters on the dispersion characteristics of SEW, Figure 4.4 shows the calculated dependences of the wave spectra versus the gap width w , the thickness of ferroelectric t_3 and ferrite δ films, as well as the width of the central strip h . One should note that the solid black lines in Figure 4.4 correspond to the dispersion characteristic shown in Figure 4.3.

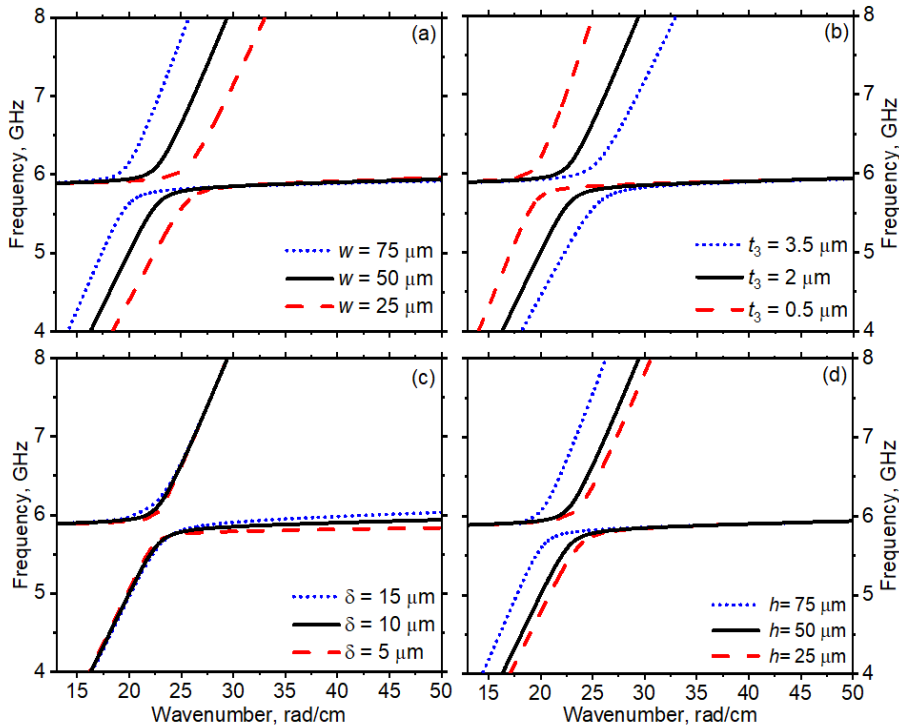


Figure 4.4: Influence of (a) the gap width w ; (b) the thickness t_3 of the ferroelectric film; (c) the thickness δ of the ferrite film; and (d) the width h of the central metal strip on the dispersion characteristics of the SEW.

As presented in Figure 4.4, a decrease of the gap width w and the width h of the central metal strip, as well as an increase in the thickness of the ferroelectric film t_3 , shifts the area of the maximum hybridisation of waves to the higher wavenumbers (see Figures 4.4a, b, d). In this case, the electrodynamic interaction of the SW in the ferrite film and

the EMW in the coplanar waveguide is enhanced. Further, the ferrite film thickness δ explicitly influences the slope of the SW dispersion branches leading to a drastic change in the SEW group velocity (see Figure 4.4 (c)).

If one follows this with an investigation of the dual (electric and magnetic) tunability of the hybrid SEW in the all-thin-film multiferroic structure with the CW, Figure 4.5 shows the results of a numerical simulation of the wave spectra for different values of an external magnetic field H and a control voltage U . One should note that the solid black lines in Figure 4.5 correspond to the dispersion characteristic shown in Figure 4.3.

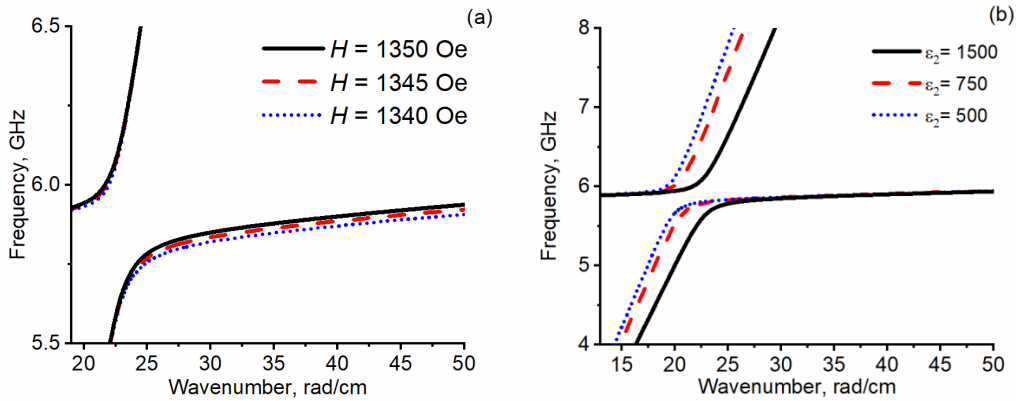


Figure 4.5: (a) Magnetic and (b) electric field tuning of the dispersion characteristics.

An increase in the external magnetic field H leads to a shift of the spin-wave spectrum towards the higher frequencies. Therefore, the area of the effective hybridisation of the EMW and SW demonstrates an up-frequency shift too (see Figure 4.5a). An application of a control voltage U to the electrodes leads to a reduction of the ferroelectric film permittivity ϵ_2 and provides an electric field tunability. As can be seen in Figure 4.5b, an increase in a control voltage provides an increase in the group velocity of the EMW in the CW. Therefore, the area of the maximum hybridisation is shifted to the lower wavenumbers. This leads to an increase in the electrodynamic interaction of waves, and, therefore, an enhancement of an electric field tunability of the SEW spectrum. According to estimates, it is possible to achieve the additional increase in the tuning efficiency by reducing the width of a gap and the width of a central metal electrode in a CW, as well as by increasing the thickness of a ferroelectric film.

5 Microwave structures with a spatial periodic modulation based on ferrite and ferroelectric films

This chapter presents the results from the investigation of novel electromagnonic crystals composed of ferroelectric and ferrite films. Previous experiments on the propagation of SEW in ferrite-ferroelectric spatially periodic structure utilised a ferroelectric slab to provide effective hybridisation of SW and EMW at microwave frequencies and, consequently, the effective electric field tuning of the SEW dispersion (Ustinov, 2014, 2019; Morozova, 2014, 2016). The thin-film multiferroic structures proposed in the previous chapters look favourable for structure miniaturisation and a reduction of the control voltage of electromagnonic crystals. As outlined in Chapter 3, the regular waveguides based on the ferrite-ferroelectric-ferrite three-layer structures enrich the properties of multiferroics because of the dipole-dipole interaction between the coupled ferrite films. These structures demonstrate an enhanced voltage-controlled phase shift of SEW. The same feature is occurred also for planar all-thin-film multiferroic structures containing a coplanar waveguide that were discussed in Chapter 4. An interest in thin-film ferrite-ferroelectric structures arises not only from possible practical applications, but also from a variety of fundamental scientific problems devoted to the physics of wave phenomena in spatially periodic magnetic multilayers.

5.1 Electromagnonic crystals based on ferrite-ferroelectric thin-film multilayers

In this Section, an experimental realisation of the electromagnonic crystal (EMC) composed of the ferrite-ferroelectric-ferrite spatially periodic structure will be presented. Here, the waveguide periodicity is realised by a thickness modulation of a ferrite film forming a free-standing magnonic crystal (MC). An image of the investigated structure is shown in Figure 5.1, where the details will be explained later in Section 5.1.2. To treat the obtained results, the free-standing MC, as well as the EMC composed of the ferrite-ferroelectric bilayer, will also be considered. The obtained band structures will be compared with numerical simulations utilising a coupled-mode approach and a transfer-matrix method.

5.1.1 Theoretical model of an electromagnonic crystal

The numerical simulation of band structures of the EMC was carried out in several stages. In the first stage, the dispersion relations for the waves propagating in the spatially periodic waveguides were obtained by a coupled-mode approach (Huang, 1984). In this approach, a variation of the ferrite film thickness representing a periodic sequence of sections of the regular transmission lines was considered a perturbation that leads to an exchange of a power among the guided modes. The resulting dispersion relation for the periodic structure is given by:

70 5 Microwave structures with a spatial periodic modulation based on ferrite and ferroelectric films

$$\cos(KA) = \cos(k_1 L_1) \cos(k_2 L_2) - \frac{k_1^2 + k_2^2}{2k_1 k_2} \sin(k_1 L_1) \sin(k_2 L_2), \quad (5.1)$$

where K is the Bloch wave-vector; A is the period being the sum of the groove width (L_1) and the groove-to-groove distance (L_2); and k_1 and k_2 are the wavenumbers of the surface SW or SEW in the unstructured film with different thickness. One should note that the wavenumbers for the free-standing magnonic crystal are found according to the dispersion relation for surface spin waves (2.4). At the same time, the wavenumbers of the SEW in the ferrite-ferroelectric structures can be obtained by a solution of the dispersion relation (3.8) derived in Chapter 3. To consider the propagation losses of the waves in different sections of the periodic structure, the elements of the permeability tensors and permittivities of each layer are taken as complex quantities. As a result, the complex dispersion relations $\omega(k_j + i\alpha_j)$ were obtained, where α_j is the spatial damping decrement of the wave in the section with the number j .

In the second stage, the transmission characteristics of the periodic structure are calculated according to the transfer-matrix method, which allows one to calculate the transmission characteristics of a finite-length periodic waveguide. According to the transfer-matrix method, both wave propagation in an unstructured ferrite film and reflections from the junctions of the consecutive sections are described by the T -matrices:

I) Matrix T_1 describes the propagation of the waves in the thick unstructured ferrite film and has the following form:

$$\mathbf{T}_1(\omega) = \begin{bmatrix} \exp[(-ik_1 + \alpha_1)L_1] & 0 \\ 0 & 1/\exp[(-ik_1 + \alpha_1)L_1] \end{bmatrix} \quad (5.2)$$

II) Matrix T_2 describes the reflections of the waves for the front edge of the grooved film and is given by:

$$\mathbf{T}_2(\omega) = \begin{bmatrix} 1/(1-\Gamma) & \Gamma/(1-\Gamma) \\ \Gamma/(1-\Gamma) & 1/(1-\Gamma) \end{bmatrix} \quad (5.3)$$

where $\Gamma = (k_1 - k_2)/(k_1 + k_2)$ is the rejection coefficient at the junction of the wider-to-narrower waveguide.

III) Matrix T_3 describes the propagation of the waves in the thin unstructured ferrite film and has the following form:

5.1 Electromagnonic crystals based on ferrite-ferroelectric thin-film multilayers 71

$$\mathbf{T}_3(\omega) = \begin{bmatrix} \exp[(-ik_2 + \alpha_2)L_2] & 0 \\ 0 & 1/\exp[(-ik_2 + \alpha_2)L_2] \end{bmatrix} \quad (5.4)$$

IV) Matrix \mathbf{T}_4 describes the reflections of the waves from the rear edge of the grooved film and is given by:

$$\mathbf{T}_4(\omega) = \begin{bmatrix} 1/(1+\Gamma) & -\Gamma/(1+\Gamma) \\ -\Gamma/(1+\Gamma) & 1/(1+\Gamma) \end{bmatrix} \quad (5.5)$$

The final transfer-matrix for the thickness-modulated ferrite film with N periods is obtained by multiplying all \mathbf{T} -matrices describing the propagation of the wave within each period:

$$\mathbf{T}_\Sigma(\omega) = (\mathbf{T}_1 \times \mathbf{T}_2 \times \mathbf{T}_3 \times \mathbf{T}_4)^N \quad (5.6)$$

According to the proposed theoretical model, the complex transfer function for the spatially periodic structure was obtained as $1/T_\Sigma(\omega)_{1,1}$. Thus, the power transmission characteristic of the periodic structure is given by:

$$S_{21}(\omega) = 20 \cdot \log_{10}(1/|T_\Sigma(\omega)_{1,1}|) \quad (5.7)$$

5.1.2 Experimental and theoretical results

The investigated structure was fabricated in the sandwich-type configuration (see Figure 5.1). The bottom ferrite layer was a 3 cm long and 2 mm wide strip made of 5.5 μm thick yttrium iron garnet (YIG) film, while the top ferrite layer was a 4 mm long and 2 mm wide strip made of 13.6 μm thick YIG film. Each film was epitaxially-grown on the single-crystal gallium gadolinium garnet (GGG) substrates of a thickness of 500 μm . The YIG films had a ferromagnetic resonance linewidth $\Delta H = 0.5$ Oe at 5 GHz frequency, and the saturation magnetisations for the top and bottom YIG films were 1800 G and 1930 G at room temperature, respectively. In order to produce MC, the thickness of the bottom YIG film was periodically modulated to a depth of 0.8 μm using the wet chemical etching. The periodic pattern consisted of 10 parallel grooves with a width of 50 μm spaced by 250 μm , so that the lattice constant was 300 μm .

The intermediate ferroelectric layer $\text{Ba}_{0.62}\text{Sr}_{0.38}\text{TiO}_3$ (BST) was fabricated by a conventional mixed oxide route followed by sintering in the air. Following this, a hydraulic press and subsequent annealing formed the BST slab. As a result, the BST slab of a relatively large thickness was produced. Characterisation of the BST slab was performed at room temperature and indicated the paraelectric nature and isotropic dielectric permittivity of 2300 at 5 GHz frequency. Then, the BST slab was polished down to a thickness of 110 μm . Finally, the slab was cut into the strips having the in-

72 5 Microwave structures with a spatial periodic modulation based on ferrite and ferroelectric films

plane dimensions of $2 \times 4 \text{ mm}^2$. As presented in the image of the EMC, its configuration corresponds to the model of the ferrite-ferroelectric multilayers discussed in Chapter 3 (see inset in Figure 5.1).

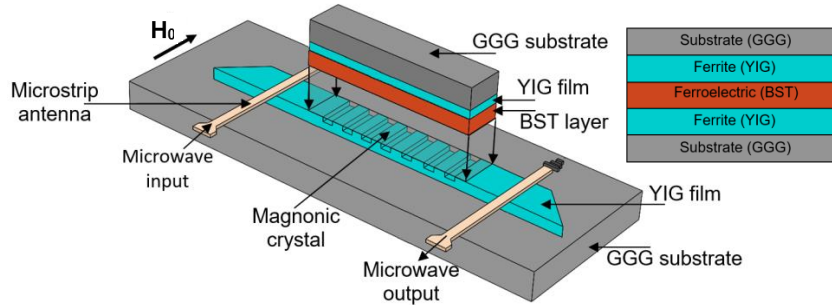


Figure 5.1: Qualitative picture showing the image of the electromagnonic crystal composed of the ferrite-ferroelectric-ferrite multilayer.

The MC was positioned in a way that the etched groove side is in contact with the short-circuited microstrip antennas with a width of $50 \mu\text{m}$ and a length of 2.5 mm . The distance between the antennas was 5.5 mm . The BST layer contacted the YIG film top and was pressed symmetrically over the spatial periodic surface of the MC. The total length of the sandwich MC-BST-YIG structure was 4 mm . The composed layered structure was magnetised by a spatially uniform bias magnetic field of 1599 Oe lying in the plane of the structure parallel to the MC grooves.

Following this, the principle of the wave propagation through the MC-BST-YIG structure will be examined. The orientation of the magnetic field in relation to the structure satisfies the condition for an excitation of the surface SW: the surface SW is excited in the uncovered bottom YIG film strip by the input microstrip antenna. At the border, where the YIG film is in contact with the BST-YIG bilayer, the surface SW transforms into the SEW, which then propagates in the layered structure and achieves the EMC region (see Figure 5.1). The SEW passes through the periodically modulated waveguide structure and transforms back to the surface SW at the output boundary of the layered structure, after which the surface SW is received by the output microstrip antenna. The microstrip antennas were fed by the microstrip transmission lines of $50\text{-}\Omega$ characteristic impedance. A vector network analyser (VNA) measured the transmission characteristics of the structure.

In order to clarify the band structure of the proposed three-layer EMC, the three types of the wave-guiding structures were investigated. The first structure was a free-standing bottom MC without a BST-YIG bilayer (see Figure 5.2a); the second one was the EMC consisting of the MC-BST bilayer (see Figure 5.2b), i.e., the BST layer was added to the bottom MC; and the third structure was the EMC composed of the complete MC-BST-YIG multilayer (Figure 5.2c).

5.1 Electromagnetic crystals based on ferrite-ferroelectric thin-film multilayers 73

The transmission characteristics of the proposed structures are presented in Figure 5.2d-f and can be summarised as follows. The black solid line in Figure 5.2d shows the calculated transmission characteristic obtained with the proposed theoretical model (see Equation (5.7)) for the free-standing MC. As seen in Figure 5.2d, the band-gaps **1**, **2**, and **3** (the shaded grey areas in Figure 5.2d) are formed at the frequencies expected from the conventional Bragg analysis. Moreover, the formation of these band-gaps is in good agreement with the experimental results presented by the red dashed line in Figure 5.2d. A small deviation of the experimental dependences from the theoretical ones could be explained by different parasitic effects such as small reflections from the film edges or weak random inhomogeneity in the waveguiding structure that usually exists in experiments.

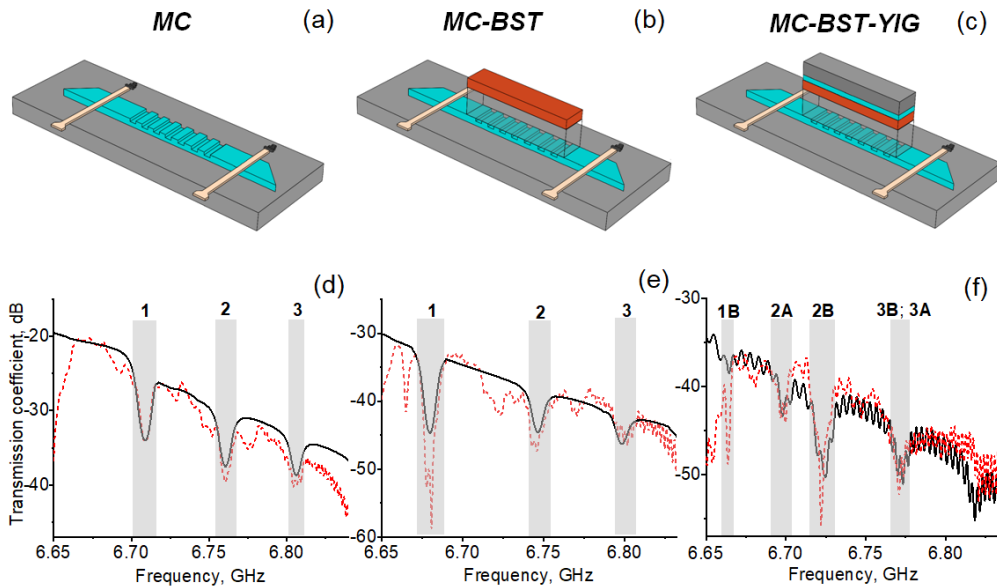


Figure 5.2: (a-c) Sketches of the experimental structures as well as (d-f) their theoretical (black solid line) and experimental (red dashed line) transmission characteristics.

For the case of the EMC consisting of the MC-BST bilayer, the band structure is modified. As Figure 5.2e shows, the band-gaps demonstrate a down-frequency shift in comparison with the band structure of the free-standing MC. The theoretically obtained transmission characteristic is shown in Figure 5.2e by the black solid line and the experimental one by the red dashed line. It is easy to see that the frequency positions of the measured and calculated band-gaps **1**, **2**, and **3** (the shaded grey areas in Figure 5.2e) coincide with a high accuracy.

The transmission coefficient of the complete EMC is shown in Figure 5.2f. Here, the black solid line represents the calculated transmission characteristic, and the dashed red

74 5 Microwave structures with a spatial periodic modulation based on ferrite and ferroelectric films

line shows the measured data. This transmission characteristic was calculated using the two-step algorithm. Initially the basic characteristics were found separately for the waves propagating as fundamental modes existing in each ferrite films. The resulting transmission characteristic was calculated as a superposition of the two interfering waves.

In contrast to the previous configurations, the band structure of the EMC composed of the MC-BST-YIG multilayer is more complicated. According to the Bragg resonance condition, the first band-gap **1A** should be observed at 6.6 GHz, which is less than the cutoff frequency of the SSW for the bottom YIG film. As a result, this band-gap lies outside the wave spectrum and cannot be observed. The first visible band-gap appeared near the 6.664 GHz frequency in the region **1B** (see the shaded grey area in Figure 5.2f). In addition, one can clearly see the formation of the two closely-spaced band-gaps **2A** and **2B** corresponding to the region of the second Bragg resonance.

In order to identify the observed band-gaps and to understand the physical reasons for their formation, a detailed theoretical analysis of the dispersion characteristics of the periodic structures under investigation was carried out. The numerical simulations were based on the solution of Equation (5.1). The validity of this approach is based on the following point: the dispersion characteristics are uniquely related to the transfer function. While the real part of the wave-number defines the phase shift of the wave in the waveguiding structure, the imaginary part describes losses. Thus, the frequency ranges, wherein the roots of (5.1) are real, correspond to the passbands while complex roots correspond to the band-gaps. The application of the dispersion characteristics for the description of the transmission characteristics is beneficial for visualisation of the transformation of the wave spectrum in both MC and EMC structures.

The spin-wave spectrum for the free-standing MC (see Figure 5.3a) will now be outlined, which will later be helpful for clarification of the band structure for the layered EMC. As seen in Figure 5.3a, the band structure of the thickness-modulated ferrite film is well-defined. An interaction among the waves in the periodical sequence of the MC sections leads to the formation of the magnonic band-gaps **1**, **2**, and **3** (see insets in Figure 5.3a) at wave-numbers corresponding to the Bragg reflection law $K_{Bn} = n\pi/\Lambda$, where n is a band-gap number.

One should note that the real band-gap with a finite frequency jump at the border of the Brillouin zone can be formed only in an idealistic loss-less artificial crystal. In a real-life lossy case, the dispersion characteristics remain continuous and zones of band-gaps are characterised by a steeper slope, which results in a local change in the SEW group velocity.

Further, the EMC composed of the MC-BST bilayer is considered; the dispersion characteristic calculated for this structure is shown in Figure 5.3b. Here, the coupled excitation of surface SW mode (blue dashed line) and electromagnetic mode TE_1 (red dashed-dotted line) leads to the SEW formation (black solid line). The spectrum of this

5.1 Electromagnetic crystals based on ferrite-ferroelectric thin-film multilayers 75

wave consists of two dispersion branches; the band-gap positions are determined by the lower dispersion branch. As one can see, the electromagnetic band structure demonstrates a down-frequency shift in comparison to the magnonic one. This phenomenon is caused by a strong repulsion between the SEW branches, which manifests itself around the point of crossing of the pure electromagnetic TE_1 and SW modes (see Figure 5.3b). For example, the frequency shift of the first electromagnetic band-gap in comparison to magnonic one is about 28 MHz. This difference is reduced for the high-order band-gaps due to a decrease of the coupling between the magnons and microwave photons.

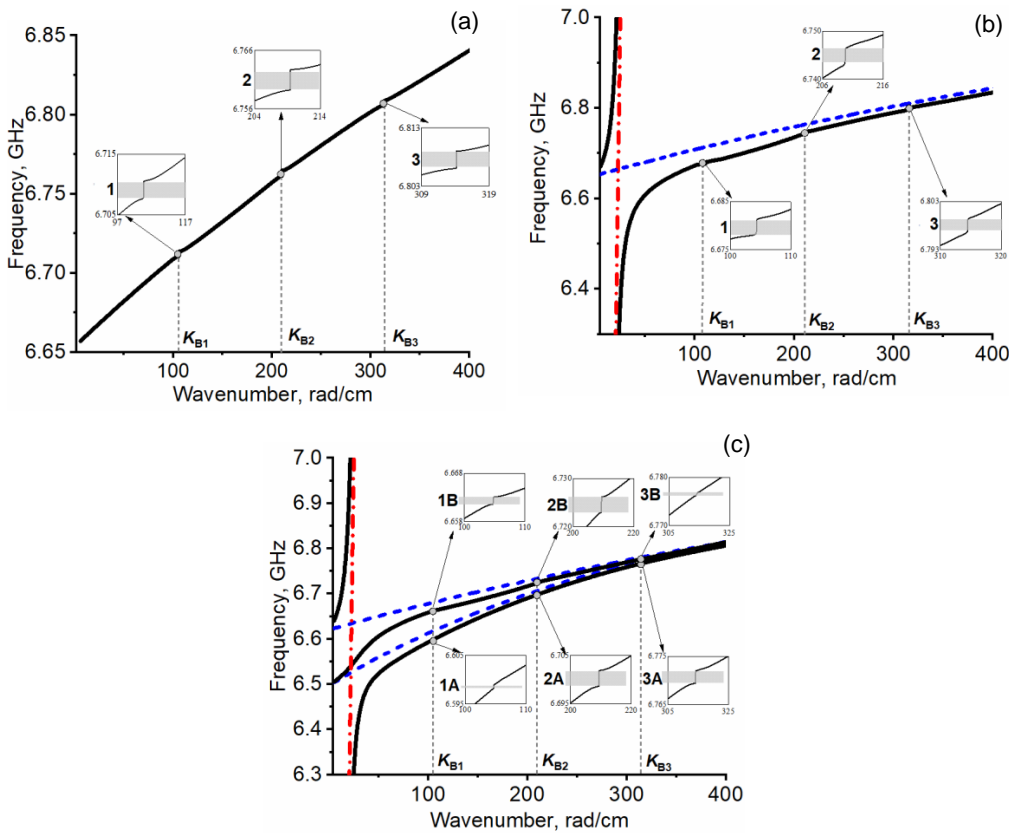


Figure 5.3: Numerical analysis of the dispersion for different configurations of the structures under investigation:

- (a) The spectrum of the spin wave in the MC. Insets here and below show peculiarities of the wave dispersion in the vicinity of the band-gaps.
- (b) The spectra of the SEW in the bilayer EMC. Dashed and dashed-dotted lines here and below represent the pure surface SW and electromagnetic mode dispersion characteristics, respectively.
- (c) The spectra of the SEW in the multilayer EMC.

76 5 Microwave structures with a spatial periodic modulation based on ferrite and ferroelectric films

Figure 5.3c shows the dispersion characteristics of the SEW in the EMC composed of the MC-BST-YIG multilayer. It is clearly visible that the wave spectrum in the frequency range under investigation consists of the three dispersion branches that are referred to as the lower, middle, and upper branches (black solid lines in Figure 5.3c). Such a spectrum is formed due to the electrodynamic interaction among the electromagnetic mode TE_1 (red dashed-dotted line) and two SW modes (blue dashed lines), as well as due to the dipole-dipole interaction between these SW modes. Because of these interactions, the SEW middle branch is clamped between the upper and lower spin-wave modes. This provides the existence of two closely spaced dispersion branches, which manifest themselves as a formation of additional band-gap corresponding to the fixed Bragg wavenumber. Therefore, in contrast to the free-standing MC and to the EMC composed of the MC-BST, the appearance of an additional band-gap in the transmission characteristic of the three-layer EMC is observed (see Figure 5.2f). For example, the first band-gap at $K_{B1} = 104.72$ rad/cm is split into two rejection regions **1A** and **1B** (shaded grey areas in insets of Figure 5.3c). The same behaviour is observed for the higher order band-gaps at $K_{B2} = 209.44$ rad/cm and $K_{B3} = 314.16$ rad/cm. For the considered geometry, the frequency distance between the band-gaps satisfying the same Bragg condition is reduced by increasing the wavenumber. Thus, the frequency difference between the band-gaps **1A** and **1B** is 63 MHz; **2A** and **2B** is 27 MHz; and **3A** and **3B** is 9 MHz. According to the SEW spectrum, the higher order band-gaps almost coincide due to a decrease of the frequency difference among them.

As already mentioned, the regular waveguides based on the ferrite-ferroelectric-ferrite three-layer structure demonstrate an enhanced voltage controlled phase shift of SEW. As a result, from a practical point of view, it would be beneficial to estimate the band-gap tuning ranges for the three-layer EMC. Electric field tunability of a band structure of this waveguide exists due to a variation of the dielectric permittivity of the ferroelectric layer. For the chosen BST composition, an electric field of 1.74 V/ μm value applied to this ferroelectric layer provides a decrease of its dielectric permittivity by 1.7 times. One should note that in the present EMC a rather thick BST slab with a thickness of 110 μm was used. Therefore, the above-mentioned variation of the BST permittivity requires the application of an electrical voltage up to 191.4 V. According to the estimations, such a voltage provides an electric tuning of the electromagnonic band-gaps **1B**, **2A**, **2B**, and **3A(3B)** up to 4.03 MHz, 2.36 MHz, 1.53 MHz, and 1.07 MHz, respectively. As one can see, an efficient electric tuning for these structures is achieved for the first band-gap, where the strong coupling between the magnons and microwave photons is observed.

5.2 Electromagnonic crystals based on a coplanar waveguide with periodic variation of the slot width

In this section, the investigations of electromagnonic crystals based on a CW that offer many promising features will be discussed: low control voltage, small out-of-band

5.2 Electromagnetic crystals based on a coplanar waveguide with periodic variation of the slot width 77

insertion losses, and deep rejection bands. Well-developed techniques of a CW fabrication, such as metal deposition and chemical etching, make it possible to produce the periodic modulation of electrodes. As explained earlier in Chapter 4, a variation in the gap width between electrodes shifts the SEW dispersion characteristics, changing significantly SEW phase velocities in the region of a strong electrodynamic coupling of the waves (see Figure 4.4a). Thus, SEW at a fixed frequency accumulate different phase shifts in the segments of the electromagnetic crystal. According to the Bragg resonance condition, the band-gaps should appear at the frequencies, where this phase shift is a multiple of π .

A thin-film electromagnetic crystal based on a CW shown in Figure 5.4 is composed of several layers enumerated with index j : a ferrite film ($j = 3$) on a dielectric substrate ($j = 4$), thin metal electrodes, and a ferroelectric film ($j = 2$) on a dielectric substrate ($j = 1$). During simulations, the parameters were as follows: $\varepsilon_1 = 10$, $t_1 = 500 \mu\text{m}$; $\varepsilon_2 = 1500$, $t_2 = 2 \mu\text{m}$; $\varepsilon_3 = 14$, $\delta = 10 \mu\text{m}$, $M_0 = 1750 \text{ G}$; $\varepsilon_4 = 14$, $t_4 = 500 \mu\text{m}$; $H = 1350 \text{ Oe}$. A central metal electrode with width of $h = 50 \mu\text{m}$ and two grounding conductors are located between the ferroelectric and ferrite layers. The segments of narrow ($w_1 = 25 \mu\text{m}$) and wide ($w_2 = 75 \mu\text{m}$) slots form a period $\Lambda = 1 \text{ mm}$. An application of a control voltage U to the CW electrodes leads to a reduction of the ferroelectric permittivity ε_2 according to (2.8). One should note that a SEW propagates along the CW, i.e. along the x -axis. The structure is magnetized to a saturation tangentially along the z -axis. As presented in the image of the EMC, its configuration corresponds to the model of the multiferroic structures with coplanar waveguides discussed in Chapter 4 (see inset in Figure 5.4).

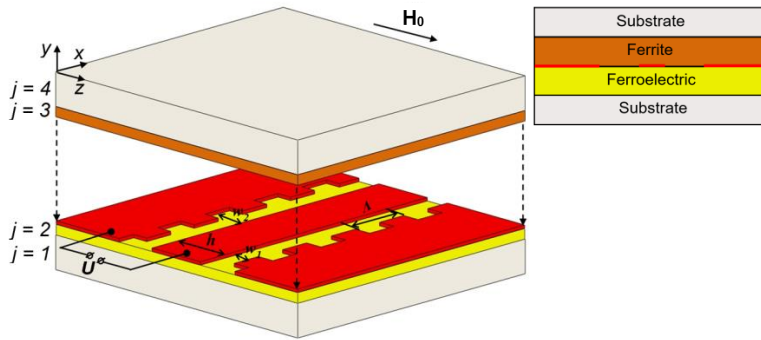


Figure 5.4: Electromagnetic crystal based on a coplanar waveguide with a rectangular modulation, w_1 and w_2 , of the slot width.

Transmission characteristics of the investigated structure are now considered; the results of the numerical simulations are presented in Figure 5.5. As in the previous Subsection, transmission characteristics of the EMC were calculated in accordance with the transfer-matrix method. Here, the wavenumbers for the sections with narrow and wide slots

78 5 Microwave structures with a spatial periodic modulation based on ferrite and ferroelectric films

were found from the dispersion relation (4.22) derived for CWs composed of thin-film ferrite-ferroelectric multilayers.

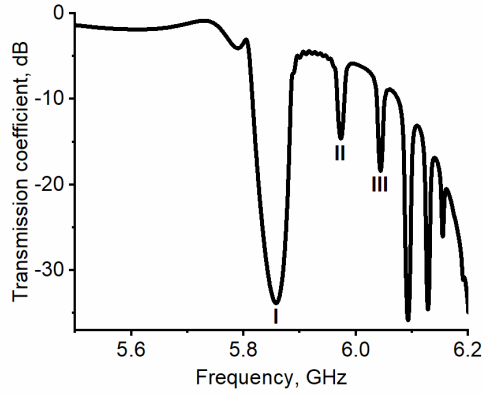


Figure 5.5: Transmission characteristic of the electromagnonic crystal containing the CW.

As can be seen in Figure 5.5, the width of the first band-gap measured at a level of 3 dB from the maximum loss of 33 dB is about 25 MHz. One should note that the band-gap position is determined by the Bragg's diffraction law, which depends on the number of a band-gap and the length of a period. Therefore, the first band-gap (denoted by I in Figure 5.5) of the electromagnonic crystal occurs near 5.86 GHz, which corresponds to the wavenumber $K_{B1} = 31.4$ rad/cm on the SEW dispersion characteristic. The widths of the high-order band-gaps and the distance between them decrease due to the essential change of the SEW group velocity in the area of the effective hybridisation of the EMW and SW modes (see Figure 4.3).

As explained in Chapter 4, the dispersion characteristics of the SEW and, consequently, the transmission characteristics of all-thin-film multiferroic structures containing a CW depend on a variety of the parameters, such as the thicknesses of the ferrite or ferroelectric films, and values of the applied magnetic or electric fields. This dependence provides an opportunity to produce an EMC with the desirable rejection efficiency and the required bandwidth. To demonstrate this, numerical simulations for various thicknesses of the ferrite and ferroelectric films were carried out (see Figures 5.6 and 5.7, respectively).

An increase in the ferrite film thickness δ influences the slope of the spin-wave dispersion branches leading to a shift of the dispersion characteristics and to a drastic change in the SEW group velocity (see Figure 5.6a). For the Bragg wavenumber ($K_{B1} = \pi/L = 31.4$ rad/cm) corresponding to the first band-gap, the shift of the dispersion characteristics leads to the shift of the band-gap position towards higher frequencies (see red dashed line in Figure 5.6b). Moreover, an increase in the SEW group velocity broadens the bandwidth (see black solid line in Figure 5.6b).

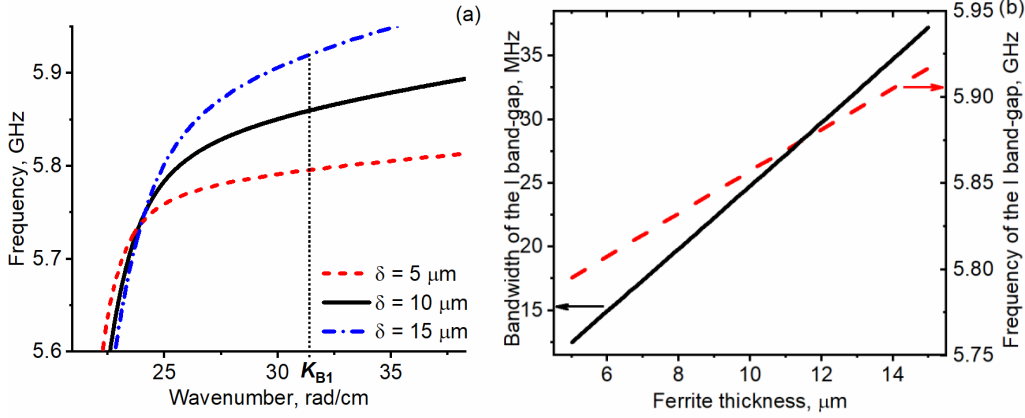


Figure 5.6: (a) Spectra of the hybrid SEW in the regular CW with slot width $w = 75 \mu\text{m}$ calculated for various ferrite thicknesses δ ; (b) The influence of the ferrite thickness on the bandwidth (black solid line), and the frequency (red dashed line) of the first band-gap corresponding to wavenumber $K_{B1} = 31.4$ rad/cm.

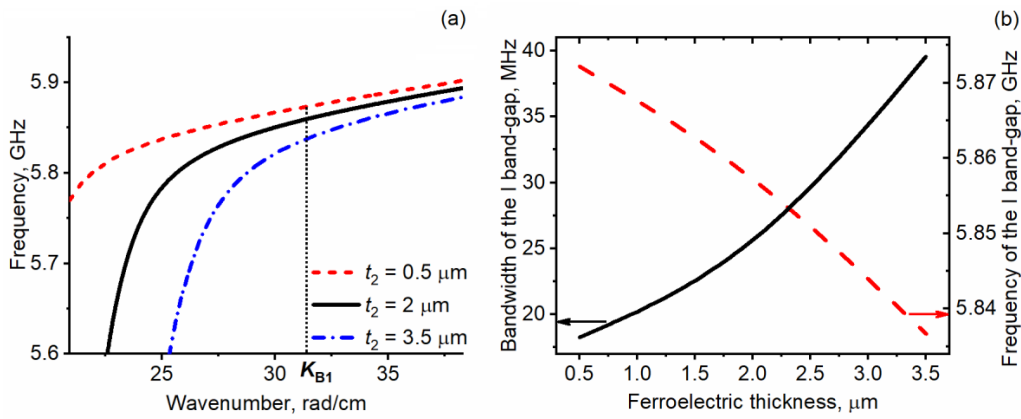


Figure 5.7: (a) Spectra of the hybrid SEW in the regular CW with slot width $w = 75 \mu\text{m}$ calculated for various ferroelectric thicknesses t_2 ; (b) The influence of the ferroelectric thickness on the bandwidth (black solid line) and frequency (red dashed line) of the first band-gap corresponding to wavenumber $K_{B1} = 31.4$ rad/cm.

A similar effect is achieved when the ferroelectric film thickness t_2 is increased (see Figure 5.7). As one can see, an increase in t_2 provides counter-directed effects. While the first band-gap is shifted to the lower frequencies (see red dashed line in Figure 5.7b), its bandwidth increases due to decreasing the SEW group velocity (black solid line).

The electric and magnetic tunability of the EMC transmission characteristics should now be considered. Figure 5.8a shows a frequency shift of the first four band-gaps

80 5 Microwave structures with a spatial periodic modulation based on ferrite and ferroelectric films

calculated for the various control voltages up to 200 V applied to the electrodes of the CW. As for the EMC composed of MC-ferrite-ferroelectric structures, the electric tuning range for the EMC with a CW decreases for the higher band-gap numbers due to a weak interaction of spin and electromagnetic waves at those frequencies higher than the first band-gap.

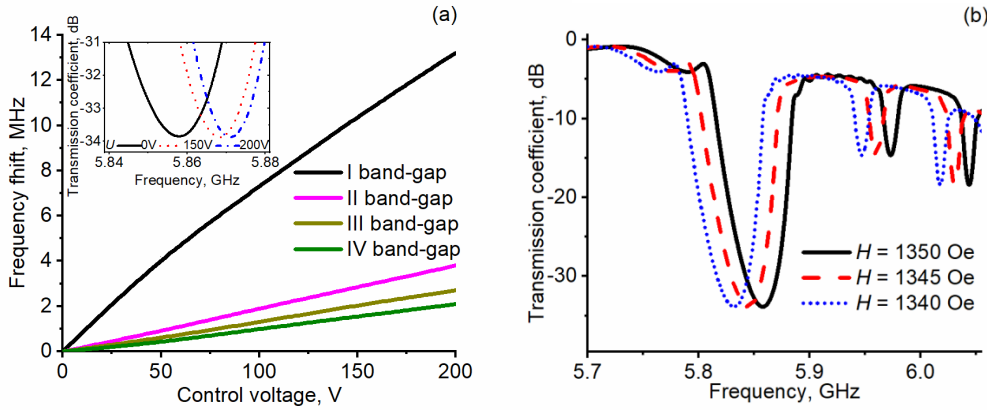


Figure 5.8: (a) Electric and (b) magnetic tuning of the transmission characteristics.

As Figure 5.8a shows, an increase of the control voltage shifts the band-gaps to the higher frequency that may be explained as follows: a decrease of the ferroelectric permittivity shifts a SEW dispersion characteristic to the lower wavenumbers, while the wavenumbers K_B satisfying the Bragg condition remain the same. Therefore, an increase of a control voltage (i.e. a decrease of ϵ_2) shifts the area of a strong coupling between the magnons and microwave photons to the lower wavenumbers, which leads to the formation of a region of enhanced microwave attenuation at higher frequency. For example, the electric tuning of the transmission characteristic for the first band-gap is about 10.45 MHz at $U = 150$ V.

Regarding the magnetic tuning, the transmission characteristics were simulated for the different values of the external magnetic field H (see Figure 5.8b). The following magnetic fields were used: 1350 Oe (solid line), 1345 Oe (dashed line), and 1340 Oe (dotted line). Figure 5.8b shows that an increase in the external magnetic field changes the frequency position of the band-gaps due to a shift of the spin-wave spectrum towards higher frequencies.

5.3 Reflection-less width-modulated magnonic crystal

Previous experimental and theoretical investigations were devoted to electromagnonic crystals undergoing Bragg scattering. In these structures the formation of spectral regions with prohibited wave propagation is caused by a reflection of waves from an artificially created periodicity. This band formation mechanism has been investigated in detail and is well understood for a variety of magnetic and dielectric media with

different physical properties and geometries, including thickness-modulated YIG-based waveguides. At the same time, rejection bands in wave spectra also arise due to peculiarities of the spin-wave excitation mechanisms inside a periodic magnetic film. This phenomenon considerably enriches the properties of conventional periodic structures used in microwave systems. However, mechanisms responsible for the formation of the rejection band, as well as spin-wave dynamics, in such waveguides are not yet clarified.

This Section is devoted to the experimental investigation of a novel magnonic crystal demonstrating the absence of any visible Bragg reflection. This is the first observation of such phenomena in magnetic media. Figure 5.9 shows an image of the experimental setup for width-modulated MC comprising the longitudinally magnetised periodically structured YIG-film waveguide. Attached microstrip antennas are serving for the inductive excitation (input) and detection (output) of SW in the gigahertz frequency range. The magnetisation geometry was chosen in such a way to allow for the excitation of backward volume spin waves having reciprocal propagation characteristics and demonstrating high scattering efficiency in MC.

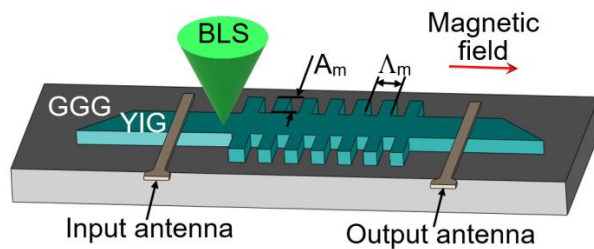


Figure 5.9: Image of the experimental setup for the width-modulated yttrium iron garnet (YIG) structures grown on the gadolinium gallium garnet (GGG). The green cone represents a laser beam scanning the sample by the Brillouin light scattering (BLS) technique.

The YIG samples were fabricated in the form strips cut out from low-damping (ferromagnetic resonance linewidth is about 0.5 Oe at 5 GHz) single-crystal films, epitaxially grown on a gallium gadolinium garnet substrate with a thickness of 0.5 mm. The width, length, and thickness of the samples were 1.9 mm, 26 mm, and 8.5 μm , respectively, and their saturation magnetisation was 1750 G. One should note that the lengths of the waveguides were chosen in order to avoid reflections from the ends which could interfere with the measurements.

In the fabrication of the width-modulated MC, conventional photolithographic and chemical etching techniques were used for the patterning. The length of the rectangular-modulated area in the middle of the strip was 6 mm, and the spatial modulation period Λ_m and depth A_m were 600 and 400 μm , respectively. A photograph of the actual waveguiding structure is shown in Figure 5.10.

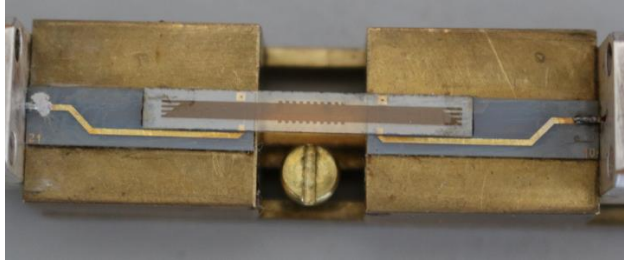


Figure 5.10: Photograph of the experimental structure.

Microwave stripline antennas with a width of $50\ \mu\text{m}$ were placed at distances of about 3 and 4 mm from the left and right ends of the modulated film area, respectively. The antennas were then connected to the VNA for continuous wave measurements. A circuit consisting of a pulsed microwave single frequency generator, a semiconductor detector, and an oscilloscope was utilised for pulse-regime measurements.

The space- and time-resolved Brillouin Light Scattering (BLS) spectroscopy was used for two-dimensional mapping of the magnon density distribution. The BLS measurements were performed in a backward scattering geometry by placing a dielectric mirror below the samples. A pulsed microwave regime was used to reveal the SW dynamics within the crystal structures and to be able to distinguish between individual responses of different parts of these structures. To accomplish this, 30 ns long microwave pulses with a power of -10 dBm were applied to the input antennas. Due to the short pulse durations, the power of the SW excitation was raised, and thus to increase the signal-to-noise ratio of the optical measurements, without any visible influence from nonlinear SW processes. To avoid any spurious influence through heating effects in the ferrite film, the repetition rate was $1.5\ \mu\text{s}$.

Figure 5.11 illustrates the transmission characteristics of the investigated sample measured by the VNA. The blue solid curve in this figure represents the transmission characteristic of the structured waveguide, while the red dashed line shows, for a comparison, the characteristic of similar waveguide without any periodicity. One can clearly identify several frequency regions with different SW dynamics in the transmission characteristic of the periodic waveguide. One should note that the bias magnetic field of 1190 Oe for the width-modulated MC was applied. The input microwave power was -30 dBm, which guaranteed a linear regime of a spin-wave propagation.

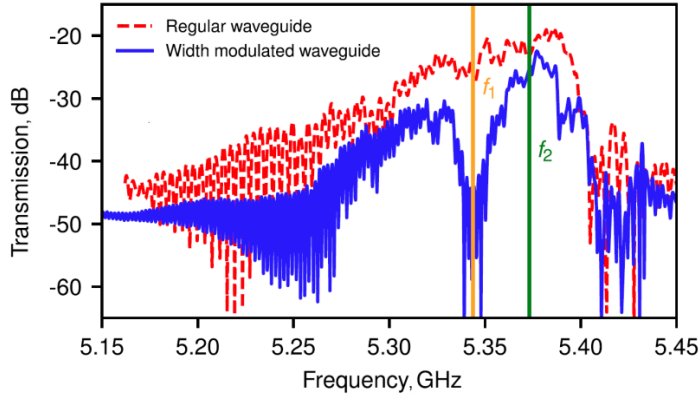


Figure 5.11: Transmission characteristics of the width-modulated MC (blue solid line) and regular (red dashed line) waveguide. The orange and green lines indicate the frequencies, where the Brillouin light scattering measurements were performed: $f_1 = 5.344$ GHz, and $f_2 = 5.373$ GHz.

The width-modulated MC shows the formation of only one pronounced rejection band at the centre frequency $f_1 = 5.344$ GHz, which is marked by the orange line in Figure 5.11. This region of the enhanced microwave attenuation is not predicted by the conventional Bragg analysis; it has a width of 5 MHz measured at a level of 6 dB from the maximum loss of 46.5 dB. One should note that the fast oscillations of the transmission characteristics caused by the interference of the SW signal and an electromagnetic wave which directly passed from the input to the output antenna were neglected in the analysis. In addition, there are regions around the rejection band, where SW modes are transmitted with a relatively low attenuation. For example, the frequency $f_2 = 5.373$ GHz with a loss level of 25 dB is marked by the green line in Figure 5.11. Here, the frequencies marked by vertical lines were chosen for further analysis of the SW dynamics with the different propagation regimes.

The Brillouin light scattering measurements of a magnon density distribution with 25 μm spatial and 400 ps time resolution will now be considered. Here, the intensity of the inelastically scattered light was proportional to the magnon occupation number, or, in other words, to the intensity of the SW in the sample.

The spin-wave intensity distributions were performed for the regular waveguide at the carrier frequency $f_2 = 5.373$ GHz and the width-modulated MC at the carrier frequencies that correspond to the rejection band ($f_1 = 5.344$ GHz) and pass band ($f_2 = 5.373$ GHz). The resulting snapshots are shown in Figure 5.12 for frames in the regular waveguide as well as for the rejection and pass band frames in the width-modulated film. The pictures are plotted in a linear colour scale, and the SW intensity is normalised in each frame, while high SW intensities are indicated as red and low intensities as blue.

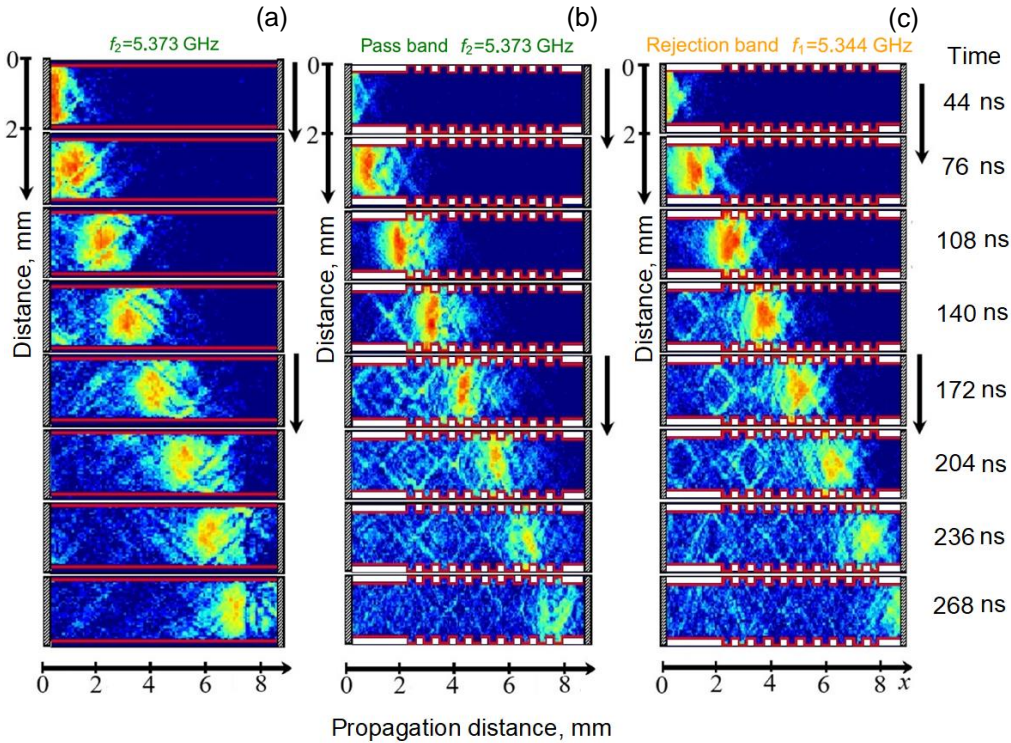


Figure 5.12: Snapshots of the spin-wave propagation for the (a) regular waveguide and width-modulated crystal in the (b) pass and (c) rejection band regime. Two-dimensional plots of the time-resolved spin-wave intensity distributions in the periodic width-modulated waveguides measured at the frequencies $f_1 = 5.344$ GHz (rejection band) and $f_2 = 5.373$ GHz (pass band).

The main feature of the measured SW intensity distributions in the width-modulated waveguide is obvious: in contrast to conventional MC, this crystal exhibits nearly zero reflected SW intensity within both the rejection and pass bands (see Figures 5.12b, c). In the absence of any visible Bragg reflection, the physical mechanisms responsible for the formation of the rejection band in Figure 5.12c might be related to, e.g., some non-resonant or resonant SW decay caused by enhanced magnon–magnon scattering processes in the rejection band frequency range. In order to clarify this issue, the magnon decay was analysed for those cases presented in Figure 5.12. The instantaneous spatial distributions of the measured magnon densities were integrated over a moving window containing the propagating SW packet and over the whole YIG-film region accessible for the BLS probing.

It was found that the lifetimes of both SW packets are about 1.6 times shorter than the lifetimes of the secondary magnons (one should note the spatially structured noise behind the SW packets in Figure 5.12) generated due to the scattering of these packets from the notched waveguide edges. However, the lifetimes of the SW packets

propagating within the rejection and pass bands differ only by 11%, equal to 73 and 82 ns, respectively. However, such a small difference in decay rates cannot explain the observed reduction of the transmitted SW power within the rejection band. The difference in group velocities and in the SW propagation times is also rather small (compare the measured positions of the SW packets in Figure 5.12): the experimentally determined group velocities are $3.88 \times 10^4 \text{ m} \cdot \text{s}^{-1}$ in the pass band and $3.65 \times 10^4 \text{ m} \cdot \text{s}^{-1}$ in the rejection band. Being the same both in the MC and in unstructured parts of the YIG waveguide, these values correspond well with theoretically calculated velocities of the first mode of backward volume SW in the regular 1.9-mm-wide YIG waveguide (3.88×10^4 and $3.65 \times 10^4 \text{ m} \cdot \text{s}^{-1}$, respectively). Together, the differences in the decay rates and group velocities may account for only two-fold reduction of SW power within the rejection band compared to the pass band, while the experimentally observed reduction exceeds 20 dB (see frequencies $f_1 = 5.344$ GHz and $f_2 = 5.373$ GHz in Figure 5.11).

For further analysis of the SW dynamics in the reflection-less width-modulated MC, a periodic magnetic structure, which undergoes Bragg scattering, was experimentally investigated. For the fabrication of this structure, a $5.5 \mu\text{m}$ thick YIG film was used. In order to produce the MC, its thickness was periodically modulated to a depth of $1 \mu\text{m}$ using the wet chemical etching. The periodic pattern consisted of 10 parallel grooves with a width of $50 \mu\text{m}$ spaced by $250 \mu\text{m}$, so that the lattice constant was $300 \mu\text{m}$. The transmission characteristic of the measured grooved waveguide is presented in Figure 5.13a, where the blue solid line represents this transmission characteristic, while the red dashed line shows the characteristic of similar YIG waveguides without any periodicity.

As shown in Figure 5.13a, the level of attenuation of microwave signal sharply increases by roughly 20 dB near the magnonic band-gaps that are formed at the frequencies expected from the conventional Bragg analysis. The width of the central band-gap is 10 MHz measured at a level of 6 dB above the maximum loss of 50 dB.

For further analysis of the SW dynamics in the grooved MC, snapshots of the spatial distribution of the SW intensity measured in the central rejection band (marked by the vertical orange line at $f_3 = 7.02$ GHz) are shown in Figure 5.13b. Here, the colour scale is the same as in Figure 5.12. The selected time frames illustrate how the SW packet enters the grooved area, stops due to the Bragg reflection around the fourth groove (grooves are indicated by the vertical grey lines), and is entirely reflected out of the crystal. The observed behaviour perfectly corresponds with the conventional SW dynamics expected in the frame of the Bragg reflection model.

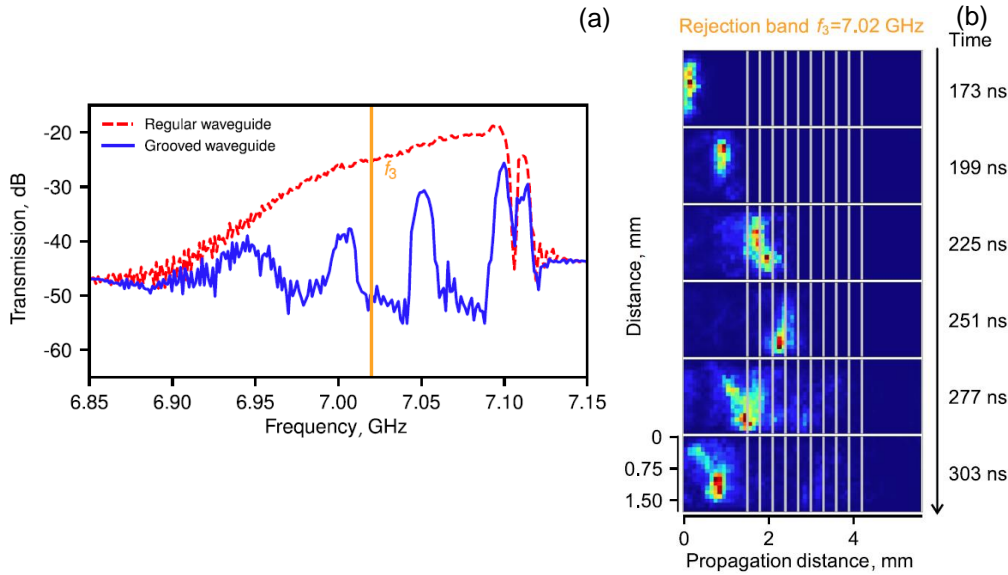


Figure 5.13: Microwave and Brillouin light scattering (BLS) measurements of the thickness-modulated MC:

(a) Transmission characteristics of the MC (blue solid line) and regular (red dashed line) waveguide. The orange line indicates the frequency, where the BLS measurements are performed: $f_3 = 7.02$ GHz.

(b) Snapshots of the spin-wave propagation for the thickness-modulated crystal at the band-gap. Two-dimensional plots of time-resolved spin-wave intensity distributions for carrier frequency f_3 in the MC. The positions of the grooves are indicated by grey solid lines.

Based on the results of the BLS and microwave measurements, it was found that the longitudinally magnetised width-modulated MC does not manifest Bragg reflections, but still demonstrates well-pronounced frequency band-gaps during the microwave measurements. The formation of such reflection-less rejection bands can be explained by the destructive interference of different frequency-degenerated SW modes excited by the MC. At the same time, obtained results significantly differ from the results of the experiments for the micro-sized width-modulated MC, where classical Bragg-gaps are clearly observed. There is a fundamental reason behind this: the reflection-less MC is macroscopic. A relatively large width results in a very dense spectrum of width modes which are separated only by a few megahertz. This fact allows direct two-magnon scattering between these modes. This process makes both backward and forward scattering possible in relation to the direction of original wave propagation. Since the wave-vector difference is also very small, the preferred scattering direction is forward. A number of forward-scattered waves with different phases and group velocities interfere with each other at the output antenna, producing the observed rejection bands without the appearance of Bragg reflections. In the case of the microscopic MC, the frequency gap between neighbouring width modes is very large. Such a spectrum allows only back-scattering, which results in the Bragg-type band gaps.

The proposed mechanism of the reflection-less formation of rejection band leads to one additional unexpected consequence: namely, higher-order SW modes, created by the MC, propagate in unstructured portion of the waveguide with slightly different phase velocities. As a result, mutual phase relations between different SW components will change during propagation of the SW pulse and the rejection frequency, measured by the microwave technique, should depend on the position of the output antenna. This prediction was verified in an additional experiment with movable output antenna while keeping all other parameters of the microwave measurement system the same. A gradual shift of the central band gap frequency (see orange line in Figure 5.11) up to 17 MHz was observed as a function of the distance between antennas (see Figure 5.14). This result strongly supports the proposed mechanism and, also, provides an additional way to control the transmission properties of this type of magnonic crystals.

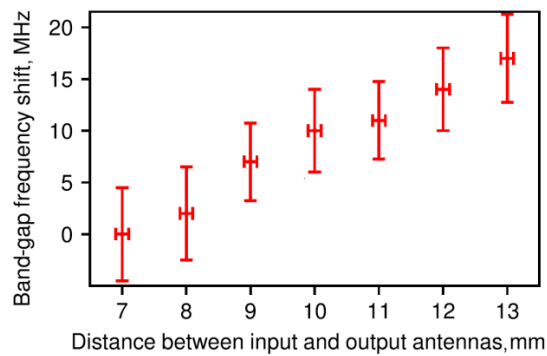


Figure 5.14: Relative shift of the band-gap frequency as a function of the distance between the antennas. The error in the band gap shift is estimated as the full-width half-maximum value of the central frequency in the rejection band, while the error of the antenna distance is 0.1 mm given by the measurement scale.

6 Conclusions

6.1 Summary of results

An investigation of wave dynamics in all-thin-film ferrite-ferroelectric (multiferroic) multilayers and artificial spatially periodic media based on these has been performed. In particular, dispersion characteristics and frequency responses of these structures have been investigated. Two sets of configurations on this topic have been investigated. First, the all-thin-film layered structure with two coupled ferrites exhibiting a strong dipole-dipole interactions of spin waves has been realised. Second, an investigation of coplanar waveguides composed of ferrite and ferroelectric thin films has been performed. Both of the proposed structures offer a host of promising features for various microwave engineering applications.

A comprehensive analysis of full wave spectra of structures consisting of two ferrite films separated by a thin ferroelectric layer has been performed using the derived dispersion relation for spin-electromagnetic waves (SEW). The developed theory provided the possibility to investigate a wide range of problems connected with hybrid SEW in both regular and spatial periodic multiferroic structures. In particular, it has been found out that the electric tuning of SEW dispersion characteristics is provided by two different mechanisms. The first is based on the hybridisation of an electromagnetic wave (EMW) and a spin wave (SW). A change in the permittivity tilts the EMW dispersion characteristic and leads, thus, to the shift of the hybridisation point. The second mechanism manifests itself only for the structures based on two ferrite layers at least. It is because two adjacently placed ferrites, although separated by a thin ferroelectric divider, interact through the electromagnetic field. An efficiency of this mechanism increases with the thinning of the ferroelectric film placed between the ferrite films. As an example, the effective tuning of SEW wavenumbers by an external electric field has been demonstrated even in the case of a 1- μm -thick ferroelectric film. Another way to reduce a control voltage has been realised by utilising planar structures consisting of thin magnetic and ferroelectric films in combination with a coplanar waveguide.

As it is known, efforts for ferroelectric film thickness reduction arise from demands to reduce the control voltage producing ferroelectric polarisation. The obtained results show that the use of all-thin-film multiferroic heterostructures allows not only to reduce the control voltage, but also to increase the phase shift of waves propagating in the structure. Through the application of this phenomenon, the miniature multiferroic interferometer for voltage-controlled spin-wave logic gates has been realised for the first time. This signal processing technique represents a completely new approach to enhanced logic control and is applicable to any spin-wave circuits.

Other promising features of the proposed ferrite-ferroelectric structures have been demonstrated for thin-film electromagnonic crystals (EMC). In contrast to the

conventional magnonic crystals, the artificially created periodic structures extend functionality of magnonic devices because they are characterised by electrically and magnetically tunable band-gaps in the wave spectrum where propagation of the electromagnons are forbidden. In addition, the utilisation of a thin ferroelectric layer has opened a possibility to reduce energy consumption of EMC.

The mechanism of formation of the electromagnonic band structure in the ferrite-ferroelectric periodic waveguides has been analysed. For example, it has been shown that utilisation of the two coupled ferromagnetic films separated by a ferroelectric layer opens up an additional possibility to exploit EMC for microwave applications. Based on the theoretical analysis and experimental measurements, the mechanism of electromagnonic band-gap splitting due to the dipole-dipole interaction between the spin-wave modes has been demonstrated for the first time. This phenomenon is caused by interaction of the three fundamental modes corresponding to each layer composing the electromagnonic crystal.

The last but not least result has been obtained by the experimental investigations of a new type of magnonic crystals that enrich the properties of artificial spatially periodic structures for modern magnonics. It was shown that rejection bands in wave spectra arise due to peculiarities of the spin-wave excitation mechanisms inside a periodic magnetic film. This investigation has interesting ramifications from the point of view of the fundamental physics and the detailed study of this artificial spatially periodic structures constitutes a part of future work.

6.2 Future work

Future work related to this thesis can be considered in three categories.

- The first category is related to an improvement of a functionality of thin-film multilayered structures reported on in this thesis. As mentioned in Chapter 3, a possible limitation of microwave devices based on ferrite-ferroelectric-ferrite structures is a relatively narrow frequency band, where effective electric-field tuning is possible. Although a reduction of a barium-strontium titanate narrows the bandwidth of the presented region, an investigation of the behaviour of this bandwidth for *other ferroelectrics* is necessary. For example, the ferroelectric films with large dielectric permittivity, such as potassium tantalate niobate ($\text{KTa}_x\text{Nb}_{1-x}\text{O}_3$), appears promising for further investigations.
- The second category is future work which is allowed to exploit the electromagnonic crystal for enhanced logic control as well as for tunable microwave devices. In this thesis, different kinds of spatially periodic structures have been suggested, but all of these have been investigated in a *linear* regime of a wave propagation. To accomplish the logical functions in this case, an external control signal (for example, the electric current) must be used. Further progress in the magnonic logic could be achieved by utilising new physical

phenomena controlling the *nonlinear* dynamics of waves propagating in ferrite-ferroelectric structures. An interest in this topic arises not only from possible practical applications, but also from a variety of fundamental scientific problems devoted to *nonlinear* physics of wave phenomena in planar multiferroic multilayers.

- The third category is future work which is a consequence of the experiments devoted to the study of reflection-less magnonic crystals. The investigation related to the mechanisms responsible for the formation of the rejection band *requires* further theoretical as well as experimental investigation. In particular, investigations of spin-wave dynamics in wide films as well as thinner films are necessary. Moreover, additional experiments with layered structures, composed of reflection-less magnonic crystal and ferroelectric film, may be of interest.

References

- Abramowitz, M. Stegun, I. A. (1965) *Handbook of Mathematical Functions: with Formulas, Graphs, and Mathematical Tables*. 0009-revised ed. New York, USA: Dover Publications.
- Adam, J. D., Davis, L. E., Dionne, et al. (2002) Ferrite devices and materials, *IEEE Transactions on Microwave Theory and Techniques*, 50(3), pp. 721-737.
- Anfinogenov, V. B., Verbitskaia, T. N., Guliaev, I. V. et al. (1989) Hybrid electromagnetic-spin waves in contacting layers of ferrite and ferroelectric, *Radiotekhnika i Elektronika*, 34, pp. 494-499.
- Bankowski, E., Meitzler, T., Khymyn, R. S. et al. (2015) Magnonic crystal as a delay line for low-noise auto-oscillators, *Applied Physics Letters*, 107(12), p. 122409.
- Barnas, J. (1988) Spin waves in superlattices. I. General dispersion equations for exchange, magnetostatic and retarded modes, *Journal of Physics C: Solid State Physics*, 21(5), p. 1021.
- Barnas, J. (1991) Transfer Matrix Formalism for Retarded Waves in Layered Magnetic Structures. Bulk and Surface Modes, *Physica status solidi (b)*, 165(2), pp. 529-537.
- Barnas, J. (1994) *Spin waves in multilayers. Linear and nonlinear spin waves in magnetic films and Superlattices*. Singapore: World Scientific Publishing Company, Ltd.
- Beginin, E. N., Grishin, S. V., Morozova, M. A. et al. (2009) Wideband chaotic microwave signal generation in a ring system with a nonlinear delay line on coupled ferromagnetic films, *Technical Physics Letters*, 35(9), p. 853.
- Behin-Aein, B., Datta, D., Salahuddin, S. et al. (2010) Proposal for an all-spin logic device with built-in memory, *Nature nanotechnology*, 5(4), pp. 266-270.
- Bongianni, W. L. (1972). Magnetostatic propagation in a dielectric layered structure. *Journal of Applied Physics*, 43(6), 2541-2548.
- Camley, R. E., and Stamps, R. L. (1993) Magnetic multilayers: spin configurations, excitations and giant magnetoresistance, *Journal of Physics: Condensed Matter*, 5(23), p. 3727.
- Chumak, A. V., Neumann, T., Serga, A. A. et al. (2009a) A current-controlled, dynamic magnonic crystal, *Journal of Physics D: Applied Physics*, 42(20), p. 205005.

- Chumak, A. V., Pirro, P., Serga, A. A. et al. (2009b) Spin-wave propagation in a microstructured magnonic crystal, *Applied Physics Letters*, 95(26), p. 262508.
- Chumak, A. V., Serga, A. A., and Hillebrands, B. (2014) Magnon transistor for all-magnon data processing, *Nature communications*, 5(1), pp. 1-8.
- Chumak, A. V., Serga, A. A., and Hillebrands, B. (2017) Magnonic crystals for data processing, *Journal of Physics D: Applied Physics*, 50(24), p. 244001.
- Chumak, A. V., Vasyuchka, V. I., Serga, A. A. et al. (2015). Magnon spintronics, *Nature Physics*, 11(6), pp. 453-461.
- Collin, R. E. (1990) *Field theory of guided waves*. New York, USA: Wiley-IEEE Press.
- Collin, R. E. (1991) *Field theory of guided waves*. New York, USA: The Institute of Electrical and Electronics Engineers.
- Csaba, G., Papp, Á., and Porod, W. (2017) Perspectives of using spin waves for computing and signal processing, *Physics Letters A*, 381(17), pp. 1471-1476.
- Damon, R. W., and Eshbach, J. R. (1961) Magnetostatic modes of a ferromagnet slab, *Journal of Physics and Chemistry of Solids*, 19(3-4), pp. 308-320.
- Damon, R. W., and Van De Vaart, H. (1965) Propagation of magnetostatic spin waves at microwave frequencies in a normally-magnetized disk, *Journal of Applied Physics*, 36(11), pp. 3453-3459.
- Demidov, V. E., and Kalinikos, B. A. (1999) Electrical tuning of the dispersion characteristics of spin waves in metal-ferroelectric-ferrite-ferroelectric-metal layered structures, *Technical Physics Letters*, 25(11), pp. 880-883.
- Demidov, V. E., Kalinikos, B. A., and Edenhofer, P. (2002a) Dipole-exchange theory of hybrid electromagnetic-spin waves in layered film structures, *Journal of applied physics*, 91(12), pp. 10007-10016.
- Demidov, V. E., Kalinikos, B. A., Karmanenko, S. F. et al. (2002b) Dispersion characteristics of the surface electromagnetic-spin waves in ferrite-ferroelectric-dielectric-metal structures, *Technical Physics Letters*, 28(6), pp. 479-482.
- Demokritov, S. O., Hillebrands, B., and Slavin, A. N. (2001) Brillouin light scattering studies of confined spin waves: linear and nonlinear confinement, *Physics Reports*, 348(6), pp. 441-489.

- Erokhin, S. G., Lisyanskiĭ, A. A., Merzlikin, A. M., et al. (2010) Photonic crystals built on contrast in attenuation in an immersion medium, *Physics of the Solid State*, 52(1), pp. 65-69.
- Fetisov, Y. K., and Srinivasan, G. (2005) Electrically tunable ferrite-ferroelectric microwave delay lines, *Applied Physics Letters*, 87(10), p. 103502.
- Fischer, T., Kewenig, M., Bozhko, D. A. et al. (2017) Experimental prototype of a spin-wave majority gate, *Applied Physics Letters*, 110(15), p. 152401.
- Gann, V. V. (1967). Nonuniform resonance in a ferromagnetic plate, *Soviet Physics Solid State*, 8(11), p. 2537.
- Gradshteyn, I. S., Ryzhik, I. M. (2007) *Table of integrals, series, and products*. 7th ed. USA: Academic Press.
- Grigorieva, N. Y., Kalinikos, B. A., Kostylev, M. P. et al. (2009) Theory and phenomena of artificial materials. In: Capolino, F., ads., *Handbook of Artificial Materials*, p. 974. Oxford, UK: Taylor and Francis Group, LLC.
- Grishin, S. V., Beginin, E. N., Morozova, M. A. et al. (2014) Self-generation of dissipative solitons in magnonic quasicrystal active ring resonator, *Journal of Applied Physics*, 115(5), 053908.
- Grishin, S. V., Sharaevskii, Y. P., Nikitov, S. A. et al. (2011) Self-generation of chaotic dissipative soliton trains in active ring resonator with 1-D magnonic crystal, *IEEE Transactions on Magnetics*, 47(10), pp. 3716-3719.
- Grünberg, P. (1980) Magnetostatic spinwave modes of a ferromagnetic double layer, *Journal of Applied Physics*, 51(8), pp. 4338-4341.
- Grünberg, P. (1981) Magnetostatic spin-wave modes of a heterogeneous ferromagnetic double layer. *Journal of Applied Physics*, 52(11), pp. 6824-6829.
- Gurevich, A. G., and Melkov G. A. (1996) *Magnetic Oscillations and Waves*. 1st ed. New York, USA: CRC Press.
- Hansen, U. H., Demidov, V. E. and Demokritov, S. O. (2009) Dual-function phase shifter for spin-wave logic applications. *Applied Physics Letters*, 94(25), p. 252502.
- Hillebrands, B. (1990) Spin-wave calculations for multilayered structures, *Physical Review B*, 41(1), p. 530.

- Huang, H. (1984) *Coupled mode theory: as applied to microwave and optical transmission*. New York, USA: CRC Press.
- Inoue, M., Baryshev, A., Takagi, H. et al. (2011) Investigating the use of magnonic crystals as extremely sensitive magnetic field sensors at room temperature, *Applied Physics Letters*, 98(13), p. 132511.
- Ishak, W. S. (1988) Magnetostatic wave technology: A review, *Proceedings of the IEEE*, 76(2), pp. 171-187.
- Iskander, M. F., and Lind, T. S. (1989) Electromagnetic coupling of coplanar waveguides and microstrip lines to highly lossy dielectric media, *IEEE Transactions on Microwave Theory and Techniques*, 37(12), pp. 1910-1917.
- Kalinikos, B. A. (1994) Dipole-exchange spin-wave spectrum of magnetic films. In: Cottam, M. G., eds, *Linear and nonlinear spin waves in magnetic films and Superlattices*, pp. 89–156. Singapore: World Scientific Publishing Company, Ltd.
- Kalinikos, B. A., and Kolodin, P. A. (1992) Excitation of propagating dipole-exchange spin waves in ferromagnetic double-film structure, *IEEE transactions on magnetics*, 28(5), pp. 3204-3206.
- Karmanenko, S. F., Nenasheva, E. A., Dedyk, A. I. et al. (2004) Frequency Dependence of Microwave Quality Factor of Doped $\text{Ba}_x\text{Sr}_{1-x}\text{TiO}_3$ Ferroelectric Ceramics, *Integrated Ferroelectrics*, 61(1), pp. 177-181.
- Khitun, A., Bao, M., and Wang, K. L. (2008) Spin wave magnetic nanofabric: A new approach to spin-based logic circuitry, *IEEE Transactions on Magnetism*, 44(9), pp. 2141-2152.
- Kostylev, M. P., Serga, A. A., Schneider, T. et al. (2005) Spin-wave logical gates, *Applied Physics Letters*, 87(15), p. 153501.
- Krawczyk, M., and Grundler, D. (2014) Review and prospects of magnonic crystals and devices with reprogrammable band structure, *Journal of Physics: Condensed Matter*, 26(12), p. 123202.
- Kruglyak, V. V., Demokritov, S. O., and Grundler, D. (2010) Magnonics, *Journal of Physics D: Applied Physics*, 43(26), p. 264001.
- Kuanr, B. K., Anderson, N. R., Celinski, Z. J. and Camley, R. E. (2015) Monolithic microwave nonlinear phase shifter, *IEEE Magnetism Letters*, 6, pp. 1-4.

- Leach, J. H., Liu, H., Avrutin, V. et al. (2010) Electrically and magnetically tunable phase shifters based on a barium strontium titanate-yttrium iron garnet layered structure, *Journal of Applied Physics*, 108(6), p. 064106.
- Lee, K. S., and Kim, S. K. (2008). Conceptual design of spin wave logic gates based on a Mach–Zehnder-type spin wave interferometer for universal logic functions, *Journal of Applied Physics*, 104(5), p. 053909.
- Liu, N., Hou, X. D., and Zhang, X. (2008) Retarded modes in layered magnetic structures containing left-handed materials. *Journal of Physics: Condensed Matter*, 20(33), p. 335210.
- Lu, C., Hu, W., Tian, Y. et al. (2015) Multiferroic oxide thin films and heterostructures, *Applied physics reviews*, 2(2), p. 021304.
- Mironenko, I. G., and Ivanov, A. A. (2001) Dispersion characteristics of slot and microstrip lines based on ferroelectric film-dielectric substrate structures, *Technical Physics Letters*, 27(7), pp. 536-537.
- Morozova, M. A., Matveev, O. V., Sharaevskii, Y. P. et al. (2016) Tuning the bandgaps in a magnonic crystal–ferroelectric–magnonic crystal layered structure, *Physics of the Solid State*, 58(2), pp. 273-279.
- Morozova, M. A., Sharaevskii, Y. P., and Nikitov, S. A. (2014) Tunable band gaps in a layered structure magnonic crystal-ferroelectric, *Journal of Communications Technology and Electronics*, 59(5), pp. 467-473.
- Nath, J., Ghosh, D., Maria, J. P. et al. (2005) An electronically tunable microstrip bandpass filter using thin-film Barium-Strontium-Titanate (BST) varactors, *IEEE Transactions on Microwave Theory and Techniques*, 53(9), pp. 2707-2712.
- Nikitin, A. A., Ustinov, A. B., Semenov, A. A. et al. (2014) All-thin-film multilayered multiferroic structures with a slot-line for spin-electromagnetic wave devices, *Applied Physics Letters*, 104(9), p. 093513.
- Nikitin, A. A., Ustinov, A. B., Semenov, A. A. et al. (2015a) A spin-wave logic gate based on a width-modulated dynamic magnonic crystal, *Applied Physics Letters*, 106(10), p. 102405.
- Nikitin, A. A., Ustinov, A. B., Vitko, V. V. et al. (2015b) Dispersion characteristics of spin-electromagnetic waves in planar multiferroic structures, *Journal of applied physics*, 118(18), p. 183901.

- Nikitov, S. A., Kalyabin, D. V., Lisenkov, I. V. et al. (2015) Magnonics: a new research area in spintronics and spin wave electronics, *Physics-Uspekhi*, 58(10), p. 1002.
- Ordóñez-Romero, C. L., Lazcano-Ortiz, Z., Drozdovskii, A. V. et al. (2016) Mapping of spin wave propagation in a one-dimensional magnonic crystal, *Journal of Applied Physics*, 120(4), p. 043901.
- Özgür, Ü., Alivov, Y., and Morkoç, H. (2009) Microwave ferrites, part 1: fundamental properties, *Journal of Materials Science: Materials in Electronics*, 20(9), pp. 789-834.
- Semenov, A. A., Beljavski, P. Y., Nikitin, A. A. et al. (2008) Dual tunable thin-film ferrite-ferroelectric slotline resonator, *Electronics letters*, 44(24), pp. 1406-1407.
- Serga, A. A., Chumak, A. V., and Hillebrands, B. (2010) YIG magnonics, *Journal of Physics D: Applied Physics*, 43(26), p. 264002.
- Seshadri, S. R. (1970) Surface magnetostatic modes of a ferrite slab, *Proceedings of the IEEE*, 58(3), pp. 506-507.
- Setter, N., Damjanovic, D., Eng, L. et al. (2006) Ferroelectric thin films: Review of materials, properties, and applications, *Journal of Applied Physics*, 100(5), p. 051606.
- Shastry, S., Srinivasan, G., Bichurin, M. I. et al. (2004) Microwave magnetoelectric effects in single crystal bilayers of yttrium iron garnet and lead magnesium niobate-lead titanate, *Physical Review B*, 70(6), p. 064416.
- Sheshukova, S. E., Beginin, E. N., Sadovnikov, A. V. et al. (2014) Multimode propagation of magnetostatic waves in a width-modulated yttrium-iron-garnet waveguide, *IEEE Magnetism Letters*, 5, pp. 1-4.
- Song, Y. Y., Ordóñez-Romero, C. L., and Wu, M. (2009) Millimeter wave notch filters based on ferromagnetic resonance in hexagonal barium ferrites, *Applied Physics Letters*, 95(14), p. 142506.
- Sorensen, N., Camley, R. E. and Celinski, Z. (2019) Exchange stiffness as a function of composition in $Cu_x(Ni_{0.80}Fe_{0.20})_{1-x}$ alloys, *Journal of Magnetism and Magnetic Materials*, 477, pp. 344-349.
- Srinivasan, S., Sarkar, A., Behin-Aein, B. et al. (2011) All-spin logic device with inbuilt nonreciprocity, *IEEE Transactions on Magnetism*, 47(10), pp. 4026-4032.

- Sun, N. X., and Srinivasan, G. (2012) Voltage control of magnetism in multiferroic heterostructures and devices, *Spin*, 2(03), p. 1240004.
- Sykes, C. G., Adam, J. D., and Collins, J. H. (1976) Magnetostatic wave propagation in a periodic structure, *Applied Physics Letters*, 29(6), pp. 388-391.
- Tagantsev, A. K., Sherman, V. O., Astafiev, K. F. et al. (2003) Ferroelectric materials for microwave tunable applications, *Journal of Electroceramics*, 11(1-2), pp. 5-66.
- Ustinov, A. B., and Kalinikos, B. A. (2008) A microwave nonlinear phase shifter, *Applied Physics Letters*, 93(10), p. 102504.
- Ustinov, A. B., and Kalinikos, B. A. (2014) Multiferroic periodic structures based on magnonic crystals for electronically tunable microwave devices, *Technical Physics Letters*, 40(7), pp. 568-570.
- Ustinov, A. B., Drozdovskii, A. V., and Kalinikos, B. A. (2010) Multifunctional nonlinear magnonic devices for microwave signal processing, *Applied physics letters*, 96(14), p. 142513.
- Ustinov, A. B., Drozdovskii, A. V., Nikitin, A. A. et al. (2019) Dynamic electromagnonic crystal based on artificial multiferroic heterostructure, *Communications Physics*, 2(1), pp. 1-7.
- Ustinov, A. B., Srinivasan, G., and Kalinikos, B. A. (2007) Ferrite-ferroelectric hybrid wave phase shifters, *Applied Physics Letters*, 90(3), p. 031913.
- Ustinov, A. B., Tiberkevich, V. S., Srinivasan, G. et al. (2006) Electric field tunable ferrite-ferroelectric hybrid wave microwave resonators: Experiment and theory, *Journal of applied physics*, 100(9), p. 093905.
- Ustinova, I. A., Nikitin, A. A., and Ustinov, A. B. (2016) Dynamic magnonic crystal based on a layered ferrite-ferroelectric structure, *Technical Physics*, 61(3), pp. 473-476.
- Vendik, O. G., Hollmann, E. K., Kozyrev, A. B. et al. (1999) Ferroelectric tuning of planar and bulk microwave devices, *Journal of Superconductivity*, 12(2), pp. 325-338.
- Vopson, M. M. (2015) Fundamentals of multiferroic materials and their possible applications, *Critical Reviews in Solid State and Materials Sciences*, 40(4), pp. 223-250.

Wang, Q., Pirro, P., Verba, R. et al. (2018) Reconfigurable nanoscale spin-wave directional coupler, *Science Advances*, 4(1), p. e1701517.

Zhang, J. S., Zhang, R. L., Hu, Q., et al. (2011) Tunable microwave multiband filters based on a waveguide with antiferromagnetic and dielectric sandwiches, *Journal of Applied Physics*, 109(7), p. 07A305.

Zhu, M., Nan, T., Peng, B. et al. (2017) Advances in magnetic epitaxial multiferroic heterostructures and applications, *IEEE Transactions on Magnetics*, 53(10), pp. 1-16.

Ziolkowski, R. W., and Heyman, E. (2001) Wave propagation in media having negative permittivity and permeability, *Physical review E*, 64(5), p. 056625.

Appendix: Transfer matrix

The matrix \mathbf{MB} expresses unknown coefficients $A_{3n}, B_{3n}, C_{3n}, D_{3n}$ by the coefficients A_{1n}, C_{1n} . The matrix has the following form: $\mathbf{MB} = ((\mathbf{M}_3)^{-1} \cdot \mathbf{N}_2) ((\mathbf{M}_2)^{-1} \cdot \mathbf{N}_1)$, where

$$\mathbf{M}_3 = \begin{bmatrix} 0 & \frac{k}{\omega \varepsilon_0 \varepsilon_3} & -a_n & 0 \\ 0 & -\frac{a_n}{\omega \varepsilon_0 \varepsilon_3} & -k & 0 \\ -a_n & 0 & 0 & \frac{k}{\omega \mu_0} \\ k & 0 & 0 & \frac{a_n}{\omega \mu_0} \end{bmatrix}; \mathbf{N}_2 = \begin{bmatrix} \frac{kW_{2n}}{\omega \varepsilon_0 \varepsilon_2} & -\frac{k}{\omega \varepsilon_0 \varepsilon_2} & a_n & a_n V_{2n} \\ -\frac{a_n W_{2n}}{\omega \varepsilon_0 \varepsilon_2} & \frac{a_n}{\omega \varepsilon_0 \varepsilon_2} & k & kV_{2n} \\ a_n & -a_n V_{2n} & -\frac{kW_{2n}}{\omega \mu_0} & -\frac{k}{\omega \mu_0} \\ -k & kV_{2n} & -\frac{a_n W_{2n}}{\omega \mu_0} & -\frac{a_n}{\omega \mu_0} \end{bmatrix},$$

$$\mathbf{N}_1 = \begin{bmatrix} -\frac{kW_{1n}}{\omega \varepsilon_0 \varepsilon_1} & -a_n V_{1n} \\ \frac{a_n W_{0n}}{\omega \varepsilon_0 \varepsilon_1} & -kV_{1n} \\ a_n & -\frac{k}{\omega \mu_0} \\ -k & -\frac{a_n}{\omega \mu_0} \end{bmatrix}, W_{jn} = \tan(\kappa_{jn} d_j) \kappa_{jn}, V_{jn} = \frac{\tan(\kappa_{jn} d_j)}{\kappa_{jn}}.$$

The matrix \mathbf{M}_2 is obtained from \mathbf{M}_3 by the following replacement: ε_3 by ε_2 .

The matrix \mathbf{MT} expresses unknown coefficients $A_{4n}, B_{4n}, C_{4n}, D_{4n}$ by the coefficients A_{6n}, C_{6n} . The matrix has the following form: $\mathbf{MT} = ((\mathbf{M}_4)^{-1} \cdot \mathbf{N}_5) ((\mathbf{M}_5)^{-1} \cdot \mathbf{N}_6)$, where

$$\mathbf{M}_4 = \begin{bmatrix} M_{11} & M_{12} & M_{13} & M_{14} \\ M_{21} & M_{22} & M_{23} & M_{24} \\ M_{31} & M_{32} & M_{33} & M_{34} \\ M_{41} & M_{42} & M_{43} & M_{44} \end{bmatrix}, \mathbf{N}_5 = \begin{bmatrix} N_{11} & N_{12} & N_{13} & N_{14} \\ N_{21} & N_{22} & N_{23} & N_{24} \\ N_{31} & N_{32} & N_{33} & N_{34} \\ N_{41} & N_{42} & N_{43} & N_{44} \end{bmatrix}, M_{11} = \frac{\delta k \kappa_f^2}{2 \omega \varepsilon_0 \varepsilon_f},$$

$$M_{12} = -\frac{k}{\omega \varepsilon_0 \varepsilon_4}, M_{13} = a_n, M_{23} = k - \frac{\delta \alpha (a_n^2 + k^2)}{2 \mu}, M_{14} = \frac{\delta a_n}{2}, M_{21} = -\frac{\delta a_n \kappa_f^2}{2 \omega \varepsilon_0 \varepsilon_f},$$

$$\begin{aligned}
M_{22} &= \frac{a_n}{\omega \varepsilon_0 \varepsilon_4}, & M_{23} &= k - \frac{\delta \alpha (a_n^2 + k^2)}{2\mu}, & M_{24} &= \frac{\delta k \mu_{\perp}}{2}, & M_{31} &= a_n \left(1 + \frac{\delta k \alpha}{2\mu} \right), \\
M_{31} &= a_n \left(1 + \frac{\delta k \alpha}{2\mu} \right), & M_{32} &= \frac{\delta \varepsilon_f a_n}{2\varepsilon_4}, & M_{33} &= \frac{\delta k \kappa_{fm}^2}{2\omega \mu_0 \mu}, & M_{34} &= \frac{-k(2\mu + \delta k \alpha)}{2\omega \mu_0 \mu}, \\
M_{41} &= \frac{\delta \alpha a_n^2}{2\mu} - k, & M_{42} &= -\frac{\delta \varepsilon_f k}{2\varepsilon_4}, & M_{43} &= \frac{\delta a_n \kappa_{fm}^2}{2\omega \mu_0 \mu}, & M_{44} &= \frac{-a_n(2\mu + \delta k \alpha)}{2\omega \mu_0 \mu}, \\
\kappa_{f_0} &= \sqrt{\omega^2 \varepsilon_0 \varepsilon_f \mu_0 - k^2 - a_n^2}, & \kappa_f &= \sqrt{\omega^2 \varepsilon_0 \varepsilon_f \mu_0 \mu_{\perp} - k^2 - a_n^2}, & \kappa_{fm} &= \sqrt{\omega^2 \varepsilon_0 \varepsilon_f \mu_0 \mu - k^2 - a_n^2}.
\end{aligned}$$

$$\begin{aligned}
N_{11} &= \frac{k(2\varepsilon_f W_{5n} + \delta \varepsilon_5 \kappa_{f_0}^2)}{2\omega \varepsilon_0 \varepsilon_5 \varepsilon_f}, & N_{12} &= \frac{k(2\varepsilon_f - \delta \varepsilon_5 V_{5n} \kappa_{f_0}^2)}{2\omega \varepsilon_0 \varepsilon_5 \varepsilon_f}, & N_{13} &= \frac{a_n(\delta W_{5n} - 2)}{2}, \\
N_{14} &= \frac{a_n(2V_{5n} + \delta)}{2}, & N_{21} &= -\frac{a_n(2\varepsilon_f W_{5n} + \delta \varepsilon_5 \kappa_f^2)}{2\omega \varepsilon_0 \varepsilon_5 \varepsilon_f}, & N_{22} &= -\frac{a_n(2\varepsilon_f - \delta \varepsilon_5 V_{5n} \kappa_f^2)}{2\omega \varepsilon_0 \varepsilon_5 \varepsilon_f}, \\
N_{23} &= \frac{\delta k W_{5n} \mu_{\perp} - 2k}{2} - \frac{\delta \alpha (a_n^2 + k^2)}{2\mu}, & N_{24} &= \frac{\delta \mu_{\perp} k + 2k V_{5n}}{2} + \frac{\delta \alpha V_{5n} (a_n^2 + k^2)}{2\mu}, \\
N_{31} &= \frac{a_n(\delta \varepsilon_f \mu W_{5n} - (2\mu - \delta k \alpha) \varepsilon_5)}{2\mu \varepsilon_5}, & N_{32} &= \frac{a_n((2\mu - \delta k \alpha) \varepsilon_5 V_{5n} + \delta \varepsilon_f \mu)}{2\mu \varepsilon_5}, \\
N_{33} &= \frac{k(\delta \kappa_{fm}^2 + (2\mu - \delta k \alpha) W_{5n})}{2\omega \mu_0 \mu}, & N_{34} &= \frac{k(2\mu - \delta k \alpha - V_{5n} \delta \kappa_{fm}^2)}{2\omega \mu_0 \mu}, \\
N_{41} &= \frac{(2\mu k + \delta a_n^2 \alpha) \varepsilon_5 - \delta \varepsilon_f \mu k W_{5n}}{2\mu \varepsilon_5}, & N_{42} &= -\frac{(2\mu k + \delta a_n^2 \alpha) \varepsilon_5 V_{5n} - \delta \varepsilon_f \mu k}{2\mu \varepsilon_5}, \\
N_{43} &= \frac{a_n(\delta \kappa_{fm}^2 + (2\mu - \delta k \alpha) W_{5n})}{2\omega \mu_0 \mu}, & N_{44} &= \frac{a_n(2\mu - \delta k \alpha - V_{5n} \delta \kappa_{fm}^2)}{2\omega \mu_0 \mu}.
\end{aligned}$$

The matrix M_5 is obtained from M_3 by the following replacement: ε_3 by ε_5 . The matrix N_6 is obtained from N_1 by the following replacement: ε_1 by ε_6 , V_{1n} by $-V_{6n}$, and W_{1n} by $-W_{6n}$.

Publication I

Nikitin, A. A., Vitko, V. V., Nikitin, A. A., Kondrashov, A. V., Ustinov, A. B.,
Semenov, A. A., and Lähderanta, E.

**Dual tuning of doubly hybridized spin-electromagnetic waves in all-thin-film
multiferroic multilayers**

Reprinted with permission from
IEEE Transactions on Magnetics
Vol. 53(11), pp. 1-5, 2017
© 2017, IEEE

Dual Tuning of Doubly Hybridized Spin-Electromagnetic Waves in All-Thin-Film Multiferroic Multilayers

Aleksei A. Nikitin¹, Vitaliy V. Vitko¹, Andrey A. Nikitin^{1,2}, Alexandr V. Kondrashov^{1,2}, Alexey B. Ustinov^{1,2}, Alexander A. Semenov¹, and Erkki Lähderanta²

¹Department of Physical Electronics and Technology, St. Petersburg Electrotechnical University, 197376 St. Petersburg, Russia

²Department of Mathematics and Physics, Lappeenranta University of Technology, 53850 Lappeenranta, Finland

Theoretical investigation of dual (electric and magnetic) tuning of dispersion characteristics has been studied for the doubly hybridized spin-electromagnetic waves (SEWs) propagating perpendicularly to the direction of static magnetization in tangentially magnetized all-thin-film multiferroic multilayers. The multilayers consisted of two thin ferrite films separated by a thin ferroelectric film. The SEW spectrum was formed as the result of the double hybridization among one electromagnetic mode and two spin-wave modes. Such hybridization took place if the initial dispersion characteristics of these modes were degenerated. The electric tuning was realized owing to the changing of the magneto-dipole interaction between the magnetic films caused by a variation of dielectric constant of the ferroelectric film. It was shown that a decrease in permittivity of the ferroelectric film of micrometer thickness by a factor of two induces change of the SEW wavenumber up to tens of radian per centimeter.

Index Terms—Ferrites, ferroelectrics, multiferroics, spin-electromagnetic waves (SEWs).

I. INTRODUCTION

INCREASED demands to frequency-agile materials used for microwave applications have led to the appearance of artificial multiferroics [1]. Artificial multiferroics are usually fabricated with a combination of ferrite and ferroelectric layers to obtain micro- and nanostructures [2], [3]. An interaction between the ferromagnetic and ferroelectric phases is realized through electrodynamic coupling of spin and electromagnetic waves. This interaction leads to a formation of spin-electromagnetic waves (SEWs) [4]. Dispersion characteristics of hybrid SEWs combine features of electromagnetic waves in ferroelectric-based materials and spin waves in ferrites. Therefore, the resulting wave spectrum is dually controllable by both electric and magnetic fields. The electric tuning is realized through the variation of dielectric permittivity of the ferroelectric layer by changing the applied electric field. The magnetic tuning is provided by a dependence of magnetic permeability of ferrites on the bias magnetic field.

As was shown earlier, degrees of hybridization strongly depend on an overlapping of the dynamics fields of the electromagnetic and spin waves. The overlapping depends on the geometry of the layered structures and parameters of the materials [4].

Until now the high research activity was mainly given to two-layered multiferroic structures consisting of one ferrite and one ferroelectric layer [4]–[17]. An effective coupling at microwave frequencies was achieved in multiferroic structures fabricated with a relatively thick (200–500 μm) ferroelectric layer [18]. Such thicknesses of the ferroelectric layer leads to relatively high control voltages (up to 1000 V) needed for an effective electric tuning of the SEW dispersion characteristics.

Recently, all-thin-film multiferroic structures based on the slot transmission line were suggested to decrease the thickness of the ferroelectrics [19] and [20]. In the latter work, a decrease in the control voltage and an increase in the tuning efficiency were achieved with the reduction of the slot-line gap width. However, in practice such a reduction is limited by the increase of losses in metal electrodes. In our opinion, further advances in the dual-tunable multiferroic devices could be achieved with development of the ferrite-ferroelectric-ferrite structures [21], [22]. One of the main advantages of these structures is the existence of magneto-dipole interaction between the ferrite films that are separated with a thin ferroelectric film. It leads to a complication of the SEW spectrum, which is formed as the result of the interaction between two pure spin-wave modes and one electromagnetic mode. Two possible situations are shown in Fig. 1. The first hybridization takes place in the point I between two spin-wave modes shown by dashed lines. The second hybridization with electromagnetic mode could take place in the same point or in the other points (e.g., points II and III) depending on the parameters of the structure. The first situation, in which all dispersion curves cross each other in one point, is called a “double hybridization.”

The purpose of this work is to theoretically investigate the SEW spectra formed resulting from double hybridization. Such a hybridization provides an effective tuning of the SEW dispersion in planar all-thin-film multiferroic structures. This tuning mechanism can be considered as a tunable interaction of the coupled spin waves propagating in two neighboring ferrite films that are separated by a thin ferroelectric film.

II. INVESTIGATION OF SEW SPECTRUM OF THIN-FILM FERRITE-FERROELECTRIC-FERRITE STRUCTURES

A thin-film multilayered structure consisting of two ferrite films separated by a ferroelectric film is shown in Fig. 2. This topology corresponds to two thin magnetic films grown on

Manuscript received March 10, 2017; accepted June 4, 2017. Date of publication June 12, 2017; date of current version October 24, 2017. Corresponding author: A. A. Nikitin (e-mail: and.a.nikitin@gmail.com).

Color versions of one or more of the figures in this paper are available online at <http://ieeexplore.ieee.org>.

Digital Object Identifier 10.1109/TMAG.2017.2714841

0018-9464 © 2017 IEEE. Personal use is permitted, but republication/redistribution requires IEEE permission. See http://www.ieee.org/publications_standards/publications/rights/index.html for more information.

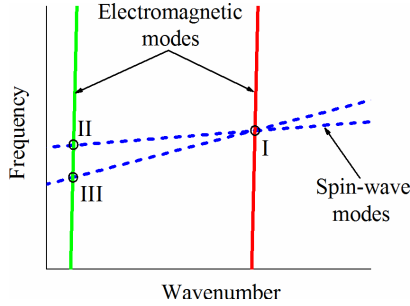


Fig. 1. Qualitative picture showing possible relative positions of two pure spin-wave modes (dotted lines) and the electromagnetic mode (solid line).

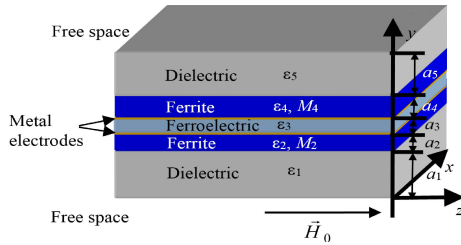


Fig. 2. Thin-film multiferroic structure consisting of two ferrite layers and a ferroelectric layer between them.

relatively thick dielectric substrates. An yttrium iron garnet films grown on the gadolinium gallium garnet substrates by liquid phase epitaxy are notable examples found in practical applications. The ferrite films have the thicknesses of a_2 and a_4 , and saturation magnetizations of M_2 and M_4 . The thicknesses of the ferroelectric film and dielectric layers are a_3 , a_1 , and a_5 , respectively. Dielectric properties of both magnetic and ferroelectric layers are described by scalar dielectric permittivity's ϵ_i , where i is a number of the layer. Note that we consider barium-strontium titanate (BST) ferroelectric, which demonstrates paraelectric phase and isotropic dielectric permittivity in the order of thousands at room temperature [23]. The dielectric permittivity of the BST film ϵ_3 , as a function of the applied electric field E , was estimated with the following relation:

$$\epsilon_3(E) = 1500 - 19.4E^2 (V/\mu m). \quad (1)$$

Thin metal electrodes should be deposited on both surfaces of the BST film to apply the electric field. If the thickness of the electrodes is much smaller than the skin depth at the operating frequencies, then the electrodes are transparent to the microwave electromagnetic fields, and they can be neglected in numerical simulations.

We assume that the layered structure is infinite in the xz plane and waves propagate along x -axis. The ferrite films are magnetized to the saturation by a spatially uniform magnetic field H_0 along z -axis. In the particular case of a single

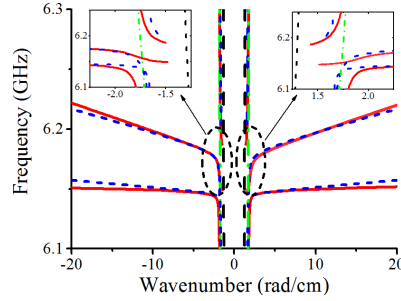


Fig. 3. Spectra of the hybrid SEW (solid curves). Dashed-dotted lines show electromagnetic mode TE_1 . Short dashed curves show hybrid SEWs for ferrite films (i.e., for $\epsilon_3 = 1$). Dashed line represents the dependence $\omega = ck$, where c is the velocity of light in a vacuum.

ferrite film, this geometry corresponds to the well-known Damon–Eshbach configuration providing propagation of surface spin waves.

The dispersion relation that describes spectrum of the SEWs in the investigated structures was obtained by using the transfer matrix method [22]. Fig. 3 shows typical dispersion characteristics for the thin-film multiferroic structure consisting of two ferrite films separated with a ferroelectric film by solid curves. The numerical calculations were carried out for the following parameters: $\epsilon_1 = \epsilon_2 = \epsilon_4 = \epsilon_5 = 14$, $E = 0$, $a_1 = a_5 = 500 \mu m$, $a_2 = 20 \mu m$, $a_3 = 1 \mu m$, $a_4 = 6 \mu m$, $M_2 = 1750 G$ (139260 A/m), and $M_4 = 1713 G$ (136316 A/m). This set of parameters was chosen to provide intersection of spin-wave modes. As is well known, this intersection takes place if ferrite layers have different magnetization and thickness. Note that for the present set of the parameters, the interaction of the spin waves should occur for $k = 1.75 \text{ rad/cm}$. To realize double hybridization, the magnetization of the top ferrite layer was chosen to be $M_4 = 1713 G$ that is less than the value of the magnetization for the bottom ferrite film. Magnetization of the top ferrite should be increased for the case of spin wave interaction at larger wavenumbers.

The results of the numerical simulations shown in Fig. 3 demonstrate the SEW spectrum (solid curves) consisting of three dispersion branches. We will call them lower, middle, and upper branches. Such a spectrum is formed as a result of electrodynamic interactions of the electromagnetic mode TE_1 with two spin-wave modes. The SEW dispersion branches tend to the branches of pure spin wave or electromagnetic modes far from points of the hybridization. As shown in Fig. 3, a magneto-dipole interaction between the ferrite layers also plays a role in the formation of the SEW spectrum for the particular set of the heterostructure parameters due to narrow ferroelectric film.

The interaction between spin-wave modes and electromagnetic mode in multilayered multiferroic structures increases if dispersion branches of pure spin-wave modes and electromagnetic mode TE_1 cross each other in one point (see point I

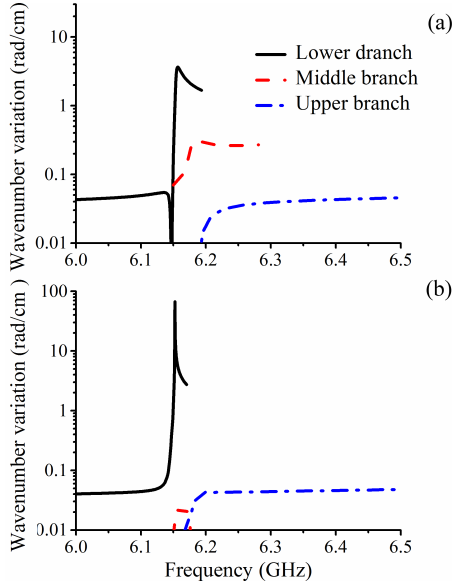


Fig. 4. Wavenumber variation of the lower, middle, and upper SEW dispersion branches versus frequency calculated for the (a) positive and (b) negative wavenumbers.

in Fig. 1). This case corresponds to the doubly hybridized spin-electromagnetic waves.

As shown in Fig. 3, a relatively strong repulsion between all SEW branches takes place for waves propagating in the forward and backward directions along the x -axis (positive and negative wavenumbers). This repulsion is produced by magneto-dipole interaction for $k = 1.7$ rad/cm for both propagation directions.

The SEW wavenumber variation Δk was calculated for the case of reduction in the ferroelectric layer permittivity ϵ_3 by two times. The results are shown in Fig. 4 by solid, dashed, and dashed-dotted lines for the lower, middle, and upper SEW dispersion branches, respectively. The parameters were taken to be the same as for Fig. 3. Fig. 4(a) and (b) corresponds to SEW dispersion branches for positive and negative wavenumbers, respectively.

As shown in Fig. 4(b), effective electric field tuning of the SEW wavenumber up to 66.8 rad/cm is achieved for the lower SEW branch for the negative wavenumbers. This phenomenon can be explained as follows. Transverse distributions of magnetostatic potential for surface spin waves with positive k have maxima on the bottom surfaces of the magnetic films. These distributions demonstrate maxima on the top surfaces for reversed propagation direction (see [24]). Therefore, spatial distance between the maxima is less for negative k for the considered geometry. This leads to stronger overlapping of alternating electric and magnetic fields of spin waves

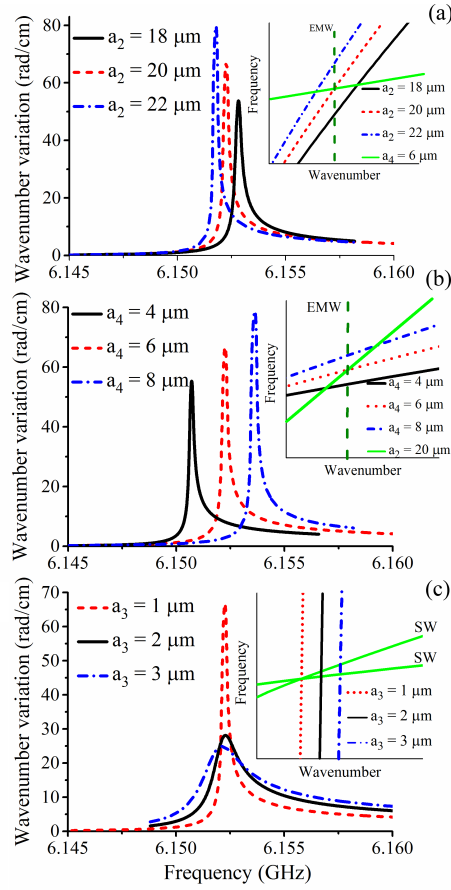


Fig. 5. Wavenumber variation versus frequency calculated for different thicknesses of (a) bottom ferrite film, (b) top ferrite film, and (c) ferroelectric film. Insets qualitatively show dispersion characteristics of pure spin and electromagnetic modes.

propagating in neighboring magnetic films and consequently to stronger coupling of all waves. As a result, the group velocity of the SEW bottom branch is reduced significantly, and this branch demonstrates huge electric field tuning of the wavenumbers in a relatively narrow frequency band.

From a physical point of view, the electric field tuning described above for the doubly hybridized waves is originated from the change of the magneto-dipole interaction between the ferrite films by the variation of the dielectric constant ϵ_3 of the thin ferroelectric film. The reduction in ϵ_3 can be considered as a reduction in effective spatial distance between the magnetic films, leading to an increase in the coupling of spin waves propagating in the magnetic films.

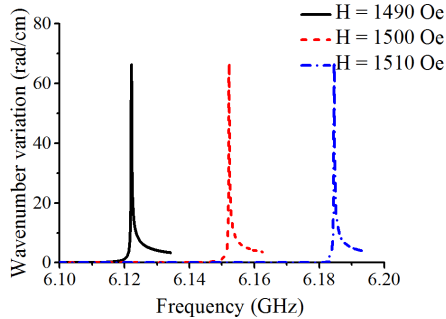


Fig. 6. Wavenumber variation versus frequency calculated for different values of magnetic field H .

III. INVESTIGATION OF ELECTRIC AND MAGNETIC FIELD TUNING OF DOUBLY HYBRIDIZED SPIN-ELECTROMAGNETIC WAVES

This section is devoted to the investigation of the dual tuning of the dispersion characteristics of doubly hybridized SEWs propagating in the thin-film multiferroic multilayers. As is shown in the previous section, the largest electric field tuning, which could be of interest for practical applications, is observed for the negative wavenumbers of the lower SEW dispersion branch. Therefore, we will consider further the tuning of this branch for various physical parameters of the layered structure.

The influence of ferrite and ferroelectric film thicknesses of the investigated structures on the electric field tuning is illustrated by the results shown in Fig. 5. As shown in the inset of Fig. 5(a), an increase in the thicknesses of the thick ferrite layer shifts the point of hybridization between two spin-wave modes to the lower wavenumbers. It leads to downshift in the frequency of the electric tuning maximum shown in Fig. 5(a). The inverse effect is observed with an increase in the thickness of the thin ferrite film [see Fig. 5(b)].

Fig. 5(c) demonstrates the influence of the ferroelectric film thickness a_3 on the electric tuning. In contrast to multiferroic structures studied earlier, the ferrite-ferroelectric-ferrite structure demonstrates the following unique feature. A reduction in the ferroelectric thickness may increase sufficiently the electric field tuning. For example, a decrease in the thickness a_3 from 2 to 1 μm increases the tuning from 28.1 to 66.8 rad/cm. Double hybridization of SEWs plays a crucial role in this effect. Indeed, as is clear from the inset in Fig. 5(c), a decrease in the thickness of the ferroelectric film shifts the dispersion branch of electromagnetic wave toward the point of the double hybridization. It increases the tuning efficiency.

Let us consider now a magnetic field tuning of the performance characteristics of the structure. The influence of the magnetic field H on the SEW wavenumber variation is shown in Fig. 6 for $H = 1490$ Oe by a solid curve, for $H = 1500$ Oe by a dashed curve, and for $H = 1510$ Oe by a dashed-dotted curve. As is seen, the change in the external magnetic field by 10 Oe shifts the region of the large wavenumber variation

on 30 MHz. Magnetic field tuning in a range of 500–2500 Oe offers an opportunity to realize highly effective electric tuning for any desirable frequency in a range from 3 to 9 GHz.

IV. CONCLUSION

Electrical tuning of the doubly hybridized SEW in all-thin-film multiferroic multilayers was analyzed. Formation of these waves by means of double hybridization of two pure spin-wave modes with the electromagnetic mode was demonstrated. A significant advantage of the investigated structures is a possibility to achieve the large electric field tuning of SEW wavenumber up to tens of rad/cm.

Influence of ferrite and ferroelectric film thicknesses on the electric field tuning was investigated. It was shown that a reduction in the ferroelectric thickness improves the tuning efficiency. This opens up new perspectives for practical application of thin-film multiferroics at microwave frequencies. Namely, because of a decrease in the ferroelectric film thickness, microwave devices based on proposed structures would demonstrate large electric tuning of the phase shift with low control voltage and high speed of operation.

A weakness of the proposed thin-film multiferroics is the narrow frequency band, where effective electric field tuning is realized. For example, the wavenumber variation larger than π rad/cm is realized in bandwidth of 15 MHz. However, the band of large wavenumber variation can be easily shifted by changing the external magnetic field. Therefore, the all-thin-film multiferroic multilayers are preferable to the development of tunable microwave devices.

ACKNOWLEDGMENT

The work at SPbETU on numerical modeling was supported by the Russian Science Foundation under Grant 16-12-10440. The work at SPbETU on the development of the computer program for numerical simulation was supported by the Ministry of Education and Science of Russian Federation under Project “Goszadanie.” The work at Lappeenranta University of Technology was supported by the Academy of Finland.

REFERENCES

- [1] M. M. Vopson, “Fundamentals of multiferroic materials and their possible applications,” *Critical Rev. Solid State Mater. Sci.*, vol. 40, no. 4, pp. 1–28, 2015.
- [2] C. Lu, W. Hu, Y. Tian, and T. Wu, “Multiferroic oxide thin films and heterostructures,” *Appl. Phys. Rev.*, vol. 2, p. 021304, May 2015.
- [3] N. X. Sun and G. Srinivasan, “Voltage control of magnetism in multiferroic heterostructures and devices,” *Spin*, vol. 2, no. 3, p. 1240004, 2012.
- [4] V. E. Demidov, B. A. Kalinikos, and P. Edenhofer, “Dipole-exchange theory of hybrid electromagnetic-spin waves in layered film structures,” *J. Appl. Phys.*, vol. 91, pp. 10007–10016, May 2002.
- [5] V. E. Demidov and B. A. Kalinikos, “Green’s tensor of the Maxwell equations for a planar metal-dielectric-ferromagnet-dielectric-metal sandwich structure,” *Tech. Phys. Lett.*, vol. 26, no. 8, pp. 729–733, 2000.
- [6] J.-M. Hu, L.-Q. Chen, and C.-W. Nan, “Multiferroic heterostructures integrating ferroelectric and magnetic materials,” *Adv. Mater.*, vol. 28, pp. 15–39, Jan. 2016.
- [7] A. V. Sadovnikov, K. V. Bublikov, E. N. Beginin, S. E. Sheshukova, Y. P. Sharaevskii, and S. A. Nikitov, “Nonreciprocal propagation of hybrid electromagnetic waves in a layered ferrite-ferroelectric structure with a finite width,” *JETP Lett.*, vol. 102, pp. 142–147, Aug. 2015.

- [8] K. V. Bublikov, A. V. Sadovnikov, E. N. Beginin, Y. P. Sharaevskii, and S. A. Nikitin, "The influence of a metal on transverse characteristics of hybrid waves in a layered ferrite-ferroelectric structure," *Tech. Phys. Lett.*, vol. 42, pp. 486–490, May 2016.
- [9] M. Liu, "Novel laminated multiferroic heterostructures for reconfigurable microwave devices," *Chin. Sci. Bull.*, vol. 59, pp. 5180–5190, Dec. 2014.
- [10] A. V. Sadovnikov, "Voltage-controlled spin-wave coupling in adjacent ferromagnetic-ferroelectric heterostructures," *Phys. Rev. Appl.*, vol. 7, p. 014013, Jun. 2017.
- [11] S. Sharma, M. Tomar, A. Kumar, N. K. Puri, and V. Gupta, "Multiferroic properties of BiFeO₃/BaTiO₃ multilayered thin films," *Phys. B, Condens. Matter*, vol. 448, pp. 125–127, Sep. 2014.
- [12] V. E. Demidov, B. A. Kalinikos, S. F. Karmanenko, A. A. Semenov, and P. Edenhofer, "Electrical tuning of dispersion characteristics of surface electromagnetic-spin waves propagating in ferrite-ferroelectric layered structures," *IEEE Trans. Microw. Theory Techn.*, vol. 51, no. 10, pp. 2090–2096, Oct. 2003.
- [13] L. Y. Fetisov, Y. K. Fetisov, G. Sreenivasulu, and G. Srinivasan, "Nonlinear resonant magnetoelectric interactions and efficient frequency doubling in a ferromagnetic-ferroelectric layered structure," *J. Appl. Phys.*, vol. 113, p. 116101, Mar. 2013.
- [14] M. A. Popov, I. V. Zavislyak, H. L. Chumak, M. B. Strugatsky, S. V. Yagupov, and G. Srinivasan, "Ferromagnetic resonance in a single crystal of iron borate and magnetic field tuning of hybrid oscillations in a composite structure with a dielectric: Experiment and theory," *J. Appl. Phys.*, vol. 118, p. 013903, Jul. 2015.
- [15] M. A. Morozova, Y. P. Sharaevskii, and S. A. Nikitin, "Tunable band gaps in a layered structure magnonic crystal-ferroelectric," *J. Commun. Technol. Electron.*, vol. 59, pp. 467–473, May 2014.
- [16] M. Popov, G. Sreenivasulu, V. M. Petrov, F. A. Chavez, and G. Srinivasan, "High frequency magneto-dielectric effects in self-assembled ferrite-ferroelectric core-shell nanoparticles," *AIP Adv.*, vol. 4, p. 097117, Sep. 2014.
- [17] F. Brandl, K. J. A. Franke, T. H. E. Lahtinen, S. van Dijken, and D. Grundler, "Spin waves in CoFeB on ferroelectric domains combining spin mechanics and magnonics," *Solid State Commun.*, vol. 198, pp. 13–17, Nov. 2014.
- [18] A. B. Ustinov *et al.*, "Electric field tunable ferrite-ferroelectric hybrid wave microwave resonators: Experiment and theory," *J. Appl. Phys.*, vol. 100, no. 9, p. 093905, 2006.
- [19] A. A. Nikitin, A. B. Ustinov, A. A. Semenov, B. A. Kalinikos, and E. Lähderanta, "All-thin-film multilayered multiferroic structures with a slot-line for spin-electromagnetic wave devices," *Appl. Phys. Lett.*, vol. 104, no. 9, p. 093513, 2014.
- [20] A. A. Nikitin *et al.*, "Dispersion characteristics of spin-electromagnetic waves in planar multiferroic structures," *J. Appl. Phys.*, vol. 118, p. 183901, Nov. 2015.
- [21] M. A. Morozova, O. V. Matveev, Y. P. Sharaevskii, and S. A. Nikitin, "Tuning the bandgaps in a magnonic crystal-ferroelectric-magnonic crystal layered structure," *Phys. Solid State*, vol. 58, pp. 273–279, Feb. 2016.
- [22] V. V. Vitko, A. A. Nikitin, A. B. Ustinov, A. A. Semenov, A. A. Nikitin, and E. Lähderanta, "Electric-field tuning of spin-electromagnetic wave dispersion in ferrite-ferroelectric multilayers," in *Proc. 45th Eur. Microw. Conf.*, Sep. 2015, pp. 1073–1076.
- [23] A. B. Ustinov, G. Srinivasan, and B. A. Kalinikos, "Ferrite-ferroelectric hybrid wave phase shifters," *Appl. Phys. Lett.*, vol. 90, no. 3, p. 031913, 2007.
- [24] D. D. Stancil and A. Prabhakar, *Spin Waves: Theory and Applications*. New York, NY, USA: Springer, 2009, p. 330.

Publication II

Nikitin, A. A., Ustinov, A. B., Vitko, V. V., Nikitin, A. A., Kondrahov, A. V., Pirro, P.,
Lähderanta, E., Kalinikos, B. A., and Hillebrands, B.

Spin-electromagnetic waves in planar multiferroic multilayers

Reprinted with permission from

Journal of Applied Physics

Vol. 122(1), p. 014102, 2017

© 2017, American Institute of Physics



Spin-electromagnetic waves in planar multiferroic multilayers

Andrey A. Nikitin,^{1,2} Alexey B. Ustinov,^{1,2} Vitalii V. Vitko,¹ Alexey A. Nikitin,^{1,3} Alexandr V. Kondrahov,^{1,2} P. Pirro,³ E. Lähderanta,² Boris A. Kalinikos,¹ and B. Hillebrands³

¹Department of Physical Electronics and Technology, St. Petersburg Electrotechnical University, St. Petersburg 197376, Russia

²Department of Mathematics and Physics, Lappeenranta University of Technology, Lappeenranta 53850, Finland

³Fachbereich Physik and Landesforschungszentrum OPTIMAS, Technische Universität Kaiserslautern, Kaiserslautern 67663, Germany

(Received 17 April 2017; accepted 17 June 2017; published online 7 July 2017)

A general electrodynamic theory is developed for dispersion characteristics of spin-electromagnetic waves (SEWs) propagating in multiferroic multilayers. The derivation is based on the full set of Maxwell's equations taking into account retardation effects. The multilayers are considered to be composed of an infinite number of ferrite and ferroelectric layers having arbitrary thicknesses, as well as arbitrary magnetic and electric parameters. As an example, spectra of SEWs are calculated and analyzed for a heterostructure containing two thin ferrite films separated by a thin ferroelectric film. An electric field tunability of the SEW dispersion characteristics at gigahertz frequencies is shown, providing an efficient control of SEW wave-numbers important for applications. Published by AIP Publishing. [<http://dx.doi.org/10.1063/1.4990991>]

I. INTRODUCTION

For many years, ferrite films have attracted increased research interest due to their possible application in microwave electronics. Distinguished features of the ferrite-film devices are low insertion losses and magnetic field tunability. Performance characteristics of such devices are determined by the dispersion of spin waves (SWs). In 1961, Damon and Eshbach developed a theory for the spin wave spectrum of a tangentially magnetized magnetic film.¹ Then, a theory of spin wave modes, in a perpendicularly magnetized ferrite film, was developed by Damon and Van de Vaart.² In both cases, dispersion equations for SWs were derived taking into account only the dipole interaction. Later, a theory of SW spectrum taking into account both dipole and exchange interactions was developed (see Refs. 3 and 4 and literature therein).

A strong interest for fabrication and investigation of ferromagnetic multilayers emerged in the 1980s of the last century owing to the development of thin-film deposition techniques. In 1980, Grünberg extended the theory of Damon and Eshbach to ferromagnetic double layer systems.^{5,6} From that time, many theoretical and experimental works investigating magnetic multilayers were carried out (see e.g., Refs. 7–12). It is worth mentioning that theories for spin wave spectra were developed mostly with a magnetostatic approximation neglecting the electromagnetic retardation. Exceptions are papers of Barnas^{13–16} and some other works.^{17,18} In these works, ferrite-dielectric superlattices were studied for identical parameters of the magnetic layers. Dielectric layers between them were assumed to be air or dielectric films with a relatively small dielectric permittivity of about 10.

Increased demands for frequency-agile materials for microwave devices have led to the appearance of artificial multiferroics.¹⁹ Multiferroics are usually fabricated by a combination of ferrite and ferroelectric (or piezoelectric)

materials so as to obtain micro- and nanostructures in the form of multilayers, pillars, spheres, wires, and others.^{20,21} A distinctive feature of the multiferroics is dual (electric and magnetic) tunability of their physical properties. The tunability is provided basically by two effects. The first one is the magnetoelectric effect based on mechanical interaction between the ferrite and the piezoelectric crystal lattices.²² The second effect is the electrodynamic coupling of SWs and electromagnetic waves (EMWs) in the ferrite-ferroelectric (FF) layered structures.^{23–25} The coupled excitations are known as hybrid spin-electromagnetic waves (SEWs).

The general dipole-exchange theory for the spectrum of SEWs propagating in multiferroic layered structures consisting of one ferrite layer and one ferroelectric layer was developed by Demidov *et al.*²⁴ The theory predicted that only relatively thick ferroelectric layers (on the order of hundreds of micrometers) provide effective hybridization of spin waves and electromagnetic waves at microwave frequencies and, consequently, effective electric field tuning of the SEW dispersion. These findings were also confirmed by experiments.^{25–27} Later, Grigorieva *et al.* extended this theory to an arbitrary number of ferrite and ferroelectric layers.²⁸ The theories were developed with a tensorial Green's function method taking into account electromagnetic retardation. However, an application of the extended theory for the investigation of SEW modes in complex multilayered structures consisting of two or more magnetic layers is not published so far. This is obviously due to computational difficulties with finding the zeroes of an infinite matrix determinant which represents the dispersion equation within the Green's function method. In this context, it is appropriate to remember works of Barnas,^{13–16} which used a transfer matrix method calculate spectra of retarded waves.

In this work, we have developed a theory to calculate the spectrum of spin-electromagnetic waves propagating in planar multiferroic multilayers consisting of multiple ferrite

and ferroelectric layers using the method of transfer matrix. In contrast to the works of Grünberg,^{5,6} our theory takes into account electromagnetic retardation and is developed for multiferroic structures having an infinite number of layers. In contrast to works of Barnas,^{13–16} the theory is developed for the case of different parameters of ferrite and ferroelectric layers. As a result, we have derived a dispersion equation based on which we have calculated and studied the spectrum of a particular all-thin-film ferrite-ferroelectric-ferrite structure. Our findings demonstrate an effective electric field control of SEW wavenumbers using thin ferroelectric films.

The paper is organized as follows. Section II describes the developed theory. Section III presents results of numerical simulations of SEW spectra for three-layer thin-film multiferroic heterostructures consisting of two similar or different ferrite layers and one ferroelectric layer between them and discusses electric field tuning of the dispersion characteristics as well. Section IV provides summary and conclusion.

II. THEORY

The ferrite-ferroelectric structure is shown in Fig. 1. It consists of $2N + 1$ layers among which are N ferrite layers and $N + 1$ ferroelectric layers. We introduce an order number for each layer as “ m ” and for ferrite layers as “ i .” We assume that the ferrite layers are surrounded by ferroelectric (dielectric) layers. Therefore, $m = 2i$ for the ferrite layers and $m = 2i + 1$ for the ferroelectric layers. The structure is surrounded by free space with numbers $m = 0$ and $m = 2N + 2$. These denotations will allow us to distinguish easily formulae for ferrite and ferroelectric layers.

We assume that each ferrite layer has a thickness of a_{2i} and a saturation magnetization M_{2i} . The thickness of the ferroelectric layers is a_{2i+1} . The magnetic properties of the magnetic layers are described by the magnetic permeability tensors $\hat{\mu}_{2i}$. The dielectric properties of both magnetic and ferroelectric layers are described by the scalar dielectric permittivities ϵ_{2i} and ϵ_{2i+1} , respectively. Note that we consider ferroelectrics such as ceramic barium-strontium titanate (BST) which at room temperature demonstrate a paraelectric phase and an isotropic dielectric permittivity on the order of thousands.²⁷

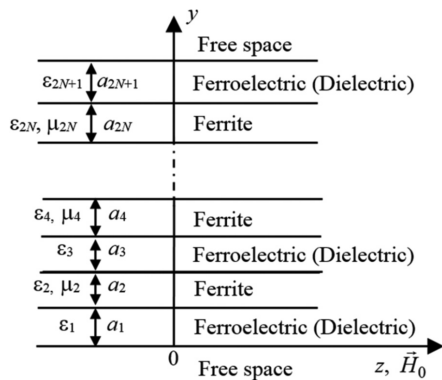


FIG. 1. Multiferroic multilayers.

We assume the layers to be infinite in the xz plane and that the wave propagates along the x -axis. The structure is magnetized to saturation by a uniform magnetic field H_0 along the z -axis. For the particular case of the single ferrite layer, this geometry corresponds to the well-known Damon-Eshbach configuration providing propagation of surface SWs.

For the described geometry, the magnetic permeability tensor has the following form:

$$\hat{\mu}_{2i} = \begin{pmatrix} \mu_{d2i} & j\mu_{a2i} & 0 \\ -j\mu_{a2i} & \mu_{d2i} & 0 \\ 0 & 0 & 1 \end{pmatrix}, \quad (1)$$

where $\mu_{d2i} = \frac{\omega_H(\omega_H + \omega_{M2i}) - \omega^2}{\omega_H^2 - \omega^2}$, $\mu_{a2i} = \frac{\omega\omega_{M2i}}{\omega_H^2 - \omega^2}$, $\omega_H = |g|\mu_0 H_0$, $\omega_{M2i} = |g|\mu_0 M_{2i}$, $|g| = 2.8 \times 10^{10} \text{ s}^{-1} \cdot \text{T}^{-1}$ is the gyromagnetic ratio of the electron, $\mu_0 = 4\pi \times 10^{-7} \text{ H} \cdot \text{m}^{-1}$ is the vacuum permeability, and H_0 is the internal magnetic field.

It is well known that Maxwell's equations can be divided into two systems of differential equations describing two fundamental sets of TE and TM modes.²⁹ For the considered geometry shown in Fig. 1, TE and TM modes have the following field structures: $\mathbf{E}(0, 0, E_z)$, $\mathbf{H}(H_x, H_y, 0)$ for TE modes and $\mathbf{E}(E_x, E_y, 0)$, $\mathbf{H}(0, 0, H_z)$ for TM modes. As it is shown in Ref. 25 for the ferrite-ferroelectric bilayer, the surface SW mode of the ferrite layer has the strongest coupling with the TE modes of the ferroelectric layer due to the effective overlapping of their dynamic components of the magnetic fields. Therefore, we will consider only TE modes of the EMW spectrum.

The Helmholtz equations are derived from the Maxwell's equations for the electric field component E_z of the TE modes for each layer. They have the following form:

$$\frac{\partial^2 E_z}{\partial y^2} + \frac{\partial^2 E_z}{\partial x^2} + \omega^2 \mu_0 \mu_m \epsilon_0 \epsilon_m E_z = 0, \quad (2)$$

where $\mu_{2i} = \mu_{\perp 2i}$ for the ferrite layers ($m = 2i$) and $\mu_{2i+1} = 1$ for the ferroelectric (dielectric) layers ($m = 2i + 1$), ϵ_m is the dielectric permittivity for each layer, and $\epsilon_0 = 8.85 \times 10^{-12} \text{ F} \cdot \text{m}^{-1}$ is the vacuum permittivity. Note that $\mu_{\perp 2i} = (\mu_{d2i}^2 - \mu_{a2i}^2) / \mu_{d2i}$.

Solutions of the Eq. (2) are

$$E_z = A_{2N+2} e^{-\kappa_0 y} e^{-jkx}, \quad (3)$$

for the free space above the structure and

$$E_z = A_0 e^{\kappa_0 y} e^{-jkx}, \quad (3^*)$$

for the free space below the structure, where $\kappa_0 = \sqrt{k^2 - \omega^2 \mu_0 \epsilon_0}$ is the transverse wavenumber for the free space, and k is the wavenumber of the carrier spin-electromagnetic wave. Inside the ferrite and ferroelectric layers, the solutions are

$$E_z = (A_m \sin \kappa_m (y - D_m) + B_m \cos \kappa_m (y - D_m)) e^{-jkx}, \quad (4)$$

where $\kappa_{2i+1} = \sqrt{\omega^2 \mu_0 \epsilon_0 \epsilon_{2i+1} - k^2}$ is the transverse wavenumber for the ferroelectric layers ($m = 2i + 1$), $\kappa_{2i} =$

$\sqrt{\omega^2 \mu_0 \epsilon_0 \epsilon_{2i} \mu_{\perp 2i} - k^2}$ is the transverse wavenumber for the ferrite layers ($m = 2i$), and $D_m = \sum_{s=1}^m a_s$ is the total thicknesses of the layers. The transverse wavenumbers κ_{2i} are imaginary in the frequency ranges corresponding to the surface SWs spectra from $\omega_{\perp 2i} = \sqrt{\omega_H(\omega_H + \omega_{M2i})}$ to $\omega_H + \omega_{M2i}/2$ that embodies the surface character for the SWs in the Damon-Eshbach configuration.

The connection between the magnetic field component H_x and the electric field component E_z was found from Maxwell's equations for each layer. Finally, unknown coefficients (A_m, B_m) for all layers are connected through the electrodynamic boundary conditions. Such connection between the coefficients in adjacent layers could be expressed as follows:

$$\mathbf{P}_i \begin{bmatrix} A_i \\ B_i \end{bmatrix} = \mathbf{Q}_i \begin{bmatrix} A_{i+1} \\ B_{i+1} \end{bmatrix}, \quad (5)$$

where \mathbf{P}_i and \mathbf{Q}_i are matrices that connect unknown coefficients A_i, B_i and A_{i+1}, B_{i+1} in the adjacent layers with numbers i and $i+1$. These matrices will hereafter be referred to as transfer matrices.

Finally, the substitution of the field components to the electrodynamic boundary conditions for the interfaces between the layers allows us to express the coefficient A_0 by the coefficient A_{2N+2} . The derived system of equations has the following form:

$$\begin{cases} A_0 = (T_{11} + T_{12})A_{2N+2}, \\ A_0 = (T_{21} + T_{22})A_{2N+2}, \end{cases} \quad (6)$$

where T_{11}, T_{12}, T_{21} , and T_{22} are the elements of the square matrix $\mathbf{T} = \prod_{m=0}^{2N+1} (\mathbf{P}_m)^{-1} \cdot \mathbf{Q}_m$ where

$$\begin{aligned} \mathbf{P}_0 &= \begin{pmatrix} -1 & 0 \\ 0 & -\kappa_0 \end{pmatrix}; \quad \mathbf{Q}_0 = \begin{pmatrix} \tan(\kappa_1 a_1) & 1 \\ -\kappa_1 & -\kappa_1 \tan(\kappa_1 a_1) \end{pmatrix}; \quad \mathbf{P}_{2i} = \begin{pmatrix} 0 & -1 \\ \frac{\kappa_{f2i}}{\mu_{\perp 2i}} & \frac{k\mu_{a2i}}{\mu_{d2i}\mu_{\perp 2i}} \end{pmatrix}; \\ \mathbf{Q}_{2i} &= \begin{pmatrix} \tan(\kappa_{2i+1} a_{2i+1}) & 1 \\ -\kappa_{2i+1} & -\kappa_{2i+1} \tan(\kappa_{2i+1} a_{2i+1}) \end{pmatrix}; \quad \mathbf{P}_{2i+1} = \begin{pmatrix} 0 & -1 \\ \kappa_{2i+1} & 0 \end{pmatrix}; \\ \mathbf{Q}_{2i+1} &= \begin{pmatrix} \tan(\kappa_{f2i+2} a_{2i+2}) & 1 \\ \frac{k\mu_{a2i+2} \tan(\kappa_{f2i+2} a_{2i+2})}{\mu_{d2i+2}\mu_{\perp 2i+2}} - \frac{\kappa_{f2i+2}}{\mu_{\perp 2i+2}} & \frac{-k\mu_{a2i+2}}{\mu_{d2i+2}\mu_{\perp 2i+2}} - \frac{\kappa_{f2i+2} \tan(\kappa_{f2i+2} a_{2i+2})}{\mu_{\perp 2i+2}} \end{pmatrix}; \\ \mathbf{P}_{2N+1} &= \begin{pmatrix} 0 & -1 \\ \kappa_{2N+1} & 0 \end{pmatrix}; \quad \mathbf{Q}_{2N+1} = (-1)\mathbf{P}_0. \end{aligned}$$

Denote the determinant of the system (6) as $f(\omega, k) = T_{11} + T_{12} - T_{21} - T_{22}$. The vanishing of the determinant results in the dispersion relation

$$f(\omega, k) = 0. \quad (7)$$

The dispersion relation (7) describes the spectrum of the spin-electromagnetic waves in the ferrite-ferroelectric structures with an arbitrary sequence of the ferrite and ferroelectric layers. Note that this dispersion relation could be easily modified for the case of the presence of metal screens below and above the structure by change of matrices \mathbf{P}_0 and \mathbf{Q}_{2N+1} .

III. DISPERSION CHARACTERISTICS OF SPIN-ELECTROMAGNETIC WAVES IN MULTIFERROIC MULTILAYERS

A. Spin-electromagnetic waves in coupled ferrite films

Let us apply the developed theory for numerical simulations of the dispersion characteristics of spin-electromagnetic waves propagating in the structure shown in Fig. 2. The structure consists of two ferrite layers contacted with dielectric layers. These ferrite layers are separated by free space. This topology corresponds to two thin magnetic films grown on

relatively thick dielectric substrates. Yttrium iron garnet (YIG) films grown on gadolinium gallium garnet (GGG) substrates by liquid phase epitaxy are brilliant examples which already found practical applications.

Dispersion characteristics calculated for the identical ferrite layers are shown in Fig. 3(a). We used the following

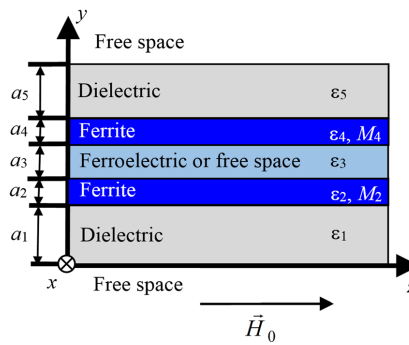


FIG. 2. All-thin-film multiferroic structure consisting of two ferrite layers separated by a free space or a ferroelectric layer.

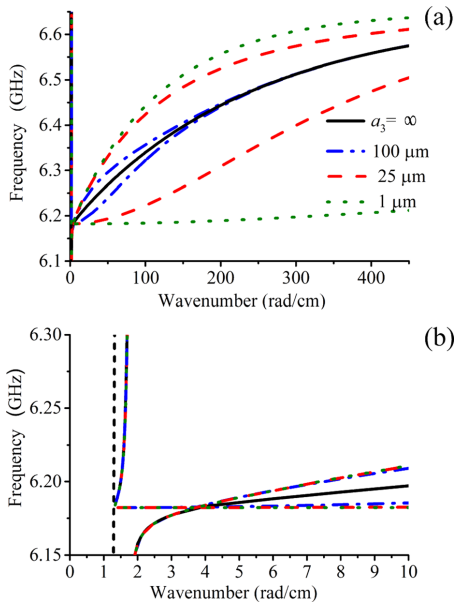


FIG. 3. Dispersion characteristics of the SEWs calculated for a heterostructure consisting of two similar ferrite layers separated by free space (a) and the same characteristics in expanded scale showing the influence of the electromagnetic retardation (b).

parameters: $a_2 = a_4 = 20 \mu\text{m}$, $M_2 = M_4 = 139\,260 \text{ A/m}$ (1750 G), and $\varepsilon_2 = \varepsilon_4 = 14$ for the ferrite layers; $a_1 = a_5 = 500 \mu\text{m}$ and $\varepsilon_1 = \varepsilon_5 = 14$ for dielectric layers. These values are typical for YIG-GGG structures. The distance between the ferrites a_3 was varied from $1 \mu\text{m}$ to infinity. The results show that the waves manifest a hybrid spin-electromagnetic nature for small wavenumbers up to 3 rad/cm as is shown in Figs. 3(b) and 4(b). This is due to the small values of the wavenumber k for the fundamental electromagnetic mode of the considered structure in the microwave range. The short dashed almost vertical line in the figures represents the dependence $\omega = ck$, where c is the speed of light in vacuum. The electromagnetic retardation can be neglected for larger wavenumbers. Therefore, the calculated dispersion branches demonstrate the well known behavior in the magnetostatic approximation. Indeed, the results for $k > 3 \text{ rad/cm}$ are similar to those reported in Refs. 5–8. On the one hand, this confirms the correctness of our theory. On the other hand, these results will be useful for the treatment of the spin-electromagnetic wave spectrum which will be investigated for a multiferroic heterostructure in the next part of this section.

It is seen from Fig. 3 that the SWs propagate independently in the ferrite layers for $a_3 \rightarrow \infty$. For the investigated geometry, the surface SWs propagate along the bottom surfaces of the ferrite layers. A decrease of the a_3 leads to reconfiguration of wave fields and splits the dispersion characteristic into two spin-wave dispersion branches (see Fig. 3). The lower branch corresponds to spin wave which propagates along the interface between the upper ferrite layer and free

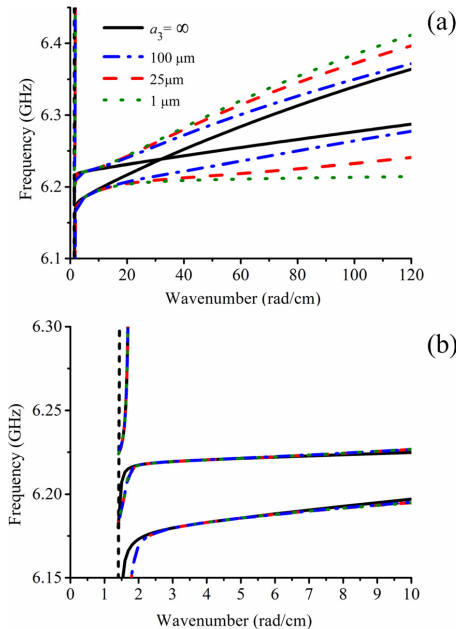


FIG. 4. Dispersion characteristics of the SEWs calculated for the heterostructure consisting of two different ferrite layers separated by free space (a) and these characteristics in expanded scale (b).

space. The upper branch corresponds to spin wave which propagates along the interface between the lower ferrite film and bottom dielectric layer. A further decrease in a_3 provides a stronger interaction between these coupled modes in a wide frequency range. The wave propagating at the interface between the upper ferrite layer and free space slows down due to this interaction. For the case of $a_3 = 1 \mu\text{m}$ [dotted lines in Fig. 3(a)], the upper dispersion branch almost coincides with the SW spectrum for the ferrite film of double thickness. For intermediate values of a_3 , the interaction between the waves propagating in the different layers depends on the wavenumber. Namely, the waves demonstrate strong coupling for relatively small wavenumbers. An increase in the wavenumbers leads to a decrease in the interaction. This is explained by the dependence of the damping decrements of the alternating fields outside the ferrite films on the wavenumber.³⁰ Therefore, waves having relatively large wavenumbers propagate independently and their dispersion branches tend to follow the dispersion of the separate ferrite film.

Dispersion characteristics shown in Fig. 4 were calculated for spin-electromagnetic waves propagating in a structure containing two ferrite films with different parameters: $a_2 = 20 \mu\text{m}$, $M_2 = 139\,260 \text{ A/m}$ (1750 G), $a_4 = 6 \mu\text{m}$, and $M_4 = 142\,443 \text{ A/m}$ (1790 G). All the remaining parameters were the same as for the previous structure. The main distinguishing feature here is that the dispersion branches for thin and thick ferrite layers cross each other in the magnetostatic region for $a_3 \rightarrow \infty$. The intersection of the dispersion branches arises from the different

saturation magnetizations M_2 and M_4 and from the different group velocities of the spin waves in magnetic films of different thickness.³⁰ The different saturation magnetizations define also different frequencies when the wave-vector approaches zero. In the considered case, the spin waves in the upper thin film have a smaller group velocity than those in the lower thick film. The region of relatively small wavenumbers of $k < 30$ rad/cm will be under examination for multiferroic heterostructures in the next part of this Section. In this region, the condition $M_2 < M_4$ leads to the situation that the upper dispersion branch corresponds to the spin waves in the upper thin film and the lower branch describes the spin waves in the lower thick film. We will use hereinafter these denominations for the pure spin-wave dispersion branches.

A reduction in a_3 leads to a coupling between the spin wave modes due to the magnetodipole interaction. This interaction manifests itself in the repulsion of the dispersion branches around the point of the intersection of the uncoupled spin wave modes. The repulsion becomes more pronounced for smaller distances between the ferrite layers because of an increase in the spin wave coupling. In contrast to the symmetric structure for the considered one, the region of the strong spin-wave coupling is around $k = 30$ rad/cm. For $k < 30$ rad/cm, the upper dispersion branch describes the coupled spin waves localized mainly in the upper ferrite layer whereas the lower one corresponds to the spin waves propagating mostly in the lower ferrite layer. This behavior is reversed for $k > 30$ rad/cm, where the upper dispersion branch describes the coupled spin waves localized mainly in the lower ferrite layer whereas the lower one corresponds to the spin waves propagating mostly in the upper ferrite layer. Figure 4(b) demonstrates clearly that the coupling does not affect the spectrum for $k < 10$ rad/cm.

B. Spin-electromagnetic waves in all-thin-film ferrite-ferroelectric-ferrite heterostructures

We consider here a structure modified in comparison with Subsection III A. Instead of a free space between the ferrite layers, we will use a thin ferroelectric film. As a result, we obtain an all-thin-film multiferroic heterostructure consisting of two ferrite layers separated by a ferroelectric layer as is shown in Fig. 2. The theoretical model described in Sec. II was used to calculate the spectra of SEWs in such a kind of structure.

As it was discussed above, the ferroelectric layer is assumed to be a thin BST film. Therefore, it was modeled as a dielectric with a large isotropic dielectric permittivity. During our simulations, the following three parameters, namely, the saturation magnetization M_4 of the top ferrite layer, the ferroelectric layer thickness a_3 , and its dielectric permittivity ϵ_3 were varied. All the remaining parameters were fixed. These are $a_2 = 20 \mu\text{m}$, $M_2 = 139\,260 \text{ A/m}$ (1750 G), $a_4 = 6 \mu\text{m}$, $a_1 = a_5 = 500 \mu\text{m}$, and $\epsilon_1 = \epsilon_5 = 14$. The spectra were calculated for two opposite directions of the wave propagation. Positive values of the wavenumber correspond to the SEW propagation along the x -axis.

Solid curves in Fig. 5 show the spectra of the SEWs calculated for $\epsilon_3 = 1500$ and different values of a_3 and M_4 . It is

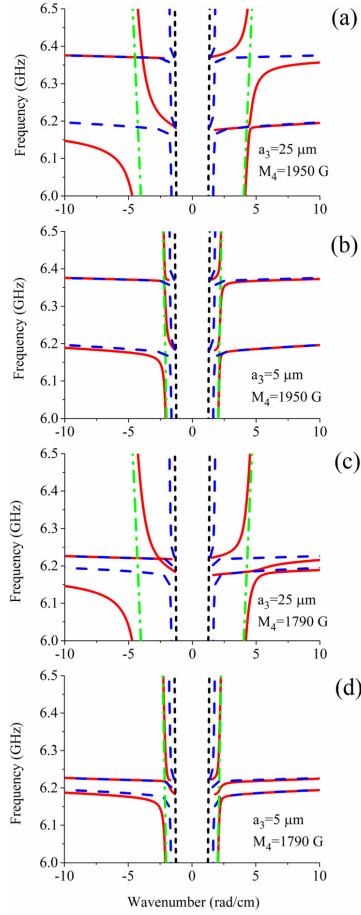


FIG. 5. The spectra of the hybrid SEWs (solid curves) in the ferrite-ferroelectric-ferrite thin-film structures calculated for different thicknesses of the ferroelectric layer a_3 and for varying saturation magnetization M_4 of the top ferrite layer. Dashed-dotted lines show the electromagnetic mode TE_1 of the structure. Dashed curves show the hybrid SEWs for coupled ferrite films (i.e., for $\epsilon_3 = 1$). The short dashed line represents the dependence $\omega = ck$, where c is the speed of light in vacuum.

clearly visible that the SEW spectrum consists of three dispersion branches. We will refer to them as lower, middle, and upper branches. Such a spectrum is formed as a result of the electrodynamic interaction of the electromagnetic mode TE_1 with two spin-wave modes. Due to the narrow ferroelectric layer, a magnetodipole interaction between the ferrite layers considered in the previous part may also play a role in the formation of the SEW spectrum for the particular set of the heterostructure parameters. Consider possible situations in details.

Figure 5(a) presents the case of a relatively large difference in M for $a_3 = 25 \mu\text{m}$ providing the situation of negligibly small spin-wave coupling for $k < 30$ rad/cm. It is easy to

see the hybridizations between one electrodynamic mode and two spin-wave modes which manifests itself as repulsions between the SEW dispersion branches. The hybridizations become more pronounced in the vicinity of the points where the dispersion branches of the electromagnetic mode TE_1 and the upper and lower spin-wave modes cross each other. Strictly speaking, the hybrid SEWs that are controllable with both electric and magnetic fields exist around these points. Far from these points, the SEW dispersion branches tend to the branches of pure spin-wave or electromagnetic modes. Similar to the coupled ferrite-film structure considered earlier, the upper and lower spin-wave modes describe the spin-wave propagation in the upper and the lower ferrite layers, respectively.

For positive wavenumbers, a relatively weak repulsion takes place between the lower and middle SEW branches around the lower point of the intersection of the modes that are hybridized. At the same time, relatively strong repulsion between the middle and upper SEW branches occurs around the upper point. This is explained as follows. Dynamic magnetic fields of the spin waves propagating along the x -axis in the lower and in the upper ferrite layers have weak exponential transverse distributions with maxima lying at the bottom surfaces of the both layers. At the same time, the electromagnetic wave fields change strongly in the cross section of the structure. The maximum of these fields is localized close to the middle of the structure and it is much smaller outside of the structure. Therefore, an interaction between the spin and electromagnetic waves is much stronger for the inner ferrite-ferroelectric interface than for the outer interface between the ferrite and dielectric substrate.

A completely different situation is observed for waves propagating in the opposite x -axis direction, i.e., for negative wavenumbers. The maxima of the spin-wave magnetic fields are now located at the top surfaces of the both ferrite layers. Therefore, a strong interaction between the spin and electromagnetic waves takes place only on the interface between the lower ferrite layer and the ferroelectric layer. As a result, the strong repulsion happens between the lower and middle SEW branches.

A reduction in the ferroelectric layer thickness a_3 does not change principally the described behavior of the SEW spectrum [see Fig. 5(b)]. Note only that this leads to an increase in group velocity of the fundamental electromagnetic mode TE_1 of the layered structure and, therefore, the regions of hybridization are shifted closer to the ordinate axis.

Consider now the case of a relatively small difference in M . As it is shown in Fig. 5(c), the SEW middle branch is clamped between the upper and lower SW branches. Therefore, its group velocity changes significantly with a reduction in the ferroelectric thickness a_3 . This can be clearly seen by comparing the SEW dispersion characteristics shown in Figs. 5(c) and 5(d). A direct influence of the spin-wave coupling on the spin-electromagnetic hybridization takes place only for the lower SEW branch with negative wavenumbers shown in Fig. 5(c). This effect is absent for the other hybridizations because of their relative weakness. As it was shown in the previous part of this Section, the coupling affects the spectrum for $k > 10$ rad/cm.

Let us now turn to the investigation of the electric field tuning of the dispersion characteristics of the SEWs. As it is well known, the application of an electric field to ferroelectrics results in a decrease of its relative dielectric permittivity. Therefore, we plot the dispersion characteristics for two values of the ferroelectric layer permittivity ϵ_3 taken to be 700 and 1500 to demonstrate the electric field tuning of the SEW dispersion. They are shown in Fig. 6 for different values of a_3 . A decrease in ϵ_3 shifts the regions of wave hybridization towards the ordinate axis and decreases the wavenumbers of the SEWs for fixed frequencies. This phenomenon is promising for applications of the all-thin-film multiferroic structure as a phase shifter.

A detailed study of the influence of the ferroelectric layer permittivity on the SEW spectrum also shows also changes in the spectrum far from spin- and electromagnetic wave hybridization regions. Namely, outside these regions, the reduction in ϵ_3 leads to a shift of the dispersion branches just like a reduction in the thickness a_3 of the ferroelectric layer and increase the coupling between spin-wave modes of the ferrite layers discussed in the previous part of this section.

The wavenumber variations versus frequency for SEWs in both propagation directions were calculated for different ferroelectric layer thickness a_3 in the case if the ferroelectric layer permittivity ϵ_3 was reduced from 1500 to 700. The results are shown in Fig. 7 by solid, dashed, and dashed-dotted lines for the lower, middle, and upper SEW dispersion branches, respectively. The parameters were taken to be the same as for Figs. 5(c) and 5(d). Figures 7(a)–(c) and

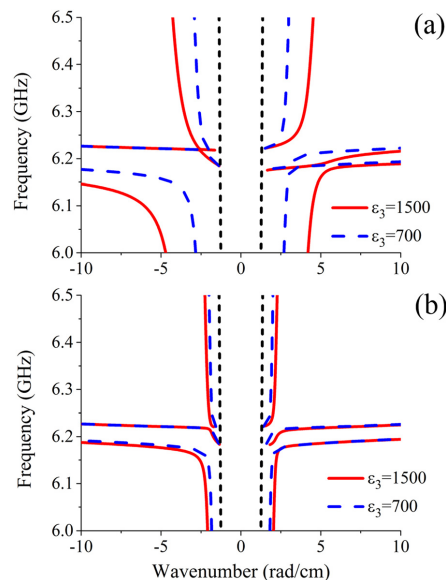


FIG. 6. The spectra of the hybrid SEWs in the ferrite-ferroelectric-ferrite thin-film structures calculated for ferroelectric thicknesses $a_3 = 25 \mu\text{m}$ (a) and $a_3 = 5 \mu\text{m}$ (b) and for different dielectric permittivities as indicated. Short dashed lines represent the dependence $\omega = ck$.

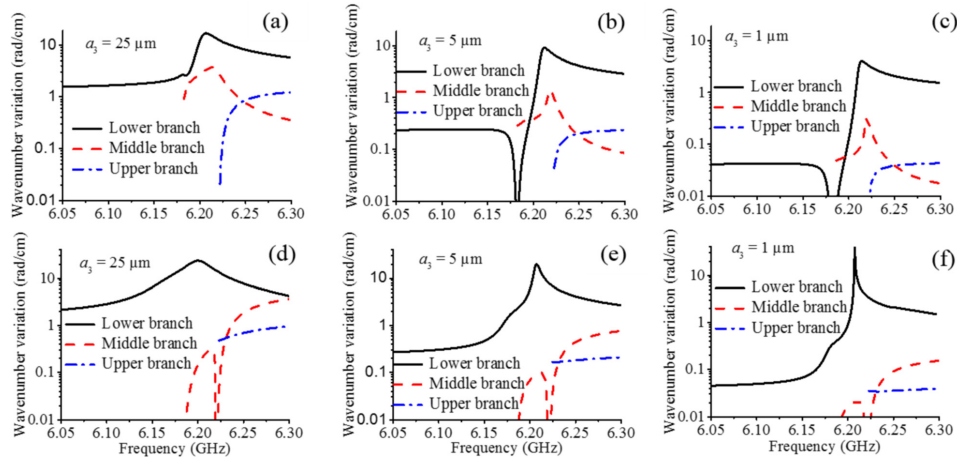


FIG. 7. Wavenumber variation of the lower, middle, and upper SEW dispersion branches versus frequency calculated for different ferroelectric layer thickness a_3 for the forward (a)–(c) and opposite to x -axis (d)–(f) propagation directions.

7(d)–7(f) correspond to SEW dispersion branches for the forward and the opposite propagation to the x -axis directions, respectively. As it was mentioned above, the hybridization of the spin- and the electromagnetic waves depends on the propagation direction. Features of the wavenumber tuning in the range of 6.175 GHz–6.25 GHz for the forward propagation shown in Fig. 5(c) are determined by the strong hybridization of EMW and SW in the upper ferrite layer. At the same time, for the opposite propagation direction shown in Fig. 5(d), strong hybridization occurs between EMW and SW in the lower ferrite layer. It provides an increase in the tuning of the SEW mode in the range of 6.15 GHz–6.25 GHz in comparison with tuning of the electromagnetic mode.

Figure 8 shows the SEW phase shifts calculated for a 1 cm long structure based on different thicknesses of the ferroelectric film. It is seen that the phase shift for a 1 μm -thick ferroelectric film at a frequency of 6.21 GHz is even larger than for the 25 μm -thick film. A phase shift of more than 2π can be accumulated in a frequency range of 5 MHz. In spite of this relatively narrow frequency range, this phenomenon

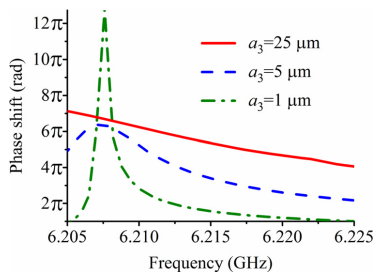


FIG. 8. Phase shift versus frequency for the lower SEW mode propagating in the propagation direction opposite to the x -axis. Characteristics were calculated for different ferroelectric layer thicknesses a_3 as indicated.

can be tuned over a broad frequency range by variation of the bias magnetic field. This feature demonstrates the yield of the all-thin-film heterostructures.

IV. CONCLUSION

In this work, we derived the dispersion relation for spin-electromagnetic waves (SEW) propagating in multiferroic heterostructures composed of a large number of ferrite and ferroelectric layers. The developed theory gives the possibility to investigate a wide range of problems connected with hybrid SEWs in different ferrite-ferroelectric multilayered structures. A comprehensive analysis of SEW spectra was carried out in the case of a ferrite-ferroelectric-ferrite thin-film structure. Nonreciprocity of the SEW spectrum for the waves propagating in opposite directions was found.

The tuning of SEW dispersion characteristics is provided by two different mechanisms. The first is based on the hybridization of an electro-magnetic wave (EMW) and a spin wave (SW). A change in the permittivity tilts the EMW dispersion characteristic and leads, thus, to the shift of the hybridization point. A wavenumber variation determined by this mechanism increases with the increase of the thickness of the ferroelectric layer. The mechanism is known and was investigated in detail in Refs. 24 and 31. The second mechanism manifests itself only for the structures based on two ferrite layers at least. It is because two adjacently placed ferrite layers, although separated by a thin ferroelectric divider, interact through the electromagnetic field. An efficiency of this mechanism increases with the thinning of the ferroelectric film placed between the ferrite films. As an example, we show here that the effective tuning of SEW wavenumbers by an external electric field is possible, even in the case of a 1- μm -thick ferroelectric film.

As it is well known, efforts for ferroelectric film thickness reduction arise from demands to reduce the control

voltage producing ferroelectric polarization. The obtained results show that the use of all-thin-film multiferroic heterostructures allows not only to reduce the control voltage, but also to increase the phase shift of SEWs propagating in the structure. Therefore, the studied structure looks promising for practical applications, in particular, for the development of thin-film microwave phase shifters.

ACKNOWLEDGMENTS

The analytical model was developed with support from the Russian Science Foundation (Grant No. 14-12-01296-P). The numerical calculations and theoretical investigation were supported in part by the Ministry of Education and Science of Russian Federation (Project “Goszadanie”), by the Academy of Finland, and by the Deutsche Forschungsgemeinschaft in the frames of the B01 project of the Transregional Collaborative Research Center SFB/TRR 173 “Spin + X” and the Project No. DE 639.

- ¹R. W. Damon and J. R. Eschbach, *J. Phys. Chem. Solids* **19**(3/4), 308–320 (1961).
- ²R. W. Damon and H. Van De Vaart, *J. Appl. Phys.* **36**(11), 3453–3459 (1965).
- ³B. A. Kalinikos and A. N. Slavin, *J. Phys. C: Solid State Phys.* **19**(35), 7013 (1986).
- ⁴R. L. Stamps and B. Hillebrands, *J. Magn. Magn. Mater.* **93**, 616–620 (1991).
- ⁵P. Grünberg, *J. Appl. Phys.* **51**(8), 4338–4341 (1980).
- ⁶P. Grünberg, *J. Appl. Phys.* **52**(11), 6824–6829 (1981).
- ⁷D. L. Mills, *Light Scattering in Solids V*. (Springer, Berlin, Heidelberg, 1989), pp. 13–48.
- ⁸R. E. Camley and R. L. Stamps, *J. Phys.: Condens. Matter* **5**(23), 3727 (1993).
- ⁹K. Vayhinger and H. Kronmüller, *J. Magn. Magn. Mater.* **62**(2–3), 159–168 (1986).
- ¹⁰B. Hillebrands, *Phys. Rev. B* **41**(1), 530 (1990).
- ¹¹B. A. Kalinikos and P. A. Kolodin, *IEEE Trans. Magn.* **28**(5), 3204–3206 (1992).
- ¹²J. Barnas, in *Linear and Nonlinear Spin Waves in Magnetic Films and Superlattices*, edited by M. G. Gottam (World Scientific Publishing Company, Singapore, 1994), pp. 157–206.
- ¹³J. Barnas, *Solid State Commun.* **61**(6), 405–408 (1987).
- ¹⁴J. Barnas, *J. Phys. C: Solid State Phys.* **21**(5), 1021 (1988).
- ¹⁵J. Barnas, *J. Phys. C: Solid State Phys.* **21**(22), 4097 (1988).
- ¹⁶J. Barnas, *Phys. Status Solidi B* **165**(2), 529–537 (1991).
- ¹⁷N. Liu, X. D. Hou, and X. Zhang, *J. Phys.: Condens. Matter* **20**(33), 335210 (2008).
- ¹⁸R. W. Ziolkowski and E. Heyman, *Phys. Rev. E* **64**(5), 056625 (2001).
- ¹⁹M. M. Vopson, *Crit. Rev. Solid State Mater. Sci.* **40**(4), 223–250 (2015).
- ²⁰C. Lu, W. Hu, Y. Tian, and T. Wu, *Appl. Phys. Rev.* **2**, 021304 (2015).
- ²¹N. X. Sun and G. Srinivasan, *Spin* **2**(03), 1240004 (2012).
- ²²S. Shastry, G. Srinivasan, M. I. Bichurin, V. M. Petrov, and A. S. Tatarenko, *Phys. Rev. B* **70**(6), 064416 (2004).
- ²³V. B. Anfinogenov, T. N. Verbitskaja, Y. V. Gulyaev, P. E. Zil'berman, S. V. Meriakri, Y. F. Ogrin, and V. V. Tikhonov, *Sov. J. Commun. Technol. Electron.* **34**(116), 494–499 (1989).
- ²⁴V. E. Demidov, B. A. Kalinikos, and P. Edenhofer, *J. Appl. Phys.* **91**, 10007 (2002).
- ²⁵V. E. Demidov, B. A. Kalinikos, S. F. Karmanenko, A. Semenov, and P. Edenhofer, *IEEE Trans. Microwave Theory Tech.* **51**(10), 2090–2096 (2003).
- ²⁶Y. K. Fetisov and G. Srinivasan, *Appl. Phys. Lett.* **87**(10), 103502 (2005).
- ²⁷A. B. Ustinov, G. Srinivasan, and B. A. Kalinikos, *Appl. Phys. Lett.* **90**(3), 031913 (2007).
- ²⁸N. Y. Grigorieva, B. A. Kalinikos, M. P. Kostylev, and A. A. Stashkevich, “Theory and phenomena of artificial materials,” in *Handbook of Artificial Materials*, edited by F. Capolino (Taylor and Francis Group, LLC, Oxford, UK, 2009), Vol. 1, p. 974.
- ²⁹R. E. Collin, *Field Theory of Guided Waves*, 2nd ed. (The Institute of Electrical and Electronics Engineers, New York, 1991).
- ³⁰D. D. Stancil and A. Prabhakar, *Spin Waves: Theory and Applications* (Springer, New York, 2009).
- ³¹A. B. Ustinov, P. I. Kolkov, A. A. Nikitin, B. A. Kalinikos, Y. K. Fetisov, and G. Srinivasan, *Tech. Phys.* **56**(6), 821–825 (2011).

Publication III

Nikitin, A. A., Nikitin, A. A., Ustinov, A. B., Lähderanta, E., and Kalinikos, B. A.

Theory of spin-electromagnetic waves in planar thin-film multiferroic heterostructures based on a coplanar transmission line and its application for electromagnonic crystals

Reprinted with permission from
IEEE Transactions on Magnetics
Vol. 54(11), pp. 1-5, 2018
© 2018, IEEE

Theory of Spin-Electromagnetic Waves in Planar Thin-Film Multiferroic Heterostructures Based on a Coplanar Transmission Line and Its Application for Electromagnonic Crystals

Aleksei A. Nikitin^{1,2}, Andrey A. Nikitin^{1,2}, Alexey B. Ustinov¹, ErkkiLähderanta², and Boris A. Kalinikos¹

¹Department of Physical Electronics and Technology, St. Petersburg Electrotechnical University, St. Petersburg 197376, Russia

²Department of Physics, Lappeenranta University of Technology, 53850 Lappeenranta, Finland

A theory of spin-electromagnetic wave spectrum has been developed for the thin-film ferrite-ferroelectric structure based on a coplanar transmission line (TL). The dispersion relation was derived through analytical solution of the full set of Maxwell's equations utilizing a method of approximate boundary conditions. The theory was used for numerical simulation of the transmission characteristics of the periodic multiferroic heterostructures containing the coplanar TL with a periodic variation of its width. We named these heterostructures "electromagnonic crystals." The transmission characteristics of the electromagnonic crystals were calculated by the transfer-matrix method. The obtained results show that a high microwave signal rejection of more than 30 dB appears in the electromagnonic crystals due to the Bragg reflections. The distinctive features of the proposed electromagnonic crystals are the thin-film planar topology and dual tunability of the electromagnonic band-gap positions.

Index Terms—Coplanar waveguide, ferrites, ferroelectrics, microwaves, spin-electromagnetic waves (SEWs).

I. INTRODUCTION

INTENSE development of the telecommunication systems requires tunable, reliable, and inexpensive components based on the frequency-agile materials. The artificial multiferroic structures, i.e., the heterostructures combining ferromagnetic and ferroelectric phases, are promising for such practical applications. They demonstrate dual (electric and magnetic) tunability of their physical properties [1], [2]. One of the possible mechanisms of the interaction between the ferromagnetic and ferroelectric phases is realized through electrodynamic coupling of spin waves (SWs) and electromagnetic waves (EMWs). These coupled excitations are known as hybrid spin-electromagnetic waves (SEWs) [3].

A strong research interest to the development and investigation of the microwave devices based on the multiferroics is determined by dual tunability of their performance characteristics combined with small insertion losses and low power consumption. Among such devices are the delay lines [4], tunable microwave resonators [5], [6], phase shifters [7], and multiband filters [8]. Besides, a new class of the microwave devices, which combine multiferroic features and periodic spatial structure, is attractive for the applications at microwaves. In order to distinguish the periodical multiferroic structures from known magnonic [9]–[13] and photonic [14] crystals, we will name them as the artificial electromagnonic crystals. This name justifies itself because quanta of SEWs can be considered as electro-active magnons or electromagnons.

The multiferroic periodical structures demonstrate electrically and magnetically tunable band gaps in the SEW spectrum. Propagation of the electromagnons within the band gaps is forbidden. The first prototype of the electromagnonic crystal consisted of a thin-film magnonic crystal and a ferroelectric slab was proposed in [15]. After that, a number of theoretical and experimental works were carried out [16]–[20]. It is worth noting that the investigated structures were fabricated with a relatively thick (more than 100 μm) ferroelectric layer, in order to provide effective hybridization of the SW and the EMW at microwave frequencies. As a result, a relatively high control voltage up to 1000 V was applied to multiferroic structures to achieve an effective electric tuning of the SEW spectra.

All thin-film multiferroic heterostructures were suggested for energy saving and down scaling of the multiferroic microwave devices [21]–[27]. One of such structures consisted of thin magnetic and ferroelectric films in combination with narrow slot lines or coplanar transmission lines (TLs) [21]–[23], [25]. Up to now, a research activity in this field was mostly aimed to multiferroic structures based on the slot TLs, while the ferrite-ferroelectric structures containing coplanar TLs were investigated only experimentally [22]. Therefore, the purpose of this paper is twofold:

- 1) to develop a theory of the SEW spectrum for multiferroic heterostructures utilized a coplanar TL;
- 2) to investigate the transmission characteristics of the electromagnonic crystals having a periodic variation of the coplanar TL geometry.

The paper is organized as follows. Section II describes the theory of SEW spectra in the thin-film multiferroic structures based on a coplanar TL. Section III presents the results of numerical simulation and analysis of the transmission

Manuscript received March 12, 2018; accepted May 7, 2018. Date of publication June 6, 2018; date of current version October 17, 2018. Corresponding author: A. A. Nikitin (e-mail: aleksei.a.nikitin@gmail.com).

Color versions of one or more of the figures in this paper are available online at <http://ieeexplore.ieee.org>.

Digital Object Identifier 10.1109/TMAG.2018.2837218

0018-9464 © 2018 IEEE. Personal use is permitted, but republication/redistribution requires IEEE permission. See http://www.ieee.org/publications_standards/publications/rights/index.html for more information.

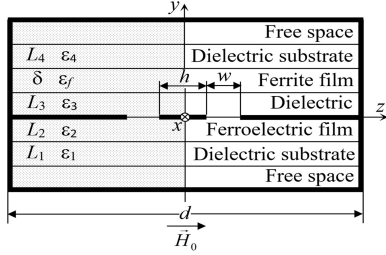


Fig. 1. Cross section of a coplanar TL with thin-film multiferroic heterostructure.

characteristics for the proposed electromagnonic crystal. Summary and conclusions are given in Section IV.

II. THEORY OF SPIN-ELECTROMAGNETIC WAVES IN PLANAR THIN-FILM MULTIFERROIC HETERO-STRUCTURES BASED ON A COPLANAR TRANSMISSION LINE

Fig. 1 shows schematically a cross section of a model multiferroic heterostructure based on a coplanar TL, which was used for the theory development. The TL consists of a central metal strip of width h and two slots of width w . The coplanar TL is placed between ferroelectric and ferrite layers. The thicknesses and dielectric permittivities of the dielectric nonmagnetic layers are denoted as L_j and ϵ_j , respectively. Here, j is a layer number according to Fig. 1. Ferrite film has thickness δ and dielectric permittivity ϵ_f . We assume that SEWs propagate along the coplanar TL in the multiferroic structure tangentially magnetized along z -axis.

To treat the multiferroic structure with the coplanar TL as a rectangular waveguide boundary-value problem, we introduce perfect metal walls surrounding the layered structure. It enables us to represent EMWs as a superposition of infinite orthogonal sets of relatively simple rectangular waveguide modes [28].

The EMW in the rectangular waveguide loaded with the multiferroic heterostructure and the coplanar TL is a superposition of the longitudinal-section magnetic (LSM) and the longitudinal-section electric (LSE) modes. Therefore, the electric and magnetic field components in the dielectric nonmagnetic layers of the structure can be found as a sum of the LSM and LSE modes $\mathbf{E}_j = \mathbf{E}_j^{\text{LSM}} + \mathbf{E}_j^{\text{LSE}}$, $\mathbf{H}_j = \mathbf{H}_j^{\text{LSM}} + \mathbf{H}_j^{\text{LSE}}$. The $\mathbf{E}_j^{\text{LSE}}$ and $\mathbf{H}_j^{\text{LSM}}$ fields are expressed through Hertzian potentials as $\mathbf{E}_j^{\text{LSE}} = -\nabla \times \mathbf{\Pi}_j^h$, $\mathbf{H}_j^{\text{LSM}} = \nabla \times \mathbf{\Pi}_j^e$, where $\mathbf{\Pi}^e$ and $\mathbf{\Pi}^h$ are electric and magnetic Hertzian potential functions, respectively.

In developing a theory of the SEW spectra in the thin-film multiferroic structures based on a coplanar TL, two important points should be noted. First, an approximate dispersion relation can be found through analytical solution of the full set of Maxwell's equations utilizing the method of approximate boundary conditions [25]. Applicability of this method is determined by a relatively weak exponential dependence of the electric and magnetic field distributions on the transverse

coordinate for the long-wave dipolar surface SW in the thin ferrite film with unpinned surface spins [29]. A high accuracy of this method was shown in [25] for a planar all thin-film multiferroic structure with a slot TL. Second, due to the symmetry of the fundamental coplanar TL mode the rectangular waveguide problem is reduced to the equivalent approach for a slot TL with "magnetic wall" boundary conditions: $(\partial/\partial z)\mathbf{\Pi}_j^e = \mathbf{\Pi}_j^h = 0$ for $z = 0$ and $z = \pm d/2$. Note that in the calculations the distance between the sidewalls d was chosen high enough to minimize the wall influence on the electrodynamic process. Taking into account the above listed assumptions, we derived the approximate dispersion relation for the SEW in thin-film multiferroic coplanar TL following the same algorithm like in our previous work [25] for a slot TL. As a result, we obtained the dispersion relation from the vanishing of the following matrix determinant composed by the G elements:

$$G_{m,s} = \sum_{n=0}^N \begin{bmatrix} X_{11} \cdot Y_{11_{n,m,s}} & X_{12} \cdot Y_{12_{n,m,s}} \\ X_{21} \cdot Y_{21_{n,m,s}} & X_{22} \cdot Y_{22_{n,m,s}} \end{bmatrix} \quad (1)$$

where X_{11} , X_{12} , X_{21} , and X_{22} are the same elements of matrix X as for the structure with slot TL (see [25])

$$\begin{aligned} Y_{11_{n,m,s}} &= (-1)^{1+m+s} J_{2s}(q_n) \frac{(2m+2)J_{2m+2}(q_n)}{q_n} S \\ Y_{12_{n,m,s}} &= (-1)^{m+s} \varphi_n J_{2m}(q_n) J_{2s}(q_n) S \\ Y_{21_{n,m,s}} &= (-1)^{1+m+s} \frac{(2m+2)J_{2m+2}(q_n)}{q_n} \frac{(2s+2)J_{2s+2}(q_n)}{q_n} S \\ Y_{22_{n,m,s}} &= (-1)^{m+s} \varphi_n J_{2m}(q_n) \frac{(2s+2)J_{2s+2}(q_n)}{q_n} S. \end{aligned}$$

The following notations are used in (1):

$$\varphi_n = \begin{cases} 1/2 & \text{at } n = 0 \\ 1 & \text{at } n \neq 0, \end{cases} \quad J_{2m}(q_n)$$

and $J_{2m+2}(q_n)$ are Bessel functions of the first kind; $S = \sin^2(a_n(h+w)/2)$; $m, s = 0, 1 \dots M$; $n = 0, 1 \dots N$; values of M and N are determined by the width of the slot gap w ; $q_n = n\pi w/2d$; $a_n = \pi n/d$.

III. INVESTIGATION OF THE ELECTROMAGNONIC CRYSTAL BASED ON THE COPLANAR TRANSMISSION LINE

This section is devoted to the numerical simulations of the transmission characteristics of the electromagnonic crystals based on a coplanar TL. The calculations were carried out in two stages. At the first stage, the dispersion relations for the SEWs propagating in the regular multiferroic coplanar TL were found according to the theoretical model discussed in Section II. At the second stage, the transmission characteristics of the periodic multiferroic structure were obtained according to the transfer-matrix method [30]. This method allows one to calculate the transmission characteristics of a finite-length periodic waveguide taking into account its dispersion properties.

Following the first stage, let us consider the regular multiferroic coplanar TL. The set of the layers corresponds to the structure described in Section II with an assumption of

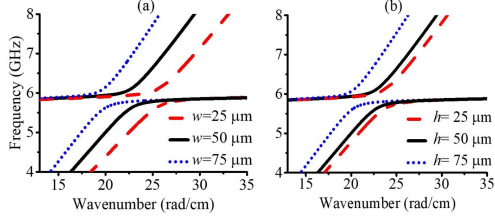


Fig. 2. Influence of the (a) slot width w and the (b) strip width h on the SEW dispersion characteristics.

zero thickness ($L_3 = 0$) of the dielectric layer with number $j = 3$. All the calculations are performed for the parameters of the experimental structures typically used in multiferroic microwave devices (see [1]). We assume that the structure consists of an epitaxial yttrium-iron garnet (YIG) film on a gadolinium gallium garnet (GGG) substrate, the coplanar TL electrodes, and polycrystalline barium-strontium titanate $\text{Ba}_{0.5}\text{Sr}_{0.5}\text{TiO}_3$ (BST) film on a sapphire substrate. In accordance with Fig. 1, the dielectric layer number $j = 1$ corresponds to the sapphire substrate with thickness and permittivity L_1 and ϵ_1 , respectively. The layer number $j = 2$ corresponds to the BST film with parameters L_2 and ϵ_2 . The parameters of the ferrite YIG film are thickness δ , dielectric permittivity ϵ_f , external magnetic field H , and saturation magnetization M_0 . The dielectric layer number $j = 4$ corresponds to the GGG substrate with parameters L_4 and ϵ_4 .

During simulations, the six parameters, namely, the YIG film thickness δ , the BST film thickness L_2 , the BST permittivity ϵ_2 , the external magnetic field H , the widths of the central electrode h , and the gap w are varied. All the rest parameters are fixed. These are: $\epsilon_f = 14$, $M_0 = 1750 \text{ G}$ ($139.2 \text{ kA} \cdot \text{m}^{-1}$), $L_0 = 0.1 \text{ m}$, $L_1 = L_4 = 500 \mu\text{m}$, $\epsilon_1 = 10$, $\epsilon_4 = 14$, and, finally, the distance between metal walls $d = 0.04 \text{ m}$. Note that values of the parameters L_0 and d were chosen to implement the conditions of the multiferroic coplanar TL structure placed in free space. Further increase of the L_0 and d had no effects on the calculation results but led to increase of N .

Fig. 2 illustrates the dispersion characteristics of the SEW in the regular coplanar TL for various geometries of the electrodes. The spectra were calculated for the following set of the parameters: $L_2 = 2 \mu\text{m}$, $\epsilon_2 = 1500$, $\delta = 10 \mu\text{m}$, and $H = 1350 \text{ Oe}$ ($107.4 \text{ kA} \cdot \text{m}^{-1}$). Black solid lines calculated for $h = 50 \mu\text{m}$ and $w = 50 \mu\text{m}$ in both Fig. 2(a) and (b) represent the reference dependence. Fig. 2(a) shows an effect of width of the gaps w for fixed $h = 50 \mu\text{m}$. Fig. 2(b) shows an effect of the central electrode width h for fixed $w = 50 \mu\text{m}$. A decrease in the w and h shifts the dispersion characteristics toward higher wavenumbers [see Fig. 2(a) and (b), respectively].

On the second stage, we considered electromagnonic crystal produced with periodic variation of the slot width w , as shown in Fig. 3. The two values of the slot width were chosen for the calculations: $w_1 = 25 \mu\text{m}$ and $w_2 = 75 \mu\text{m}$. The dispersion characteristics of the SEW in the regular

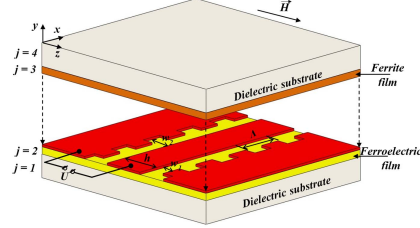


Fig. 3. Electromagnonic crystal based on a coplanar TL with periodic modulation of the slot width.

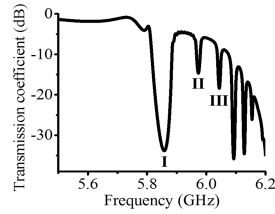


Fig. 4. Transmission characteristic of the electromagnonic crystal containing a coplanar TL.

coplanar TL with w_1 and w_2 are shown in Fig. 2(a) by the red dashed and blue dotted lines, respectively.

In accordance with the transfer-matrix method, a transmission characteristic of the electromagnonic crystal was calculated and shown in Fig. 4. In the calculations, we assumed that the lengths of the segments with narrow w_1 and wide w_2 slots were equal $\Lambda/2$; the period of the electromagnonic crystal was $\Lambda = 1 \text{ mm}$; the number of periods was $T = 10$. The band gaps in the transmission characteristics were formed according to Bragg's diffraction law $k_{\Pi} = n\pi/\Lambda$, where n is a number of a band gap. The first band gap (denoted by I in Fig. 4) of the investigated electromagnonic crystal occurred near 5.86 GHz that corresponded to the wavenumber $k_{\pi} \approx 31.4 \text{ rad/cm}$ on the SEW dispersion characteristic.

As can be seen from Fig. 4, the width of the first band gap measured at a level of 3 dB from the maximum loss of 33 dB is 24.6 MHz. The widths of the high-order band gaps and the distance between them are decreased due to the reduction of group velocity of the SEW for the higher frequencies [see Fig. 2(a)].

The dispersion characteristics of the SEWs and, consequently, the transmission characteristics of the electromagnonic crystal depend on a variety of the parameters, such as the thicknesses of the ferrite or ferroelectric films, and values of the applied magnetic or electric fields. These dependences provide an opportunity to produce the electromagnonic crystal with the desirable rejection efficiency and the required band-gap bandwidth. To demonstrate this, the numerical simulations were carried out for the various thicknesses of the YIG and BST films. (see Figs. 5 and 6, respectively.)

An increase in the ferrite film thickness δ influences on the slope of the spin-wave dispersion branches leading to a shift

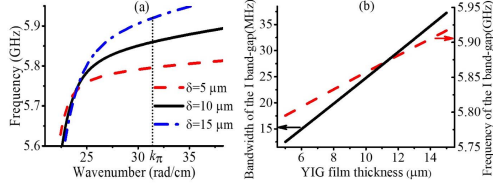


Fig. 5. (a) Spectra of the hybrid SEWs in the regular coplanar TL with slot width $w = 75 \mu\text{m}$ calculated for various YIG thicknesses δ . (b) Influence of the YIG thickness on the bandwidth (black solid line) and frequency (red dashed line) of the first band gap.

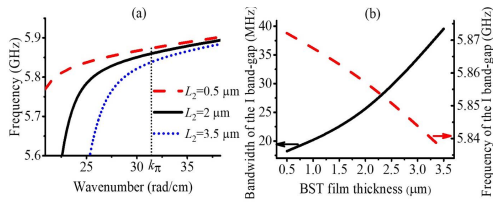


Fig. 6. (a) Spectra of the hybrid SEW in the regular coplanar TL with slot width $w = 75 \mu\text{m}$ calculated for various BST thicknesses L_2 . (b) Influence of the BST thickness on the bandwidth (black solid line) and frequency (red dashed line) of the first band gap.

of the dispersion characteristics and to a drastic change in the SEW group velocity [see Fig. 5(a)]. Thus, for the Bragg wavenumber ($k_{\Pi} = \Pi/\Lambda \approx 31.4 \text{ rad/cm}$) corresponding to the first band gap, the shift of the dispersion characteristics leads to shift of the band gap toward higher frequencies [see red dashed line in Fig. 5(b)]. From the other hand, an increase in the group velocity broadens the band-gap bandwidth [see black solid line in Fig. 5(b)]. A similar effect is achieved when the BST film thickness L_2 is increased [see Fig. 6(a)]. As one can see, an increase in L_2 provides counter-directed effects. While the first band gap is shifted to the lower frequencies [see red dashed line in Fig. 6(b)], its bandwidth increases due to decreasing the SEW group velocity [see black solid line in Fig. 6(b)].

Let us consider now the electric and magnetic tunability of the transmission characteristics. An application of a control voltage U to the coplanar TL electrodes with rectangular modulation leads to a reduction of the ferroelectric film permittivity ϵ_2 and provides an electric tunability. Note that due to different widths of the electromagnonic crystal slots, the electric field is not equal for different segments and is calculated as $E_{1,2} = U/w_{1,2}$. The expression approximating the dependence of the ferroelectric permittivity versus the control voltage U has the form

$$\epsilon_2(E_{1,2}) = \epsilon_2(0) - a \cdot E_{1,2}^2 \quad (2)$$

where the following typical parameters for the BST film are used: $\epsilon_2(0) = 1500$ and $a = 0.194 \text{ cm}^2/\text{kV}^2$ [7].

In particular, an increase in a control voltage provides a shift the band gaps toward higher frequencies. Fig. 7(a) shows

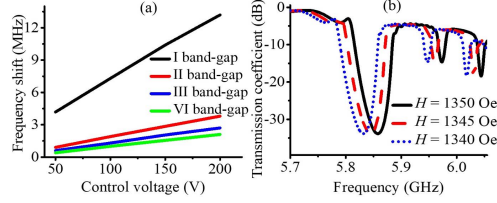


Fig. 7. (a) Electric and (b) magnetic tuning of the transmission characteristics.

a frequency shift of the first four band gaps calculated for the various control voltages up to 200 V. Thus, the electric tuning of the transmission characteristic for the first band gap reaches values of 13.2 MHz for $U = 200 \text{ V}$. Note that the electric tuning range is decreased for the higher band-gap numbers due to a weak interaction of SW and EMW at the frequencies higher than the first band gap.

Turn now to the magnetic tuning role. The transmission characteristics were simulated for different values of the external magnetic field H [see Fig. 7(b)]. The following magnetic fields were used: 1350 Oe (solid line), 1345 Oe (dashed line), and 1340 Oe (dotted line). Fig. 7 shows that an increase in the external magnetic field brings a change in a frequency position of the band gaps due to a shift of the SW spectrum toward higher frequencies.

IV. CONCLUSION

The dispersion relation for the SEWs propagating in the thin-film ferrite-ferroelectric structures based on a coplanar TL has been derived with the method of approximate boundary conditions. Using the developed theory, the dispersion characteristics of SEWs were calculated and analyzed. The multiferroic heterostructure based on the coplanar periodic TL, the electromagnonic crystal, has been proposed and described. It was found that a microwave signal rejection of more than 30 dB appeared at the band-gap frequencies of the electromagnonic crystals. Under a low control voltage, a high-efficient electric tuning was achieved. In particular, an application of the bias voltage of 200 V to the 2 μm-thick ferroelectric film led to the shift of the band gap by 13.2 MHz. All these advantages make the investigated electromagnonic crystals perspective for development of new microwave devices.

ACKNOWLEDGMENT

The work on numerical modeling was supported by the Russian Science Foundation under Grant 14-12-01296P, and the work on development of computer program for numerical simulation was supported by the Ministry of Education and Science of the Russian Federation through the Project "Goszadanie."

REFERENCES

- [1] M. M. Vopson, "Fundamentals of multiferroic materials and their possible applications," *Crit. Rev. Solid State Mater. Sci.*, vol. 40, no. 4, pp. 223–250, Mar. 2015.

- [2] M. Zhu *et al.*, "Advances in magnetics epitaxial multiferroic heterostructures and applications," *IEEE Trans. Magn.*, vol. 53, no. 10, Oct. 2017, Art. no. 0800116.
- [3] V. E. Demidov, B. A. Kalinikos, and P. Edenhofer, "Dipole-exchange theory of hybrid electromagnetic-spin waves in layered film structures," *J. Appl. Phys.*, vol. 91, pp. 10007–10016, May 2002.
- [4] Y. K. Fetisov and G. Srinivasan, "Electrically tunable ferrite-ferroelectric microwave delay lines," *Appl. Phys. Lett.*, vol. 87, no. 10, p. 103502, 2005.
- [5] A. B. Ustinov *et al.*, "Electric field tunable ferrite-ferroelectric hybrid wave microwave resonators: Experiment and theory," *J. Appl. Phys.*, vol. 100, no. 9, p. 093905, 2006.
- [6] M. A. Popov, I. V. Zavislyak, G. Srinivasan, and V. V. Zagorodnii, "Coupled magnetostatic and electromagnetic oscillations in hexaferrite-dielectric heterostructures," *J. Appl. Phys.*, vol. 105, no. 8, p. 083912, Apr. 2009.
- [7] A. B. Ustinov, G. Srinivasan, and B. A. Kalinikos, "Ferrite-ferroelectric hybrid wave phase shifters," *Appl. Phys. Lett.*, vol. 90, no. 3, p. 031913, 2007.
- [8] J. S. Zhang, R. L. Zhang, Q. Hu, R. H. Fan, and R. W. Peng, "Tunable microwave multiband filters based on a waveguide with antiferromagnetic and dielectric sandwiches," *J. Appl. Phys.*, vol. 109, no. 7, p. 07A305, Apr. 2011.
- [9] V. V. Kruglyak, S. O. Demokritov, and D. Grundler, "Magnonics," *J. Phys. D: Appl. Phys.*, vol. 43, no. 26, p. 264001, 2010.
- [10] J. Ding and A. O. Adeyeye, "Binary ferromagnetic nanostructures: Fabrication, static and dynamic properties," *Adv. Funct. Mater.*, v. 23, pp. 1684–1691, Apr. 2013.
- [11] M. Krawczyk and D. Grundler, "Review and prospects of magnonic crystals and devices with reprogrammable band structure," *J. Phys.: Condens. Matter*, vol. 26, no. 12, p. 123202, 2014.
- [12] S. A. Nikitov *et al.*, "Magnonics: A new research area in spintronics and spin wave electronics," *Phys.-Uspekhi*, vol. 58, no. 10, pp. 1002–1028, Jun. 2015.
- [13] A. V. Chumak, A. A. Serga, and B. Hillebrands, "Magnonic crystals for data processing," *J. Phys. D: Appl. Phys.*, vol. 50, p. 244001, May 2017.
- [14] K. Sakoda, *Optical Properties of Photonic Crystals*. Heidelberg, Germany: Springer, 2014.
- [15] A. B. Ustinov and B. A. Kalinikos, "Multiferroic periodic structures based on magnonic crystals for electronically tunable microwave devices," *Tech. Phys. Lett.*, vol. 40, no. 7, pp. 568–570, Jul. 2014.
- [16] A. V. Drozdovskii, A. A. Nikitin, A. B. Ustinov, and B. A. Kalinikos, "Theoretical analysis of microwave properties of ferrite-ferroelectric magnonic crystals," *Tech. Phys.*, vol. 59, no. 7, pp. 1032–1035, Jul. 2014.
- [17] F. Brandl, K. J. A. Franke, T. H. E. Lahtinen, S. van Dijken, and D. Grundler, "Spin waves in CoFeB on ferroelectric domains combining spin mechanics and magnonics," *Solid State Commun.*, vol. 198, pp. 13–17, Nov. 2014.
- [18] M. A. Morozova, S. V. Grishin, A. V. Sadovnikov, D. V. Romanenko, Y. P. Sharaevskii, and S. A. Nikitov, "Tunable bandgaps in layered structure magnonic crystal-ferroelectric," *IEEE Trans. Magn.*, vol. 51, no. 11, Nov. 2015, Art. no. 2802504.
- [19] I. A. Ustinova, A. A. Nikitin, and A. B. Ustinov, "Dynamic magnonic crystal based on a layered ferrite-ferroelectric structure," *Tech. Phys.*, vol. 61, no. 3, pp. 473–476, Mar. 2016.
- [20] M. A. Morozova, O. V. Matveev, Y. P. Sharaevskii, and S. A. Nikitov, "Tuning the bandgaps in a magnonic crystal-ferroelectric-magnonic crystal layered structure," *Phys. Solid State*, vol. 58, pp. 273–279, Feb. 2016.
- [21] W. J. Kim *et al.*, "Electrically and magnetically tunable microwave device using (Ba, Sr) TiO₃/Y₃Fe₅O₁₂ multilayer," *Appl. Phys. A: Solids Surf.*, vol. 71, no. 1, pp. 7–10, Jul. 2000.
- [22] J. H. Leach *et al.*, "Electrically and magnetically tunable phase shifters based on a barium strontium titanate-yttrium iron garnet layered structure," *J. Appl. Phys.*, vol. 108, no. 6, p. 064106, Sep. 2010.
- [23] A. A. Nikitin, A. B. Ustinov, A. A. Semenov, B. A. Kalinikos, and E. Lähderanta, "All-thin-film multilayered multiferroic structures with a slot-line for spin-electromagnetic wave devices," *Appl. Phys. Lett.*, vol. 104, no. 9, p. 093513, 2014.
- [24] I. S. Maksymov, J. Hutomo, D. Nam, and M. Kostylev, "Rigorous numerical study of strong microwave photon-magnon coupling in all-dielectric magnetic multilayers," *J. Appl. Phys.*, vol. 117, no. 19, p. 193909, May 2015.
- [25] A. A. Nikitin *et al.*, "Dispersion characteristics of spin-electromagnetic waves in planar multiferroic structures," *J. Appl. Phys.*, vol. 118, p. 183901, Nov. 2015.
- [26] R. Bodeux, D. Michau, M. Maglione, and M. Josse, "Thin films sputtered from Ba₂NdFeNb₄O₁₅ multiferroic targets on BaFe₁₂O₁₉ coated substrates," *Mater. Res. Bull.*, vol. 81, pp. 49–54, Sep. 2016.
- [27] A. A. Nikitin *et al.*, "Spin-electromagnetic waves in planar multiferroic multilayers," *J. Appl. Phys.*, vol. 122, no. 1, p. 014102, Jul. 2017.
- [28] R. E. Collin, *Field Theory of Guided Waves*. New York, NY, USA: Wiley, 1990.
- [29] D. D. Stancil and A. Prabhakar, *Spin Waves: Theory and Application*. Springer, 2009.
- [30] A. V. Chumak, A. A. Serga, S. Wolff, B. Hillebrands, and M. P. Kostylev, "Design and optimization of one-dimensional ferrite-film based magnonic crystals," *J. Appl. Phys.*, vol. 105, no. 8, p. 083906, Apr. 2009.

Publication IV

Nikitin, A. A., Vitko, V. V., Nikitin, A. A., Ustinov, A. B., and Kalinikos, B. A.
Miniature multiferroic interferometer for voltage-controlled spin-wave logic gates

Reprinted with permission from
PIERS Proceedings
Pp. 1547-1551, 2019
© 2019, IEEE

Miniature Multiferroic Interferometer for Voltage-controlled Spin-wave Logic Gates

A. I. A. Nikitin, V. V. Vitko, An. A. Nikitin, A. B. Ustinov, and B. A. Kalinikos
Saint Petersburg Electrotechnical University “LETI”, St. Petersburg, Russia

Abstract— Novel Mach-Zender-type interferometer based on thin-film multiferroic structure has been proposed and described. The performance of the main element of such device, a tunable phase shifter, has been analysed. The distinctive features of the proposed interferometer are high efficiency and small device area in comparison with other spin-wave logic gates. We expect that our results allow exploiting spin-electromagnetic wave phenomena for enhanced logic functionality and efficient data transfer.

1. INTRODUCTION

An increased research interest for development of the energy efficient miniature computational devices for modern information and communication systems is apparent. In particular, reconfigurable elements are required for logic circuit construction [1]. There exist various platforms including complementary metal-oxide-semiconductor (CMOS) [2], optical [3], molecular [4], and magnonic [5] logic circuits. The latter have recently received a great attention as novel beyond the CMOS platform that promises more efficient mechanism for information processing [6–8]. A general idea of this mechanism is that a spin-wave quantum can be regarded as a state variable instead of charge in conventional electronics [6, 9]. This approach allows one to transmit and process a bit of information by exploiting wave phenomena.

The first spin-wave logic gate was a Mach-Zender type current-controlled interferometer based on a ferromagnetic film [10]. After that, a number of theoretical and experimental work was carried out. For example, a Mach-Zehnder-type spin-wave interferometer for universal logic functions [11], an all-spin logic device with built-in memory [12], a micrometre-scale spin-wave interferometer [13], a logic gate based on a dynamic magnonic crystal [14], a spin-wave majority gate [15] were developed. However, the key issues inherent to the above-mentioned applications are associated with the energetic efficiency and scale of the device area.

In order to solve them, a magnetic waveguide can be replaced by a multiferroic structure, which combines more than one ferroic properties [16]. One of the possible mechanisms providing an interaction between the ferromagnetic and ferroelectric phases is realized through electrodynamic coupling of the spin waves (SW) and electromagnetic waves (EMW). This coupling leads to a formation of spin-electromagnetic waves (SEW) [17, 18] that was experimentally observed for the ferrite-ferroelectric layered structure [19]. It was shown that advantages of the multiferroics in comparison with the ferrites are powered by possibility of an electric-field tuning via control of a ferroelectric permittivity. A great number of theoretical and experimental works in this area were carried out (see, e.g., [20–22] and literature therein). As is seen from these works, multiferroic structures have great success in development of microwave devices.

An application of multiferroics for logic circuits is promising for development of a new class of elements such as magnetoelectric amplifiers [25] or multiferroic interconnects [26]. Also in our recent work [27] we experimentally investigated a principle of operation of a novel logic gate based on multiferroics structure with rather thick ferroelectric layer (200 μm). This limitation was caused by the necessity to provide an effective coupling of the SW and EMW at the microwave frequencies. However, such thickness of the ferroelectric layer leads to high control voltages needed for an effective electric tuning of the SEW spectrum. A further progress of multiferroic logic gates is connected with enhancing the tunability efficiency and decreasing control voltage. In order to release these demands, we propose miniature interferometer based on the thin-film ferrite-ferroelectric-ferrite structure. As it was shown earlier in our previous works [23, 24], these structures open up new perspectives for practical application of thin-film multiferroics at microwave frequencies due to existence of a magneto-dipole interaction between the ferrite films, which is tunable by a control of ferroelectric permittivity.

2. THEORY

A schematic view of a typical Mach-Zehnder interferometer is shown in Fig. 1(a). It represents a bridge circuitry with two branches. The first branch comprises a tunable phase shifter (TPS) based on a thin-film ferrite-ferroelectric-ferrite waveguide. The second branch contains a variable attenuator.

Consider a principle of operation of the TPS. It represents a thin-film multilayered structure consisting of two ferrite layers (2) and (4) separated by a ferroelectric film (3) (see Fig. 1(b)). Yttrium-iron garnet (YIG) films formed on dielectric substrates (1) and magnetized in z -direction were chosen as a ferrite waveguides. We assume that a barium-strontium titanate $\text{Ba}_{0.5}\text{Sr}_{0.5}\text{TiO}_3$ (BST) is ferroelectric, which demonstrates paraelectric phase and isotropic dielectric permittivity on the order of thousands at room temperature [28].

Thin metal electrodes on the both surfaces of the BST film provide a possibility for application of voltage for the reduction of the ferroelectric film permittivity ϵ_3 . The expression approximating the dependence of the ferroelectric permittivity versus the control voltage U is used in the following form [29]:

$$\epsilon_3(U) = \frac{\epsilon_3(0) - \epsilon_3(\infty)}{1 + (U/U_{00})^2} + \epsilon_3(\infty), \quad (1)$$

where $\epsilon_3(0)$ and $\epsilon_3(\infty)$ are ferroelectric film permittivities for zero bias voltage U and for $U \rightarrow \infty$, respectively; $U_{00} = \frac{3}{2} S_{eff} E_n (\frac{\epsilon_{00}}{\epsilon_3(0)})^{3/2}$. Here E_n and ϵ_{00} are phenomenological parameters that depend on Curie temperature, S_{eff} is an effective length of the electric field strength line. For the considered case of a sandwich capacitor, this parameter is approximately equal to the ferroelectric thickness ($S_{eff} \approx L_3$). Note that the thickness of the electrodes is much smaller than the skin depth at the operating frequencies. It means that the electrodes are supposed transparent to the microwave electromagnetic fields and can be neglected in numerical simulations.

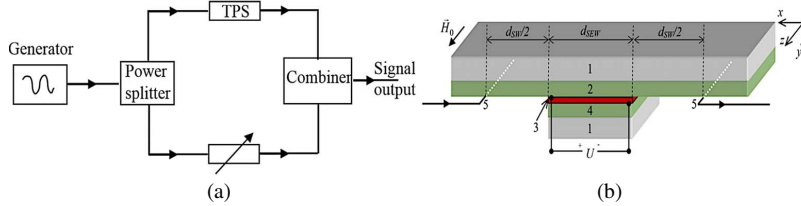


Figure 1: (a) A schematic diagram of the Mach-Zehnder interferometer. (b) Tunable phase shifter based on a thin-film multiferroic structure.

Turn now to the principle of operation of the miniature multiferroic interferometer. A microwave signal is applied to the input and is splitted into two branches, as is shown in Fig. 1(a). In the first branch (see Fig. 1(b)), the microstrip antenna (5) excites a SW in the YIG film (2). After travelling a short distance in this film, the waves enter the multiferroic structure. This is the region where the YIG film (2) is in the contact with the BST-YIG (3)–(4) layered structure. At the border of this region, the SW transforms into the SEW. After passing the layered structure, the SEW propagates through the YIG film (2), where it is transformed back to the SW and is received by the output microstrip antenna. After passing different branches, the signals interfere in the combiner. The power of the output signal can be calculated as follows:

$$P_{out} = P_{out1} + P_{out2} + 2\sqrt{P_{out1}P_{out2}} \cos(\varphi_2 - \varphi_1), \quad (2)$$

where P_{out1} , φ_1 , P_{out2} , and φ_2 are the powers and phase shifts of microwave signals in the branches. The phase shift φ_1 is determined as follows:

$$\varphi_1 = k_{SW}d_{SW} + k_{SEW}d_{SEW} + \varphi_0, \quad (3)$$

where k_{SW} and k_{SEW} are the wavenumbers of the SW and SEW, respectively, d_{SW} and d_{SEW} are the propagation distances (see Fig. 1(b)), and φ_0 is the phase shift in the rest microwave circuit of the first branch, which is assumed to be equal φ_2 . The wavenumbers of the SW were found

according to the well-known dispersion relation for surface spin waves [30]. The wavenumbers of the SEW in the ferrite-ferroelectric-ferrite structures can be obtained according to the theoretical model describing wave processes in thin-film multilayered multiferroics [31].

3. RESULTS AND DISCUSSION

Numerical simulations of the interferometer characteristics were performed using the theoretical model discussed in the previous Section. For the calculations, typical parameters of the experimental multiferroic structures based on YIG and BST films were used. In particular, the distance between the microstrip antennas was 3.75 mm, which was originated from the sum of $d_{SW} = 2.75$ mm and $d_{SEW} = 1$ mm. The thicknesses of the top and the bottom YIG films were $L_2 = 6$ μm and $L_4 = 20$ μm , respectively. These materials had saturation magnetizations of $M_2 = 1713$ G and $M_4 = 1750$ G with dielectric permittivity $\epsilon_2 = \epsilon_4 = 14$. The bias magnetic field H was 1500 Oe. For the BST film the following parameters were used: $L_3 = 1$ μm , $\epsilon_3(0) = 1500$, $E_n = 40$ V/ μm and $\epsilon_{00} = 300$ [29].

This set of parameters was chosen to provide formation of the doubly hybridized SEW spectrum as a result of intersection of the two spin-wave modes in YIG films with the pure electromagnetic mode TE_1 in BST film (see Fig. 2) [24]. The obtained spectrum consists of three dispersion branches. A strong repulsion between all SEW branches is observed due to a strong magneto-dipole interaction between the SW in the ferrite films. As a result, the group velocity of the SEW bottom branch is reduced significantly, that enhances an electric-field tunability of the wavenumbers in a relatively narrow frequency band.

Figure 3(a) demonstrates the SEW bottom branch calculated for $U = 0$ V (solid line) and $U = 6.57$ V (dashed line). One can see that maximum tunability is achieved for the frequencies corresponding to the minimal group velocity.

Figure 3(b) shows the dependence of the phase shift on the frequency by dashed line for $U = 6.57$ V in 1-mm length TPS. The control voltage provides the phase shift of the signal in the first branch of more than 180 degrees.

Figure 3(c) shows the amplitude-frequency characteristic (AFC) of the interferometer for $U = 0$ V (solid line) and $U = 6.57$ V (dashed line). As is seen, one of the maxima in the transmission coefficient profile is observed at the frequency $f_0 = 6.1522$ GHz for zero voltage. The application of

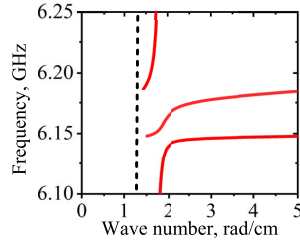


Figure 2: The spectra of the hybrid SEW (solid curves). Dashed line represents the dependence $\omega = ck$, where c is the velocity of light in vacuum.

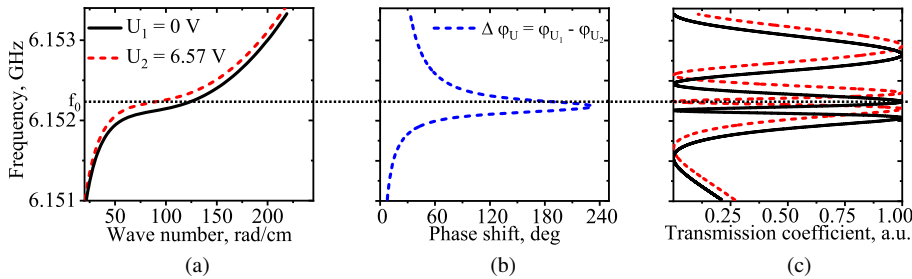


Figure 3: (a) The spectra of the hybrid SEW in the TPS, (b) the phase difference of the interfering signals, and (c) the AFC of the interferometer for different control voltage.

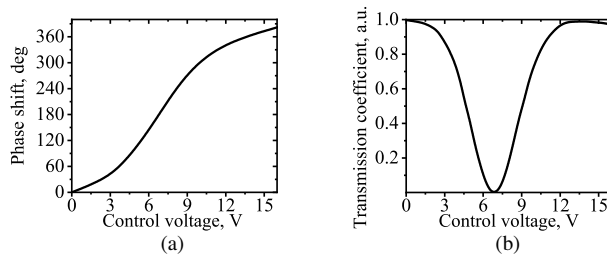


Figure 4: (a) The dependences of the phase difference of the interfering signals and (b) the transmission coefficient of the interferometer on the applied voltage at the fixed frequency $f_0 = 6.1521$ GHz.

6.57 V leads to the phase shift of 180 degrees at the frequency f_0 , which provides the destructive interference of the microwave signals and the minimum signal transmission.

In order to clarify an influence of the control voltage on the performance characteristics of the proposed interferometer, Fig. 4(a) presents the dependence of the phase shift of interfering signals on the applied voltage at the frequency f_0 . It is seen that an increase of the control voltage leads to an increasing in the phase shift. At $U = 13.6$ V the phase shift attains the value of 360 degrees that provides constructive interference and the maximum at the AFC, which is shown in Fig. 4(b).

A possible limitation of the proposed interferometer applications is due to the narrow frequency band, where an effective electric-field tuning is realized. However, the frequency width of this band can be easily tuned through changing the external magnetic field. Thus, a magnetic-field tuning in a range of 500–500 Oe offers an opportunity to realize a highly effective electric tuning for any desirable frequency in a range from 3 to 9 GHz.

4. CONCLUSION

This work shows that the use of the thin-film ferrite-ferroelectric-ferrite structures is promising for miniaturization of the microwave Mach-Zehnder interferometers. In addition, these structures provide a significant reduction in the control voltage down to unities of volts. Therefore, the developed interferometer could find application in spin-wave logic circuits. Note, that the studied device represents the NO logic gate. The use of similar tunable phase shifters in the both interferometer arms allows obtaining XNOR or XOR gates as was shown in [27]. For further reduction in size of the interferometer, the magnetic micro-waveguides (e.g., made of Permalloy) could be used.

ACKNOWLEDGMENT

The work was supported by the Ministry of Education and Science of the Russian Federation through the Project “Goszadanie”.

REFERENCES

1. Hafiz, M. A. A., L. Kosuru, and M. I. Younis, “Microelectromechanical reprogrammable logic device,” *Nat. Commun.*, Vol. 7, 11137, 2016.
2. Ferlet-Cavrois, V., L. W. Massengill, and P. Gouke, “Single event transients in digital CMOS — A review,” *IEEE Trans. Nucl. Sci.*, Vol. 60, No. 3, 1767–1790, 2013.
3. Xu, Q. and R. Soref, “Reconfigurable optical directed-logic circuits using microresonator-based optical switches,” *Opt. Express*, Vol. 19, No. 6, 5244–5259, 2011.
4. Sun, H., J. Ren, and X. Qu., “Carbon nanomaterials and DNA: From molecular recognition to applications,” *Acc. Chem. Res.*, Vol. 49, No. 3, 461–470, 2016.
5. Khitun, A., M. Bao, and K. L. Wang, “Magnonic logic circuits,” *J. Phys. D Appl. Phys.*, Vol. 43, No. 26, 264005, 2010.
6. Khitun, A., M. Bao, and K. L. Wang, “Spin wave magnetic nanofabric: A new approach to spin-based logic circuitry,” *IEEE Trans. Magn.*, Vol. 44, No. 9, 2141–2152, 2008.
7. Chumak, A. V., A. A. Serga, and B. Hillebrands, “Magnon transistor for all-magnon data processing,” *J. Nat. Commun.*, Vol. 5, 4700, 2014.
8. Csaba, G., A. Papp, and W. Porod, “Perspectives of using spin waves for computing and signal processing,” *Phys. Lett. A*, Vol. 381, No. 17, 1471–1476, 2017.

9. Wang, Q., “Voltage-controlled nanoscale reconfigurable magnonic crystal,” *Phys. Rev. B*, Vol. 95, No. 13, 134433, 2017.
10. Kostylev, M. P., et al., “Spin-wave logical gates,” *Appl. Phys. Lett.*, Vol. 87, No. 15, 153501, 2015.
11. Lee, K.-S. and S.-K. Kim, “Conceptual design of spin wave logic gates based on a Mach-Zehnder-type spin wave interferometer for universal logic functions,” *J. Appl. Phys.*, Vol. 104, No. 5, 053909, 2008.
12. Srinivasan, S., et al., “All-spin logic device with inbuilt nonreciprocity,” *IEEE Trans. Magn.*, Vol. 47, No. 10, 4026–4032, 2011.
13. Fischer, T., et al., “Experimental prototype of a spin-wave majority gate,” *Appl. Phys. Lett.*, Vol. 110, No. 15, 152401, 2017.
14. Nikitin, A. A., et al., “A spin-wave logic gate based on a width-modulated dynamic magnonic crystal,” *Appl. Phys. Lett.*, Vol. 106, No. 10, 102405, 2015.
15. Behin-Aein, B., et al., “Proposal for an all-spin logic device with built-in memory,” *Nat. Nanotechnol.*, Vol. 5, No. 4, 266–270, 2010.
16. Vopson, M. M., “Fundamentals of multiferroic materials and their possible applications,” *Crit. Rev. Solid State*, Vol. 40, No. 4, 223–250, 2015.
17. Anfinogenov, V. B., et al., “Hybrid electromagnetic-spin waves in contacting layers of ferrite and ferroelectric,” *Radiotekhnika i Elektronika*, Vol. 34, 494, 1989.
18. Demidov, V. E., B. A. Kalinikos, and P. Edenhofer, “Dipole-exchange theory of hybrid electromagnetic-spin waves in layered film structures,” *J. Appl. Phys.*, Vol. 91, No. 12, 10007–10016, 2002.
19. Anfinogenov, V. B., et al., “Resonant interaction of magnetostatic backward volume waves with slow electromagnetic waves in ferrite-ferroelectric structures,” *Soviet physics. Technical physics*, Vol. 35, No. 9, 1068–1069, 1990.
20. Srinivasan, G., “Magnetoelectric composites,” *Annu. Rev. Mater. Res.*, Vol. 40, 153–178, 2010.
21. Morozova, M. A., et al., “Tuning the bandgaps in a magnonic crystal-ferroelectric-magnonic crystal layered structure,” *Phys. Solid State*, Vol. 58, 273–279, 2016.
22. Zhu, M., et al., “Advances in magnetics epitaxial multiferroic heterostructures and applications,” *IEEE Trans. Magn.*, Vol. 53, No. 10, 1–16, 2017.
23. Vitko, V. V., “Electric-field tuning of spin-electromagnetic wave dispersion in ferrite-ferroelectric multilayers,” *Proc. EuMC*, 1073–1076, Paris, France, September 2015.
24. Nikitin, A. A., et al., “Dual tuning of doubly-hybridized spin-electromagnetic waves in all-thin-film multiferroic multilayers,” *IEEE Trans. Magn.*, Vol. 53, No. 11, 1–5, 2017.
25. Khitun, A., D. E. Nikonov, and K. L. Wang, “Magnetoelectric spin wave amplifier for spin wave logic circuits,” *J. Appl. Phys.*, Vol. 106, No. 12, 123909, 2009.
26. Khitun, A., “Synthetic multiferroic interconnects for magnetic logic circuits,” arXiv preprint arXiv:1309.7399, 2013.
27. Ustinova, I. A., et al., “Logic gates based on multiferroic microwave interferometers,” *Proc. EMCCompo*, 104–107, Russia, Saint-Petersburg, July 2017.
28. Ustinov, A. B., G. Srinivasan, and B. A. Kalinikos, “Ferrite-ferroelectric hybrid wave phase shifters,” *Appl. Phys. Lett.*, Vol. 90, No. 3, 031913, 2007.
29. Vendik, O. G., *Ferroelectrics for Microwave Applications*, Soviet Radio, Moscow, 1979.
30. Stancil, D. D. and A. Prabhakar, *Spin Waves: Theory and Applications*, Springer, New York, 2009.
31. Nikitin, A. A., et al., “Spin-electromagnetic waves in planar multiferroic multilayers,” *J. Appl. Phys.*, Vol. 122, No. 1, 014102, 2017.

Publication V

Frey, P., Nikitin, A. A., Bozhko, D. A., Bunyaev, S. A., Kakazei, G. N., Ustinov, A. B.,
Kalinikos, B. A., Ciubotaru, F., Chumak, A. V., Wang, Q., Tiberkevich, V. S.,
Hillebrands, B., and Serga, A.A.

Reflection-less width-modulated magnonic crystal

Reprinted with permission from
Communications Physics
Vol. 3(1), pp. 1-7, 2020
© 2020, Springer Nature

ARTICLE

<https://doi.org/10.1038/s42005-020-0281-y>

OPEN

Reflection-less width-modulated magnonic crystal

Pascal Frey^{1*}, Aleksei A. Nikitin², Dmytro A. Bozhko^{1,3,4}, Sergey A. Bunyaev⁵, Gleb N. Kakazei⁵, Alexey B. Ustinov², Boris A. Kalinikos², Florin Ciubotaru⁶, Andrii V. Chumak^{1,7}, Qi Wang¹, Vasyi S. Tiberkevich⁸, Burkard Hillebrands¹ & Alexander A. Serga¹

The interest in artificial magnetic media such as magnonic crystals increased substantially in recent years due to their potential applications in information processing at microwave frequencies. The main features of these crystals are the presence of band gaps in the spin-wave spectra, usually formed due to Bragg reflections of spin-waves on the artificially created periodic structures. Here, we study spin-wave propagation in longitudinally magnetized width- and thickness-modulated yttrium iron garnet waveguides by means of Brillouin light scattering and microwave spectroscopy techniques. It is found that the width modulated crystal does not manifest noticeable Bragg reflections, but still demonstrates a pronounced band gap in its transmission characteristic. The phenomenon can be explained by the destructive interference between different frequency-degenerated spin-wave modes excited by the crystal. Such a reflection-less crystal is promising for future design of multi-element magnonic devices.

¹Fachbereich Physik and Landesforschungszentrum OPTIMAS, Technische Universität Kaiserslautern, 67663 Kaiserslautern, Germany. ²Department of Physical Electronics and Technology, St. Petersburg Electrotechnical University, 197376 St. Petersburg, Russia. ³James Watt School of Engineering, University of Glasgow, Glasgow G12 8LT, UK. ⁴Department of Physics and Energy Science, University of Colorado at Colorado Springs, Colorado Springs, CO 80918, USA. ⁵Institute of Physics for Advanced Materials, Nanotechnology and Photonics (IFIMUP)/Departamento de Física e Astronomia, Universidade do Porto, 4169-007 Porto, Portugal. ⁶Imec, 3001 Leuven, Belgium. ⁷Faculty of Physics, University of Vienna, 1090 Wien, Austria. ⁸Department of Physics, Oakland University, Rochester, MI 48309, USA. *email: pfrey@rhrk.uni-kl.de

In recent years, propagation of spin waves (SWs) in ferromagnetic film structures attracts considerable attention in connection with their applications in novel data transfer and processing technologies^{1,2}. This strong research interest is determined by efficient mechanisms of signal transmission based on the general idea that characteristics of SW quanta—magnons—such as their phase and occupation numbers can be regarded as state variables instead of charge in conventional electronics^{3–9}. Among different physical phenomena, which shape the mainstream research directions of magnonics², selective SW propagation is one of the most promising tools for information processing at microwave frequencies^{10–14}. An SW spectrum can be engineered using artificial magnetic media—magnonic crystals (MC)—created by a spatial periodic modulation of a SW-carrying magnetic material¹⁵. These structures have recently received a great attention as promising building blocks of linear and nonlinear magnonics^{10,16–20}. A distinctive feature of MCs is the possibility to design a desired functionality for a given application by variation of the magnon band structure^{10,11}. Magnonic crystals have been successfully utilized for the realization of various microwave devices such as magnon transistors⁴, microwave filters²¹, phase shifters²², SW logic gates²³, magnetic field sensors²⁴, memory cells²⁵, for wavevector-dependent mode selection in SW oscillators²⁶, time reversal²⁷, and other cases.

Magnonic crystals are produced using different types of magnetic materials: metals such as Ni and Co^{28,29}, alloys such as Permalloy (Ni₈₀Fe₂₀)^{28,30–33} and CoFeB^{34,35}, Heusler compounds such as Co₂(Fe_{0.4}Mn_{0.6})Si^{36,37}, and dielectrics like yttrium iron garnet (YIG, Y₃Fe₅O₁₂)^{11,16,18,20–27,38,39}. The main advantages in choosing μm -thick single-crystal YIG films over nm-thick metallic materials such as Permalloy or CoFeB is the small magnetic damping⁴⁰ and higher group velocity of dipolar SWs. These two properties result in a long SW propagation length, which is crucial for future spintronic and magnonic applications. From the technological point of view, MCs based on epitaxially grown YIG films possess essential advantages: (i) small out-of-band insertion losses; (ii) deep rejection bands; (iii) conventional methods of MC production, ranging from metal deposition, chemical etching, ion implantation, or other methods that produce a periodic variation of a given magnetic parameter^{3,11,18,23}. Among various types of YIG-based MCs, geometrically structured MCs produced by modulation of thickness or width of YIG SW waveguides (see Fig. 1) are most promising candidates to gain broad applications due to their high robustness, predictability of characteristics, stability of parameters, and simplicity of fabrication.

Typically, SWs in periodic magnetic structures undergo Bragg scattering, resulting in the formation of spectral regions with prohibited propagation known as SW band gaps by analogy to photonic^{41,42} and phononic^{43,44} crystals. This band formation mechanism has been investigated in detail and is well understood

for a variety of MCs with different physical properties and geometries, including thickness-modulated YIG-based waveguides. At the same time, it was predicted that for some cases band gaps can arise due to peculiarities of the SW excitation mechanisms inside an MC⁴⁵.

In this article, we combine electrical and optical detection of SWs in order to investigate SW propagation in a width-modulated MC (Fig. 1a). We show that transmission characteristics of such a crystal exhibit a single well-pronounced rejection band, which, however, cannot be described in terms of a simple Bragg scattering model. Contrary to a thickness-modulated structure (Fig. 1b), the width-modulated crystal demonstrates no resonant back-scattering of SWs at the central frequency of the band gap. The formation of such unusual rejection band can be associated with destructive interference of different spatial SW components at the MC's output antenna due to phase shifts accumulated in the course of their propagation through the crystal structure.

Results

Experimental set-up. Figure 1a, b shows spatially modulated MCs comprising the longitudinally magnetized periodically structured YIG-film waveguides and attached microstrip antennas serving for inductive excitation and detection of SWs in the GHz frequency range. The magnetization geometry is chosen in a way allowing for the excitation of backward volume magneto-static spin waves (BVMSWs)³⁸ having reciprocal propagation characteristics⁴⁶ and demonstrating high scattering efficiency in thickness-modulated MCs^{47,48}.

The optical access to the YIG film was especially ensured for a two-dimensional mapping of the magnon density distribution by means of space- and time-resolved Brillouin Light Scattering (BLS) spectroscopy^{49,50}. The BLS measurements were performed in backward scattering geometry by placing a dielectric mirror below the samples⁵¹.

The YIG samples were fabricated in the form of 1.9 mm broad stripes cut out from low-damping (ferromagnetic resonance linewidth is about 0.5 Oe at 5 GHz) single-crystal YIG films, epitaxially grown in the (111) crystallographic plane on a gallium gadolinium garnet substrate. The thickness- and width-modulated samples (see Fig. 1) were produced in Kaiserslautern and St. Petersburg, respectively. Conventional photolithographic and chemical etching techniques were used for the patterning in both cases.

For the fabrication of the grooved (thickness-modulated) crystal (see Fig. 1b) a 5.5- μm -thick YIG film was used. The pattern consists of 10 parallel grooves with a width of 50 μm spaced by 250 μm , so that the lattice constant is 300 μm . The grooves were etched to a depth of 1 μm , controlled by a surface profilometer.

The width-modulated sample is 26 mm long and 8.5 μm thick. The length of the rectangular-modulated area in the middle of the stripe is 6 mm (see Fig. 1a). The spatial modulation period and depth are 600 and 400 μm , respectively.

The microwave stripline antennas with a width of 50 μm were placed at distances of about 3 and 4 mm from the left and right ends of the modulated film area, respectively. The antennas were connected to a vector network analyzer (VNA) for continuous wave (CW) measurements. A circuit consisting of a pulsed microwave single frequency generator, a semiconductor detector, and an oscilloscope was utilized for pulse-regime measurements.

Microwave measurements. Figure 2 illustrates the transmission characteristics of the investigated samples measured by VNA. Here, a bias magnetic field of 120 mT for the width-modulated

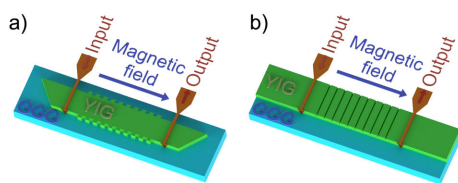


Fig. 1 Sample structures. Sketches of the experimental setups for the width-modulated (a) and thickness-modulated (b) yttrium iron garnet (YIG) structures grown on gadolinium gallium garnet (GGG). The sketches also show orientation of the external magnetic field as well as the excitation and receiving antennas.

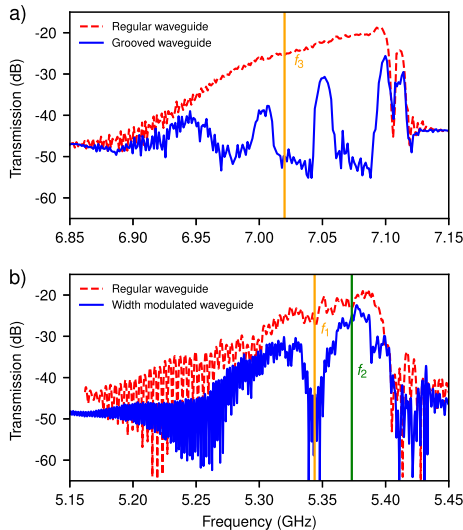


Fig. 2 Transmission spectra in continuous wave regime. Transmission characteristics of the modulated (blue solid line) and regular (red dashed line) waveguides for the grooved crystal (a) and the width-modulated crystal (b). Orange and green lines indicate the frequencies, where the Brillouin light scattering (BLS) measurements are performed: $f_1 = 5.344$ GHz, $f_2 = 5.373$ GHz, and $f_3 = 7.02$ GHz.

and 182 mT for the grooved MCs was applied. The input microwave power was -30 dBm that guaranteed a linear regime of SW propagation.

The blue solid curves in Fig. 2 represent the transmission characteristics of the structured waveguides, while the red dashed lines show, for comparison, the characteristics of similar YIG waveguides without periodic structures. One can clearly identify several frequency regions with different SW dynamics in the transmission characteristic of the periodic waveguides.

For the thickness-modulated crystal (see Fig. 2a), we observe the formation of three magnonic band gaps, where the level of attenuation sharply increases by roughly 20 dB. The width of the central band gap is 10 MHz measured at a level of 6 dB above the maximum loss of -50 dB.

The width-modulated MC shows formation of only one pronounced band gap at the center frequency $f_1 = 5.344$ GHz, which is marked by the orange line in Fig. 2b. The region of enhanced microwave attenuation has a width of 5 MHz measured at a level of 6 dB from the maximum loss of -46.5 dB (in our analysis we neglected the fast oscillations of the transmission characteristics caused by the interference of the SW signal and an electromagnetic wave directly passed from the input to the output antenna). In addition, there are regions around the band gap, where BVMSW modes are transmitted with relatively low attenuation. For example, the frequency $f_2 = 5.373$ GHz with loss level of -25 dB is marked by the green line in Fig. 2b. The frequencies marked in Fig. 2 by vertical lines are chosen for further analysis of the SW dynamics for the different crystals and different propagation regimes.

Brillouin light scattering measurements. In order to reveal the SW dynamics within the crystal structures and to be able to

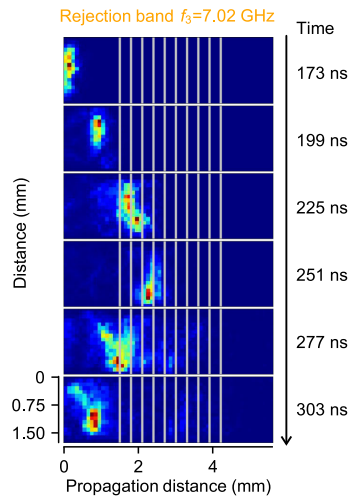


Fig. 3 Timeshots of the spin-wave propagation for the thickness-modulated crystal at the rejection band. Two-dimensional plots of time-resolved spin-wave intensity distributions for carrier frequency $f_3 = 7.02$ GHz in the thickness-modulated magnonic crystal. The positions of the grooves are indicated by gray solid lines.

distinguish between individual responses of different parts of these structures, we performed BLS measurements in a pulsed microwave regime. To this end, we applied 30-ns-long microwave pulses with a power of -10 dBm to the input antennas. Due to the short pulse durations we were able to raise the power of the SW excitation, and thus to increase the signal-to-noise ratio of our optical measurements, without any visible influence from nonlinear SW processes. The repetition rate was 1.5 μ s to avoid any spurious influence through heating effects in the magnetic material.

The used BLS technique allowed us to carry out the study of the magnon density distribution with 25 μ m spatial and 400 ps time resolution. In these measurements, the intensity of the inelastically scattered light is proportional to the magnon occupation number, or, in other words, to the intensity of the SW in the sample.

In Fig. 3, snapshots of the spatial distribution of the SW intensity measured in the central rejection band ($f_3 = 7.02$ GHz) of the grooved structure are shown. The pictures are plotted in a linear color scale, and the SW intensity is normalized in each frame. High SW intensities are indicated as red and low ones as blue. The selected time frames illustrate how the SW packet enters the grooved area, stops due to the Bragg reflection around the fourth groove (grooves are indicated by the vertical gray lines) and gets entirely reflected out of the crystal. The observed behavior perfectly corresponds with the conventional SW dynamics expected in the frame of the Bragg reflection model.

The same measurements were also performed for the width-modulated crystal at the carrier frequencies that correspond to the rejection band ($f_1 = 5.34$ GHz) and pass band ($f_2 = 5.373$ GHz). The resulting snapshots are shown in Fig. 4a for the rejection band frames and in Fig. 4b for the pass band frames. The color scale is the same as in Fig. 3.

The main feature of the measured SW intensity distributions in the width-modulated waveguide is obvious: In contrast to

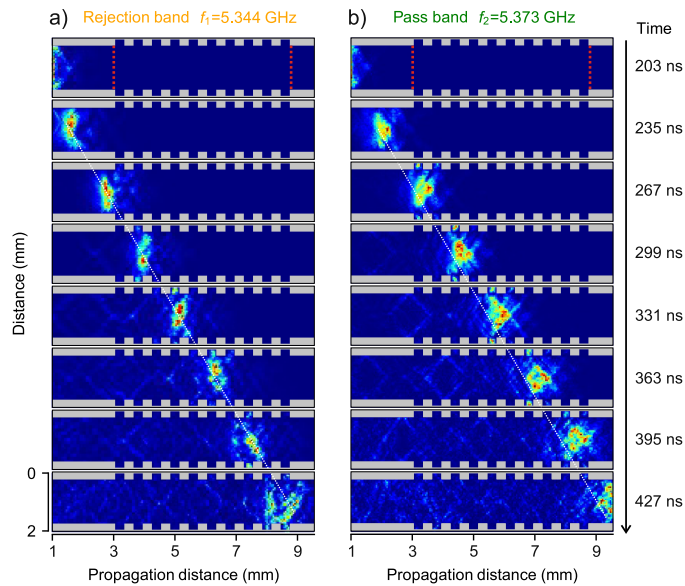


Fig. 4 Timeshots of the spin-wave propagation for the width-modulated crystal in pass and rejection band regime. Two-dimensional plots of the time-resolved spin-wave intensity distributions in periodic width-modulated waveguides for the frequencies $f_1 = 5.34$ GHz (rejection band **(a)**) and $f_2 = 5.373$ GHz (pass band **(b)**). The dotted white lines show the motion of the center of the spin-wave (SW) packet excited within the rejection band. The positions of the input and output microstrip microwave antennas are outside of the measurement area of the sample at 0 and 13 mm. The dashed red lines in the top frames represent the virtual antennas used for later analysis of the SW pulse intensity by comparing a vector network analyzer and Brillouin light scattering measurements.

conventional MCs, this crystal exhibits nearly zero reflected SW intensity within both the rejection and pass bands (see Fig. 4a, b).

In the absence of any visible Bragg reflection, the physical mechanisms responsible for the formation of the rejection band in Fig. 2b might be related to, e.g., some non-resonant or resonant SW decay caused by enhanced magnon–magnon scattering processes in the rejection band frequency range. In order to clarify this issue, the magnon decay was analyzed for both cases presented in Fig. 4. The instantaneous spatial distributions of the measured magnon densities were integrated over a moving window containing the propagating SW packet and over the whole YIG-film region accessible for the BLS probing. The obtained integral data were fitted with an exponential decay function.

It was found that the lifetimes of both SW packets are about 1.6 times shorter than the lifetimes of the secondary magnons (note the spatially structured noise behind the SW packets in Fig. 4a, b) generated due to scattering of these packets from the notched waveguide edges. However, the lifetimes of the SW packets propagating within the rejection and pass bands differ only by 11%, being equal to 73 and 82 ns, respectively. Such a small difference in decay rates cannot explain the observed reduction of the transmitted SW power within the rejection band. The difference in group velocities and, respectively, in the SW propagation times is also rather small (compare the measured positions of the SW packets in Fig. 4): the experimentally determined group velocities are 3.88×10^4 m s⁻¹ in the pass band and 3.65×10^4 m s⁻¹ in the rejection band. Being the same both in the MC and in unstructured parts of the YIG waveguide, these values correspond well with theoretically calculated velocities

of the first width BVMSW mode in a regular 1.9-mm-wide YIG waveguide (3.83×10^4 and 3.65×10^4 m s⁻¹, respectively). Together, the differences in the decay rates and group velocities may account for only two-fold reduction of SW power within the rejection band compared to the pass band, while the experimentally observed reduction exceeds 20 dB (see Fig. 2b).

Comparison of BLS results and pulsed microwave measurements.

For further analysis of the pulsed SW dynamics in the width-modulated MC and for comparison with the microwave signals detected at the output antenna, we used the BLS data shown in Fig. 4 to calculate the dependence of the SW pulse energy (defined as an integral of the magnon density over the waveguide width and magnon arrival time) on the propagation distance. The results of this analysis are presented in Fig. 5. As one can see, the spatial decay of SW pulses within both the pass and rejection bands can be accurately described by a simple exponential function (see solid lines in Fig. 5) with slightly different decay rates. Being extended to the position of the output microwave antenna, these exponential fits provide the estimated two-fold relative decay in the SW pulse within the rejection band compared to the SW pulse within the pass band. At the same time, the experimental microwave measurements of the output pulses demonstrate much stronger (6 times; see data points at 13 mm in Fig. 5) decay. Note that the observed decay of the microwave output from a pulsed 30-ns-long SW signal differs from the decay of CW signals shown in Fig. 2 because of the finite spectral width of the SW pulses used in the experiments. Thus, our experiments clearly demonstrate the substantial difference in

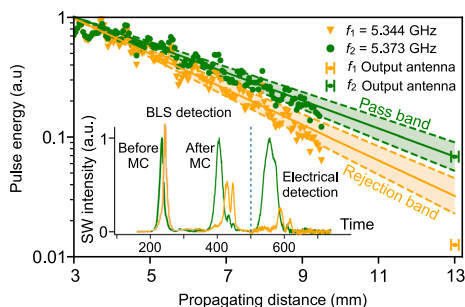


Fig. 5 Spin-wave intensity decay in width-modulated magnonic crystal. The main panel shows the energy of the spin-wave (SW) pulses at different positions along the magnonic crystal (MC). Solid circles and triangles—experimental data as measured by the Brillouin light scattering (BLS) technique; solid lines—exponential fits; the shaded area between the dashed lines indicate the 3-sigma confidence interval of the decay fit parameter. Solid squares at 13 mm correspond to the results of microwave measurements. The errorbars in the x-dimension are given through the measurement scale to 0.1 mm, while the error in y-dimension is given through the noise in the signal, which is too small to be visible in the graph. Inset: Temporal profiles of the SW pulses at the input and output of the MC, as measured by BLS, in comparison with signals measured by the output microwave antenna.

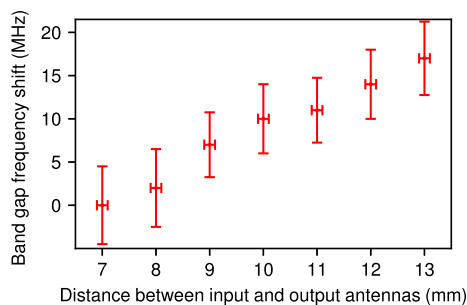


Fig. 6 Band gap frequency shift. Relative shift of the band gap frequency as a function of the distance between the antennas. The error in the band gap shift is estimated as the full-width half-maximum value of the central frequency in the rejection band, while the error of the antenna distance is given through the measurement scale to 0.1 mm.

the output signal power within the MC's rejection band measured by the BLS and microwave techniques.

As a possible nature of this discrepancy we could assume a destructive interference between different components of the SW packet, namely, different frequency-degenerated width and thickness SW modes co-propagating in the waveguide. The role of the width-modulated crystal in this mechanism is to partially transfer the SW energy from the lowest SW modes (which are primarily excited by the input microwave antenna) to highest ones and, also, to introduce additional phase shift between different SW modes. The output microwave antenna integrates the SW amplitude over the waveguide width (e.g., sums different SW components with account of mutual phase relations) and, if the phase relation between different SW modes is destructive, the output microwave signal will be substantially attenuated. At the same time, the spectroscopic BLS measurements are insensitive to the phases of individual SW modes and measure the total SW energy. Thus, this mechanism naturally explains appearance of a rejection band in microwave measurements accompanied by the absence of pronounced reflection or additional damping in the BLS measurements.

The proposed mechanism of reflection-less formation of rejection band lead to one additional unexpected consequence. Thus, higher-order SW modes, created by the MC, propagate in the unstructured portion of the waveguide with slightly different phase velocities. As a result, mutual phase relations between different SW components will change during propagation of the SW pulse and the rejection frequency, measured by the microwave technique, should depend on the position of the output antenna. We have verified this prediction in an additional experiment with movable output antenna, while keeping all other parameters of the microwave measurement system the same. We observed the gradual shift of the central band gap frequency (see orange line in Fig. 2b) up to 17 MHz as a function of the distance between antennas (see Fig. 6). This result strongly supports the proposed mechanism and, also,

provides an additional way to control transmission properties of this type of MCs.

Discussion

Based on the results of the BLS and microwave electric measurements, we have found that the longitudinally magnetized width-modulated MC does not manifest Bragg reflections, but still demonstrates well-pronounced frequency band gaps in the microwave measurements. The formation of such a reflection-less rejection band can be explained by the destructive interference of different frequency-degenerated SW modes excited by the MC. At the same time, our results significantly differ from the results of the experiments and the simulations presented in refs. ^{30,52,53} for micro-sized width-modulated MCs, where the classical Bragg-gaps were clearly observed. And there is a fundamental reason behind it. The MC under consideration in this work is macroscopic. Relatively large width results in a very dense spectrum of width modes, which are separated only by a few MHz. This fact allows direct two-magnon scattering between these modes. This process allows for both backward and forward scattering in relation to the direction of original wave propagation. Since the wavevector difference is also very small, the preferred scattering direction is forward. A number of forward-scattered waves with different phases and group velocities interfere with each other at the output antenna, producing the observed rejection bands without appearance of Bragg reflections. In the case of microscopic MCs the frequency gap between neighboring width modes is very large. Such a spectrum allows only back-scattering, which results in the Bragg-type band gaps.

We believe, that the reflection-less SW propagation is a general property of the macroscopic width-modulated MCs. As we showed above, the appearance of the rejection bands is the result of interference of different width modes. The spectral content of the output SW packet strongly depends on mutual positions of the scattering centers (period of width modulation) as well as on scattering efficiencies. Thus, in general, the number and the depth of the rejection bands should be described by some non-monotonic function of the crystal geometry. Also, rejection band positions of such width-modulated MCs depend strongly on the position of the receiving antenna (see Fig. 6). The detailed study of properties of width-modulated MCs falls outside of the scope of this manuscript. However, we believe that it deserves to be a subject for another research paper and we sincerely hope that our paper will become a trigger for such studies.

From the practical point of view, such a reflection-less artificial crystal looks very promising for cascading of magnonic-crystal-based devices in magnonics circuits due to the significant reduction of back-coupling between the contiguous cascades. The position dependence of the effective rejection frequency can be used for development of simple MC-based frequency multiplexers and demultiplexers.

Data availability

The data that support the findings of this study are available from the corresponding author upon reasonable request.

Received: 8 July 2019; Accepted: 23 December 2019;

Published online: 22 January 2020

References

- Kruglyak, V. V., Demokritov, S. O. & Grundler, D. Magnonics. *J. Phys. D Appl. Phys.* **43**, 264001 (2010).
- Chumak, A. V., Vasyuchka, V. I., Serga, A. A. & Hillebrands, B. Magnon spintronics. *Phys. Rev. Lett.* **109**, 160401 (2012).
- Khitun, A., Bao, M. & Wang, K. L. Spin-wave magnetic nanofabric: a new approach to spin-based logic circuitry. *IEEE Trans. Magn.* **44**, 2141–2152 (2008).
- Chumak, A. V., Serga, A. A. & Hillebrands, B. Magnon transistor for all-magnon data processing. *Nat. Commun.* **5**, 4700 (2014).
- Brächer, T. et al. Phase-to-intensity conversion of magnonic spin currents and application to the design of a majority gate. *Sci. Rep.* **6**, 38235 (2016).
- Csaba, G., Papp, A. & Porod, W. Perspectives of using spin waves for computing and signal processing. *Phys. Lett. A* **381**, 1471–1476 (2017).
- Fischer, T. et al. Experimental prototype of a spin-wave majority gate. *Appl. Phys. Lett.* **110**, 152401 (2017).
- Dobrovolskiy, O. V. et al. Spin-wave phase inverter upon a single nanodefekt. *ACS Appl. Mater. Interfaces* **11**, 17654–17662 (2019).
- Bozhko, D. A. et al. Bogoliubov waves and distant transport of magnon condensate at room temperature. *Nat. Commun.* **10**, 2460 (2019).
- Krawczyk, M. & Grundler, D. Review and prospects of magnonic crystals and devices with reprogrammable band structure. *J. Phys. Condens. Matter* **26**, 123202 (2014).
- Chumak, A. V., Serga, A. A. & Hillebrands, B. Magnonic crystals for data processing. *J. Phys. D Appl. Phys.* **50**, 244001 (2017).
- Heussner, F. et al. Frequency-division multiplexing in magnonic logic networks based on caustic-like spin-wave beams. *Phys. Stat. Sol. RRL* **12**, 1800409 (2018).
- Gieniusz, R. et al. The switching of strong spin wave beams in patterned garnet films. *Sci. Rep.* **7**, 8771 (2017).
- Vogel, M., Hillebrands, B. & von Freymann, G. Spin-wave optical elements: towards spin-wave Fourier optics. Preprint at <https://arxiv.org/abs/1906.02301> (2019).
- Nikitov, S. A., Taihades, P. & Tsai, C. S. Spin waves in periodic magnetic structures—magnonic crystals. *J. Magn. Magn. Mater.* **236**, 320 (2001).
- Ustinov, A. B., Drozdovskii, A. V. & Kalinikos, B. A. Multifunctional nonlinear magnonic devices for microwave signal processing. *Appl. Phys. Lett.* **96**, 142513 (2010).
- Lenk, B., Ulrichs, H., Garbs, F. & Münzenberg, M. The building blocks of magnonics. *Phys. Rep.* **507**, 107 (2011).
- Ustinov, A. B., Kalinikos, B. A., Demidov, V. E. & Demokritov, S. O. Formation of gap solitons in ferromagnetic films with a periodic metal grating. *Phys. Rev. B* **81**, 180406 (2010).
- Liu, X. M., Ding, J., Kakazei, G. N. & Adeyeye, A. O. Magnonic crystals composed of $\text{Ni}_{80}\text{Fe}_{20}$ film on top of $\text{Ni}_{80}\text{Fe}_{20}$ two-dimensional dot array. *Appl. Phys. Lett.* **103**, 062401 (2013).
- Klos, J. W., Krawczyk, M., Dadoenkova, Y. S., Dadoenkova, N. N. & Lyubchanskii, I. L. Photonic-magnonic crystals: multifunctional periodic structures for magnonic and photonic applications. *J. Appl. Phys.* **115**, 174311 (2014).
- Sadovnikov, A. V., Gubanov, V. A., Sheshukova, S. E., Sharaevskii, Y. P. & Nikitov, S. A. Spin-wave drop filter based on asymmetric side-coupled magnonic crystals. *Phys. Rev. Appl.* **9**, 051002 (2018).
- Zhu, Y., Chi, K. H. & Tsai, C. S. Magnonic crystals-based tunable microwave phase shifters. *Appl. Phys. Lett.* **105**, 022411 (2014).
- Nikitin, A. A. et al. A spin-wave logic gate based on a width-modulated dynamic magnonic crystal. *Appl. Phys. Lett.* **106**, 102405 (2015).
- Inoue, M. et al. Investigating the use of magnonic crystals as extremely sensitive magnetic field sensors at room temperature. *Appl. Phys. Lett.* **98**, 132511 (2011).
- Chumak, A. V. et al. Storage-recovery phenomenon in magnonic crystal. *Phys. Rev. Lett.* **108**, 257207 (2012).
- Karenowska, A. D., Chumak, A. V., Serga, A. A., Gregg, J. F. & Hillebrands, B. Magnonic crystal based forced dominant wavenumber selection in a spin-wave active ring. *Appl. Phys. Lett.* **96**, 082505 (2010).
- Chumak, A. V. et al. All-linear time reversal by a dynamic artificial crystal. *Nat. Commun.* **1**, 141 (2010).
- Gubbiotti, G. et al. Brillouin light scattering studies of planar metallic magnonic crystals. *J. Phys. D. Appl. Phys.* **43**, 264003 (2010).
- Mruczkiewicz, M. et al. Spin-wave nonreciprocity and magnonic band structure in a thin permalloy film induced by dynamical coupling with an array of Ni stripes. *Phys. Rev. B* **96**, 104411 (2017).
- Chumak, A. V. et al. Spin-wave propagation in a microstructured magnonic crystal. *Appl. Phys. Lett.* **95**, 262508 (2009).
- Oby, B. et al. A micro-structured ion-implanted magnonic crystal. *Appl. Phys. Lett.* **102**, 202403 (2013).
- Kakazei, G. N., Liu, X. M., Ding, J. & Adeyeye, A. O. $\text{Ni}_{80}\text{Fe}_{20}$ film with periodically modulated thickness as a reconfigurable one-dimensional magnonic crystal. *Appl. Phys. Lett.* **104**, 042403 (2014).
- Dobrovolskiy, O. V. et al. Magnon-fluxon interaction in a ferromagnet/superconductor heterostructure. *Nat. Phys.* **15**, 477 (2019).
- Schwarze, T. & Grundler, D. Magnonic crystal wave guide with large spin-wave propagation velocity in CoFeB. *Appl. Phys. Lett.* **102**, 222412 (2013).
- Mansurova, M. et al. Magnetization dynamics in magnonic structures with different geometries: interfaces, notches and waveguides. *J. Phys. Condens. Matter* **29**, 214001 (2017).
- Mizukami, S. & Serga, A. A. Advancement in Heusler compounds and their spintronics material designs and applications. *J. Phys. D Appl. Phys.* **48**, 160301 (2015).
- Langer, M. et al. Parameter-free determination of the exchange constant in thin films using magnonic patterning. *Appl. Phys. Lett.* **108**, 102402 (2016).
- Serga, A. A., Chumak, A. V. & Hillebrands, B. YIG magnonics. *J. Phys. D Appl. Phys.* **43**, 264002 (2010).
- Langner, T. et al. Spin-wave propagation through a magnonic crystal in a thermal gradient. *J. Phys. D Appl. Phys.* **51**, 344002 (2018).
- Mihalceanu, L. et al. Temperature dependent relaxation of dipolar-exchange magnons in yttrium-iron-garnet films. *Phys. Rev. B* **97**, 214405 (2018).
- Lu, L., Joannopoulos, J. D. & Soljačić, M. Topological photonics. *Nat. Photonics* **8**, 821 (2014).
- Sakoda, K. *Optical Properties of Photonic Crystals* (Springer, Heidelberg, 2014).
- Brun, M., Movchan, A. B. & Jones, I. S. Phononic band gap systems in structural mechanics: finite slender elastic structures and infinite periodic waveguides. *J. Vib. Acoust.* **135**, 041013 (2013).
- Hussein, M. I., Leamy, M. J. & Ruzzene, M. Dynamics of phononic materials and structures: Historical origins, recent progress, and future outlook. *Appl. Mech. Rev.* **66**, 040802 (2014).
- Polushkin, N. I. Forward mode coupling and bandgap formation in magnonic crystals. *Phys. Lett. A* **377**, 2221 (2013).
- Schneider, T., Serga, A. A., Neumann, T., Hillebrands, B. & Kostylev, M. Phase reciprocity of spin-wave excitation by a microstrip antenna. *Phys. Rev. B* **77**, 214411 (2008).
- Chumak, A. V., Serga, A. A., Wolff, S., Hillebrands, B. & Kostylev, M. P. Scattering of surface and volume spin waves in a magnonic crystal. *Appl. Phys. Lett.* **94**, 172511 (2009).
- Mohseni, M. et al. Backscattering immunity of dipole-exchange magnetostatic surface spin waves. *Phys. Rev. Lett.* **122**, 197201 (2019).
- Demokritov, S. O., Hillebrands, B. & Slavin, A. N. Brillouin light scattering studies of confined spin waves: linear and nonlinear confinement. *Phys. Rep.* **348**, 441–489 (2001).
- Sandweg, C. W. et al. Wide-range wavevector selectivity of magnon gases in Brillouin light scattering spectroscopy. *Rev. Sci. Instrum.* **81**, 073902 (2010).
- Bozhko, D. A. et al. Unconventional spin currents in magnetic films. Preprint at <https://arxiv.org/abs/1904.12610> (2019).
- Lee, Ki-Suk, Han, Dong-Soo & Kim, Sang-Koog Physical origin and generic control of magnonic band gaps of dipole-exchange spin waves in width-modulated nanostrip waveguides. *Phys. Rev. Lett.* **v.102**, 127202 (2009).
- Wang, Q. et al. Voltage-controlled nano-scale reconfigurable magnonic crystal. *Phys. Rev. B* **95**, 134433 (2017).

Acknowledgements

The work was supported in part by the Deutsche Forschungsgemeinschaft (DFG) within projects B01 and B04 of the Transregional Collaborative Research Centre (SFB/TRR) 173 “Spin+X”, by the Ministry of Science and Higher Education of the Russian Federation, by the EU Horizon 2020 research, by the ERC Starting Grant 678309 MagnonCircuits and innovation program within the CHIRON project (contract number 801055), by DAAD-FCT project “Spin-wave detection beyond the limit of inductive methods”, and by the grants Nos. EFMA-1641989 and ECCS-1708982 from the NSF of the USA. D. A. Bozhko acknowledges support from the Alexander von Humboldt Foundation. S. A.

Bunyaev and G. N. Kakazei acknowledge the Network of Extreme Conditions Laboratories-NECL and Portuguese Foundation of Science and Technology (FCT) support through Project Nos. NORTE-01-0145-FEDER-022096, POCI-0145-FEDER-030085, and EXPL/IF/00541/2015 (to S.A.B.).

Author contribution

A.A.N. and A.B.U. designed and created the width-modulated sample, while A.V.C. produced the thickness-modulated sample. P.F. performed the experiments on the width-modulated sample in collaboration with A.A.N. and S.A.B. and analyzed the experimental data. F.C. and A.V.C. performed the experiments on the thickness-modulated sample. A.A.S., D.A.B., V.S.T. and Q.W. created the interpretation. P.F., A.A.N. and A.A.S. wrote the paper with contribution from all the authors. A.B.U., A.A.S., G.N.K., B.A.K. and B.H. contributed to the experimental idea, planned, and supervised the project. All authors analyzed the experimental data and discussed the results.

Competing interests

The authors declare no competing interests.

Additional information

Supplementary information is available for this paper at <https://doi.org/10.1038/s42005-020-0281-y>.

Correspondence and requests for materials should be addressed to P.F.

Reprints and permission information is available at <http://www.nature.com/reprints>

Publisher's note Springer Nature remains neutral with regard to jurisdictional claims in published maps and institutional affiliations.



Open Access This article is licensed under a Creative Commons Attribution 4.0 International License, which permits use, sharing, adaptation, distribution and reproduction in any medium or format, as long as you give appropriate credit to the original author(s) and the source, provide a link to the Creative Commons license, and indicate if changes were made. The images or other third party material in this article are included in the article's Creative Commons license, unless indicated otherwise in a credit line to the material. If material is not included in the article's Creative Commons license and your intended use is not permitted by statutory regulation or exceeds the permitted use, you will need to obtain permission directly from the copyright holder. To view a copy of this license, visit <http://creativecommons.org/licenses/by/4.0/>.

© The Author(s) 2020

Publication VI

Nikitin, A. A., Nikitin, A. A., Mylnikov, I. L., Ustinov, A. B., and Kalinikos, B. A.
Electromagnonic crystals based on ferrite-ferroelectric-ferrite multilayers

Reprinted with permission from
IET Microwaves, Antennas & Propagation
Vol. 14(12), pp. 1304-1309, 2020
© 2020, Institution of Engineering and Technology

Electromagnonic crystals based on ferrite–ferroelectric–ferrite multilayers

 ISSN 1751-8725
 Received on 20th February 2020
 Revised 28th May 2020
 Accepted on 22nd June 2020
 E-First on 21st July 2020
 doi: 10.1049/iet-map.2020.0162
 www.ietdl.org

 Aleksei A. Nikitin¹ , Andrey A. Nikitin¹, Ivan L. Mylnikov¹, Alexey B. Ustinov¹, Boris A. Kalinikos¹
¹Department of Physical Electronics and Technology, St. Petersburg Electrotechnical University, St. Petersburg 197376, Russia

✉ E-mail: aleksei.a.nikitin@gmail.com

Abstract: In recent years, the microwave processes in artificial multiferroic media such as electromagnonic crystals have attracted increased research interest due to their potential applications for voltage-controlled spintronic devices. In contrast to the conventional magnonic crystals, the artificially created periodic structures are characterised by electrically and magnetically tunable band gaps in the wave spectrum where the propagation of the electromagnons is forbidden. In this study, an experimental realisation of an electromagnonic crystal based on a ferrite–ferroelectric–ferrite multilayer has been proposed. The authors have demonstrated for the first time a band-gap splitting, which arises from an interaction of three fundamental modes of two ferrite films separated by a ferroelectric layer. This splitting manifested itself as an additional stop-band appearance in the frequency response of the electromagnonic crystal. The obtained band structures are confirmed by numerical modelling using the coupled-mode approach and the transfer-matrix method. The authors expect that their results allow exploiting the electromagnonic crystal for enhanced logic control as well as for tunable microwave devices.

1 Introduction

Artificial magnetic materials with a spatial periodic modulation of their physical properties or geometry, known as magnonic crystals (MCs), are promising for a new microwave and spintronic devices [1–4]. These MCs possess desirable band gaps that appeared due to the Bragg reflection. Among different types of the magnetic materials, the epitaxial yttrium-iron garnet (YIG) films are widely used for MC fabrication due to certain essential advantages: (i) small out-of-band insertion losses; (ii) deep rejection bands; (iii) well-developed techniques of MC fabrication ranging from metal deposition, chemical etching, ion implantation, or other methods to produce a periodical variation of any magnetic parameter. As a result, the MCs are successfully utilised for realisation of the various microwave devices such as power limiters [5], magnetic field sensors [6, 7], microwave oscillators [8, 9], spin-wave logic gates [10], magnon transistors [11] and filters [12].

Further progress in the development of voltage-controlled novel devices can be achieved by fabrication of the layered structures based on MCs [13–25]. In particular, an electrodynamic interaction between high-frequency electromagnetic and spin waves leads to a formation of the hybrid spin-electromagnetic waves (SEWs) in the ferrite–ferroelectric layered structures [26–33]. By analogy to natural multiferroic solids, the quanta of these waves are considered as electro-active magnons or electromagnons. The multiferroic periodical structures, called electromagnonic crystals (EMCs), demonstrate the electrically and magnetically tunable band gaps, where propagation of the electromagnons is forbidden [13, 14, 34–38].

The EMCs are usually fabricated as a combination of a spatially periodic magnetic film with a ferroelectric slab into a layered structure [13]. Advantages of the multiferroic periodic waveguides in comparison with conventional MCs are due to their tunability through an application of the electric field to a ferroelectric layer. Thus, a dynamic EMC demonstrating a voltage-controlled depth of the stop bands has been realised recently [38]. Promising functionalities of this crystal arise from the desired band structure, which originate from a spatial variation of dielectric permittivity of periodically poled regions of a ferroelectric slab by an application of a local electric field. Thin-film multiferroics provide an opportunity for a reduction in the control voltage that is desirable for exploiting the EMC [30, 39–41].

It has been recently shown that the regular waveguides made of the ferrite–ferroelectric–ferrite three-layer structures enrich the properties of multiferroics because of a magneto-dipole interaction between spin-wave modes in the closely spaced ferrite films [30, 42–44]. These structures demonstrate an enhanced voltage-controlled phase shift of SEW [45]. In this work, we report for the first time on an experimental realisation of the three-layer EMC composed of the ferrite–ferroelectric–ferrite spatially periodic structure. We have carried out a theoretical analysis clarifying a mechanism responsible for the band-gap formation in this EMC. To treat the obtained results, we also consider a free-standing MC as well as an EMC composed of the ferrite–ferroelectric bilayer.

2 Design of the EMC

The investigated structure was fabricated in the sandwich-type configuration (see Fig. 1). The bottom ferrite layer was a 3-cm-long and 2-mm-wide stripe made of the 5.5- μm -thick YIG film. The top ferrite layer was the 4-mm-long and 2-mm-wide stripe made of the 13.6- μm -thick YIG film. Each film was epitaxially grown on the single-crystal gallium gadolinium garnet substrates of 500- μm thickness. The YIG films had a ferromagnetic resonance linewidth $\Delta H = 0.5$ Oe at 5 GHz frequency. The saturation magnetisations for the top and bottom YIG films were 1800 and 1930 G at room temperature, respectively. In order to produce MC, the thickness of the bottom YIG film was periodically modulated to a depth of $\delta = 0.8$ μm using the wet chemical etching. The periodic pattern consisted of ten parallel grooves with a width of $L_1 = 50$ μm spaced by $L_2 = 250$ μm , so that the lattice constant was $\Lambda = 300$ μm (see inset in Fig. 1).

A ceramic barium strontium titanate (BST, $\text{Ba}_{0.62}\text{Sr}_{0.38}\text{TiO}_3$) slab, which at room temperature demonstrates a paraelectric phase, was chosen as the intermediate ferroelectric layer. Among various ferroelectrics, BST is considered as one of the most suitable dielectric materials for voltage-controlled microwave devices. It is caused not only by high dielectric permittivity on the order of thousands at room temperature, but also by its low dielectric loss [28]. Moreover, BST solid solutions do not exhibit any dispersion of their dielectric permittivity in a vast frequency range from 10^2 to 10^{11} Hz [46].

The BST layer was fabricated by a conventional mixed oxide route followed by sintering in the air. After that, a hydraulic press

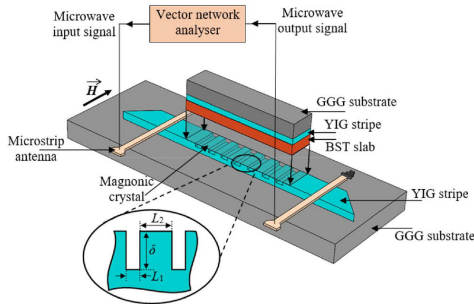


Fig. 1 Scheme of an EMC based on the ferrite-ferroelectric-ferrite multilayer and of the measurement setup used in the experiments

and subsequent annealing formed the BST slab. As a result, the BST slab of a relatively large thickness was produced. Characterisation of the BST slab was performed at the room temperature and indicated the paraelectric nature and isotropic dielectric permittivity of 2300 at 5 GHz frequency. Then, the BST slab was polished down to a thickness of 110 μm . Finally, the slab was cut into the stripes having the in-plane dimensions of $2 \times 4 \text{ mm}^2$.

The MC was positioned in a way that the etched groove side is in contact with the short-circuited microstrip antennas with a width of 50 μm and a length of 2.5 mm. The distance between antennas was 5.5 mm. The BST layer contacted the YIG film top and was pressed symmetrically over the spatial periodic surface of the MC to minimise a thin air gap between the two surfaces. Note that the investigated effect manifests due to the electrodynamic coupling of the electromagnetic fields in the layered structure. As far as the relative magnetic permeability of the ferrites and the relative dielectric permittivity of the ferroelectric significantly exceed unity, a negligibly small intermediate layer of air has no impact on the investigated effect. This was proved previously in work [47]. The total length of the sandwich MC-BST-YIG structure was 4 mm. The composed layered structure was magnetised by a spatially uniform bias magnetic field of 1599 Oe lying in the plane of the structure in parallel to the MC grooves.

Let us consider the principle of wave propagation through the MC-BST-YIG structure. The orientation of the magnetic field in relation to the structure satisfies the condition for excitation of the surface spin wave (SSW). The SSW is excited in the uncovered bottom YIG film stripe by the input microstrip antenna. At the border, where the YIG film is in contact with the BST-YIG bilayer, the SSW transforms into SEW, which then propagates in the layered structure and achieves the EMC region (see Fig. 1). The SEW passes through the periodically modulated waveguide structure and transforms back to the SSW at the output boundary of the layered structure. After that, the SSW is received by the output microstrip antenna. The microstrip antennas were fed by the microstrip transmission lines of 50- Ω characteristic impedance. A vector network analyser measured the transmission characteristics of the structure.

3 Theoretical model of the EMC

The numerical simulation of the band structures of the EMCs was carried out in several stages. In the first stage, the dispersion relations for the waves propagating in the spatially periodic waveguides were obtained by a coupled-mode approach [48]. In this approach, a variation of the ferrite film thickness representing a periodical sequence of sections of the regular transmission lines is considered as a perturbation that leads to the coupling and exchange of power among the guided modes. The resulting dispersion relation for the periodic structure can be calculated by the formula

$$\cos(K\Lambda) = \cos(k_1 L_1) \cos(k_2 L_2) - \frac{k_1^2 + k_2^2}{2k_1 k_2} \sin(k_1 L_1) \sin(k_2 L_2), \quad (1)$$

where K is the Bloch wave-vector; Λ is the period being the sum of the groove width (L_1) and the groove-to-groove distance (L_2); and k_1 and k_2 are the wave-numbers of the SSWs or SEWs in the unstructured film with different thickness. Note that the SSW wave-numbers for free-standing MC can be found according to the well-known dispersion relation [49]. At the same time, the wave-numbers of the SEW in MC-BST and MC-BST-YIG structures can be obtained by means of the theoretical model for wave processes in the thin-film multilayered multiferroics [33]. To consider the propagation losses of the waves in the MC-BST-YIG different sections, the elements of the permeability tensors and permittivities of each layer are taken as complex quantities. As a result, the complex dispersion relations $\omega(k_i + j\alpha_i)$ are obtained, where α_i is the spatial damping decrement of the wave in the section with the number i .

In the second stage, the transmission characteristics of the periodic structure are calculated according to the transfer-matrix method. This method allows one to calculate the transmission characteristics of a finite-length periodic waveguide. According to the transfer-matrix method, both wave propagation in an unstructured ferrite film and reflections from the junctions of the consecutive sections are described by the T -matrices:

(i) Matrix T_1 describes the propagation of the waves in the thick unstructured ferrite film and has the following form:

$$T_1(\omega) = \begin{bmatrix} \exp[-(jk_1 + \alpha_1)L_1] & 0 \\ 0 & 1/\exp[-(jk_1 + \alpha_1)L_1] \end{bmatrix} \quad (2)$$

(ii) Matrix T_2 describes the reflections of the waves for the front edge of the grooved film and can be calculated by the formula:

$$T_2(\omega) = \begin{bmatrix} 1/(1-G) & G/(1-G) \\ G/(1-G) & 1/(1-G) \end{bmatrix}, \quad (3)$$

where $G = (k_1 - k_2)/(k_1 + k_2)$ is the rejection coefficient at the junction of the wider-to-narrower waveguide.

(iii) Matrix T_3 describes the propagation of the waves in the thin unstructured ferrite film and has the following form:

$$T_3(\omega) = \begin{bmatrix} \exp[-(jk_2 + \alpha_2)L_2] & 0 \\ 0 & 1/\exp[-(jk_2 + \alpha_2)L_2] \end{bmatrix} \quad (4)$$

(iv) Matrix T_4 describes the reflections of the waves from the rear edge of the grooved film and can be calculated by the formula:

$$T_4(\omega) = \begin{bmatrix} 1/(1+G) & -G/(1+G) \\ -G/(1+G) & 1/(1+G) \end{bmatrix}. \quad (5)$$

The final transfer matrix for the thickness-modulated ferrite film with N periods is obtained by multiplying all T -matrices describing the propagation of the wave within each period:

$$T_\Sigma(\omega) = (T_1 \times T_2 \times T_3 \times T_4)^N. \quad (6)$$

According to the proposed theoretical model, the complex transfer function for the spatially periodic structure was obtained as $1/T_\Sigma(\omega)_{1,1}$. Thus, the power transmission characteristic of the periodic structure has the following form:

$$S_{21}(\omega) = 20 \cdot \log_{10}(1/|T_\Sigma(\omega)_{1,1}|). \quad (7)$$

4 Experimental and theoretical results

In this section, the microwave measurements and numerical simulations of the transmission characteristics of the spatially periodic structures are presented. In order to clarify the band

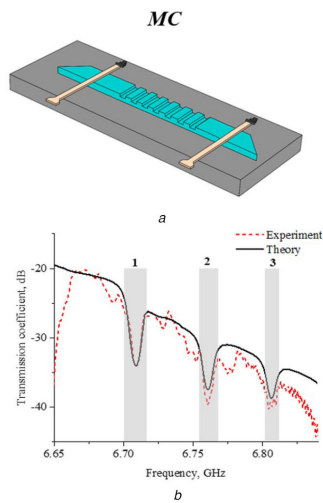


Fig. 2 Numerical analysis of the transmission characteristics for MC
(a) The sketch of the thickness-modulated MC, (b) The theoretical (black solid line) and experimental (red dashed line) transmission characteristics of the MC

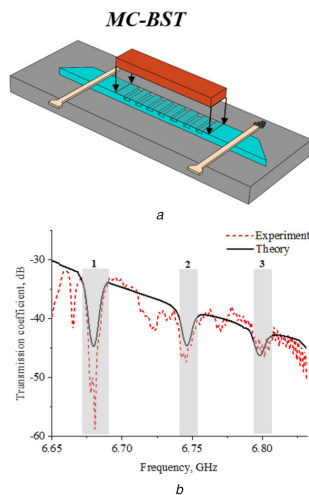


Fig. 3 Numerical analysis of the transmission characteristics for bilayer EMC
(a) The sketch of the EMC consisting of the MC-BST bilayer, (b) The theoretical (black solid line) and experimental (red dashed line) transmission characteristics of the EMC

structure of the proposed three-layer EMC, three types of waveguiding structures were investigated. The first one was the free-standing bottom MC without the BST-YIG bilayer (see Fig. 2a). The second one was the EMC consisting of the MC-BST bilayer (see Fig. 3a), i.e. the BST layer was added to the bottom MC. The third one was the EMC composed of the complete MC-BST-YIG multilayer (Fig. 4a). The first and the second waveguiding structures are discussed in detail [5–14, 34–38] while the third one was not investigated. The experimental and theoretical investigations of transmission characteristics of the third waveguiding structure validate the mechanism of the band structure formation when compared with other structures.

The transmission characteristics of the proposed structures are presented in Figs. 2–4 and can be summarised as follows. The black solid line in Fig. 2b shows the calculated transmission characteristic obtained with the proposed theoretical model [see (7)] for the free-standing MC. As is seen, the band-gaps 1, 2, and 3 (the shaded grey areas in Fig. 2b) are formed at the frequencies expected from the conventional Bragg analysis. Moreover, the formation of these band gaps is in good agreement with the experimental data presented by the red dashed line in Fig. 2b. A small deviation of the experimental dependences from the theoretical ones could be explained by different parasitic effects such as small reflections from the film edges or weak random inhomogeneity in the waveguiding structure that usually exists in experiments.

For the case of the EMC consisting of the MC-BST bilayer, the band structure is modified. As is seen from Fig. 3b, the band gaps demonstrate a down-frequency shift in comparison with the band structure of the free-standing MC. This behaviour of the transmission characteristic will be explained in detail in the next section. The theoretically obtained transmission characteristic is shown in Fig. 3b by the solid black line and the experimental one by the dashed red line. It is easy to see that the frequency positions of the measured and calculated band gaps 1, 2, and 3 (the shaded grey areas in Fig. 3b) coincide with a high accuracy.

The transmission coefficient of the complete EMC is shown in Fig. 4b. Here, the solid black line represents the calculated transmission characteristic, while the dashed red line shows the measured data. Initially, the constituting characteristics were found separately for the waves propagating as fundamental modes existing in each ferrite film. The resulting transmission characteristic was calculated as a superposition of the two interfering waves.

In contrast to the previous configurations, the band structure of the EMC composed of the MC-BST-YIG multilayer is more complicated. According to the Bragg resonance condition, the first band gap 1A should be observed at 6.6 GHz, which is less than the cutoff frequency of the SSW for the bottom YIG film. As a result, this band gap lies outside of the wave spectrum and cannot be observed. The first visible band gap appeared near the 6.664 GHz frequency in region 1B (see the shaded grey area in Fig. 4b). In addition, one can clearly see the formation of the two closely spaced band gaps 2A and 2B corresponding to the region of the second Bragg resonance.

5 Discussion

In order to identify the band gaps observed in the previous section and to understand the physical reasons for their formation, we carried out a detailed theoretical analysis of the dispersion characteristics of the periodic structures under investigation. The numerical simulations were based on the solution of (1). The validity of this approach is based on the following point. The dispersion characteristics are uniquely related to the transfer function. While the real part of the wave-number defines the phase shift of the wave in the waveguiding structure, the imaginary part describes losses. Thus, the frequency ranges, wherein the roots of (1) are real, correspond to the passbands while complex roots correspond to the band gaps. The application of the dispersion characteristics for the description of the transmission characteristics benefits for a visualisation of the transformation of the wave spectrum in both MC and EMC structures.

Let us briefly outline the spin-wave spectrum for the free-standing MC (see Fig. 5a) that later would be helpful for a clarification of the band structure for the layered EMCs. As is seen, the band structure of the thickness-modulated ferrite film is well defined. Interaction among the waves in the periodical sequence of the MC sections leads to the formation of the magnonic band gaps 1, 2, and 3 (see insets in Fig. 5a) at wave-numbers corresponding to the Bragg reflection law $K_{Bn} = n\pi/\Lambda$, where n is a band-gap number.

Note that the real band gap with a finite frequency jump at the border of the Brillouin zone can be formed only in an idealistic loss-less artificial crystal. In a real-life lossy case, the dispersion

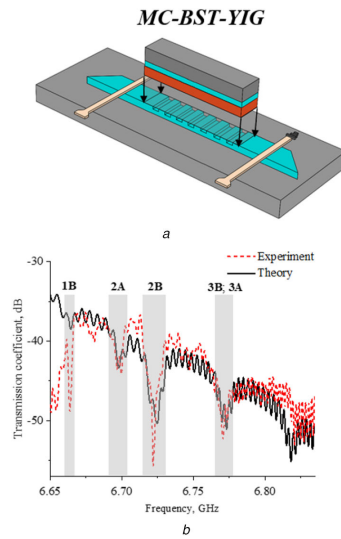


Fig. 4 Numerical analysis of the transmission characteristics for multilayer EMC (a) The sketch of the EMC consisting of the MC-BST-YIG multilayer, (b) The theoretical (black solid line) and experimental (red dashed line) transmission characteristics of the EMC

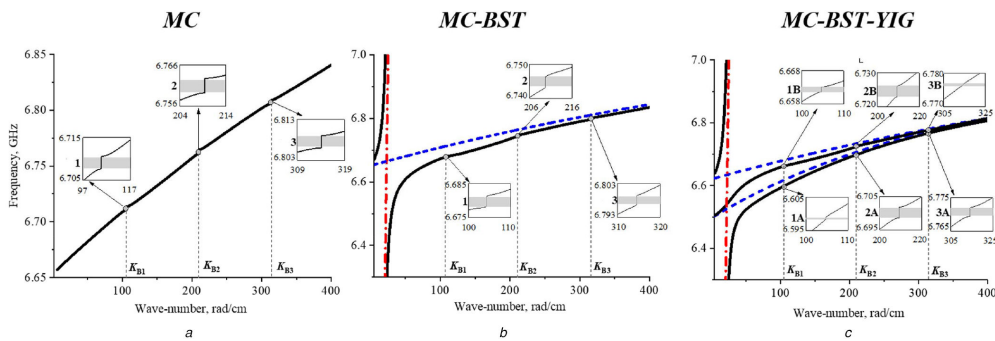


Fig. 5 Numerical analysis of the dispersion for different configurations of the structures under investigation (a) The spectrum of the spin waves in the MC. Insets here and below show peculiarities of the wave dispersion in the vicinity of the band gaps, (b) The spectrum of the SEWs in the bilayer EMC. Dashed and dashed-dotted lines here and below represent the pure SSW and electromagnetic mode dispersion characteristics, respectively, (c) The spectrum of the SEWs in the multilayer EMC

characteristics remain continuous and zones of band gaps are characterised by a steeper slope, which result in a local change in the SEW group velocity [38].

Further, we will consider the EMC composed of the MC-BST bilayer. The dispersion characteristic calculated for this structure is shown in Fig. 5b. Here the coupled excitation of SSW mode (blue dashed line) and electromagnetic mode TE_1 (red dashed-dotted line) leads to the SEW formation (see the black solid line in Fig. 5b). The spectrum of this wave consists of two dispersion branches. The band-gap positions are determined by the lower dispersion branch. As one can see, the electromagnonic band structure demonstrates a down-frequency shift in comparison to the magnonic one. This phenomenon is caused by a strong repulsion between SEW branches, which manifests itself around the point of crossing of the pure electromagnetic TE_1 and SSW modes (see Fig. 5b). For example, the frequency shift of the first electromagnonic band gap in comparison to the magnonic one is about 28 MHz. This difference is reduced for the high-order band

gaps due to a decrease in the coupling between the magnons and microwave photons.

Fig. 5c shows the dispersion characteristics of the SEWs in the EMC composed of the MC-BST-YIG multilayer. It is clearly visible that the wave spectrum in the frequency range under investigation consists of three dispersion branches that are referred to as the lower, middle, and upper ones (see the black solid lines in Fig. 5c). Such a spectrum is formed due to the electrodynamic interaction among the electromagnetic mode TE_1 (red dashed-dotted line) and two SSW modes (blue dashed lines) as well as due to the magneto-dipole interaction between these SSW modes. Due to these interactions, the SEW middle branch is clamped between the upper and lower spin-wave modes. It provides the existence of two closely spaced dispersion branches, which manifests itself as a formation of additional band gap corresponding to the fixed Bragg wave-number. Therefore, in contrast to the MC and MC-BST structures, the appearance of an additional stop-band in the transmission characteristic of the three-layer EMC is observed (see Fig. 4b). For example, the first band gap at $K_{B1} = 104.72$ rad/cm is

split into two rejection regions **1A** and **1B** (shaded grey areas in insets of Fig. 5c). The same behaviour is observed for the higher order band gaps at K_{B2} and K_{B3} . For the considered geometry, the frequency distance between the band gaps satisfying the same Bragg condition is reduced with increasing the wave-number. Thus, the frequency difference between the band gaps **1A** and **1B** is 63 MHz; **2A** and **2B** it is 27 MHz; **3A** and **3B** it is 9 MHz. According to the SEW spectrum, the higher order band gaps almost coincide due to a decrease in the frequency difference among them.

As was already mentioned in the Introduction, the regular waveguides based on the ferrite–ferroelectric–ferrite three-layer structure demonstrate an enhanced voltage-controlled phase shift of SEW. Thereby, it would be beneficial from a practical point of view to estimate the band gap tuning ranges for the three-layer EMC. Electric field tunability of a band structure of this waveguide exists due to variation of the dielectric permittivity of ferroelectric layer. An electric field of 1.74 V/ μ m value applied to the BST layer decreases its dielectric permittivity by 1.7 times. Note that a rather thick BST slab with a thickness of 110 μ m was used in the proposed EMCs. Therefore, the above-mentioned variation of the BST permittivity requires the application of electrical voltage up to 191.4 V. According to the estimations, such a voltage provides an electric tuning of the electromagnonic band gaps **1B**, **2A**, **2B**, and **3A(3B)** up to 4.03, 2.36, 1.53, and 1.07 MHz, respectively. As one can see, an efficient electric tuning for these structures is achieved for the first band gap where the strong coupling between the magnons and microwave photons is observed.

6 Conclusion

We have described and analysed the mechanism of formation of the electromagnonic band structure in the ferrite–ferroelectric–ferrite periodic waveguides. It has been shown that utilisation of the two coupled ferromagnetic films separated by a ferroelectric layer opens up a possibility to extend the functionality of conventional MCs. Based on the proposed theoretical model, we have demonstrated for the first time the mechanism of electromagnonic band gap splitting due to the magneto-dipole interaction between the spin-wave modes. This phenomenon is caused by the interaction of the three fundamental modes corresponding to each layer composing the EMC. Following the nature of the Bragg resonance, a spatially periodic modulation of the waveguide properties determines a set of the wave-number values, which defines the band-gap positions in accordance with the dispersion properties. Closely spaced dispersion branches allow for an appearance of additional band gaps in the spectrum of the waves propagating in the multilayered EMC.

Our estimates show that exploiting the hybrid SEWs in the proposed periodic structures allows one to obtain the well-pronounced electric field tuning of the band-gap positions via control of the ferroelectric layer dielectric parameters. A further reduction in the control voltage can be achieved by utilising the all-thin-film ferrite–ferroelectric–ferrite structures. As was shown in our previous work, the efficiency of electric tuning of wave spectra in such structures is increased by reducing the thickness of the intermediate ferroelectric layer [33], as well as by employing the phenomenon of the double hybridisation of the pure electromagnetic mode and two pure surface spin-wave modes [42].

The proposed EMCs offer promising technological features, such as small size and low-energy consumption. In addition, these crystals are compatible with conventional spintronic devices enabling efficient data transfer and enhanced logic functionality. As a result, the considered crystals look favourable for not only investigations of the new physical phenomena but also for the applications as a complimentary part to the traditional approach for general computing and microwave signal processing.

7 Acknowledgments

This work was supported in part by the Ministry of Science and Higher Education of the Russian Federation (Project ‘Goszadanie’).

8 References

- [1] Krawczyk, M., Grundler, D.: ‘Review and prospects of magnonic crystals and devices with reprogrammable band structure’, *J. Phys. Condens. Matter*, 2014, **26**, p. 123202
- [2] Chumak, A.V., Serga, A.A., Hillebrands, B.: ‘Magnonic crystals for data processing’, *J. Phys. D*, 2017, **50**, (24), p. 244001
- [3] Csaba, G., Papp, A., Porod, W.: ‘Perspectives of using spin waves for computing and signal processing’, *Phys. Lett. A*, 2017, **381**, (17), pp. 1471–1476
- [4] Zingsem, B.W., Feggeler, T., Terwey, A., *et al.*: ‘Biologically encoded magnonics’, *Nat. Commun.*, 2019, **10**, (1), pp. 1–8
- [5] Ustinov, A.B., Drozdovskii, A.V., Kalinikos, B.A.: ‘Multifunctional nonlinear magnonic devices for microwave signal processing’, *Appl. Phys. Lett.*, 2010, **96**, (14), p. 142513
- [6] Inoue, M., Baryshev, A., Takagi, H., *et al.*: ‘Investigating the use of magnonic crystals as extremely sensitive magnetic field sensors at room temperature’, *Appl. Phys. Lett.*, 2011, **98**, (13), p. 132511
- [7] Atalay, S., Kaya, A.O., Kolat, V.S., *et al.*: ‘One-dimensional magnonic crystal for magnetic field sensing’, *J. Supercond. Novel. Magn.*, 2015, **28**, (7), pp. 2071–2075
- [8] Grishin, S.V., Beginin, E.N., Morozova, M.A., *et al.*: ‘Self-generation of parametric soliton-like pulses in a magnonic quasi-crystal active ring resonator’, *IEEE Trans. Magn.*, 2014, **50**, (11), pp. 1–4
- [9] Bankowski, E., Meitzler, T., Khymyn, R.S., *et al.*: ‘Magnonic crystal as a delay line for low-noise auto-oscillators’, *Appl. Phys. Lett.*, 2015, **107**, (12), p. 122409
- [10] Nikitin, A.A., Ustinov, A.B., Semenov, A.A., *et al.*: ‘A spin-wave logic gate based on a width-modulated dynamic magnonic crystal’, *Appl. Phys. Lett.*, 2015, **106**, (10), p. 102405
- [11] Chumak, A.V., Serga, A.A., Hillebrands, B.: ‘Magnon transistor for all-magnon data processing’, *Nat. Commun.*, 2014, **5**, (1), pp. 1–8
- [12] Frey, P., Nikitin, A.A., Bozhko, D.A., *et al.*: ‘Reflection-less width-modulated magnonic crystal’, *Commun. Phys.*, 2020, **3**, p. 17
- [13] Ustinov, A.B., Kalinikos, B.A.: ‘Multiferroic periodic structures based on magnonic crystals for electronically tunable microwave devices’, *Tech. Phys. Lett.*, 2014, **40**, (7), pp. 568–570
- [14] Morozova, M.A., Sharaevskii, Y.P., Nikitov, S.A.: ‘Tunable band gaps in a layered structure magnonic crystal-ferroelectric’, *J. Commun. Technol. Electron.*, 2014, **59**, (5), pp. 467–473
- [15] Yang, Q., Zhou, Z., Sun, N.X., *et al.*: ‘Perspectives of voltage control for magnetic exchange bias in multiferroic heterostructures’, *Phys. Lett. A*, 2017, **381**, (14), pp. 1213–1222
- [16] Wang, Q., Chumak, A.V., Jin, L., *et al.*: ‘Voltage-controlled nanoscale reconfigurable magnonic crystal’, *Phys. Rev. B*, 2017, **95**, (13), p. 134433
- [17] Sietsema, G., Liu, T., Flatté, M.E.: ‘Electric-field control of magnon gaps in a ferromagnet using a spatially-periodic electric field’, *Spin*, 2017, **7**, (3), p. 1740012
- [18] Yang, Q., Nan, T., Zhang, Y., *et al.*: ‘Voltage control of perpendicular magnetic anisotropy in multiferroic (Co/Pt)₃/PbMg_{1/3}Nb_{2/3}O₃-PbTiO₃ heterostructures’, *Phys. Rev. Appl.*, 2017, **8**, (4), p. 044006
- [19] Hämäläinen, S.J., Brandl, F., Franke, K.J., *et al.*: ‘Tunable short-wavelength spin-wave emission and confinement in anisotropy-modulated multiferroic heterostructures’, *Phys. Rev. Appl.*, 2017, **8**, (1), p. 014020
- [20] Zhu, M., Zhou, Z., Xue, X., *et al.*: ‘Voltage control of spin wave resonance in La_{0.5}Sr_{0.5}MnO₃/PMN-PT (001) multiferroic heterostructures’, *Appl. Phys. Lett.*, 2017, **111**, (10), p. 102903
- [21] Kryshal, R.G., Medved, A.V.: ‘Influence of magnetic anisotropy on dynamic magnonic crystals created by surface acoustic waves in yttrium iron garnet films’, *J. Magn. Magn. Mater.*, 2017, **426**, pp. 666–669, p. 102903
- [22] Bukharaev, A.A., Zvezdin, A.K., Pyatakov, A.P., *et al.*: ‘Straintronics: a new trend in micro-and nanoelectronics and materials science’, *Phys.-Usp.*, 2018, **61**, (12), p. 1175
- [23] Rana, B., Otani, Y.: ‘Voltage-controlled reconfigurable spin-wave nanochannels and logic devices’, *Phys. Rev. Appl.*, 2018, **9**, (1), p. 014033
- [24] Zhao, X., Hu, Z., Yang, Q., *et al.*: ‘Voltage control of ferromagnetic resonance and spin waves’, *Chin. Phys. B*, 2018, **27**, (9), p. 097505
- [25] Vysotskii, S.L., Pavlov, E.S., Kozhevnikov, A.V., *et al.*: ‘Self-action effects in the propagation of surface magnetostatic wave pulses in a magnonic crystal–dielectric–metal structure’, *Tech. Phys.*, 2019, **64**, (11), pp. 1629–1635
- [26] Demidov, V.E., Kalinikos, B.A., Edenhofer, P.: ‘Dipole-exchange theory of hybrid electromagnetic-spin waves in layered film structures’, *J. Appl. Phys.*, 2002, **91**, (12), pp. 10007–10016
- [27] Ustinov, A.B., Tiberkevich, V.S., Srinivasan, G., *et al.*: ‘Electric field tunable ferrite-ferroelectric hybrid wave microwave resonators: experiment and theory’, *J. Appl. Phys.*, 2006, **100**, (9), p. 093905
- [28] Ustinov, A.B., Srinivasan, G., Kalinikos, B.A.: ‘Ferrite-ferroelectric hybrid wave phase shifters’, *Appl. Phys. Lett.*, 2007, **90**, (3), p. 031913
- [29] Leach, J.H., Liu, H., Avrutin, V., *et al.*: ‘Electrically and magnetically tunable phase shifters based on a barium strontium titanate-yttrium iron garnet layered structure’, *J. Appl. Phys.*, 2010, **108**, (6), p. 064106
- [30] Nikitin, A.A., Ustinov, A.B., Semenov, A.A., *et al.*: ‘All-thin-film multilayered multiferroic structures with a slot-line for spin-electromagnetic wave devices’, *Appl. Phys. Lett.*, 2014, **104**, (9), p. 093513
- [31] Maksymov, I.S., Hutomo, J., Nam, D., *et al.*: ‘Rigorous numerical study of strong microwave photon-magnon coupling in all-dielectric magnetic multilayers’, *J. Appl. Phys.*, 2015, **117**, (19), p. 193909
- [32] Nikitin, A. A., Ustinov, A. B., Vitko, V. V., *et al.*: ‘Dispersion characteristics of spin-electromagnetic waves in planar multiferroic structures’, *J. Appl. Phys.*, 2015, **118**, (18), p. 183901

- [33] Nikitin, A.A., Ustinov, A.B., Vitko, V.V., *et al.*: 'Spin-electromagnetic waves in planar multiferroic multilayers', *J. Appl. Phys.*, 2017, **122**, p. 014102
- [34] Ustinova, I.A., Nikitin, A.A., Ustinov, A.B.: 'Dynamic magnonic crystal based on a layered ferrite-ferroelectric structure', *Tech. Phys.*, 2016, **61**, (3), pp. 473–476
- [35] Morozova, M.A., Matveev, O.V., Sharaevskii, Y.P., *et al.*: 'Tuning the bandgaps in a magnonic crystal-ferroelectric-magnonic crystal layered structure', *Phys. Solid State*, 2016, **58**, (2), pp. 273–279
- [36] Nikitin, A.A., Nikitin, A.A., Kondrashov, A.V., *et al.*: 'Theory of dual-tunable thin-film multiferroic magnonic crystal', *J. Appl. Phys.*, 2017, **122**, (15), p. 153903
- [37] Nikitin, A.A., Nikitin, A.A., Ustinov, A.B., *et al.*: 'Theory of spin-electromagnetic waves in planar thin-film multiferroic heterostructures based on a coplanar transmission line and its application for electromagnetic crystals', *IEEE Trans. Magn.*, 2018, **54**, (11), pp. 1–5
- [38] Ustinov, A.B., Drozdovskii, A.V., Nikitin, A.A., *et al.*: 'Dynamic electromagnetic crystal based on artificial multiferroic heterostructure', *Commun. Phys.*, 2019, **2**, p. 137
- [39] Lu, C., Hu, W., Tian, Y., *et al.*: 'Multiferroic oxide thin films and heterostructures', *Appl. Phys. Rev.*, 2015, **2**, (2), p. 021304
- [40] Vopson, M.M.: 'Fundamentals of multiferroic materials and their possible applications', *Crit. Rev. Solid State Mater. Sci.*, 2015, **40**, (4), pp. 223–250
- [41] Zhu, M., Nan, T., Peng, B., *et al.*: 'Advances in magnetism epitaxial multiferroic heterostructures and applications', *IEEE Trans. Magn.*, 2017, **53**, (10), pp. 1–16
- [42] Nikitin, A.A., Vitko, V.V., Nikitin, A.A., *et al.*: 'Dual tuning of doubly-hybridized spin-electromagnetic waves in all-thin-film multiferroic multilayers', *IEEE Trans. Magn.*, 2017, **53**, (11), pp. 1–5
- [43] Morozova, M.A., Romanenko, D.V., Matveev, O.V., *et al.*: 'Suppression of periodic spatial power transfer in a layered structure based on ferromagnetic films', *J. Magn. Magn. Mater.*, 2018, **466**, pp. 119–124
- [44] Graczyk, P., Zeleny, M., Krawczyk, M.: 'Co- and contra-directional vertical coupling between ferromagnetic layers with grating for short-wavelength spin wave generation', *New J. Phys.*, 2018, **20**, (5), p. 053021
- [45] Nikitin, A.A., Vitko, V.V., Nikitin, A.A., *et al.*: 'Miniature multiferroic interferometer for voltage-controlled spin-wave logic gates'. 2019 Photonics & Electromagnetics Research Symp.-Spring (PIERS-Spring), Italy, Rome, June 2019, pp. 1547–1551
- [46] Houzet, G., Burgines, L., Velu, G., *et al.*: 'Dispersion and loss of ferroelectric Ba_{0.5}Sr_{0.5}TiO₃ thin films up to 110 GHz', *Appl. Phys. Lett.*, 2008, **93**, (5), p. 053507
- [47] Demidov, V.E., Kalinikos, B.A., Karmanenko, S.F., *et al.*: 'Dispersion characteristics of the surface electromagnetic-spin waves in ferrite-ferroelectric-dielectric-metal structures', *Tech. Phys. Lett.*, 2002, **28**, (6), pp. 479–482
- [48] Huang, H.: 'Coupled mode theory: as applied to microwave and optical transmission' (VNU Science Press, Utrecht, The Netherlands, 1984)
- [49] Stancil, D.D., Prabhakar, A.: 'Spin waves: theory and applications' (Springer, New York, 2009)

ACTA UNIVERSITATIS LAPPEENRANTAENSIS

960. MALYSHEVA, JULIA. Faster than real-time simulation of fluid power-driven mechatronic machines. 2021. Diss.
961. SIEVINEN, HANNA. Role of the board of directors in the strategic renewal of later-generation family firms. 2021. Diss.
962. MENDOZA MARTINEZ, CLARA. Assessment of agro-forest and industrial residues potential as an alternative energy source. 2021. Diss.
963. OYEWU, AYOBAMI SOLOMON. Transition towards decarbonised power systems for sub-Saharan Africa by 2050. 2021. Diss.
964. LAHIKAINEN, KATJA. The emergence of a university-based entrepreneurship ecosystem. 2021. Diss.
965. ZHANG, TAO. Intelligent algorithms of a redundant robot system in a future fusion reactor. 2021. Diss.
966. YANCHUKOVICH, ALEXEI. Screening the critical locations of a fatigue-loaded welded structure using the energy-based approach. 2021. Diss.
967. PETROW, HENRI. Simulation and characterization of a front-end ASIC for gaseous muon detectors. 2021. Diss.
968. DONOGHUE, ILKKA. The role of Smart Connected Product-Service Systems in creating sustainable business ecosystems. 2021. Diss.
969. PIKKARAINEN, ARI. Development of learning methodology of additive manufacturing for mechanical engineering students in higher education. 2021. Diss.
970. HOFFER GARCÉS, ALVARO ERNESTO. Submersible permanent-magnet synchronous machine with a stainless core and unequal teeth widths. 2021. Diss.
971. PENTTILÄ, SAKARI. Utilizing an artificial neural network to feedback-control gas metal arc welding process parameters. 2021. Diss.
972. KESSE, MARTIN APPIAH. Artificial intelligence : a modern approach to increasing productivity and improving weld quality in TIG welding. 2021. Diss.
973. MUSONA, JACKSON. Sustainable entrepreneurial processes in bottom-of-the-pyramid settings. 2021. Diss.
974. NYAMEKYE, PATRICIA. Life cycle cost-driven design for additive manufacturing: the frontier to sustainable manufacturing in laser-based powder bed fusion. 2021. Diss.
975. SALWIN, MARIUSZ. Design of Product-Service Systems in printing industry. 2021. Diss.
976. YU, XINXIN. Contact modelling in multibody applications. 2021. Diss.
977. EL WALI, MOHAMMAD. Sustainability of phosphorus supply chain – circular economy approach. 2021. Diss.
978. PEÑALBA-AGUIRREZABALAGA, CARMELA. Marketing-specific intellectual capital: Conceptualisation, measurement and performance. 2021. Diss.

979. TOTH, ILONA. Thriving in modern knowledge work: Personal resources and challenging job demands as drivers for engagement at work. 2021. Diss.
980. UZHEGOVA, MARIA. Responsible business practices in internationalized SMEs. 2021. Diss.
981. JAISWAL, SURAJ. Coupling multibody dynamics and hydraulic actuators for indirect Kalman filtering and real-time simulation. 2021. Diss.
982. CLAUDELIN, ANNA. Climate change mitigation potential of Finnish households through consumption changes. 2021. Diss.
983. BOZORGMEHRI, BABAK. Finite element formulations for nonlinear beam problems based on the absolute nodal coordinate formulation. 2021. Diss.
984. BOGDANOV, DMITRII. Transition towards optimal renewable energy systems for sustainable development. 2021. Diss.
985. SALTAN, ANDREY. Revealing the state of software-as-a-service pricing. 2021. Diss.
986. FÖHR, JARNO. Raw material supply and its influence on profitability and life-cycle assessment of torrefied pellet production in Finland – Experiences from pilot-scale production. 2021. Diss.
987. MORTAZAVI, SINA. Mechanisms for fostering inclusive innovation at the base of the pyramid for community empowerment - Empirical evidence from the public and private sector. 2021. Diss.
988. CAMPOSANO, JOSÉ CARLOS. Integrating information systems across organizations in the construction industry. 2021. Diss.
989. LAUKALA, TEIJA. Controlling particle morphology in the in-situ formation of precipitated calcium carbonate-fiber composites. 2021. Diss.
990. SILLMAN, JANI. Decoupling protein production from agricultural land use. 2021. Diss.
991. KHADIM, QASIM. Multibody system dynamics driven product processes. 2021. Diss.
992. ABDULKAREEM, MARIAM. Environmental sustainability of geopolymer composites. 2021. Diss.
993. FAROQUE, ANISUR. Prior experience, entrepreneurial outcomes and decision making in internationalization. 2021. Diss.
994. URBANI, MICHELE. Maintenance policies optimization in the Industry 4.0 paradigm. 2021. Diss.
995. LAITINEN, VILLE. Laser powder bed fusion for the manufacture of Ni-Mn-Ga magnetic shape memory alloy actuators. 2021. Diss.
996. PITKÄOJA, ANTTI. Analysis of sorption-enhanced gasification for production of synthetic biofuels from solid biomass. 2021. Diss.
997. MASHLAKOV, ALEKSEI. Flexibility aggregation of local energy systems—interconnecting, forecasting, and scheduling. 2021. Diss.



ISBN 978-952-335-750-1
ISBN 978-952-335-751-8 (PDF)
ISSN-L 1456-4491
ISSN 1456-4491
Lappeenranta 2021